SAPIENZA
UNIVERSITÀ DI ROMA

Exoteric effects at nanoscopic interfaces

Uncommon negative compressibility of nanoporous materials and unexpected cavitation at liquid/liquid interfaces

Scuola dottorale in Scienze e tecnologie per l'innovazione industriale

Dottorato di Ricerca in Theoretical and Applied Mechanics – XXXV Ciclo

Candidate

Marco Tortora
ID number 1224415

Thesis Advisor

Prof. Carlo Massimo Casciola

Co-Advisor

Prof. Simone Meloni

2021/2022

Thesis defended on January 24, 2023,
in front of a Board of Examiners composed by:

Prof. Giuseppe Vairo (chairman)

Prof.ssa Erika Ottaviano

Prof. Mauro Sbragaglia

Exoteric effects at nanoscopic interfaces
Ph.D. thesis. Sapienza – University of Rome

This thesis has been typeset by LaTeX and the Sapthesis class.

Author's email: marco.tortora@uniroma1.it

Ai miei genitori

Contents

List of publications

Journal articles

- **M. Tortora**, S. Meloni, B. H. Tan, A. Giacomello, C.-D. Ohl, and C. M. Casciola, "The interplay among gas, liquid and solid interactions determines the stability of surface nanobubbles',' Nanoscale, vol. 12, pp. 22698–22709, 2020.

- **M. Tortora**, P. Zajdel, A. R. Lowe, M. Chorazewski, J. B. Leão, G. V. Jensen, M. Bleuel, A. Giacomello, C. M. Casciola, S. Meloni, and Y. Grosu, "Giant negative compressibility by liquid intrusion into superhydrophobic flexible nanoporous frameworks", Nano Letters, vol. 21, pp. 2848–2853, 04 2021.

- P. Zajdel, D. G. Madden, R. Babu, **M. Tortora**, D. Mirani, N. N. Tsyrin, L. Bartolomé, E. Amayuelas, D. Fairen-Jimenez, A. R. Lowe, M. Chorazewski, J. B. Leao, C. M. Brown, M. Bleuel, V. Stoudenets, C. M. Casciola, M. Echeverría, F. Bonilla, G. Grancini, S. Meloni, and Y. Grosu, "Turning molecular springs into nano-shock absorbers: The effect of macroscopic morphology and crystal size on the dynamic hysteresis of water intrusion–extrusion intofrom hydrophobic nanopores", ACS Applied Materials & Interfaces, vol. 14, pp. 26699–26713, 06 2022.

- P. Pfeiffer, M. Shahrooz, **M. Tortora**, C. M. Casciola, R. Holman, R. Salomir, S. Meloni, and C.-D. Ohl, "Heterogeneous cavitation from atomically smooth liquid-liquid interfaces", Nature Physics, 2022.

List of Figures

List of Tables

Abstract

This PhD thesis is devoted to the investigation of some peculiar effects happening at nanoscopic interfaces between immiscible liquids or liquids and solids via molecular dynamics simulations.

The study of the properties of interfaces at a nanoscopic scale is driven by the promise of many interesting technological applications, including: a novel technology for developing both eco-friendly energy storage devices in the form of mechanical batteries, as well as energy dissipation systems and, in particular, shock absorbers for the automotive market; biomedical applications related to cavitation, such as High-Intensity Focused Ultrasound (HIFU) ablation of cancer tissues and localised drug delivery, and many more.

The kinetics of phenomena taking places at these scales is typically determined by large free-energy barriers separating the initial and final states, and even intermediate metastable states, when they are present. Because of such barriers, the phenomena we are interested in are "rare events", i.e. the system attempts the crossing of the barrier(s) many times before finally succeeding when an energy fluctuation makes it possible. At the same time, the magnitude of the barrier is determined by the energetics and dynamics of atoms, which forces us to model the system by taking into account both the femtosecond atomistic timescale and the timescale of the relevant phenomena, typically exceeding the former by several orders of magnitude. These longer timescales are inaccessible to standard molecular dynamics, so, in order to tackle this issue, advanced MD techniques need to be employed.

The thesis is divided into two parts, corresponding to the main lines of research investigated, which are (I) the interfaces between water and complex nanoporous solids, and (II) planar solid-liquid and liquid-liquid interfaces. Anticipating some results, atomistic simulations helped uncovering the microscopic mechanism behind the (incredibly rare!) giant negative compressibility exhibited by the ZIF-8 metal organic framework (MOF) upon water intrusion. Molecular dynamics simulations also supported experimental results showing how it is possible to change the intermediate intrusion-extrusion performance of ZIF-8 by changing its grain morphology and arrangement, from a fine powder to compact monolith. Free-energy MD calculations allowed to explain the exceptional stability of surface nanobubbles in water, at undersaturated conditions, on a surprisingly wide variety of substrates, characterized by disparate hydrophobicities and gas affinities; and yet, how they catastrophically destabilize in organic solvents. Finally, through simulations, some light was shed upon the working mechanism behind the novelly discovered phenomenon of how the interface between two immiscible liquids can act as a nucleation site for cavitation.

Chapter 1

Introduction

An introduction to the research developed during the PhD program and its foreseen applications are found here. The chapter is divided into two sections, shadowing the the main areas the research focused on.

1.1 Porous lyophobic crystalline (PLC) materials and their applications

Porous systems with cavities of different size have been considered in many disciplines, including:

- chemistry, where these materials can be used for catalysis, thanks to their large contact area[4, 5, 6];
- physics, in which they are considered, for example, to study the peculiar properties of highly confined molecular or liquid systems[7, 8, 6, 9];
- medicine, where porous systems can be exploited for specific and controllable drugs release[10, 11, 12];
- engineering, in which nanofluidics became a hot topic[6].

Among the general porous systems, crystalline nanoporous ones, in which the porosity is determined by the regular distribution of atoms and molecules in a crystalline lattice, are very interesting because they are typically characterized by:

1) a very high specific surface area,
2) high porosity (ratio of empty over total volume),
3) high regularity of the characteristics of the pores,
4) and are highly designable, i.e. one can tune their characteristics by selecting suitable metal and linker components[13, 14, 15].

Among the other classes, (nano)porous lyophobic[1] crystalline (PLC) materials, such as metal organic frameworks (MOFs) or covalent organic frameworks (COFs), offer several advantages. PLCs can be designed and fabricated with controlled porous shape and size using well established laboratory and industrial techniques. Also, PLCs have, ideally, mono-disperse pores size (and shape), which simplifies the operativity of devices based on these materials (they have a well defined intrusion and extrusion pressure, intrusion kinetics, etc.). PLCs have high applicative potential. However, the development and use of PLCs requires understanding the wetting properties of these materials, possibly deriving a general theory that can complement capillary theory at the atomistic scale, together with degradation mechanism with intrusion/extrusion cycles.

1.1.1 Intrusion/extrusion processes in PLCs

Lyophobic nanoporous materials immersed in a liquid offer a unique opportunity not only to store, but also to transform or even dissipate energy through intrusion/extrusion processes (see Fig. 1.1).

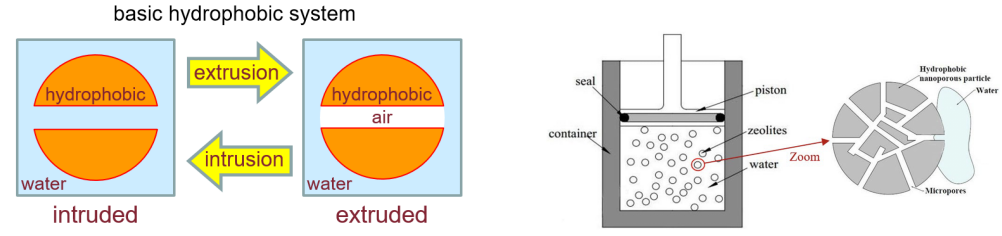

(a) **(b)**

Figure 1.1. On the right, schematization of the intrusion/extrusion processes for an hydrophobic system and on the left, sketch of the instrument used in the laboratory for the experiments (which could also represent an hypothetical device based on this technology).

Starting by thermodynamic conditions in which the liquid is extruded and then increasing the hydrostatic pressure up to a threshold value P_{int} (intrusion pressure), the liquid intrudes and is forced to wet the pores, building up the solid-liquid interface energy. Then, one of the following scenarios will happen:

A. just by releasing the external pressure slightly below the P_{int}, the liquid is extruded by the material and the stored energy is released;

B. only lowering the external pressure sizably below P_{int}, the liquid is extruded by the material and a part of the stored energy is released, while the rest of the energy is dissipated;

C. regardless of the external pressure, none of the liquid is extruded, hence all the energy is dissipated.

[1] the term lyophobic is a compound word made up of the Ancient Greek terms "lyo-", which stands for "solvent", and "-phobic", or "having aversion to"; so a lyophobic material is one which has no affinity towards the considered liquid.

The picture presented so far is actually over-simplified: in general, the intrusion and extrusion processes are characterized by continuous PV curves. The area between the intrusion and the extrusion curves quantifies the dissipated energy as well as the hysteresis of the system: the closer the two curves are, the lower the area, the lower the hysteresis, and vice versa.

In the following, I will assume the volume of the extruded liquid to be equal to that of the intruded liquid, and indicate with ΔV such volume; moreover, P_{ext} will represent the extrusion pressure (not the external pressure).

In case A, $P_{int} = P_{ext}$, hence $(P_{int} - P_{ext})\,\Delta V = 0$; so case A corresponds to null hysteresis, in fact it performs as a storage mechanism, which proves to be very effective and compact (stored energy density of the order of tens/hundreds of J/g).

In case B, $P_{int} > P_{ext}$, therefore an energy corresponding to $(P_{int} - P_{ext})\Delta V$ is wasted in the hysteresis cycle. This energy is dissipated as heat, increasing the temperature of the solid/liquid system. The energy dissipation appears to span a very broad range of frequencies., which makes a lyophobic system with (large) hysteresis an ideal device to absorb vibrations.

In case C, the energy given to the system is completely lost and can never be retrieved (the area between the curves is "infinite"). Even though such performance may appear to be counterproductive and useless, given the huge energy that the system can dissipate, one can think of shock-absorption applications.

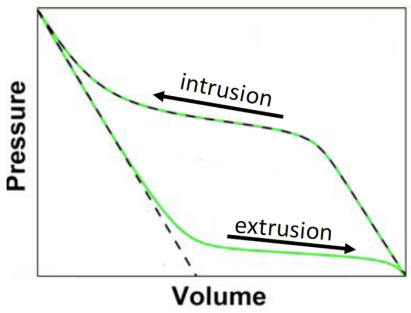

Figure 1.2. P-V chart sketch along an intrusion/extrusion process. Pressure is applied on the liquid until it reaches a critical value, P_{int}, when it penetrates the pores of the lyophobic material. Upon release of pressure, when it reaches the critical extrusion value P_{ext}, the liquid gets extruded from the porous material. Figure adapted from Ref. [1].

A realistic sketch of the pressure-volume trace of the intrusion/extrusion of a liquid in a porous lyophobic system is illustrated in Fig. 1.2. Hysteresis between these intrusion and extrusion processes can be significant, especially when the pore diameter is several nanometers.

1.1.2 Energy scavenging and energy dissipation applications in the automotive sector via shock absorbers

We already observed that the area enclosed by the hysteric loop is the mechanical energy that can, in principle, be recovered (scavenged). As shown very recently by our experimental collaborators of the Thermal Energy Storage Group at the CIC EnergiGUNE[16, 1], it is possible to transform a large part of this energy into

electric current[2] thanks to the triboelectric effect (a type of contact electrification by which two originally neutral bodies become electrically charged when brought into contact and then separated). To have an idea of the potential benefits of this energy scavenging approach, it is worth remarking that the power dissipated as thermal energy in shock absorbers goes from 400 W for city cars to 7.5 kW for large trucks or buses[17]. The recovery of even a fraction of this dissipated energy can significantly boost the efficiency of vehicles.

Shock absorbers[18] keep the tires of a vehicle in contact with the ground at all times by taking the kinetic energy of the suspension, i.e. absorbing vibrations, and converting it to thermal energy (i.e. heat) that is then dissipated into the atmosphere through convection. For the sake of simplicity, here the suspension of a vehicle can be identified with the springs connected to the tires. A spring is fully described by the spring constant k [N/m], which determines exactly how much force will be required to deform the spring: a higher spring constant means a stiffer spring, and vice-versa. In particular, the spring constant is related to the natural frequencies (or normal modes) of the spring, thus to the frequencies of the vibrations it can absorb. The spring constant can be expressed as

$$k = \frac{Gd^4}{8nD^3} \tag{1.1}$$

in other words, it depends upon the following parameters:

- the shear modulus G, which takes into account the material making up the spring, along with other physical properties of the spring;
- the wire diameter d, i.e. the diameter of the wire comprising the spring;
- the coil diameter D, i.e. the diameter of each coil, measuring the tightness of the coil;
- the number of active coils n, i.e. the number of coils that are free to expand and contract.

In general, helical (or coil) springs are preferred, because they allow to have a constant distance between each coil, hence to better control the number of active coils, granting the possibility to absorb a broader (yet still limited) range of frequencies.

Shock absorbers are basically oil pumps: a piston is attached to the end of a piston rod and works against a hydraulic fluid (oil) in the pressure tube. As the suspension is compressed/decompressed by the discontinuities of the road, the hydraulic fluid is forced through orifices inside the piston. Because the orifices only allow a small amount of fluid through the piston, the piston is slowed, which in turn slows down spring and suspension movement. The friction between the fluid and the piston generates heat, which raises the temperature of the shock absorbers and is then dissipated as described above.

Employing porous lyophobic materials for absorbing shocks and vibrations is an interesting technological application on its own. Indeed, if one cannot transform the energy corresponding to the hysteric loop into electric current, this gets dissipated as thermal energy. Suitably designing the system, one can:

[2] such possibility is being explored at this time within a project funded by the European Union

- dissipate a large amount of energy per intrusion/extrusion cycle, much larger than the energy dissipated by traditional shock absorbers;
- absorb vibrations over a very broad frequency spectrum[19], while standard vibration aborbers operate on a narrower band.

The suggested approach would allow to develop shock and vibration absorbers for a wide range of applications, even beyond the automotive sector, including aerospace, home appliances, industrial apparatuses and many more.

The intrusion and extrusion pressures and the energy associated to the process are related to the pore chemistry and morphology, and to the characteristics of the liquid (including solutions). Therefore, to make intrusion/extrusion efficient, for either electric energy production or energy dissipation, one has to maximize the area enclosed in the hysteric P-V loop and select or design porous materials and liquids with suitable values of the intrusion/extrusion pressure, within the operative range of the source of dissipated mechanical energy triggering the process.

Clearly, a large (lyophobic) pore surface implies that one has a large energy to transform into electric current or to dissipate when absorbing shocks or vibrations. In fact, the energetics of intrusion is related to the solid/liquid interface energy when the material is intruded by the liquid, hence to the solid/liquid interface area. Thus, metal-organic frameworks (MOFs), with their huge surface area per gram, are ideal candidates. Surprisingly, though the very narrow pores of few nanometers, some MOFs, e.g. ZIF-8 and Cu2(tebpz), have shown relatively low intrusion pressures, around $\sim$25 MPa,[16] which conflicts with macroscopic predictions relating the intrusion pressure to the size of the pores, more specifically to the so-called pores mouth, the aperture through which the liquid must pass through to enter in the porous system, or to pass from cavity to cavity.[20]

We remark that - even though here we focused on energy applications of porous lyophobic systems - MOFs, covalent organic frameworks (COFs), zeolites and others have a wider range of applications, including chromatography, controlled/enhanced drug delivery, water purification and many more. We expect our results to have impact in these fields as well.

1.1.3 Renewable energy sources and energy storage applications

In the last 70 years the rapid growth of the world population lead to a rise of the energy demand, especially in developing countries. Such situation results in the risk of depletion of cheap fossil energy and environmental pollution as well as climate change. According to prof. Noam Lior, editorial board member for many journals about energy resources and their environmental impact, there will probably be sufficient oil and gas for this century, and coal for 2 or more[21]. Industrialized countries decided to cooperate to tackle and hopefully solve these serious problems, signing the Kyoto Protocol and, more recently, the Accord de Paris. The EU even encompasses the issue of energy technologies and services in its White Paper on the future of Europe.

Energy production, storage and distribution are main subjects of scientific and technological research with high societal impact. Identification of renewable energy sources, energy scavenging to minimize waste of this resource, identification of novel

reservoirs of conventional sources of energy, e.g. clathrate hydrates of natural gas, are some of the research directions which have attracted significant attention of the scientific community, and often appeared on the media.

One of the problems to be addressed for the desirable shift from conventional to renewable energy sources is energy storage, which is the general subject of this project. Energy storage is necessary especially with renewable energies (e.g. solar, wind, and hydro energy), not only to compensate the temporal mismatch between production and use, but mainly because of their discontinuity. Indeed, renewable energy sources are inherently discontinuous: for example, solar energy is trivially bound to the day-night cycle; wind energy is tied to the weather conditions and the orientation of the turbines; hydro energy is highly dependent on the precipitation amounts. Due to their irregular availability, in order to properly harvest and exploit sustainable sources, new energy storage technologies have to be designed; the general guidelines such novel systems should aim to fulfill are the following: high energy density (the device should achieve the maximum possible stored energy per unit volume or per unit mass), high efficiency of energy transformation, durability, low price, eco-compatibility, no fire and explosion hazard.

Among electrical, chemical, thermal, and mechanical energy storage, the latter is the least developed. Three main strategies exist for the accumulation of mechanical energy: flywheels, compressed air, and pumped hydro energy. A flywheel is a gyroscope, i.e. a simple device, in principle, consisting of a wheel storing energy under the form of rotational energy. It provides very high energy density, efficiency, and good durability. However, flywheels have also severe drawbacks, such as that the wheel must be contained in a vacuum chamber. Compressed air energy storage is based on the thermodynamics of gasses: upon expansion, a gas, namely air, releases the energy which has been spent to compress it. Yet, also in this case its use suffers important shortcomings, such that utility plants require huge installations because of the low storage density, and heat generated during compression must not be dispersed to avoid a significant reduction of efficiency. Pumped hydro energy storage consists in pumping water from a lower to a higher reservoir. Here, a significant weakness is that this solution requires a suitable geographical location, with water basins of suitable size at suitable different quotes.

Mechanical storage offers advantages in terms of efficiency, simplicity of design, and hence lower price and environmental impact, especially for production of electrical energy from mechanical sources, e.g. wind and hydro energy. Indeed, mechanical-to-mechanical storage might be more efficient, eco-friendly, geopolitically neutral (does not need special materials and elements produced/extracted in few countries), and cost effective than other storage.

One technology satisfying all/most of these requirements is the storage of energy as interface energy through the intrusion/extrusion of a non-wetting liquid in a suitable porous material (Fig. 1.1): energy is stored during the charging process when forcing the non-wetting liquid to enter into the lyophobic pores of the solid during the intrusion step and it is released upon spontaneous extrusion when the application of external pressure is ceased. A simple yet profitable choice would be to couple water with an hydrophobic material: using water makes bio-compatibility much easier to guarantee, since any other liquid would likely be more complex to handle and dispose of.

The performance of the storage devices (mechanical batteries) and dampers hinges on the peculiar transitions of the liquid under extreme confinement: the intrusion of the liquid and its extrusion due to the nucleation and growth of a gas bubble within them. The conditions in which these transitions happen strongly depend on the morphology (pore size and distribution) and on the chemical composition of the confining material.

1.1.4 The need of an atomistic model

We explore here the reason why it was essential to adopt an atomistic approach to analyze the PLCs behavior.

1.1.4.1 The continuum model

Intrusion of liquid in a porous system can be described by the well established, macroscopic Kelvin and Young-Laplace equations.

Kelvin equation The Kelvin equation links the vapor pressure of a given species to the shape of its vapor-liquid interface, which is accounted for by means of its radius of curvature. The equation is equal to:

$$\ln \frac{p_r}{p_\infty} = \frac{2\gamma V_{mol}}{rRT}$$

where p_r is the actual vapor pressure when the radius of curvature is r, p_∞ is the saturated vapor pressure when the radius of curvature is ∞ (corresponding to a flat surface), γ is the surface tension, V_m is the molar volume of the liquid, R is the universal gas constant, and T is temperature.

As a simple example, let us consider the surface of a liquid in contact with its vapor phase: if the surface is convex, r is positive, $p_r > p_\infty$, and so the liquid tends to evaporate; inversely, when the surface is concave, r is negative, $p_r < p_\infty$, and so the vapor will tend to condensate. The Kelvin equation is completely general, in the sense that it is derived from thermodynamic principles and does not depend on the material.

Young-Laplace equation The Young-Laplace equation is a nonlinear pde governing the pressure difference across the interface between two static phases; more specifically, the Δp is related to the shape of the surface associated with the interface.

Derivation of the Young-Laplace equation Let us consider a membrane, described geometrically as a 2D differentiable manifold Σ embedded in a Euclidean 3D space. The conservation equation for the (linear) momentum of the membrane, analogous to that of hydrodynamics, is equal to:

$$\sigma \frac{\mathrm{D}\vec{u}}{\mathrm{D}t} = \nabla_\pi \cdot Q_\pi + \vec{t} \qquad \left[\frac{\mathrm{D}}{\mathrm{D}t} \coloneqq \frac{\partial}{\partial t} + \vec{u} \cdot \nabla\right]$$

where σ is the superficial mass density of the membrane, $u(x,t)$ is the (Eulerian) velocity field, ∇_π is the nabla operator on the plane tangent to the membrane, Q_π is

the superficial stress (tangent) tensor, which maps normal vectors (to the membrane) onto tangent ones, and (the last) t is the total body force per unit length acting on the membrane.
Often the dissipative phenomena for the mechanical energy turn out to be negligible, which allows to reduce the constitutive relation for Q_π to $Q_\pi = \gamma I_\pi$, being γ the surface tension and I_π the identity tangent tensor. Indicating with g_μ and g^ν the covariant and controvariant base vector of the tangent space (at a given point) of the membrane (the dependence on space and time is omitted as to simplify the notation), one finds:

$$I_\pi = I^\alpha_\beta \vec{g}_\alpha \otimes \vec{g}^{\,\beta} = I^{\alpha\beta}\vec{g}_\alpha \otimes \vec{g}_\beta$$
$$I^{\alpha\beta} = I^\alpha_\lambda g^{\lambda\beta} = \delta^\alpha_\lambda g^{\lambda\beta} = g^{\alpha\beta}$$

hence the identity tangent tensor is just the metric tensor g of the manifold representing the membrane. If $\hat{n}$ is the normal to the membrane, massaging the above equations yields:

$$\nabla_\pi \cdot Q_\pi = Q^{\alpha\beta}_{,\beta}\vec{g}_\alpha - C_{\alpha\beta}Q^{\alpha\beta}\hat{n}$$
$$\left[\text{where } Q^{\alpha\beta}_{,\beta} = \frac{\partial Q^{\alpha\beta}}{\partial \xi^\gamma} + \Gamma^\alpha_{\gamma\lambda}Q^{\lambda\beta} + \Gamma^\beta_{\gamma\lambda}Q^{\alpha\lambda}\right]$$

$$\sigma\frac{\mathrm{D}\vec{g}}{\mathrm{D}t} = \nabla_\pi \cdot Q_\pi + \vec{t} = \left(Q^{\alpha\beta}_{,\beta} + t^\alpha\right)\vec{g}_\alpha + \left(t_n - C_{\alpha\beta}Q^{\alpha\beta}\right)\hat{n} =$$
$$= \left(\frac{\partial\gamma}{\partial\xi^\beta}g^{\alpha\beta} + \cancel{\gamma g^{\alpha\beta}_{,\beta}} + t^\alpha\right)\vec{g}_\alpha + \left(t_n - \gamma g^{\alpha\beta}C_{\alpha\beta}\right)\hat{n} =$$
$$= \vec{t}_\pi + \nabla_\pi\gamma + (t_n - \gamma C^\alpha_\alpha)\,\hat{n} = 0 \quad \text{at equilibrium or stationarity}$$

The above expression can be broken into two parts:

$$\vec{t}_\pi + \nabla_\pi\gamma = 0$$

which accounts for the exchange of tangential forces between the membrane and the environment (e.g., Marangoni effect and coffee ring effect); and also

$$t_n = \gamma C^\alpha_\alpha = \gamma\left(\frac{1}{R_1} + \frac{1}{R_2}\right)$$

which is the Young-Laplace equation, according to which pressure gradients across the membrane induce a modification of its curvature, and vice versa. In the spherical interface approximation (where $R_1 = R_2 = R_0$), the YL eq. becomes

$$t_n = \gamma C^\alpha_\alpha = \gamma\frac{2}{R_0} \quad \longrightarrow \quad \Delta p = p_{inside} - p_{outside} = \gamma\frac{2}{R_0}$$

The Gibbs condition for intrusion states that: given a cylindrical cavity partially intruded by a liquid and complementarily filled by the corresponding vapor phase, indicating by θ the current contact angle, if $\theta > \theta_Y$, with θ_Y being the Young (equilibrium) contact angle, the liquid will keep advancing through the cavity, while if $\theta < \theta_Y$ the liquid will recede.

Being more precise, the current contact angle θ is evaluated with respect to the walls of the cylindrical pore during intrusion, and the plane of the pore during recession. This gives rise to pinning, i.e. a given interval of θ within which the liquid neither intrudes nor recedes.

If we hypothesize that in correspondence of $\theta = \theta_Y$ the pore (barely but actually) starts to get intruded by the liquid, we can use the YL eq. to estimate the intrusion pressure P_{int} as follows. The radius of the pore a can be related to the radius of curvature of the (approximately) spherical meniscus of liquid as:

$$a = R_0 \cos\theta_Y$$

Inverting the previous relations and noting that $P_{in} \gg P_{out} = 1\,\text{atm}$, one finds:

$$P_{int} = -2\frac{\gamma_{LV}\cos\theta_Y}{a}$$

1.1.4.2 Failure of the continuum model

The intrusion pressure of water in pores of several nanometers is still well described by the macroscopic Kelvin-Laplace equation[22, 23]; however, for smaller pores, significant deviations from this law arise due to various nanoscale effects. The modeling becomes even more complicated in the case of PLCs: fluids within these materials experience extreme confinement and are expected to substantially deviate from their bulk behavior, and thus macroscopic theories are expected to fail.

As an example, let us apply the equation found for P_{int} at the end of the previous section to deduce the intrusion pressure of water into ZIF-8 at room temperature: at the specified condition, the surface tension of water γ_{LV}^{W} is equal to 0.073 N/m, the Young contact angle θ_Y between water and ZIF-8 is around 130°, and, lastly, the characteristic size of the pores of ZIF-8 is around 1 nm, hence $a = 1$ nm. Plugging all these values into the equation, we get:

$$P_{int}^{\text{water/ZIF-8}} = -2\frac{\gamma_{LV}^{W}\cos\theta_Y}{a} = -2\frac{0.073\cdot\cos 130^\circ}{10^{-9}}\ \text{N/m}^2 \approx 94\ \text{MPa}$$

which is almost 4 times higher than the corresponding experimental value of 25 MPa!

In order to account for nanoscale effects, it proved to be necessary to adopt a different model, i.e. an atomistic one. But how does the continuum and the atomistic frameworks reconcile? Actually, this question was answered in a notorious paper by J. H. Irving and J. G. Kirkwood from 1950[24]. In the article, "the equations of hydrodynamics - continuity equation, equation of motion, and equation of energy transport - are derived by means of the classical statistical mechanics"; namely, the macroscopic quantities are expressed in terms of the atomic variables and the intermolecular forces, disclosing a one to one correspondence between the two theories.

1.1.4.3 The atomistic model

The atomistic model consists in breaking down the system into single particles (atoms and/or molecules) and studying their dynamics individually by means of

molecular dynamics (MD). The macroscopic properties of the whole structure are then retrieved averaging over the microscopic ones.

In MD, atoms are typically described as point charges with an associated mass, while molecules are represented as a number of atomic sites connected by bonds. The interaction between atoms is described by a potential, commonly known as a force field; the basic functional form of potential energy in molecular mechanics includes bonded and non-bonded terms. Bonded interactions includes bond stretches, bond angle bends, torsional rotations, improper dihedral angles, and so on, and allow to describe the interactions within molecules; on the other hand, non-bonded terms, namely electrostatic (computed based on Coulomb's law) and van der Waals forces, describe intermolecular interactions. The Lennard-Jones 12-6 potential is commonly used to represent van der Waals interactions. Additional terms related to coupling between different distortions or other interactions, such as hydrogen bonding, may also be present. The specific decomposition as well as the exact form of each term can vary from force field to force field.

The system evolves according to Hamilton's equations of motion, which are an alternative yet equivalent formulation of Newton's laws of motion and Euler-Lagrange equations. The Hamiltonian $H(q, p)$ is a function of the positions and the conjugate momenta of all the particles from which their time evolution equations can be easily derived as:

$$\dot{q} = \frac{\partial H}{\partial p}, \dot{p} = -\frac{\partial H}{\partial q}$$

The Hamiltonian,in most cases (e.g. it is not true for the Hamiltonian of a charged particle in an electromagnetic field), represents the total energy of the system, hence it can be written as the sum of the kinetic and the potential energy (i.e. the forcefield).

There are cases in which the equations of motion of a system cannot be derived by an Hamiltonian. Systems can be non-Hamiltonian as one operates in a set of non-canonical coordinates, i.e. a set of coordinates obtained from the Cartesian positions of the atoms via a non-canonical transformation, a transformation whose Jacobian is non-unit. This is the case, for example, of the equations of motion introduced to sample the constant temperature (NVT) and constant pressure (NPT) ensembles[25, 26, 27].

1.2 Cavitation-related effects and their applications

Cavitation is a phenomenon consisting in the formation of tension-induced bubbles, i.e. cavities, within a liquid at below-atmospheric- or negative-pressure regions. Such cavities nucleate where the pressure of the liquid is reduced to its vapour pressure; then, they expand as the pressure is further reduced along with the flow and suddenly collapse when they reach regions of higher pressure. The sudden growth and collapse of these bubbles produces a strong pressure wave, i.e. a shock wave, so intense that can nick and progressively damage the solid surfaces exposed to the cavitating liquid. This circumstance is commonly observed near the blades of centrifugal pumps, water turbines, and marine propellers. Cavitation is generally

an undesirable effect, because it produces extensive erosion of the solid, additional noise from the resultant knocking and vibrations, as well as a significant reduction of overall efficiency, because it distorts the flow pattern.

Up until today, the origin of heterogeneous cavitation was considered to be nucleation sites where stable gas cavities may dwell, e.g. on impurities, submerged surfaces or shell-stabilized microscopic bubbles. However, we found out that cavitation may also appear at the interface between two immiscible liquids (e.g., oil and water): the non-polar liquid of the two has a higher gas solubility and acts upon pressure reduction as a gas reservoir that accumulates at the interface.

On one side, this discovery casts a shadow over the possibility to cure this phenomenon, making it virtually impossible to avoid: in fact, as a result, cavitation would occur even if the solid were to be taken out of the system, because oils can create a gaseous thin film at the interface with water. In addition, separating two immiscible liquids is a much more complex operation (than separating a solid from a liquid), because oils tend to emulsify in water. Vice versa, on the bright side, this finding may find interesting applications in two areas, quite far from each other: the biomedical and fuel injectors fields.

Ultrasound drug delivery medical treatment[12] is particularly attractive as it is non-invasive, enables the regulation of tissue penetration depth, and does not rely on ionizing radiation. In addition, drug delivery approaches can be targeted, i.e. they can localize either the drug release or its activation at the target site, allowing to reduce its dosage and, in turn, its side-effects and/or toxicity. Ultrasound strategies that harness the mechanical activity of cavitation nuclei for beneficial therapeutic effects are actively under development.[11] The oscillations of circulating microbubbles (the most widely investigated cavitation nuclei) can be exploited to induce mechanical stresses on nearby tissue (up to its disrupture), as to permeabilize biological barriers and enable or enhance drug penetration, concentration and effectiveness. The same microbubbles may be used to encapsulate or shield a therapeutic agent in the bloodstream, to further improve localized uptake efficiency.

Ultrasound-Targeted Microbubble Destruction (UTMD)[12] is an ultrasound therapy, in which low-frequency moderate-power ultrasound is combined with microbubbles to trigger cavitation: microbubbles are intravenously injected and circulate freely in the blood vasculature; then, upon ultrasound exposure using a focused transducer, the interested microbubbles undergo cavitation, which produces shock-waves, which, in turn, lead to breakdown of cell junctions, cell membrane perforation, and tissue permeabilization.

High-Intensity Focused Ultrasound (HIFU)[28, 29, 30, 31] is another ultrasound therapeutic technique that hinges on ultrasonic waves to heat or ablate tissue, both benign and malignant. HIFU is non-ionizing and non-invasive, since ultrasound waves can pass through the skin and soft tissue without causing damage outside of the focal volume. For these reasons too, HIFU has been widely accepted for ablation[3] of a variety of solid tumors. The clinical applications of HIFU are rapidly growing, but safety is still a concern. The clinical use of HIFU is currently limited by the long treatment times (of the order of hours) and high acoustic powers required, which cause the formation of superficial skin burns. Microbubbles are known to

[3] ablation leads to coagulative necrosis or cellular apoptosis, i.e. the death of the cell.

reduce the acoustic energy required to induce heating and lesion formation; thus, they can be exploited to increase and tune the heating rate and/or lesion volumes achieved within each ultrasound exposure, hitting two birds with one stone. However, microbubbles present outside the targeted treatment area can also damage nearby healthy tissue. Also, microbubbles have a relatively short life-span in vivo, limiting the time over which they are effective during a HIFU surgical procedure.

The cited medical procedures can clearly benefit from a better understanding of how cavitating microbubbles formation and stabilization are affected by the presence of non-polar liquids which may act as gas reservoirs.

On a wildly different context, the performance and pollutant formation of a Diesel engine are heavily dependent on the characteristics of the spray produced by its injector nozzles. The spray development is directly determined by the flow inside the nozzle, therefore an improvement of the nozzle geometry and design can lead to a better atomisation behavior, and in turn to a better air-fuel mixing. There are experimental evidence and a rich bibliography (see for example[32, 33] and the citations therein) showing that cavitation within the nozzle modifies the characteristics of the nozzle exit spray. Thus, the above discovery (that cavitation may also appear at the interface between two immiscible liquids) may have a direct impact on this field: the understanding and potential control of cavitation within an engine could help improve combustion, both enhancing its efficiency and reducing its byproducts.

Chapter 2

Theory and methods

As it will be shown in the next chapters, the thermodynamic and the kinetic analysis of the considered phenomena (e.g., the intrusion/extrusion of water in/from ZIF-8) require the calculation of the expectation value of certain variables, i.e. the ensemble average of specific macroscopic observables expressed as functions of the *phase space* point $\mathbf{\Gamma} = (\mathbf{q}, \mathbf{p})$. Such expectation values cannot be evaluated analytically, but rather can only be estimated through numerical techniques, among which Molecular Dynamics.

Molecular Dynamics (MD) allows to solve numerically the equations of motions of systems of particles, representing atoms, interacting among them through an effective potential depending on their reciprocal position. The main objective of equilibrium classical MD is to compute the value of physical observables at equilibrium by sampling them and then averaging the homologous samples over time along the system's trajectory. Since the MD approach is based on the integration of the equations of motion, its methods can be extended to non-equilibrium conditions. Historically, the need to develop and adopt numerical tools arose from the impossibility to solve analytically the equations of motions describing real physical systems, since they are characterized by many degrees of freedom and highly non-linear atomic and molecular interactions. MD works hand in hand with statistical mechanics: while the former deals with the behavior of the microscopic components of a physical system, the latter aims to deduce from these its macroscopic properties. In other words, statistical mechanics builds a bridge between classical mechanics and thermodynamics.

In order to better understand the foundations of the research work of my PhD thesis, the next section is dedicated to a brief introduction to both theories. The second section in this chapter, on the other hand, deals with advanced MD methods that were exploited in my research, i.e. rare events techniques. These techniques, as the name suggests, allow to simulate phenomena which are intrinsically highly improbable, being associated with energy barriers that the system should overcome solely based on thermal fluctuations; however, such barriers as well as the related obstacles may be exceeded by properly tweaking the simulation conditions, as it will be shown.

2.1 A brief introduction to Statistical Mechanics and Molecular Dynamics

Let us consider an isolated classical system comprised of N particles in a volume V. The (microscopic) state of such system is uniquely defined once the canonical coordinates $q_1, q_2, \ldots, q_{3N}$ and the conjugate momenta $p_1, p_2, \ldots, p_{3N}$ of each one of the N particles are known Thus, the state of the system is described by a point in a $6N$-dimensional space, called the *phase space*, and its evolution in time can be represented as a trajectory in that same space.

The time evolution of an isolated system is governed by the Hamilton's equations

$$\begin{cases} \dot{q}_i = \dfrac{\partial H(\mathbf{\Gamma})}{\partial p_i} \\ \dot{p}_i = -\dfrac{\partial H(\mathbf{\Gamma})}{\partial q_i} \end{cases} \quad \text{or} \quad \begin{cases} \dot{\mathbf{q}} = \dfrac{\partial H(\mathbf{q},\mathbf{p})}{\partial \mathbf{p}}^T \\ \dot{\mathbf{p}} = -\dfrac{\partial H(\mathbf{q},\mathbf{p})}{\partial \mathbf{q}}^T \end{cases} \tag{2.1}$$

where $H(\mathbf{\Gamma})$ is the Hamiltonian function of the system[1] and

$$\mathbf{\Gamma} = (q_1, q_2, \ldots, q_{3N}, p_1, p_2, \ldots, p_{3N})^T = \left(\mathbf{q}^T, \mathbf{p}^T\right)^T \tag{2.2}$$

is a point in the phase space[2]. The points of the trajectory generated by the system of equations 2.1 belong to a $(6N-1)$-dimensional surface in the phase space, defined by the equation $H(\mathbf{\Gamma}) = E$, which is nothing else than the conservation law for the total energy E of the system.

Real physical systems are composed by a number of particles of the order of the Avogadro's number, $N_A = 6.02214076 \times 10^{23}$ mol^{-1}, interacting among them through highly non-linear potentials. In such circumstances, it is impossible to solve analytically the system of Hamilton's equations, and consequently to know position and velocity of each particle at every instant. However, one is interested in the macroscopic properties of the physical systems, rather than atomic-level details. That is the reason why the concept of Gibbs' ensemble was introduced and statistical mechanics was born.

[1] here we follow the so-called *numerator-layout convention*, where the derivative of a scalar with respect to a vector is a row vector.

[2] When canonical coordinates coincide with the positions of the particles, i.e.

$$(q_1, q_2, q_3, \ldots, q_{3N-2}, q_{3N-1}, q_{3N})^T = (r_{1x}, r_{1y}, r_{1z}, \ldots, r_{Nx}, r_{Ny}, r_{Nz})^T \coloneqq \mathbf{r} = \left(\mathbf{r}_1^T, \mathbf{r}_2^T, \ldots, \mathbf{r}_N^T\right)^T ,$$

and

$$(p_1, p_2, p_3, \ldots, p_{3N-2}, p_{3N-1}, p_{3N})^T = (p_{1x}, p_{1y}, p_{1z}, \ldots, p_{Nx}, p_{Ny}, p_{Nz})^T \coloneqq \mathbf{p} = \left(\mathbf{p}_1^T, \mathbf{p}_2^T, \ldots, \mathbf{p}_N^T\right)^T .$$

One can use the latter as independent variables for the Hamiltonian

$$H(\mathbf{r},\mathbf{p}) = H(\mathbf{r}_1, \mathbf{r}_2, \ldots, \mathbf{r}_N, \mathbf{p}_1, \mathbf{p}_2, \ldots, \mathbf{p}_N)$$

It is just a matter of notation. Doing so, the system 2.1 can be written in a perhaps more familiar fashion as:

$$\begin{cases} \mathbf{r}_i = \dfrac{\mathbf{p}_i}{m} \\ \mathbf{p}_i = \mathbf{F}_i\left(\mathbf{r}_1, \mathbf{r}_2, \ldots, \mathbf{r}_N\right) \end{cases}$$

An ensemble is a collection of copies of the same system, all characterized by the same value of a given set of macroscopic observables (i.e., physical quantities). To each ensemble is associated a probability density defined over the phase space. The ensemble corresponding to an isolated single-component non-reacting system is called microcanonical, and it is defined by 3 parameters: the number of particles N, the volume V and the total energy E. In fact, the microcanonic ensemble is also know as (N, V, E) ensemble.

A great variety of thermodynamic conditions can be modeled through ensembles: under the hypothesis of being at equilibrium, one can study systems coupled to a thermostat (a mechanism keeping the temperature constant), a barostat (a mechanism keeping the pressure constant), other mechanism keeping other quantities constant (i.e., the enthalpy), a reservoir of particles, and so on, defining a family of equilibrium ensembles. It is also possible to analyze out-of-equilibrium systems, i.e. systems subjected to external force fields; in such cases, we talk about non-equilibrium ensembles.

In general, the time-dependent ensemble probability density function over the phase space $\rho(\mathbf{\Gamma}, t)$ is defined such that $\rho(\mathbf{\Gamma}, t) \cdot \mathrm{d}\mathbf{\Gamma}$ is the probability, at time t, to find the system inside the volume $\mathrm{d}\mathbf{\Gamma}$ centered at the point $\mathbf{\Gamma}$. From such definition, it is clear that the following two conditions must hold for every t

$$\rho(\mathbf{\Gamma}, t) \geq 0\,, \tag{2.3}$$

$$\int \mathrm{d}\mathbf{\Gamma}\, \rho(\mathbf{\Gamma}, t) = 1 \tag{2.4}$$

The time evolution of the probability density function $\rho(\mathbf{\Gamma}, t)$ is described by the *Liouville's equation*, which can be derived[25] to be equal to

$$\frac{\mathrm{d}\rho}{\mathrm{d}t} = \frac{\partial \rho}{\partial t} + \dot{\mathbf{\Gamma}} \cdot \nabla_{\mathbf{\Gamma}} \rho = 0 \tag{2.5}$$

where

$$\dot{\mathbf{\Gamma}} = \left(\dot{\mathbf{q}}^T, \dot{\mathbf{p}}^T\right)^T = \left(\frac{\partial H}{\partial \mathbf{q}}, -\frac{\partial H}{\partial \mathbf{p}}\right)^T \tag{2.6}$$

and

$$\nabla_{\mathbf{\Gamma}} = \left(\frac{\partial}{\partial \mathbf{q}}, \frac{\partial}{\partial \mathbf{p}}\right) \tag{2.7}$$

Eq. 2.5 can be rewritten explicitly as

$$\frac{\mathrm{d}\rho}{\mathrm{d}t} = \frac{\partial \rho}{\partial t} + \frac{\partial \rho}{\partial \mathbf{q}} \cdot \frac{\partial H}{\partial \mathbf{p}} - \frac{\partial \rho}{\partial \mathbf{p}} \cdot \frac{\partial H}{\partial \mathbf{q}} = 0 \tag{2.8}$$

or even

$$\frac{\mathrm{d}\rho}{\mathrm{d}t} = \frac{\partial \rho}{\partial t} + \{\rho, H\} = 0 \tag{2.9}$$

having introduced the *Poisson brackets*, defined as

$$\{a, b\} = \frac{\partial a}{\partial \mathbf{q}} \cdot \frac{\partial b}{\partial \mathbf{p}} - \frac{\partial a}{\partial \mathbf{p}} \cdot \frac{\partial b}{\partial \mathbf{q}} \tag{2.10}$$

If the ensemble probability density is known, the macroscopic observables $O(t)$ we are interested in can be computed as the expectation values of homologous functions defined over the phase space $O(\mathbf{\Gamma})$

$$O(t) = \left\langle \hat{O}(\mathbf{\Gamma}) \right\rangle_t = \int \mathrm{d}\mathbf{\Gamma}\, \hat{O}(\mathbf{\Gamma})\, \rho(\mathbf{\Gamma}, t) \tag{2.11}$$

If $\rho(\mathbf{\Gamma}, t)$ has an explicit time dependence, then so will the observable $O(t)$, regardless whether the microscopic observable $\hat{O}(\mathbf{\Gamma})$ depends on time. On the other hand, a system in thermodynamic equilibrium, by definition, is in fixed thermodynamic state. This implies that the thermodynamic variables characterizing such equilibrium state do not change in time. As a consequence, if $O(t)$ is an equilibrium observable, the ensemble average in eq. 2.11 must yield a time-independent result, which is only possible if the ensemble distribution of a system in thermodynamic equilibrium has no explicit time dependence, i.e.

$$\frac{\partial \rho}{\partial t} = 0 \tag{2.12}$$

This will be the case, for example, when no external driving forces act on the system. When eq. 2.12 holds, the Liouville's equation 2.9 reduces to

$$\frac{\mathrm{d}\rho}{\mathrm{d}t} = \{\rho, H\} = 0 \tag{2.13}$$

The general solution to eq. 2.13 is any function $F(\ldots)$ of the Hamiltonian $H(\mathbf{q}, \mathbf{p})$

$$\rho(\mathbf{q}, \mathbf{p}) \propto F[H(\mathbf{q}, \mathbf{p})] \tag{2.14}$$

This is as much as we can say from eq. 2.13 without further information about the ensemble. In order to ensure that $f(\mathbf{q}, \mathbf{p})$ is properly normalized according to eq. 2.4, the solution can be rewritten as

$$\rho(\mathbf{q}, \mathbf{p}) = \frac{1}{Z} F[H(\mathbf{q}, \mathbf{p})] \tag{2.15}$$

where Z is defined to be

$$Z = \int \mathrm{d}\mathbf{\Gamma}\, F[H(\mathbf{q}, \mathbf{p})] \tag{2.16}$$

The quantity Z is referred to as the *partition function* and is one of the central quantities in equilibrium statistical mechanics. The partition function is a measure of the number of microscopic states in the phase space accessible at given thermodynamic conditions. Each ensemble has a specific partition function that depends on the macroscopic observables used to define the ensemble itself. It can be proven that the thermodynamic properties of a system are calculated as partial derivatives of the partition function. Recalling eq. 2.11, other equilibrium observables are computed in terms of the partition function as

$$O = \left\langle \hat{O}(\mathbf{\Gamma}) \right\rangle = \frac{1}{Z} \int \mathrm{d}\mathbf{\Gamma}\, \hat{O}(\mathbf{\Gamma})\, F[H(\mathbf{q},\mathbf{p})] = \tag{2.17}$$

$$= \frac{\int \mathrm{d}\mathbf{\Gamma}\, \hat{O}(\mathbf{\Gamma})\, F[H(\mathbf{q},\mathbf{p})]}{\int \mathrm{d}\mathbf{\Gamma}\, F[H(\mathbf{q},\mathbf{p})]} \tag{2.18}$$

Let us now consider the case of a system whose dynamics is stationary and such that, given an infinite amount of time[3], the system is able to visit all the accessible points $\mathbf{\Gamma} = (\mathbf{q},\mathbf{p})$ in the phase space (except sets of points of measure zero) with a frequency proportional to to their probability density $\rho(\mathbf{q},\mathbf{p})$. A system with this property is said to satisfy the so-called *ergodic hypothesis*, and thus to be *ergodic*. Upon the ergodic hypothesis, phase space averages can be replaced by time averages over the system's trajectory, obtained by integrating the equation of motion, according to

$$\left\langle \hat{O}(\mathbf{\Gamma}) \right\rangle = \frac{\int \mathrm{d}\mathbf{\Gamma}\, \hat{O}(\mathbf{\Gamma})\, F[H(\mathbf{q},\mathbf{p})]}{\int \mathrm{d}\mathbf{\Gamma}\, F[H(\mathbf{q},\mathbf{p})]} \overset{\text{ergodicity}}{=} \lim_{T \longrightarrow +\infty} \frac{1}{T} \int_{t_0}^{T} \mathrm{d}t\, O(t) = \bar{O} \tag{2.19}$$

To put it in different prospective, the phase-space points along a the trajectory of an ergodic system constitute a sampling of the probability density function of the considered ensemble.

2.2 Rare events techniques

Many processes under investigation in MD may implicate transitions between metastable states, i.e. minima in the free energy surface. If the energy required to pass from one metastable state to another is significantly higher than the thermal energy $k_B T$ available to the system, transitions would occur infrequently and, possibly, on timescales not accessible to MD. In such conditions, the system is expected to exhibit a persistent motion around one of the minima, preventing a complete sampling of the phase space. In other words, a metastable state is a state where the system can be trapped in by thermodynamic energy barriers; the higher these barriers with respect to the thermal energy available to the system, the more difficult will be for it to explore different states. A process involving the transition between metastable states is usually referred to as an *activated* or *rare event*. Simulating a system with metastabilities is computationally inefficient by standard MD: in fact, the system could take a considerable amount of time to overcome a barrier, therefore one would not be able to achieve convergence within the timescale accessible by atomistic simulations: the brute force integration of classical equations of motion 2.1 for a system made of thousand of particles can be typically carried out for a time interval up to hundreds of nanoseconds[4]. Several methods have been developed to cope with rare events. These are aimed at addressing typical questions, such as: the

[3] theoretically infinite, practivally big enough.

[4] a MD system is evolved in time with very small timesteps of the order of one femtosecond, 1 fs $= 10^{-15}$ s

identification of the mestastable states, the mechanism of the transition from one state to another, and the evaluation of the transition rate. In the following sections, two different rare events methods are discussed. The first is Restrained Molecular Dynamics (RMD), introducing a controlled bias, allows to efficiently sample the space of configurations (positions and velocities) of the system. From the output of the simulation, it is possible to estimate the gradient of the free energy, from which, by numerical integration, one obtains the free energy itself. The second technique that will be considered is the string method, which aims to calculate the minimum free energy path between to metastable states, in the space of a set of reaction coordinates, which is typically highly dimensional.

2.2.1 Collective variables and free energy

The free energy plays a crucial role in the framework of statistical mechanics. Related to the logarithm of the partition function, the free energy is the thermodynamic potential (in NVT or NPT ensemble) from which the other thermodynamic quantities can be derived via mathematical operations. Often, the free energy difference between two thermodynamic states is as important as the absolute free energy: e.g. free energy differences determine, among other things, weather a chemical reaction can proceed spontaneously or rather needs energy inputs from other sources, and are directly related to activity coefficients and equilibrium constants.

The free energy can be defined in function of one or more generalized coordinates in a system: this is the so-called *Landau free energy*. A famous example of this is given by the Ramachandran plot, which visualizes a free energy surface as a function of a pair of dihedral angles (ψ, ϕ) of amino acid residues in protein structure; the plot is a map of the stable conformations of the molecule, their relative stability, and the energy barriers among them.

In this chapter, we will properly recall the definition of *Landau free energy* and describe a way to sample it by means of *restrained molecular dynamics* (RMD); in other words, we will lay the theoretical foundation upon which the free energy calculation we conducted are based.

2.2.1.1 Collective variables

Quite often, it is convenient to describe a generic thermodyamical process in terms of a reduced set of n generalized coordinates q_α, which can be expressed as a function of the coordinates of the N particles composing the system:

$$q_\alpha = f_\alpha(\mathbf{r}_1, \ldots, \mathbf{r}_N) \ , \ \text{with } \alpha = 1, 2, \ldots, n \, . \tag{2.20}$$

The q_αs are typically referred to as *reaction coordinates*, *collective variables* or *order parameters*, depending on the context and type of system.

A simple yet effective example of a collective variable is the following: let us consider the dissociation of a diatomic gas into two species, AB $\longrightarrow$ A + B, and assume that their interaction potential depends only on the relative distance $r = |\mathbf{r}_B - \mathbf{r}_A|$ between the two atoms A and B. Then a collective variable which characterizes the process could be r itself.

Collective variables can be very useful and powerful investigation tools, however, poorly chosen ones can bias the system and thus lead to flawed results and identifying good reaction coordinates for complex systems is far from trivial. In fact, there is not a step-by-step procedure to define these variables, so often they are chosen purely by intuition or based on the positive outcomes of previous works on similar settings. Also, to these days, the validation of these variables can only be done *a posteriori*, via the so-called committor analysis, and it is also quite expensive to carry out. Aware of the possible issues, in the next section we will describe the sampling method along a preselected reaction coordinate which was employed in our calculations.

2.2.1.2 Landau free energy

The probability density that n collective variables q_α, for which eq. 2.20 holds, will take values s_α in the canonical ensemble is given by

$$\begin{aligned} P(s_1,\dots,s_n) &= \left\langle \prod_{\alpha=1}^{n} \delta(f_\alpha(\mathbf{r}) - s_\alpha) \right\rangle = \\ &= \frac{C_N}{Q(N,V,T)} \int \mathrm{d}^N\mathbf{r}\ \mathrm{d}^N\mathbf{p}\ e^{-\beta H(\mathbf{r},\mathbf{p})} \prod_{\alpha=1}^{n} \delta(f_\alpha(\mathbf{r}) - s_\alpha)\ , \end{aligned} \tag{2.21}$$

where $Q(N,V,T)$ is the canonical partition function,

$$Q(N,V,T) = C_N \int \mathrm{d}^N\mathbf{r}\ \mathrm{d}^N\mathbf{p}\ e^{-\beta H(\mathbf{r},\mathbf{p})}\ , \tag{2.22}$$

and constant pre-factors were grouped in the term C_N, which is given by

$$C_N = \frac{1}{N!\,h^{3N}}\ . \tag{2.23}$$

Also, the following contractions have been made in order to slightly simply the notation: $H(\mathbf{r}_1,\dots,\mathbf{r}_N,\mathbf{p}_1,\dots,\mathbf{p}_N) \equiv H(\mathbf{r},\mathbf{p})$ and $f_\alpha(\mathbf{r}_1,\dots,\mathbf{r}_N) \equiv f_\alpha(\mathbf{r})$.

Despite appearing a bit intimidating, eq. 2.21 as a straightforward interpretation: it is an ensemble average, i.e. the ratio between the number of states having certain features, versus the total number of available states, both properly weighted according to the probability density of the given ensemble. The counting operation is carried out by integrals over the system phase space, thus we can deduce that the delta functions at the numerator of eq. 2.21 perform the selection of the states we are interested in. Indeed, from a geometrical point of view, integrating n delta functions over an N dimensional space corresponds to compute the $(N-n)$-hypervolume identified by (setting to zero) the deltas arguments, which in our case conveniently represent the conditions $q_\alpha = s_\alpha$.

From $P(s_1,\dots,s_n)$, one defines the *Landau free energy* as

$$A(s_1,\dots,s_n) = -k_B T \ln P(s_1,\dots,s_n)\ . \tag{2.24}$$

In the above definition, the logarithm serves the purpose of taming the sharp changes of probability from one point to another; on the other hand, the factor

kT, which gives $A(s_1, \ldots, s_n)$ the units of energy, is introduced just to comply with an historical language, as one could address the subject only in terms of probability. In the present research, using an "energy language" is functional to the combination of the microscopic description of hydrophobic attraction and the macroscopic characterization of nanobubbles dynamics and stability.

In our simulations we will deal not only with the canonical, but with the isothermal-isobaric ensemble as well. Fortunately, the generalization is straightforward. In order to prove it, now we show how to extend the definitions of $P(s_1, \ldots, s_n)$ and its associated free energy to the NPT case. Instead, from the next section, all the calculations will be only carried out in the canonical ensemble. The probability density $P(s_1, \ldots, s_n)$ in the NPT ensemble is equal to

$$P(s_1, \ldots, s_n) = \left\langle \prod_{\alpha=1}^{n} \delta(f_\alpha(\mathbf{r}) - s_\alpha) \right\rangle = \tag{2.25}$$
$$= \frac{I_N}{\Delta(N,V,T)} \int_0^\infty \mathrm{d}V \int \mathrm{d}^N\mathbf{r}\, \mathrm{d}^N\mathbf{p}\, e^{-\beta(H(\mathbf{r},\mathbf{p})+PV)} \prod_{\alpha=1}^{n} \delta(f_\alpha(\mathbf{r}) - s_\alpha) \ ,$$

where now $\Delta(N,V,T)$ is the NPT partition function,

$$\Delta(N,P,T) = I_N \int_0^\infty \mathrm{d}V \int \mathrm{d}^N\mathbf{r}\, \mathrm{d}^N\mathbf{p}\, e^{-\beta(H(\mathbf{r},\mathbf{p})+PV)} =$$
$$= \frac{1}{V_0} \int_0^\infty \mathrm{d}V\, e^{-\beta PV} Q(N,V,T) \ , \tag{2.26}$$

and the factor I_N is given by

$$I_N = \frac{1}{V_0 N! h^{3N}} = \frac{C_N}{V_0} \ , \tag{2.27}$$

where V_0 is a reference volume to make the overall expression dimensionless.

In this setting, *Landau free energy* naturally becomes

$$G(s_1, \ldots, s_n) = -k_B T \ln P(s_1, \ldots, s_n) \ . \tag{2.28}$$

It is worth remarking how the letters A and G identifying the Landau free energy in the canonical and NPT ensemble, echoes those representing the *Helmholtz* and *Gibbs free energies*. This comes from the fact that the latter quantities are linked to the canonical and isothermal-isobaric partition functions, respectively, by relations analogous to eqn. 2.21 and eqn. 2.25:

$$A(N,V,T) = -k_B T \ln Q(N,V,T) \ , \tag{2.29}$$
$$G(N,P,T) = -k_B T \ln \Delta(N,P,T) \tag{2.30}$$

According to eqn. 2.26, the NPT partition function is the Laplace transform of the canonical partition function w.r.t. volume, just as the canonical partition function is the Laplace transform of the microcanonical partition function w.r.t. energy. In both cases, the variable used to form the Laplace transform between partition functions is the same variable used to form the Legendre transform between the corresponding thermodynamic potentials[25]. The possibility of changing the order of integration, given by the fact that V is independent of $\mathbf{r}$ and $\mathbf{p}$ and vice versa, is the very key element which makes elementary to extend all the results one gets for the canonical ensemble to NPT.

2.2.2 Free energy calculation through Restrained Molecular Dynamics (RMD)

In our work, the status of the system was monitored using a single reaction coordinate, so from now on let us limit to consider the case of $\alpha = 1$, setting $s_1 \equiv s$, $q_1 \equiv q$ and $f_1 \equiv f$. Before proceeding, we remark that, in principle, one could achieve the same result by: (i) running a single, long, unbiased MD, (ii) compute the histogram of $f(\mathbf{r})$ and (iii) by taking the log of the histogram to compute the free energy. However, since the probability of sampling a point in the configuration space decreases exponentially with the value of the corresponding potential energy, this approach requires infeasibly long simulations to sample points far from the minimum of the potential $V(\mathbf{r})$. RMD solves this problem by biasing the potential so as to "shift the minimum" along the relevant range of values of the collective coordinate.

Restrained molecular dynamics is one of many techniques that allow to calculate the Landau free energy. Actually, RMD does not yield $A(s)$ directly, but rather its gradient

$$\frac{\mathrm{d}A}{\mathrm{d}s} = -\frac{k_B T}{P(s)} \frac{\mathrm{d}P}{\mathrm{d}s} \ , \tag{2.31}$$

from which the free energy profile $A(q)$ along the collective variable can be retrieved by integration

$$A(q) = A(s^{(i)}) + \int_{s^{(i)}}^{q} \frac{\mathrm{d}A}{\mathrm{d}s} \, \mathrm{d}s \ . \tag{2.32}$$

The reason of this bizarre procedure will be clarified shortly. The term $A(s^{(i)})$ is just the integration constant that can be neglected, setting it equal to zero, or adequately adjusted, e.g. so that the convergence value of the profile corresponds to $A(\infty) = A(s^{(f)}) = 0$. In practice, the integral in eqn. 2.32 is evaluated numerically on the set of points $s^{(1)}, \ldots, s^{(n)}$ where the gradient of $A(s)$ has been computed. The opposite of the gradient of $A(s)$ is called *mean force*; thus, the free energy profile $A(q)$ is also known as the *potential of mean force*, because it can be treated as an effective potential that governs the dynamics of the collective variable q.

Let us now compute the derivative in eqn. 2.31; from 2.21, one can write

$$\frac{1}{P(s)} \frac{\mathrm{d}P}{\mathrm{d}s} = \frac{\displaystyle\int \mathrm{d}^N\mathbf{r} \, \mathrm{d}^N\mathbf{p} \; e^{-\beta H(\mathbf{r},\mathbf{p})} \frac{\partial}{\partial s} \delta(f(\mathbf{r}) - s)}{\displaystyle\int \mathrm{d}^N\mathbf{r} \, \mathrm{d}^N\mathbf{p} \; e^{-\beta H(\mathbf{r},\mathbf{p})} \delta(f(\mathbf{r}) - s)} \ , \tag{2.33}$$

There are multiples ways to proceed from this point (for examples, one could check [25]). However, let us consider the following: in eqn. 2.33, one can replace the Dirac delta functions with a smooth Gaussian approximation,

$$\sqrt{\frac{\beta\kappa}{2\pi}} \exp\left\{ \left(-\frac{1}{2} \beta\kappa \left(f(\mathbf{r}) - s \right)^2 \right) \right\} \ ; \tag{2.34}$$

within such approximation, and assuming a standard Hamiltonian

$$H(\mathbf{r},\mathbf{p}) = \frac{\mathbf{p}^2}{2m} + V(\mathbf{r}) \ , \tag{2.35}$$

eqn. 2.33 becomes

$$\begin{aligned}\frac{1}{P(s)}\frac{\mathrm{d}P}{\mathrm{d}s} &\approx \frac{\int \mathrm{d}^N\mathbf{r}\ e^{-\beta V(\mathbf{r})}\frac{\partial}{\partial s}\exp\left\{\left(-\frac{1}{2}\beta\kappa\left(f(\mathbf{r})-s\right)^2\right)\right\}}{\int \mathrm{d}^N\mathbf{r}\ e^{-\beta V(\mathbf{r})}\exp\left\{\left(-\frac{1}{2}\beta\kappa\left(f(\mathbf{r})-s\right)^2\right)\right\}} = \\ &= \frac{\int \mathrm{d}^N\mathbf{r}\ \left(\beta\kappa\left(f(\mathbf{r})-s\right)\right)e^{-\beta V(\mathbf{r})}\exp\left\{\left(-\frac{1}{2}\beta\kappa\left(f(\mathbf{r})-s\right)^2\right)\right\}}{\int \mathrm{d}^N\mathbf{r}\ e^{-\beta V(\mathbf{r})}\exp\left\{\left(-\frac{1}{2}\beta\kappa\left(f(\mathbf{r})-s\right)^2\right)\right\}} \ .\end{aligned} \tag{2.36}$$

In terms of the derivative of the free energy, the above equation reads

$$\frac{\mathrm{d}A}{\mathrm{d}s} \approx \frac{\int \mathrm{d}^N\mathbf{r}\ \left(-\kappa\left(f(\mathbf{r})-s\right)\right)\exp\left\{\left[-\beta\left(V(\mathbf{r})+\frac{1}{2}\kappa\left(f(\mathbf{r})-s\right)^2\right)\right]\right\}}{\int \mathrm{d}^N\mathbf{r}\ \exp\left\{\left[-\beta\left(V(\mathbf{r})+\frac{1}{2}\kappa\left(f(\mathbf{r})-s\right)^2\right)\right]\right\}} \tag{2.37}$$

It is worth noting that this is not the same as having a mechanical constraint, since the condition $\dot{q}=0$ is not established. As for the Dirac approximation, eqn.s 2.36 and 2.37 become exact in the limit of $\kappa \to \infty$.

Assuming the validity of the ergodic hypothesis within the constrained distribution, i.e. that do not exist any other degrees of freedom bearing metastabilities apart from q_α, the ensemble average in eqn. 2.37 can be computed as a time average

$$\lim_{\mathcal{T}\to+\infty}\frac{1}{\mathcal{T}}\int_{t_0}^{\mathcal{T}}\mathrm{d}t\ \left[-\kappa\left(f(\mathbf{r})-s\right)\right] \ , \tag{2.38}$$

where $\mathbf{r}=\mathbf{r}(t)$ is the configuration part of the trajectory curve driven by the extended potential

$$V(\mathbf{r}) + \frac{1}{2}\kappa\left(f(\mathbf{r})-s\right)^2 \ .$$

Eq. 2.38 can be approximated by a sum over discrete times (with N being the number of integration steps)

$$\frac{1}{N}\sum_{k=1}^{N}\left\{-\kappa\left[f\left(\mathbf{r}\left(k\Delta t\right)\right)-s\right]\right\} \ , \tag{2.39}$$

over an NVT MD driven by the *augmented potential* $V(\mathbf{r})+\frac{1}{2}\kappa\left(f(\mathbf{r})-s\right)^2$, the so called restrained molecular dynamics, or RMD. This last point is subtle but crucial: in this technique one is using MD as a mere sampling tool for the phase space of the system being studied. In other words, the MD trajectory generated by the simulations can not be interpreted as the actual time evolution, because it is driven by a biased potential; rather, the trajectory is just a sequence of points of a sample of the system configurations under the specified conditions. From this point of view,

the above discretized time average conceptually reduces to a plain average between the values assumed by the quantity $-\kappa\left[f(\mathbf{r}\left(k\Delta t\right))-s\right]$, which in our case is the force exerted by the constraint and felt by the reaction coordinate q: it is no coincidence $\mathrm{d}A/\mathrm{d}s$ is called *mean force*. However, since those values are extracted from a MD, they will most likely preserve some level of correlation, which de facto will cut down the number of actually useful samples. In order to properly account for this effect, one must perform an error analysis such as binning or Jackknife analysis.

2.2.2.1 Estimation of the error on the free energy

The error on a derived observable $O=O\left(s\right)$, with s being the variable that is directly measured, is usually obtained by error propagation:

$$\delta O^2=\left(\frac{\mathrm{d}O\left(s\right)}{\mathrm{d}x}\delta s\right)^2 \tag{2.40}$$

Here, δs^2 and δO^2 are the variances of s and the estimated variance of O, respectively. Assuming that the error on O is pure statistical error, δO or low multiples - $2\delta O$, $3\delta O$, etc. – are a good estimation of error. However, δO obtained from error propagation is an upper bound of the actual statistical error of a derived observable.

In free energy calculations or analogous techniques, e.g., RMD, where the free energy $A(s)$ is obtained (cfr. eq. 2.37) by numerical integration of

$$A'(s)=\frac{\mathrm{d}A(s)}{\mathrm{d}s}\,, \tag{2.41}$$

error propagation (eq. 2.40) brings to a severe overestimation of the error on $A(s)$:

$$\delta A(s_i^*)^2=\sum_{i=1}\frac{A'(s_i^*)^2+A'\left(s_{i-1}^*\right)^2}{2}\left(\delta s_i^*-\delta s_{i-1}^*\right)^2 \tag{2.42}$$

where s_i^* represents a realization of the variable s. To reduce the overestimation, one can use a different approach[34, 7, 20, 35, 36]: let us say we have a set of N points s_i^*

$$\{s_i^*\}_{i=1,\ldots,N}\ ; \tag{2.43}$$

for each s_i^*, we divide the M configurations used to estimate $A'(s_i^*)$,

$$\left\{A'_j(s_i^*)\right\}_{j=1,\ldots,M}\,, \tag{2.44}$$

into L smaller sets S_k (L being a divisor of M, i.e., $M/L=h$, where h is a positive integer) :

$$\left\{\left\{A'_j(s_i^*)\right\}_{A'_j\in S_1},\left\{A'_j(s_i^*)\right\}_{A'_j\in S_2},\ldots,\left\{A'_j(s_i^*)\right\}_{A'_j\in S_k},\ldots,\left\{A'_j(s_i^*)\right\}_{A'_j\in S_L}\right\} \tag{2.45}$$

For each s_i^*, the sets S_k are defined in same way and, for example, can be taken as follows:

$$S_1 = \{A'_1(s_i^*), A'_2(s_i^*), \ldots, A'_n(s_i^*)\} \tag{2.46}$$
$$S_2 = \{A'_{n+1}(s_i^*), A'_{n+2}(s_i^*), \ldots, A'_{2n}(s_i^*)\} \tag{2.47}$$
$$\vdots \tag{2.48}$$
$$S_k = \left\{A'_{(n-1)k+1}(s_i^*), A'_{(n-1)k+2}(s_i^*), \ldots, A'_{nk}(s_i^*)\right\} \tag{2.49}$$
$$\vdots \tag{2.50}$$
$$S_L = \{A'_{L-n+1}(s_i^*), A'_{L-n+2}(s_i^*), \ldots, A'_L(s_i^*)\} \tag{2.51}$$

Now, taking the same group, say the k-th, for each s_i^*, we get:

$$\left\{\left\{A'_j(s_1^*)\right\}_{A'_j \in S_k}, \left\{A'_j(s_2^*)\right\}_{A'_j \in S_k}, \ldots, \left\{A'_j(s_N^*)\right\}_{A'_j \in S_k}\right\} \tag{2.52}$$

from which, taking the mean of each sub-set,

$$\bar{A}'_{(k)}(s_1^*) = \frac{1}{h} \sum_{\substack{j=1 \\ A'_j \in S_k}}^{h} A'_j(s_1^*) \ , \tag{2.53}$$

we obtain an estimate profile of the mean force

$$\left\{\bar{A}'_{(k)}(s_1^*), \bar{A}'_{(k)}(s_2^*), \ldots, \bar{A}'_{(k)}(s_N^*)\right\} \tag{2.54}$$

For each series of gradients of the free energy like this one, one obtains by numerical integration the corresponding free energy curve

$$\left\{A_{(k)}(s_1^*), A_{(k)}(s_2^*), \ldots, A_{(k)}(s_N^*)\right\} \tag{2.55}$$

The set of all such free energy profiles can be used to directly compute the variance $\delta A(s_i^*)^2$ at each value s_i^*:

$$\delta A(s_i^*)^2 = \frac{1}{L-1} \sum_{k=1}^{L} \left[A_{(k)}(s_i^*) - A(s_i^*)\right]^2 \tag{2.56}$$

Here, $A(s_i)$ is obtained from the numerical integration of $A'(s_i)$ determined with the complete set of simulation data. Correlation effects can be properly taken into account by using standard techniques, such as, for example, the *block average* or the *Jackknife* methods[37].

2.2.2.2 Restraining a particle's degree of freedom

In my work about nanobubbles[38], I used a single collective variable z, defined as the coordinate of a N_2 molecule COM orthogonal to a given surface:

$$z = z(z_{N1}, z_{N2}) = \frac{z_{N1} + z_{N2}}{2} \ . \tag{2.57}$$

where z_{N1} and z_{N2} represent the z-coordinate of the first and the second nitrogen atoms respectively. Basically, through z, I managed to keep track of the N_2 distance

from the surface and observe how the effective force felt by the nitrogen molecule changed w.r.t. it.

In order to find the Landau free energy associated with z, I had to run NVT/NPT RMD adding to the physical potential $V(\mathbf{r})$ the extra term

$$V(z) = \frac{1}{2}\kappa \left(z(z_{N1}, z_{N2}) - z^*\right)^2 \ , \tag{2.58}$$

where z^* was fixed to a prescribed value. The implementation of 2.58 is not obvious, because it demand for the ability to write a function of the atoms coordinates, something not every MD simulator is configured to do. Fortunately, such functionality is integrated within LAMMPS, so I was able to define the function z, use it to evaluate the force acting on each nitrogen atom as

$$F_{N1} = -\frac{\partial}{\partial z_{N1}} V(z) = -\frac{\kappa}{2}\left(z - z^*\right) \ , \tag{2.59}$$

$$F_{N2} = -\frac{\partial}{\partial z_{N2}} V(z) = -\frac{\kappa}{2}\left(z - z^*\right) \ , \tag{2.60}$$

and finally, apply such forces upon their destination atoms. I want to remark, however, that the *mean force* is the force acting on the N_2 COM, i.e.

$$F_{N_2} = -\frac{\partial}{\partial z} V(z) = -\kappa \left(z - z^*\right) \ , \tag{2.61}$$

which one obviously recognizes being equal to the sum of 2.59 and 2.60; this quantity was the one printed in LAMMPS output and elaborated through post-processing.

2.2.2.3 Restraining particles in a target domain

An indicator (or characteristic) function is a function that indicates if a given element from its domain belongs to a target subset of the domain itself. If X is the entire domain and A is a subset of X, the indicator function associated to A is defined to assume the value 1 for all elements of A and the value 0 for all elements of X not in A:

$$\mathbf{1}_A(x) \coloneqq \begin{cases} 0, & \text{if } x \in A \\ 1, & \text{if } x \notin A \end{cases} \tag{2.62}$$

An indicator function can easily be used to build a counter. Let us consider a collection of N elements, e.g. N particles, scattered in 3D space and a target volume region Ω; then, the sum of N indicator functions associated to Ω, each evaluated at the position of a different particle, is, by definition, the number Φ of items inside it:

$$\Phi(r_1, \ldots, r_N) = \sum_{i=1}^{N} \mathbf{1}_\Omega(r_i) \tag{2.63}$$

Notice how Φ is a function of the positions of all the N particles.

The Heaviside step function $\Theta(x)$ constitutes an example of indicator function; in fact, $\Theta(x)$ is the indicator function of the one-dimensional positive half-line, i.e. the domain $[0, \infty)$. The definition[5] of the Heaviside step function is

$$\Theta(x) \coloneqq \begin{cases} 0, & \text{for } x < 0 \\ 1, & \text{for } x \leq 0 \end{cases} \tag{2.64}$$

Combining multiple Heaviside functions, one can easily build indicator functions for different regions of space. For example, the difference between two conveniently translated Θs corresponds to the indicator function of a given closed interval, as follows[6]

$$\mathbf{1}_{[x_{\min}, x_{\max}]} = \Theta(x - x_{\min}) - \Theta(x - x_{\max}) \tag{2.65}$$

Then, multiplying three of these, one will get the indicator function for a 3D box region

$$\begin{aligned} \mathbf{1}_{[x_{\min}, x_{\max}] \times [y_{\min}, y_{\max}] \times [z_{\min}, z_{\max}]} &= \mathbf{1}_{[x_{\min}, x_{\max}]} \mathbf{1}_{[y_{\min}, y_{\max}]} \mathbf{1}_{[z_{\min}, z_{\max}]} = \qquad (2.66) \\ &= [\Theta(x - x_{\min}) - \Theta(x - x_{\max})] \\ &\quad [\Theta(y - y_{\min}) - \Theta(y - y_{\max})] \\ &\quad [\Theta(z - z_{\min}) - \Theta(z - z_{\max})] \qquad (2.67) \end{aligned}$$

Now, what we are really interested in is to impose a restraint on the number of particles inside a given domain, not just to count them; in other words, we must be able to push and pull objects in or out of the target region. This is achievable by subjecting the particles to an harmonic potential of the form

$$U_{\text{res}} = \frac{1}{2} \kappa \big[\Phi(r_1, \ldots, r_N) - \Phi^* \big]^2 \tag{2.68}$$

The negative gradient of such potential translates into a conservative force, proportional to the difference between the current number of particles inside the region and the target value, and directed inward the domain if it is underpopulated and outward in the opposite case. Using the following notation

$$\nabla_{r_i} = \frac{\partial}{\partial r_i} = \left(\frac{\partial}{\partial x_i}, \frac{\partial}{\partial y_i}, \frac{\partial}{\partial z_i} \right)^T \tag{2.69}$$

the force acting on the i-indexed particle is

[5] the one given above is the original definition; however, in the context of Fourier Transforms, there exists the so called half-maximum convention

$$\Theta(x) \coloneqq \begin{cases} 0, & \text{for } x < 0 \\ \frac{1}{2}, & \text{for } x = 0 \\ 1, & \text{for } x > 0 \end{cases}$$

In the latter case, if a particles sits exactly at $x = 0$, i.e. on the left boundary of the domain $[0, \infty)$, it is accounted for only half.

[6] obviously, it is assumed $x_{\min} < x_{\max}$, and, further below, also that $y_{\min} < y_{\max}$ and $z_{\min} < z_{\max}$.

$$\boldsymbol{f}_{\text{res}}^{(i)} = -\nabla_{r_i} U_{\text{res}} = -\frac{\partial U_{\text{res}}}{\partial \Phi}\frac{\partial \Phi}{\partial r_i} = \tag{2.70}$$

$$= -\kappa\big[\Phi(r_1,\ldots,r_N) - \Phi^*\big]\,\nabla_{r_i}\Phi(r_1,\ldots,r_N) = \tag{2.71}$$

$$= -\kappa\big[\Phi(r_1,\ldots,r_N) - \Phi^*\big]\,\nabla_{r_i}\mathbf{1}_{\Omega}(r_i) \tag{2.72}$$

As a consequence of the chain rule, one sees there is another important factor involved, that is the derivative of the indicator function. A delicate factor indeed. As an example, the derivative of the Heaviside step function makes sense only in the theory of distributions; as a matter of fact, the distributional derivative of $\Theta(x)$ is equal to the Dirac delta function

$$\frac{\mathrm{d}\Theta}{\mathrm{d}x} = \delta(x) \tag{2.73}$$

Distributions are generalized functions, generalized in the sense that are defined and characterized merely in terms of their mathematical properties, rather than analytically or graphically. This means that, more often than not, these are abstract objects, living only in the mathematical realm and impossible to connect to reality. The Dirac delta function $\delta(x)$ constitutes a renowned and well-known example of a distribution.

In our specific case, dealing with δs poses the following practical problem. Let us consider a simple monodimensional case, where the target domain is the interval $[0, +\infty)$ and, as we have seen, the corresponding indicator function is the Heaviside step function $\Theta(x)$. In this setting, the forces applied to the particles would be exactly proportional to $\delta(x)$, which means that a given particle would actually experience a force only if it were positioned precisely at $x = 0$. And note that is precision in the mathematical sense, i.e. within the accuracy of a single point on the real axis. Obviously, that is unfeasible in a computational framework, where data is intrinsically subjected to finite precision, round-off errors and other forms of approximations. In fact, it is undoable anywhere outside the mathematical world. Unfortunately, this pathological behaviour makes the Dirac delta function unusable for any restraining application.

One way[7] out of this *impasse* is to approximate the indicator function with a similar but everywhere continuous function

$$\mathbf{1}_{[x_{\min}, x_{\max}]}(x) \approx \phi(x) \tag{2.74}$$

In the specific case of the Heaviside step function, the choice for such replacement fell on the Fermi (distribution) function, or fermian

$$\theta(x) = \frac{1}{e^{-\lambda x} + 1} \tag{2.75}$$

The total derivative of a fermian is equal to

[7] An alternative approach would have been to smooth out the derivative of the indicator function and then reclaim the new indicator function via integration: following the same example, the Dirac delta function could have been smeared into a gaussian and (so) the Heaviside step function approximated with its primitive, i.e. the error function. Yet, being the error function non-analytical, this path would have taken a higher toll on the computational resources.

$$\frac{\mathrm{d}\theta}{\mathrm{d}x} = \frac{\lambda e^{-\lambda x}}{\left(e^{-\lambda x}+1\right)^2} = \lambda\left(1 - \frac{1}{e^{-\lambda x}+1}\right)\frac{1}{e^{-\lambda x}+1} = \lambda\big[1-\theta(x)\big]\theta(x) \tag{2.76}$$

Notice how it was possible to express the derivative of the fermian as a function of the fermian itself. This derivative does not present any of the previous issues and, in fact, allows to apply a force to the particles near the boundary. Of course, the other side of the coin is that we are no longer performing an exact counting, because the particles across the boundary give a fractional contribution to the total, due to the indicator function being now continuous. This effect can be contained by reducing the (effective) extent of such diffuse interface, which is tunable through the parameter λ: the higher its value, the sharper the interface, and vice versa. After performing some test simulations, we found out that $\lambda = 4.6$ deliver a good compromise between the two worlds.

Box domain Here we derive the smooth indicator function, its gradient and the forces that will be acting on each particle, all specialized for the case of a 3D box domain, defined as the Cartesian product of 3 one-dimensional intervals $[x_{min}, x_{max}] \times [y_{min}, y_{max}] \times [z_{min}, z_{max}]$, hence identified by 6 scalar values (cfr. eq. 2.66). First of all we establish a one-dimensional window function, smoothing out the Θs in eq. 2.65 with the Fermian in eq. 2.75, as follows

$$w(x) = \theta(x - x_{min}) - \theta(x - x_{max}) \tag{2.77}$$

Using eq. 2.76, the total derivative of this function is equal to

$$\frac{\mathrm{d}w}{\mathrm{d}x} = \lambda\big[1-\theta(x-x_{min})\big]\theta(x-x_{min}) - \lambda\big[1-\theta(x-x_{max})\big]\theta(x-x_{max}) \tag{2.78}$$

Then we build our 3D box function by simply multiplying together 3 one-dimensional window functions, one for each dimension, as seen in eq.s 2.66 and 2.67

$$\phi(r) = \phi(x,y,z) = w(x)\,w(y)\,w(z) \tag{2.79}$$

The partial derivatives along each coordinate axis of the box function can be easily computed from eq.s 2.77 and 2.78 as

$$\frac{\partial\phi}{\partial x} = \frac{\mathrm{d}w}{\mathrm{d}x} w(y)\,w(z) \tag{2.80}$$

$$\frac{\partial\phi}{\partial y} = w(x)\,\frac{\mathrm{d}w}{\mathrm{d}y} w(z) \tag{2.81}$$

$$\frac{\partial\phi}{\partial z} = w(x)\,w(y)\,\frac{\mathrm{d}w}{\mathrm{d}z} \tag{2.82}$$

From eq. 2.63, the total number of particles inside the 3D box becomes

$$\Phi(r_1,\ldots,r_N) = \sum_{i=1}^{N} \phi(r_i) \tag{2.83}$$

and so, the force acting on the particle i is

$$\boldsymbol{f}_{\mathrm{res}}^{(i)} = -\kappa\big[\Phi(r_1,\ldots,r_N) - \Phi^*\big]\,\nabla_{r_i}\phi(r_i) = \tag{2.84}$$

$$= -\kappa\big[\Phi(r_1,\ldots,r_N) - \Phi^*\big]\,\left(\frac{\partial\phi}{\partial x}, \frac{\partial\phi}{\partial y}, \frac{\partial\phi}{\partial z}\right)^T \tag{2.85}$$

Spherical domain In this subsection we derive the smooth indicator function, its gradient and the forces that will be acting on each particle, but this time all specialized for the case of a spherical region. The domain is now identified by 4 values, the 3 coordinates of the sphere center (x_0, y_0, z_0) and its radius R. First, we define a "distance from the sphere center" function

$$d(x,y,z) = \sqrt{(x-x_0)^2 + (y-y_0)^2 + (z-z_0)^2} \tag{2.86}$$

and, for future convenience, we evaluate the partial derivative with respect to one of its variables (the other two are perfectly analogous)

$$\frac{\partial d}{\partial x} = \frac{x - x_0}{\sqrt{(x-x_0)^2 + (y-y_0)^2 + (z-z_0)^2}} \tag{2.87}$$

Now we compose the fermian with our distance function

$$\theta[d(x,y,z)] = \frac{1}{e^{-\lambda d(x,y,z)} + 1} \tag{2.88}$$

and again, we calculate explicitly one of its partial derivatives

$$\frac{\partial \theta}{\partial x} = \frac{\partial \theta}{\partial d}\frac{\partial d}{\partial x} = \frac{\lambda\,(x-x_0)}{\sqrt{(x-x_0)^2 + (y-y_0)^2 + (z-z_0)^2}}\big[1 - \theta[d(x,y,z)]\big]\theta[d(x,y,z)] \tag{2.89}$$

Finally, we are able to build our smooth indicator function, the one selecting the particles which lie within our diffuse sphere, as simply as

$$\phi(x,y,z) = 1 - \theta[d(x,y,z) - R] \tag{2.90}$$

Since we translated the argument of the fermi function by a mere constant, the partial derivative of ϕ, using 2.89, is just equal to

$$\frac{\partial \phi}{\partial x} = \frac{-\lambda\,(x-x_0)}{\sqrt{(x-x_0)^2 + (y-y_0)^2 + (z-z_0)^2}}\big[1 - \theta[d(x,y,z) - R]\big]\theta[d(x,y,z) - R] \tag{2.91}$$

Note how, given the peculiar functional form of eq. 2.90, the previous partial derivative can also be written as

$$\frac{\partial \phi}{\partial x} = \frac{-\lambda\,(x-x_0)}{\sqrt{(x-x_0)^2 + (y-y_0)^2 + (z-z_0)^2}}\big[1 - \phi(x,y,z)\big]\phi(x,y,z) \tag{2.92}$$

2.2.3 The string method

In the presence of a single collective variable, there is only one transition path between two states, which can be parameterized by varying the collective variable itself (e.g., using RMD) between the values corresponding to such states. If the collective variables are two or more, an infinite number of possible paths become

available; in such circumstance, exploring even a few different paths managing individually each collective variable may be computationally unfeasible. The natural extension of RMD[8] to deal with similar cases is the string method.

The string method[39, 40] allows one to identify the most likely transition path, i.e., the optimal path connecting initial and final states among the many. We remark that this method is not the only one available to determine transition paths: for example, the string method itself is based on another technique, called the nudged elastic band algorithm. Once the transition path is known, one can deduce the energetics of the process, namely the relative energy of the initial and final state, and the transition barrier, i.e. the barrier that has to be overcome to accomplish the process.

In the string method, one represents the transition path as a parametric curve, $\boldsymbol{r}(\lambda)$, in the space of the atomic configurations ($\boldsymbol{r}$ is the $3N$ vector of the atomic positions). λ is a parameter measuring the degree of progress of the transition: $\lambda = 0$ when the system is in the initial state, and $\lambda = 1$ when it is in the final one. It can be shown[39, 40] that the most probable path is the one with zero component of the atomic forces in the direction orthogonal to the path:

$$-\nabla V[\boldsymbol{r}(\lambda)]\Big|_{\perp \boldsymbol{r}(\lambda)} = 0$$

In the string method, the continuous path (λ) is discretized into a finite number, L, of configurations (snapshots), $\{\boldsymbol{r}(\lambda_i)\}_{i=1,\dots,L}$. These snapshots satisfy the additional condition to be at a constant distance from each other:

$$\Big|\boldsymbol{r}(\lambda_i) - \boldsymbol{r}(\lambda_{i+1})\Big| = \Big|\boldsymbol{r}(\lambda_j) - \boldsymbol{r}(\lambda_{j+1})\Big|.$$

Starting from an initial guess, the path is evolved according to the steepest descent dynamics driven by the component of the forces perpendicular to the path:

$$-\nabla V[\boldsymbol{r}(\lambda_i)]\Big[\boldsymbol{I} - \alpha[\boldsymbol{r}(\lambda_i)] \otimes \alpha[\boldsymbol{r}(\lambda_i)]\Big],$$

with $\boldsymbol{I}$ being the identity matrix and $\alpha[\boldsymbol{r}(\lambda_i)]$ the unit vector tangent to the path at the i-th point. In practice, $I - \alpha[\boldsymbol{r}(\lambda_i)] \otimes \alpha[\boldsymbol{r}(\lambda_i)]$ is a projector on the plane orthogonal to the path at the point $\boldsymbol{r}(\lambda_i)$. Indeed, since the tangential component of the force has only the effect of changing the distance between successive snapshots, a more efficient algorithm consists in:

i) evolving the path according to the entire force, and

ii) imposing the equidistance condition by moving the snapshots along the polygonal joining the configurations $\{\boldsymbol{r}(\lambda_i)\}_{i=1,\dots,L}$ obtained in i).

This two-step process is repeated until the maximum component of the atomistic force orthogonal to the path is below 10^{-3} Hartree/Bohr (atomic units), the same convergence criterion that is typically used in cell optimizations. On the converged string we apply the "climbing algorithm", which moves the higher-in-energy snapshot upwards, towards the maximum of the energy along the path. This allows one to accurately determine the transition barrier.

[8] as well as other rare events techniques not discussed here, such as blue moon, thermodynamic integration, etc.

Part I

Water-complex nanoporous solids interfaces

Preamble

Nanoporous hydrophobic crystalline materials are becoming increasingly popular nowadays: the thermodynamics associated with their water intrusion and extrusion processes makes them relevant for promising engineering and technological applications, as mechanical energy storage systems (i.e., mechanical batteries), or energy scavenging and/or dissipation devices for the automotive market in the form of vehicle shock absorbers.

The only instrument available today to predict the intrusion pressure of a pore, as a function of its size and the properties of the liquid and the solid involved, is the Young-Laplace equation, which can be derived in the context of continuum mechanics of membranes. An analogous equation for extrusion does not exist. In addition, the industrial ability to manufacture pores whose characteristic size is getting smaller and smaller, reaching a nanoscopic and sometimes even subnanoscopic scale, is casting doubts on the validity of the aforementioned macroscopic theory for intrusion.

For this reason, I chose a reference hydrophobic material, for which the community already expressed technological interest, and started studying its water intrusion and extrusion processes. Experiments and high-pressure technological applications of this material assume the material itself as well the water to be degassed. So, consistently with experimental phenomenology, we carried out our experiments in conditions where the solid and the liquid were completely degassed (except for the water, which was free to intrude the solid, either as a liquid or a gas). Also, we focused only on pressures within or near the (pressure) range associated with intrusion and extrusion.

I tried to answer different questions, as whether the shape assumed by the water density field inside this material were uniform, hence bulk-like, or exhibited a complex structure, suggesting the unsuitability of the classical capillary theory description; or if the flexibility of the material, which is systematically overlooked in this context, plays an important role during the intrusion and extrusion processes. Another aspect I focused on is that, typically, when studying the intrusion and extrusion of liquids in porous materials, only the intrusion and extrusion into/from the pore itself are considered, as if all the kinetics and the thermodynamics depended solely on it. Indeed, nanoscopic porous materials are generally constituted of grains, which in turn are comprised of aggregated crystallites: so, in order for the water to percolate into the pores of the inner crystallites, first it has to diffuse through the grain boundaries (GB)! And, as the reader will see, it is not obvious which process, GB diffusion or pore percolation, is faster and which, on the contrary, constitutes a bottleneck.

Since this has been a pioneering study of these topics, it was necessary to start from a simplified model, still preserving all the main properties of this material, and verify the legitimacy of our assumptions by comparison with the experiments. In this work, I did not account neither for the MOF's mechanical fragility (the interaction potential does not allow the slab to break, at any level), nor for the effects produced by the presence of defects. On the other hand, X-ray diffraction, and SEM and TEM images reveal how the crystallites do not exhibit significant changes, even after several intrusion and extrusion cycles. As for defects, (i) intrusion and extrusion experiments involving with ZIF-8 samples at different degrees of crystallinity and perfection, showed only minor changes in the intrusion and extrusion characteristics;

in any case, (ii) theoretical and computational work is being carried out to clarify the issue.

Colleagues belonging to the same research group I have been working for, have recently published papers on high-impact journals, e.g., Y. Bushuev et al.[41] (Nano Letters) and G. Paulo et al. (under consideration by Comm. Phys.), where the knowledge and methods developed during my thesis are used to interpret the mechanism and wetting properties of other hydrophobic zeolites.

Chapter 3

Giant Negative Compressibility by Liquid Intrusion into Superhydrophobic Flexible Nanoporous Frameworks

3.1 Abstract

Materials or systems demonstrating Negative Linear Compressibility (NLC), whose size increases (decreases) in at least one of their dimensions upon compression (decompression) are very rare. Materials demonstrating this effect in all their dimensions, Negative Volumetric Compressibility (NVC), are exceptional. Here, by liquid porosimetry and in situ neutron diffraction, we show that one can achieve exceptional NLC and NVC values by non-wetting liquid intrusion in flexible porous media, namely in ZIF-8 metal-organic framework (MOF). Atomistic simulations show that the volumetric expansion is due to the presence of liquid in the windows connecting the cavities of ZIF-8. This discovery paves the way for designing novel materials with exceptional NLC and NVC at reasonable pressures suitable for a wide range of applications.

3.2 Introduction

Negative Linear (NLC) and volumetric compressibility (NCV),[42, 43] the properties of materials to increase (decrease) in one dimension or in volume upon compression (decompression), attracted considerable attention due to the wide potential applicability, which includes sensors, actuators, composites with effective zero compressibility, artificial muscles, smart body armours[44, 45] and acoustic shielding.[46] NLC- and NVC-materials are quantitively characterized by coefficient of linear compressibility,

$$\kappa_l = -\frac{1}{l}\frac{\partial l}{\partial P} < 0\,,$$

and coefficient of volumetric compressibility,

$$\kappa = -\frac{1}{V}\frac{\partial V}{\partial P} < 0\,,$$

respectively. Here l is the size of one of the unit cell along the three crystalline lattice directions a, b and c, which in the case of ZIF-8 can be made coincident with the Cartesian axes x, y and z (Scheme S1 in the Supplementary information), V is the volume of the crystalline unit cell and P is pressure. There are several classes of (smart) materials exhibiting NLC, whose functioning mechanism can be understood in terms of simple mechanical models (see, e.g., the seminal work of Grima et al.[47]). However, materials with κ_l having absolute value larger than 10 TPa^{-1} are notoriously rare.[42] Some of the highest values are provided in Table 3.1. NLC can be achieved using auxetics and applying non-isotropic stresses. Here the negative response is associated either with a porous auxetic geometry[48] or elastic properties of the system[49] and can be predicted by computational methods.[50] However, more recently it has been shown that NLC can result also from the application of hydrostatic pressure to suitably designed negative Poisson's ratio materials.[47] The general strategy here is the use of materials with anisotropic mechanical behavior, more specifically, with orientation-dependent directional Poisson's ratios, which causes an expansion under tension rather than contraction.[44]

Mechanisms and broad range of NLC materials were reviewed by Cairns and Goodwin.[42] The NLC effect was mainly reported for inorganic compounds such as a few zeolites,[51, 52] oxides,[53, 54] and fluorides.[55] The discovery of pronounced NLC in a variety of coordination compounds/networks (particularly, cyanometallates) reignited this field.[42]

Some porous materials can expand upon isotropic pressure increase due to sorption or infiltration of guest molecules, which is understood at the microscopic level by selective guest-host interactions and lowering of the overall energy. More recently, the upsurge of MOF chemistry has provided vast opportunities for NLC studies[56, 57] owing to their diversity in topology, porosity and flexibility. Flexible MOF MIL-53 was demonstrated to show NLC along the b direction under an increasing hydrostatic pressure, showing a classical wine-rack mechanism.[58] Modified versions of the wine-rack mechanism for NLC were most recently reported for Cu(bpy)·SiF[59] and MCF-34.[60] Uncommon NLC effects were reported for a Zn-MOF with square grids pillared by helices, featuring very rare NLC along two directions,[61] as well as for a Zr-MOF MFM-133 with a fluorite **(flu)** topology which contains an octahedral cage that can be elongated along the c direction under compression.[62] The mechanisms of the latter two are attributed to their unusual topologies.

3.3 Analysis and results

In this work we demonstrate that one can achieve exceptional κ_l and κ values by non-wetting liquid intrusion into flexible porous media. To demonstrate our approach, *in situ* neutron scattering experiments were performed for the ZIF-8 + D_2O system at increasing pressures (see experimental details in Supplementary Information, Sec. SI2): at each value of pressure we collect neutron diffraction data for ∼10 min, from which we derive the lattice parameter of ZIF-8 at the given conditions. As can be seen from Fig. 3.1a, the initial compression of ZIF-8 + D_2O system brings

Material	$\kappa_l \left[\mathrm{TPa}^{-1}\right]$	Reference
BiB_3O_6 (0 - 5 GPa)	-6.7(3)	[42]
BiB_3O_6 (P $\rightarrow$ 0)	-12.5	[42]
MIL-53 MOF	-28	[58]
$[Ag(en)]NO_3$	-28.4(18)	[63]
$Zn[Au(CN)_2]_2$	-42(5)	[64]
MCF-34 MOF	-47.3	[60]
$InH(BDC)_2$	-62.4	[65]
$[Zn(L)_2(OH)_2]n$	-72*	[61]
$Ag_3[Co(CN)_6]$	-76.9	[66]
ZIF-8 MOF	-37.2**	[57]
ZIF-8 MOF (intrusion)	-1020(130)**	
ZIF-8 MOF (extrusion 1)	-770(120)**	this work
ZIF-8 MOF (extrusion 2)	-610(40)**	

Table 3.1. Experimental linear compressibility coefficients for materials with pronounced NLC effect (*negative area compressibility was reported; **negative volumetric compressibility was reported).

no anomalies in the framework response, which shrinks down upon compression. However, surprisingly at 26 MPa we observe a rapid (but not immediate) increase of the lattice parameter, that for the isotropic (cubic) ZIF-8 lattice corresponds to the unprecedented NVC and NLC coefficients of $\kappa = -3060$ TPa^{-1} and $\kappa_l = -1020$ TPa^{-1}, respectively, within a narrow pressure range of around 2 MPa (here and in 3.1 for isotropic materials, like ZIF-8, $\kappa = 3\kappa_l$). This is more than one order of magnitude higher than for any material reported so far. By further increasing the pressure, one recovers the usual positive volumetric and linear compressibilities. Following the opposite path, i.e., reducing the pressure, a giant NVC is also observed, but it occurs within a broader pressure range and in a two-step process corresponding to two different coefficients (Fig. 3.1a, Table 3.1 and next paragraph).

3.3.1 Expertimental study

To prove that the giant NVC is associated with water intrusion in ZIF-8, we performed liquid porosimetry experiments (see experimental details in Supplementary Information, Sec. SI2). Due to the pronounced hydrophobicity of ZIF-8 MOF (Fig. 3.1b, inset), a relatively high pressure must be applied to cause water intrusion into its pores. This can be seen in Fig. 3.1b, where compression of the ZIF-8 immersed in water up to $\sim$25 MPa (pre-intrusion region) results in a relatively small volume variation of the whole system due to the flexibility of the empty framework.

However, within the 26-28 MPa pressure range, in correspondence to the rapid increase of the ZIF-8 lattice parameter, i.e. when κ_l becomes negative, a sharp step is observed. This step-like volume variation indicates the intrusion process in which water molecules enter the pores and consequently, the overall system (ZIF-8 and water both inside and outside of the framework) shrinks considerably (Fig. 3.1b). We stress that the shrinking of the overall volume is associated with the penetration of water into the empty pores of ZIF-8 and does not imply a positive compressibility of ZIF-8 upon intrusion (see footnote on page 1 and Supplementary Information, Sec. SI1). Once the pores are filled, further pressure increase leads to a limited decrease in volume, as can be seen in the post-intrusion region in Fig. 3.1b. Upon decompression, the reverse process takes place, where water extrudes from the pores in a two-step manner at pressures lower than the intrusion pressure (Fig. 3.1b), which is consistent with neutron diffraction results. A one-step intrusion and two-step extrusion can be clearly seen by the derivative of the overall volume vs. pressure, i.e. the compressibility of the entire system (Fig. SI1): during compression a single peak is observed defining intrusion, while decompression features a double peak during the extrusion.

Above we remarked that the change of the lattice parameter during intrusion/extrusion is rapid but *not impulsive* (Fig. 3.1a). This could be due to heterogeneities present in the sample, the most important of which is the dispersion of ZIF-8 grain size. However, experiments, which will be discussed in detail in a forthcoming article, show a negligible dependence of intrusion pressure of ZIF-8 on the size of grains of the dimension used in this work. An alternative hypothesis, consistent with the observation that intrusion/extrusion can be arrested at intermediate levels of filling, is that the is a hierarchy of metastabilities along forward and reverse process: a principal level of metastability, corresponding to the fully intruded and fully extruded states, responsible for the hysteresis, and a second level represented by intermediate filling states, corresponding to partly filled/partly empty ZIF-8. These long living, partly filled/partly empty, metastable states are responsible for intermediate values of the lattice parameter during intrusion/extrusion (Fig. 3.1a). We further discuss metastabilities below, in the context of the presentation of simulation results, and more extensively in a forthcoming article (see also Supplementary Information, Sec. SI4).

The process bearing negative compressibility can be illustrated by geometrical simplification of the topology of ZIF-8 (Fig. 3.1c). Here, the brown sphere represents a ZIF-8 cavity; the black circles and the apertures on the black circumference around the 2D projection of the spherical cavity in the inset of Fig. 3.1c are windows (pore openings) connecting neighboring cavities. Fig. 3.1d-f shows a representation of the effect of pressure on the structure of a ZIF-8 cell before (from panel d to e) and during (from panel e to f) intrusion. Before intrusion, the cavity is empty of water (Fig. 3.1d), so an increase of pressure brings to a compression of ZIF-8 cages (Fig. 3.1e). During intrusion, the interior of the cavity turns from brown to light blue in the schematic to denote that the cavity is filled by water and the cage expands beyond the initial volume (Fig. 3.1f).

3.3.2 MD simulation study

To confirm this mechanism, and identify its microscopic details, Restrained Molecular Dynamics, (RMD),[67, 68] simulations were performed on a slab of ZIF-8 immersed in water (Fig. SI2, see computational details in Supplementary Information, Sec. SI2.d). RMD allows one to control the amount of water intruded into ZIF-8 and, for each value, determines the free energy of the system and the corresponding structure of the framework, including the size of its unit cell. The absolute minimum of the free energy, corresponding to a given level of filling of ZIF-8, shifts from the fully extruded to the fully intruded state within a pressure range of ∼1 MPa at a pressure of ∼50 MPa (Fig. SI3). The mismatch with the experimental value of the intrusion pressure is attributed to the force field,[69] which has been designed to model the flexibility of ZIF-8 at ambient pressure and has been successfully used for water-intruded ZIF-8,[70] but was neither optimized for liquid intrusion into the material, nor to quantitatively reproduce the stiffness of the solid at the relatively high pressures of present experiments. Indeed, it is remarkable that the pressure interval, ∼1MPa, over which intrusion takes place in simulations is in good agreement with the experiments. In addition to the two extreme states, empty and fully intruded ZIF-8, the free energy profile presents a number of intermediate minima that become absolute minima at intermediate pressures. This explains the relatively gradual intrusion/extrusion transitions: while the pressure increases/decreases the system evolves moving from one absolute minimum at one pressure to another one at a higher (lower) pressure (see also Supplementary Information, Sec. SI4). By computing the lattice parameter of the framework at the level of filling corresponding to the absolute minimum of the free energy at the given pressure, the theoretical lattice parameter vs. pressure dependence was determined (Fig. 3.1g and Fig. SI5). The presence of metastabilities at intermediate level of filling together with the progressive increase of the lattice parameter with amount of water in the ZIF-8 slab (Fig. SI5) explain the origin of intermediate values of the lattice parameter during the intrusion and extrusion branches of the lattice parameter vs. pressure curves (Fig. 3.1a). We remark that, at a variance with the experimental data, we report a single theoretical profile for lattice parameter vs. pressure curve because the simulations are performed in *quasi-static* conditions, i.e. the system is left to reach the local (ensemble) equilibrium distribution at each level of filling. In these conditions there is no hysteresis (see also Supplementary Information, Sec. SI4).

Consistently with experiments, in the lattice parameter vs. pressure plot (Fig. 3.1g) we observe a shrinking of the lattice parameter with increasing pressure in the pre- and post-intrusion/extrusion states. While during intrusion we observe a ∼0.08 Å increase of the lattice parameter, which is in quantitative agreement with experimental results. Moreover, consistently with experiments, upon intrusion ZIF-8 expands more than it gets compressed in the pre-intrusion branch of the lattice parameter vs. pressure curve. We notice that the compression of the lattice upon increase of the pressure before and after complete extrusion is more marked than in experiments. We attribute this to the force field, which has been designed to reproduce the flexibility of ZIF-8 at ambient conditions rather than at the much higher pressure of liquid intrusion. Despite the quantitative differences, the qualitative consistence between experimental and theoretical results, and the further

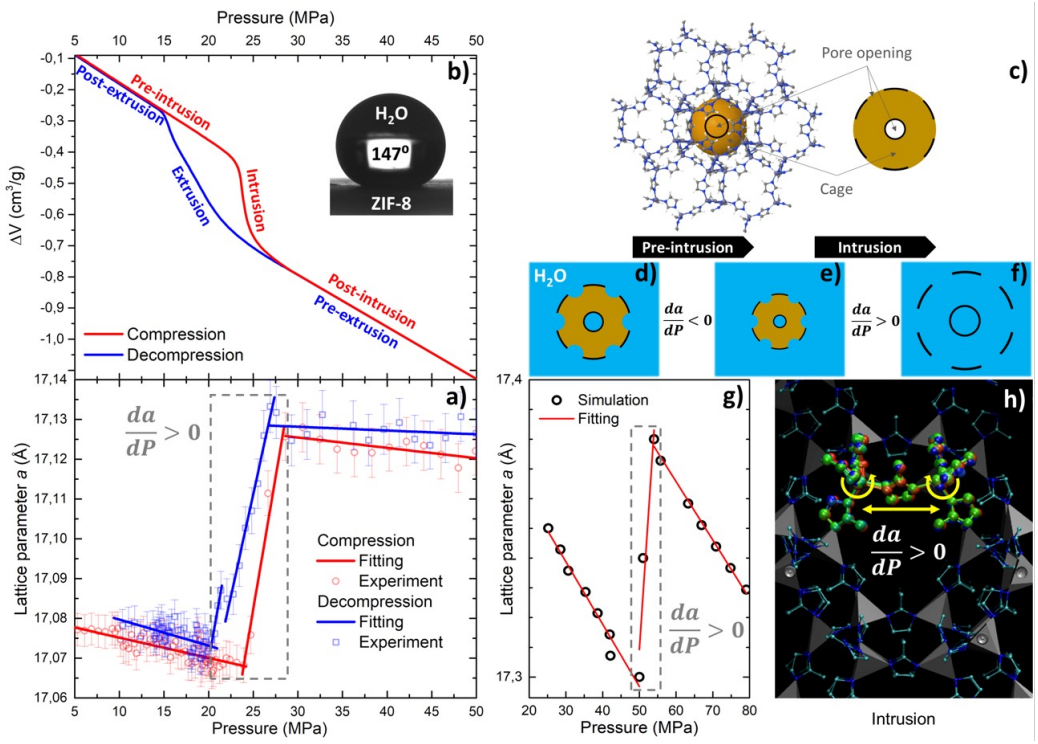

Figure 3.1. ZIF-8 + water system: a) experimental evolution of lattice parameter a with pressure (the error bars are plotted on a 1-sigma confidence level). b) PV-isotherm and contact angle; c) topological model of cavity of ZIF-8; d), e) and f) schemes of framework response to compression before and during water intrusion, respectively. Here, the blue colour represents water, while the black colour is used to indicate the dimensions of the framework; g) theoretical evolution of lattice parameter a with pressure and h) stroboscopic trajectory of two connected $ZnIm_4$ tetrahedra, i.e., two tetrahedra sharing an Im ligand. One observes a counter-rotation of the two tetrahedra that makes the Zn-Im-Zn triad more colinear, which increases the Zn-Zn distance, hence the lattice size. Note, due to cubic symmetry of ZIF-8, all the lattice parameters are equal and evolve with pressure in a similar way.

consistency between classical and *ab initio* calculations, convinced us that present simulation data allow us to identify the microscopic origin of the NVC of ZIF-8 upon intrusion.

The expansion of the lattice during liquid intrusion is the result of two phenomena: rotation of $ZnIm_4$ tetrahedra (Im stands for 2-methylimidazole) and stretching of the Zn-N bonds (Fig. 3.1h and Fig. SI6). These processes are mainly induced by water molecules occupying the pseudo-hexagonal windows joining ZIF-8 cavities (Fig. SI7), thus pushing apart the corresponding Im ligands and Zn atoms associated to them. To confirm this mechanism and to check that it is not the result of a limited accuracy of the *classical force field*, we performed *ab initio* calculations on the unit cell of (empty) ZIF-8 at several values of the lattice parameter, stretching and compressing an ideal ZIF-8 crystal with respect to its equilibrium structure (see computational details in Supplementary Information, Sec. SI2d). These simulations mimic the stretching induced by water intrusion in ZIF-8. Here, considering that water has no chemical interactions with the hydrophobic framework, we assume that the liquid

plays only a mechanical action on ZIF-8. We observe that, at room temperature, the ZIF-8 framework can easily expand by ∼0.05 Å (Fig. SI8), i.e., the energetic cost of expanding the lattice by this amount is just ∼5 k_BT (k_BT thermal energy at the experimental temperature). This lattice expansion is consistent with experimental intrusion/extrusion results and is achieved by $ZnIm_4$ tetrahedra rotation and Zn-N bonds stretching (Fig. SI9), in accord with RMD intrusion/extrusion simulations. Interestingly, negative volumetric compressibility achieved by rotation of $ZnIm_4$ tetrahedra resembles the mechanism at the basis of metamaterials with analogous properties.[71]

3.3.3 Results summary

Summarizing, the proposed approach for NLC and NVC offers several unique advantages:

- extremely rare Volumetric NC, i.e., an increase of the overall volume of the MOF upon compression. This can be exploited to design, for example, a smart flow-regulating valve for nano- and micro-fluidic devices, where a nano- or micro-scale grains of ZIF-8 regulate the flux of liquid through the channel depending on pressure;
- NC coefficients of ∼103 TPa^{-1}, an order of magnitude greater than the highest values ever reported;
- in contrast to the typical ∼GPa values, the presented approach allows NLC and NVC at moderate pressure of ∼25 MPa. This is a technologically relevant pressure for the majority of storage reservoirs, from scuba diving bottles to liquified gas tanks (liquid air, CO_2, nitrogen, etc.);
- reversibility of negative compressibility.

The reported approach for NLC and NVC requires MOF crystals to be immersed in a non-wetting fluid. On the one hand, it obviously narrows down the applicability, as it will not work in the absence of liquids. On the other hand, it can be used under conditions of isostatic pressure variation for applications such as micro- and nanofluidics. As depicted in Scheme 3.2, one can use grains of ZIF-8 to regulate a fluid flow in a narrow channel. More specifically, as pressure rises above intrusion value, water infiltrates into the grains of ZIF-8, which leads to their expansion (NCV), hence to a corresponding reduction of the flow. The fact that intrusion/extrusion takes place at a specific pressure, rather than continuously, like in some metamaterial, allows to use ZIF-8, and hopefully more materials in the future, as a valve. Moreover, within the narrow range between inception and completion of intrusion the process shows intermediate states (Figure 3.1a), suggesting that such a valve can regulate the flow gently, rather than in an "on-off" mode. Finally, ZIF-8 crystallites as small as 26 nm can be fabricated,[72] which makes this approach suitable for pressure regulation in the ever-shrinking domain of nanofluidics.

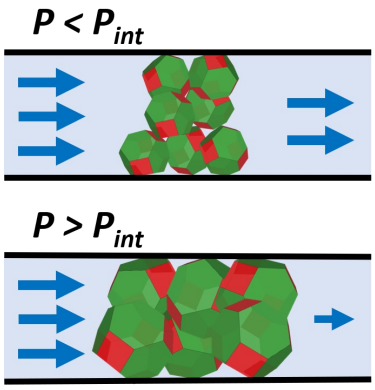

Scheme 3.2. ZIF-8 as a flow-regulating valve for micro- and nanofluidics.

3.4 Conclusions

In conclusion, we have presented a novel and efficient strategy for achieving giant negative compressibilities one order of magnitude larger than best systems reported in the literature. The microscopic mechanism, as revealed by a combination of in situ neutron scattering and advanced molecular dynamics simulations, is due to the significant volumetric expansion of the ZIF-8 cages induced by liquid intrusion. We expect this mechanism to be rather general, beyond ZIF-8+water, and can be exploited in other non-wetting liquid-porous materials pairs, opening the door to new applications of flexible porous materials.

3.5 Supplementary Information (extract[1])

SI1 - Negative volumetric compressibility

With the term *negative volumetric compressibility* one usually refers to a negative value of the so-called *effective compressibility*, which is defined with reference to the volume enclosed by the porous material rather than the entire volume of the sample[71]. Within the field, one typically uses the term *compressibility* as synonymous to *effective compressibility* for traditional materials[53, 61, 44, 73, 74] as well as metamaterials[71, 75, 76]. For example, NVC in the family of small-pore zeolites is achieved by the incorporation of additional water molecules into the respective nanochannels[53]. To this incorporation corresponds, of course, a reduction of the overall volume of the sample. In a more recent work[61], negative area compressibility is achieved by the absorption of chemical species from the fluid in which the porous material is immersed, resulting in an overall decrease of the volume of the sample. In the realm of metamaterials, typically negative compressibility induced by hydrostatic pressure refers to *relative compressibility* of the observable solid phase, not of the overall volume of the sample (the expanding metamaterial plus the fluid used to apply hydrostatic pressure)[71, 76]. For example, in Ref. [76] the author remarks that they refer only to the so-called effective volume, the volume enclosed by the solid. Concerning the *overall* or *true compressibility*, it is known that the overall volume of a bulk system cannot expand with increasing pressure. Within statistical mechanics, for example, one can show that the derivative of the volume of the entire sample with respect to pressure is proportional to the negative volume fluctuations,

$$\frac{\mathrm{d}V}{\mathrm{d}P} = \frac{\mathrm{d}}{\mathrm{d}P} \frac{\int \mathrm{d}V \int \mathrm{d}\Gamma \, V \exp\{[-\beta \left(H(\Gamma) + PV\right)]\}}{\int \mathrm{d}V \int \mathrm{d}\Gamma \, \exp\{[-\beta \left(H(\Gamma) + PV\right)]\}} = -\beta \left\langle (\Delta V)^2 \right\rangle_{NPT} < 0 \,,$$

where $\langle \cdot \rangle_{NPT}$ denotes ensemble average in the NPT ensemble. Hence,

$$-\frac{1}{V}\frac{\mathrm{d}V}{\mathrm{d}P}$$

must be positive. One gets to the same conclusion using thermodynamic arguments (see, for example, Ref. [77]). However, it must be remarked that the argument developed above is valid only for bulk systems; for particular low-dimensional systems, 2D/3D negative volumetric compressibility is allowed and has been experimentally observed[78, 79, 43].

SI2 - Methods

SI2.a - Transitiometry

Transitiometer SN201202 from BGR-Tech was used to record the PV-isotherms at 10 °C according to the procedure described elsewhere[43].

[1] parts already covered in the Methods chapter (Chapter 2) were omitted.

SI2.b - Wettability

The contact angle of water on the smoothed surface of ZIF-8 powder was measured using a DSA 100S Krüss Tensiometer. The reported value is the average of three independent measurements at 30 °C according to the procedure described elsewhere[70].

SI2.c - In-Operando Small-Angle Neutron Scattering

The *in-operando* Small-Angle Neutron Scattering (vSANS) study was carried out at the NIST Centre for Neutron Research (Gaithersburg, USA) using the 45 m vSANS instrument. A complete description of the instrument is located at the NCNR website[2]. The neutron wavelength $\lambda = 4.75$ Å was selected using double reflection Pyrolytic Graphite monochromator with a spread $\Delta\lambda/\lambda$ of 0.95%. In a He glovebox, the samples were first outgassed, *ex-situ* using a turbomolecular pump at 90 °C down to 10^{-6} mbar and then weighed into the vSANS pressure cell (approx. 1 g of ZIF-8) and evacuated again to remove He at room temperature. The D_2O was added to the cell at ambient pressure and then pressure was applied and dynamically kept constant (within 0.05 MPa) using an ISCO 100HLX syringe pump with D_2O as the pressure medium. A variable offset between the applied pressure and the sensor was less than 0.2 MPa. The temperature was maintained at 10 °C within ±1 K using a heating block. The collected dataset for each pressure includes one 600 s scattering run with a respective transmission file of 100 s. The SANS data were reduced using NCNR SANS macros[80], analysed and visualized using DAVE[81]. The lattice parameters of cubic $Zn(Im)_2$ MOF were calculated from centroids of Gaussian fit to (110) Bragg reflection present in the vSANS data. The lattice parameter a was calculated using Bragg's formula from the d-spacing of the (110) reflection.

SI2.d - Compressibility of ZIF-8 + water system

See Fig. 3.3.

SI2.e - Computational details

Classical Molecular Dynamics simulations were performed using the LAMMPS code in combination with the well-established Zheng et al. force field for the ZIF-8[69] combined with TIP4P/2005 model of water. ZIF-8 interacts with H_2O via electrostatics plus the modified Lennard-Jones interaction

$$4\varepsilon\left[\left(\frac{\sigma}{r}\right)^{12} - c\left(\frac{\sigma}{r}\right)^{6}\right]$$

to tune the hydrophobicity of ZIF-8[82]. The computational sample consists of a 7-unit cell-thick slab of ZIF-8 (∼19.0 nm), with a 2×2 unit cell extension in the x-y plane (∼3.5×3.5 nm) and 4800 water molecules, for a total (ZIF-8 + H_2O) of ∼20000 atoms (Fig. SI2). To determine the structure, free energy and other characteristics of ZIF-8 during water intrusion we used the well-established restrained molecular

[2] http://www.ncnr.nist.gov/

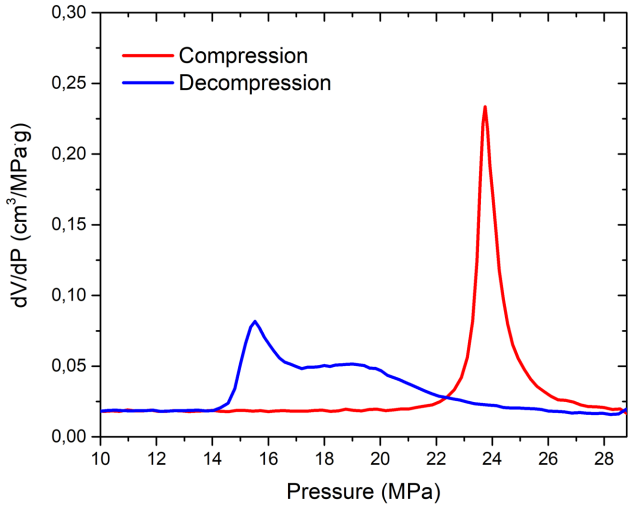

Figure SI1 - Figure 3.3. Compressibility of ZIF-8 + water system during the compression-decompression process. The single-peak during compression corresponds to one-step intrusion. The double-peak during decompression corresponds to two-step extrusion.

dynamics (RMD, see Sec. SI3.a) technique[67, 68]. The value of the RMD coupling constant λ was set to 15 kcal/mol.

Density Functional Theory (DFT) calculations were performed using the pw.x module of the Quantum Espresso package employing the Perdew, Burke, Ernzerhof (PBE) exchange and correlation functional[83]. Kohn-Sham orbitals were expanded on a plane wave basis set with a 50 Ry cutoff, and nuclei and core electrons interactions with valence electrons were treated using ultrasoft pseudopotentials. The computational sample consisted of the ZIF-8 unit cell (276 atoms) with a 4×4×4 mesh of k-points.

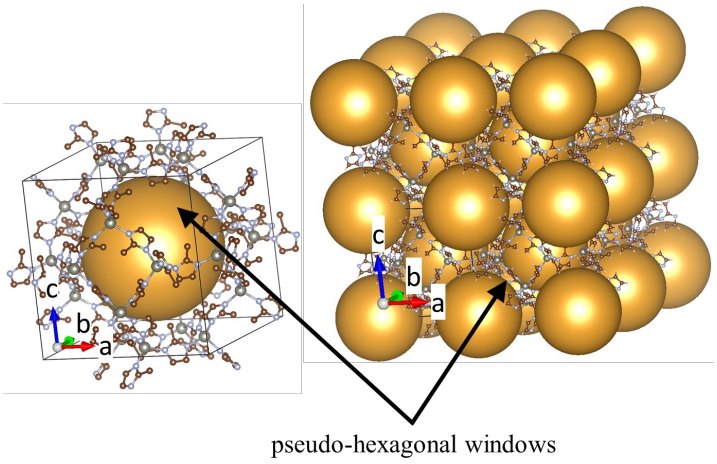

Scheme SI1 - Scheme 3.4. Left: unit cell of ZIF-8. For the sake of clarity, hydrogen atoms are not shown. The large golden sphere at the center of the unit cell highlights the cavity that gets filled by water during intrusion. The red-green-blue 3D compass at the bottom-left of the panel shows the directions of the lattice directions a, b and c. Right: crystalline structure of ZIF-8 illustrating the packing of cavities and their connection via pseudo-hexagonal windows.

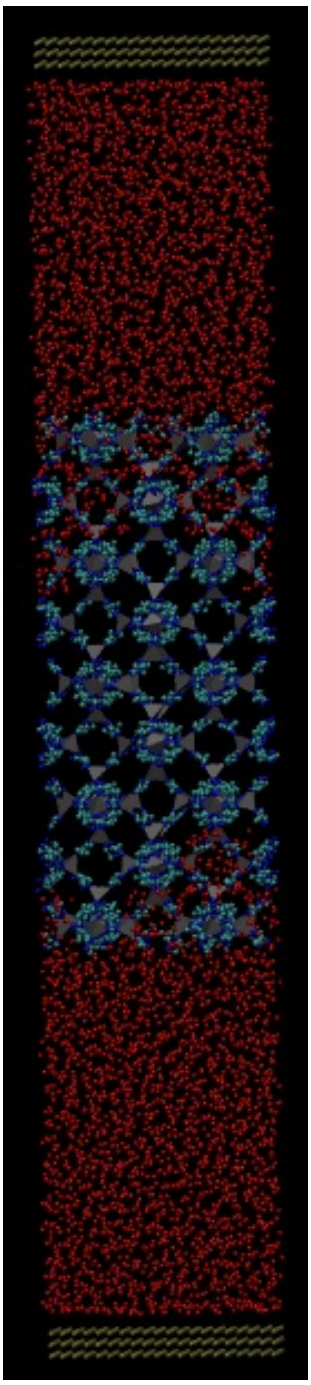

Figure SI2 - Figure 3.5. Snapshot of the computational sample. The ZIF-8 slab is surrounded by two large portions of water (red spheres represent oxygen atoms of water molecules). Above and below the slabs of water, two pistons apply hydrostatic pressure in the direction orthogonal to the ZIF-8 slab. This is required to avoid some artefacts associated to conventional barostats, which have been designed for homogeneous systems[84]. The simulation box is left free to fluctuate also on the plane of the ZIF-8 slab. In this case, fluctuations are controlled by the Tobias-Klein-Martyna barostat[85].

SI4 - Metastabilities and hysteresis

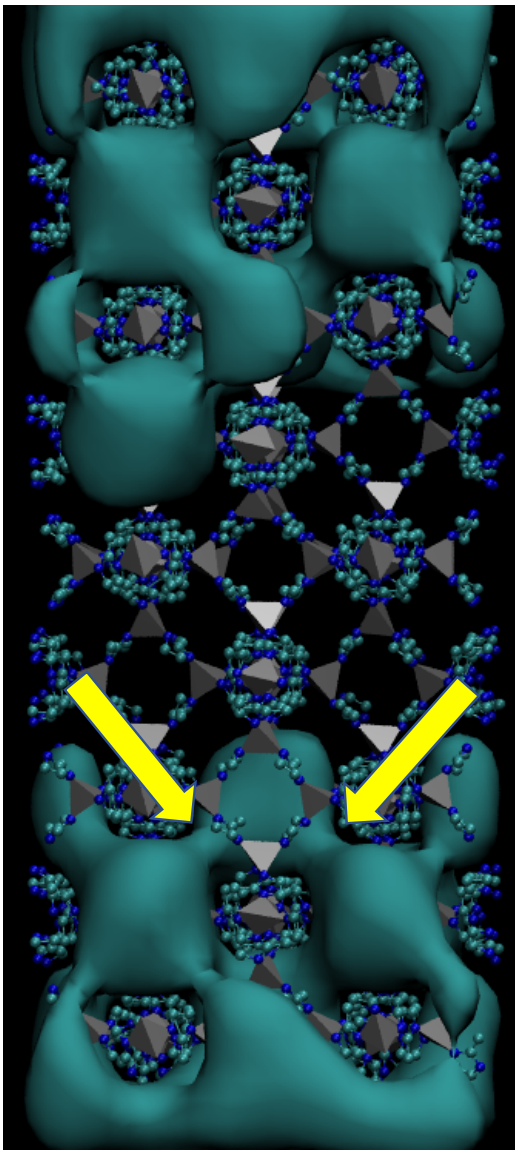

Figure SI7 - Figure 3.6. Atomic configuration during the intrusion process. $ZnIm_4$ units are drawn as tetrahedra, Im molecules are shown in the ball-and-stick representation (hydrogen atoms are not reported), and water as the isosurface of its density at one-half of its bulk value. The yellow arrows help identifying pseudo-hexagonal windows occupied by water. The reader may identify other analogous structures in the figure.

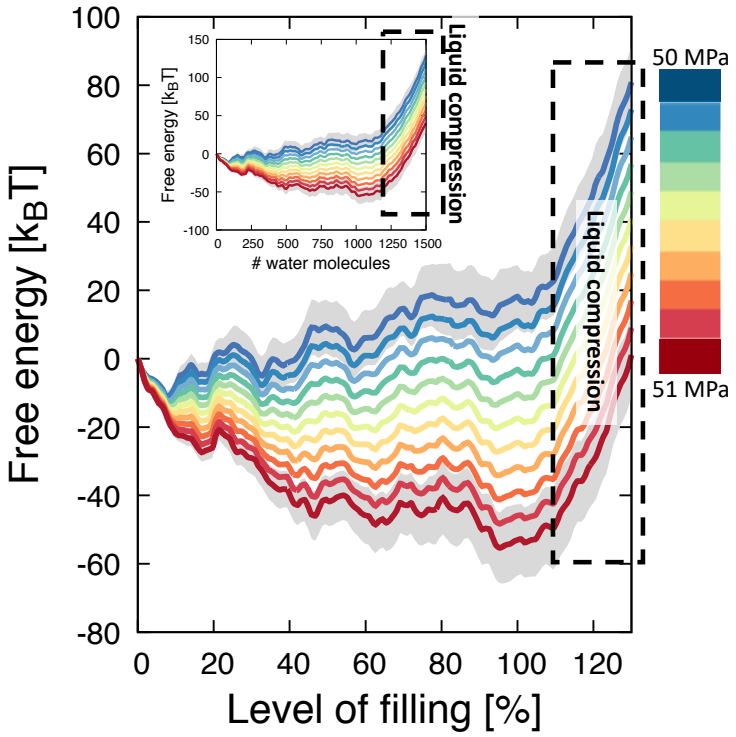

Figure SI3 - Figure 3.7. Free energy vs. level of filling in the ZIF-8 sample at increasing pressure (from blue to red) in a range of 1 MPa across the intrusion value. Free energy profiles are plotted at intervals of 0.1 MPa. The shaded regions represent the error associated with the free energy profiles computed at 50 and 51 MPa; free energy profiles for intermediate values of the pressure are obtained by interpolation. The trend of free energy profiles with pressure is due to the bulk liquid and gas contribution to $G(N_{H_2O})$ in the capillary theory of liquid interfaces, $-(P_l - P_g)\,V_l$, where P_l and P_g are the liquid and gas/vapor pressures, respectively, V_l is the volume of liquid in the porous material (see, e.g., Refs. [34, 7, 20, 86, 87, 88, 89]). This term favors (reduces the free energy) more liquid intruded states as the pressure increases. In the x axis we report the level of filling expressed in terms of percentage of maximum filling, corresponding to the absolute minimum of the free energy at the maximum pressure considered (∼1000 water molecules in the slab, see inset). Higher levels of filling are associated with a steep increase of the free energy, corresponding to the compression of water within the ZIF-8 pores. In terms of absolute number of water molecule, the x axis spans the range 0-1500 water molecules. As a reference, the free energy of the empty ZIF-8 sample is set to zero. One notices that at any pressure the free energy surface is characterized by one absolute and several local minima separated by maxima. We report also values of filling beyond the maximum value, filling $> 100\%$, region denoted by a dashed box in the graph. These states, that cannot be observed in experiments, can be produced in atomistic RMD simulations and consistently with the common sense bring to a significant increase of the free energy above its minimum value (see also the inset).

The free energy profile, Fig. SI3, shows many local minima corresponding to possible metastable states at different level of water filling of the ZIF-8 slab. Local minima are separated by free energy barriers whose value depends on the pressure value but, within the 50-51 MPa range considered, definitively fall in the 5-15 k_BT interval. Local and absolute minima of the free energy typically correspond to states in which ZIF-8 cavities are filled by water, ∼40 molecules per cavity. One observes that increasing the pressure the absolute minimum shifts from low to high levels of filling. In particular, for the theoretical sample used in this work (see computational details, Sec. SI2.d), we observe three absolute minima at low (50 MPa), intermediate (∼51.5 MPa) and high pressures (51 MPa), corresponding to ∼10%, ∼40% and 100% of liquid filling of the ZIF-8 slab. This explains why the intrusion and extrusion occurs in steps, corresponding to intermediate lattice values between the values taken when ZIF-8 is completely empty and completely filled. The hysteresis observed in the experimental a-P and P-V curves, Fig.s 3.1a and 3.1b, respectively, this can be explained by the kinetic trapping associated to the highest barrier separating the completely extruded and completely intruded states.

According to Kramers' theory of transitions between states separated by free energy barriers[90], the transition time for the process to occur is proportional to the exponential of the free energy barrier $\Delta G^{\dagger}$: $\tau = \tau_0 \exp\left[\Delta G^{\dagger}/k_BT\right]$. Of course, as the rugged free energy profile suggests, here the intrusion/extrusion mechanism can be significantly more complex and will be discussed in detail in a forthcoming article; here we consider the qualitative consequences of the Kramers' theory, focusing on the highest barriers separating any pairs of local minima between the completely extruded and completely intruded states.

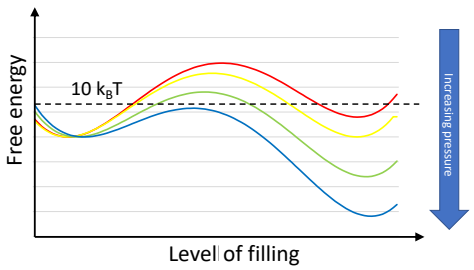

Figure SI4 - Figure 3.8. Cartoon illustrating the effect of pressure on the free energy profile and the consequences on the intrusion (extrusion) time. The dashed black line represents the free energy barrier threshold, 10 k_BT, below which one expects the intrusion to occur on the experimental time scale[86].

Consider the cartoon shown in Fig. SI4, characterized by two minima of the free energy corresponding to empty and water-filled ZIF-8 and a barrier between them. At ambient conditions, the absolute minimum is the empty state. By increasing the pressure, first the free energy of the two minima becomes the same, which is the thermodynamic condition for the transition. By further increasing the pressure, the water-filled state becomes the more stable one; however, due to the large barrier between the empty and water-filled state, the transition does not occur on the experimental timescale. Only at even higher pressures, when the barrier is sufficiently low, the transition can occur within the 10 minutes of the experiments at each pressure value. As discussed in a previous article of some of the authors

of the present one[86], $\Delta G^{\dagger}$ must be lower than 10 $k_B T$ for the transition to be observable in the experimental timescale. Hence, in the experiments intrusion is observed at pressures higher than the thermodynamic transition value and, conversely, extrusion at lower ones, producing the hysteresis observed in both the a-P and P-V curves. Apparently, in the experiments there are more metastable states during extrusion than intrusion (Fig. 3.1a). This is associated to a lower slope of the lattice parameter vs. pressure curve during extrusion than during intrusion in the negative compressibility region, resulting in a slightly smaller κ_l values (3.1). Moreover, we remark than more measurements have been performed along extrusion in this domain. The different compressibility in intrusion and extrusion is very likely associated to the different barrier in two directions to move between pairs of metastable states. Here, we refrain to explain these important but very detailed aspects of the intrusion/extrusion mechanism based on our simulations. In addition to the limited quantitative accuracy of classical force field, we remark that the intrusion/extrusion hysteresis and metastability of the real material might be further complicated by defects present in the material, air occupying porosity before intrusion, and many other effects that in our simulations, as in any other theoretical investigation of complex phenomena, cannot be taken into account. In the main text we report a single theoretical lattice vs. pressure curve, which apparently conflicts with the discussion above that simulation data allow to explain the hysteresis of a-P and P-V curves. The reason is that a quantitative analysis requires an estimation of the pre-exponential term τ_0, which, also in simpler but related cases resulted computationally very challenging [87, 88]. Thus, for determining the a-P, we opted for an equilibrium approach: (i) we assume that the system is always given sufficient time to reach equilibrium, i.e., to go into the state corresponding to the absolute minimum of the free energy at a given pressure, and (ii) we associate to this pressure the lattice parameter corresponding to the absolute minimum state. Since the system is always at the equilibrium configuration at the present pressure, hysteresis disappears.

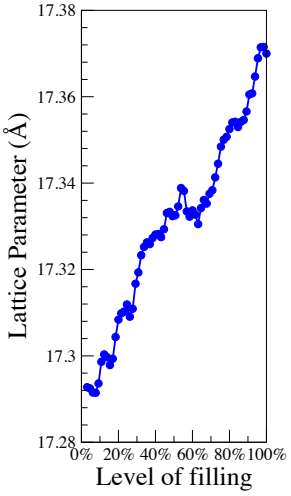

Figure SI5 - Figure 3.9. Lattice parameter as a function of the level of filling of the ZIF-8 sample. The lattice parameter is determined averaging the instantaneous value along RMD simulations at a fixed value for the number of water molecules within the MOF framework.

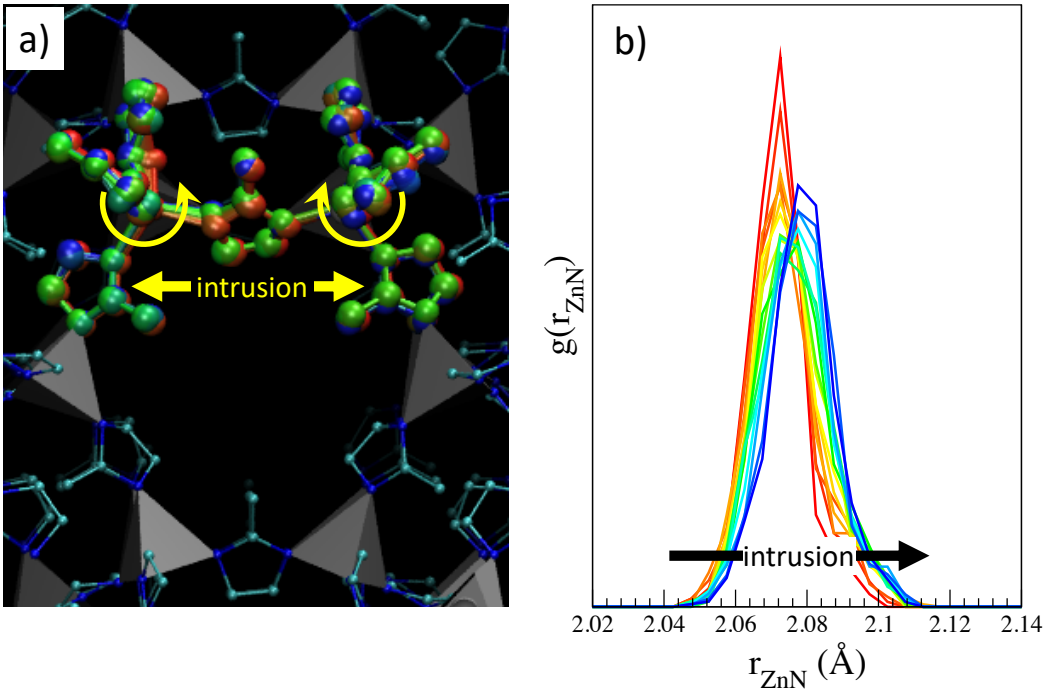

Figure SI6 - Figure 3.10. Structural characteristics of the ZIF-8 framework along water intrusion (from red to blue). a) stroboscopic trajectory of two connected $ZnIm_4$ tetrahedra, i.e. two tetrahedra sharing an Im ligand. One observes a counter-rotation of the two tetrahedra that makes the Zn-Im-Zn triad more colinear, which increases the Zn-Zn distance, hence the lattice size. b) Pair correlation function of chemically bonded Zn-N pairs, $g(r_{Zn-N})$, which measures the probability that a Zn-N connected pair is at a given distance, shows that the most likely Zn-N distance increases with the level of filling, which contributes to the expansion of the ZIF-8 lattice. The mechanism of the Zn-N stretching presents some remarkable features: before intrusion, $g(r_{Zn-N})$ is sharp and peaked at shorter distances; when water starts to intrude the ZIF-8, the $g(r_{Zn-N})$ becomes broader and shifts to higher distances; this is because only some of the ZIF-8 cages are intruded. When intrusion is completed, the $g(r_{Zn-N})$ returns sharper.

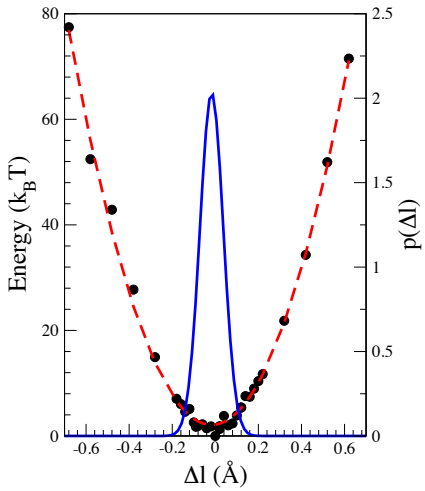

Figure SI8 - Figure 3.11. Energy (black points) as a function of compression/expansion of the lattice parameter (Δl) as obtained by density functional theory (DFT) calculations. The energy is reported in thermal units, i.e. in k_BT, where k_B is the Boltzmann constant and T is the temperature. The dashed red line is the quadratic interpolation of DFT results. The blue line represents the probability to observe an expansion/compression of amplitude Δl: $p(\Delta l) \propto \exp\{[-E/k_BT]\}$. One notices that the full width at half maximum (FWHM) is ∼0.1 Å, corresponding to an expansion of ∼0.05 Å, which is consistent with experimental and intrusion RMD simulations results.

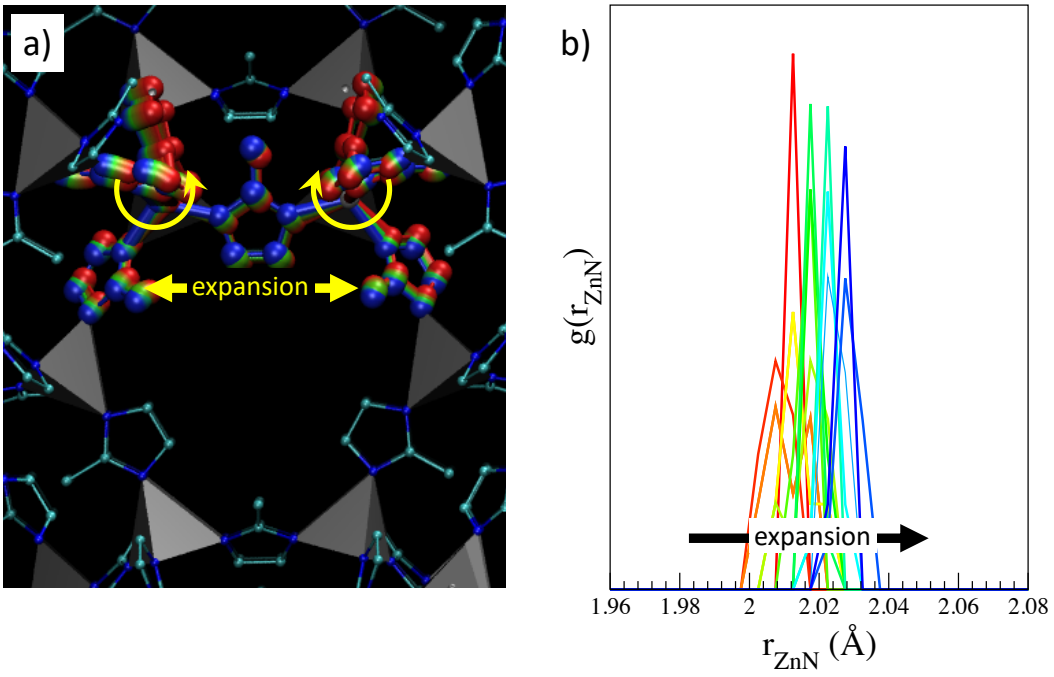

Figure SI9 - Figure 3.12. Structural characteristics of the ZIF-8 framework subjected to expansion/compression as obtained from *ab initio* calculations. This figure is analogous to Fig. SI6 obtained along water intrusion in ZIF-8. Consistently with those results, also in this case we observe the rotation of $ZnIm_4$ tetrahedra (a) and the stretching of Zn-N bonds (b) upon expansion of the ZIF-8 lattice.

Chapter 4

Turning molecular spring into nano-shock absorber: the effect of macroscopic morphology and crystal size on the dynamic hysteresis of water intrusion-extrusion into-from hydrophobic nanopores

4.1 Abstract

Controlling the pressure at which liquids intrude (wet) and extrude (dry) nanopore is of paramount importance for a broad range of applications, such as energy conversion, catalysis, chromatography, separation, ionic channels, and many more. To tune these characteristics, one typically acts on the chemical nature of the system or pore size. In this work, we propose an alternative route for controlling both intrusion and extrusion pressures via proper arrangement of the grains of nanoporous material. To prove the concept, dynamic intrusion-extrusion cycles for powdered and monolithic ZIF-8 Metal-Organic Framework were conducted by means of water porosimetry and in operando neutrons scattering. We report a drastic increase in intrusion-extrusion dynamic hysteresis when going from a fine powder to a dense monolith configuration, transforming an intermediate performance of ZIF-8 + water system (poor molecular spring) into a desirable shock-absorber with more than one order of magnitude enhancement of dissipated energy per cycle. The obtained results are supported by MD simulations and pave the way for an alternative methodology of tuning intrusion-extrusion pressure using solely macroscopic arrangement of nanoporous material.

4.2 Introduction

The process of wetting-drying in nanopores is relevant to a very broad range of applications from catalysis, chromatography and separation to ionic channels and energy conversion.[4, 91, 92, 93] In particular, the process of solid-liquid interface development-reduction has been widely explored for energy storage, conversion and dissipation applications[94, 95, 96, 97, 98] in view of compactness[99, 100, 101] and an associated rapid charging-discharging cycle.[97, 102, 103] The process of forced intrusion – spontaneous extrusion of a non-wetting liquid into-from a lyophobic nanopore constitutes a charge-discharge cycle, where mechanical (work of intrusion-extrusion), thermal (heat of solid-liquid interface development-reduction) and electrical (solid-liquid triboelectrification) energies manifest themselves simultaneously.[1, 16] The operational cycle of Heterogenous Lyophobic Systems (HLSs) is depicted in Scheme 1. Due to a non-wetting condition (Scheme 1, top left) under ambient pressure lyophobic pores tend to stay dry and empty. However, at certain pressures intrusion can be provoked (Scheme 1, bottom left). The intrusion is associated with a plateau at the pressure-volume diagram (Scheme 1, right) and a corresponding accumulation of mechanical energy (work of compression). For the majority of HLSs, intrusion is an endothermic process,[98, 1, 16, 104, 105] meaning that the system simultaneously accumulates thermal energy in the form of heat from the solid-liquid interface development as a non-wetting liquid spreads over a lyophobic pore (Scheme 1, bottom left). Recently, it was demonstrated that intrusion is also associated with pronounced solid-liquid triboelectrification,[1, 16] which means that also electrical energy is generated during this process. Energetically a lyophobic pore is an unfavorable environment for a non-wetting liquid, therefore, upon decompression the spontaneous extrusion (drying) of the pore occurs (Scheme 1, bottom left). If the extrusion pressure is similar to the intrusion pressure, the system behaves like a spring. Considering that breaking-forming of intermolecular bonds is at the heart of charging-discharging process these systems have been termed as Molecular Springs[106, 107, 108] – Scheme 1, right. These systems can be used for energy storage. Conversely, if the extrusion pressure is considerably lower than the intrusion pressure, the system behaves as a shock-absorber[97, 102] and can be used for energy dissipation applications – Scheme 1, right.

Typical examples of shock-absorber HLSs include mesoporous grafted silica gels + water/aqueous solutions[109, 110, 19, 111, 112, 113] and recently extensions were made to metal-organic framework (MOF) + water/aqueous solution systems.[114] MOFs, due to their unique mechanical properties,[115, 116] allow additional tuning of the intrusion-extrusion process and novel applications.[16, 117] Alternatives to water/aqueous systems have also been studied using ionic liquid,[8] ferromagnetic fluids[118] or glycerin and glycerol.[119, 119] These systems demonstrated good reproducibility and durability[97, 103] and were rather quickly used as a basis to construct novel shock-absorbers and bumpers.[102, 120, 121] On the other hand, examples for molecular spring behavior have only been reported for intrusion of water/aqueous solutions into handful of microporous materials such as zeolites[122, 123, 124] and MOFs.[108]

From these examples, it is evident that a hysteresis loop in PV-diagrams for HLS (Scheme 1) defines its technological applicability: storage by molecular springs

or dissipation by shock-absorbers. With this in mind, several strategies have been utilized to tune the intrusion-extrusion hysteresis such as salt concentration in a non-wetting liquid,[114, 125, 126, 127] viscosity,[8] topology of a lyophobic porous material[128] and porous materials´ flexibility.[16] Each of these strategies obviously require the careful selection of a proper porous material and/or non-wetting liquids.

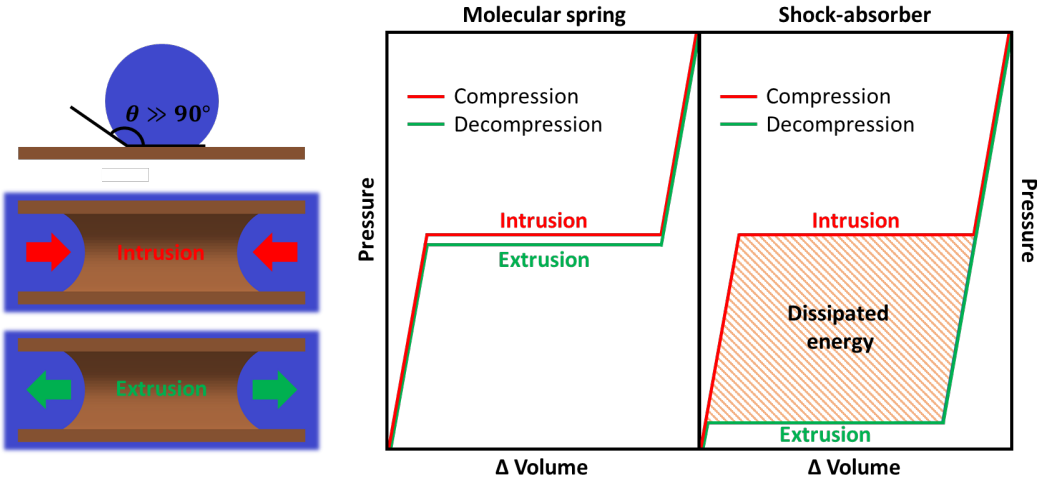

Scheme 4.1. Top left: a drop of a non-wetting liquid on a lyophobic material. Bottom left: cross-section view of a non-wetting liquid as it intrudes (wets) /extrudes (dries) a lyophobic pore. Right: PV-isotherm of an intrusion-extrusion cycle with low (molecular spring) and high (shock-absorber) hysteresis loops

In this work, we demonstrate, for the first time, that a macroscopic grain arrangement of a nanoporous material can be used to drastically affect the dynamic hysteresis of the intrusion-extrusion process. To demonstrate the concept, we have combined water intrusion-extrusion with *in operando* neutron diffraction experiments for one of a benchmark metal-organic frameworks, highly hydrophobicity zeolitic imidazolate framework - 8 (ZIF-8), prepared in three configurations – a fine powder of macroscopic crystals $_{\text{powder}}$ZIF-8, a fine powder of nanoscopic crystals $_{\text{powder_nano}}$ZIF-8 and a dense monolith made of nanoscopic crystals $_{\text{mono_nano}}$ZIF-8.[129] The obtained results demonstrate that by densely packing grains of ZIF-8, one can effectively transform a molecular spring into a nano-shock-absorber enhancing the amount of dissipated energy per cycle by more than one order of magnitude. This opens a new route for tuning heterogeneous lyophobic systems for energy storage/dissipation applications solely by varying macroscopic grain arrangement while maintaining the same porous material and a non-wetting liquid.

4.3 Materials and methods

4.3.1 Materials

Three porous MOF materials were used in this work: powdered ZIF-8 $_{\text{powder}}$ZIF-8, which was purchased from Sigma-Aldrich as Basolite Z1200, CAS# 59061-53-9, monolithic ZIF-8 $_{\text{mono_nano}}$ZIF-8, synthesized using the previously reported method[130] and powder of nanoscopic crystals $_{\text{powder_nano}}$ZIF-8. In a typical $_{\text{mono}}$ZIF-8 synthesis,

solutions containing 2-methylimidazole (20 ml, 0.395 M) and $Zn(NO_3) \cdot 6\,H_2O$ (20 ml, 0.049 M) in ethanol were mixed and stirred for 15 min at room temperature. The mixture is then transferred to a 50 mL Falcon tube and centrifuged (91⅔ Hz) for 10 min before decanting the excess ethanol and replacing it with 10 mL of fresh ethanol and centrifuged again. This process was repeated three times. After centrifuging, a white solid was collected and dried at room temperature overnight to form glassy-looking, transparent $_{mono}$ZIF-8. Fully activated MOF materials were obtained by heating to 120 °C under vacuum for 12 h. The synthesis of $_{powder_nano}$ZIF-8 was performed as follows. $Zn(NO_3)_2 \cdot 6\,H_2O$, 2-methylimidazole and methanol were bought from Sigma-Aldrich and used as received. To prepare ZIF-8 nanoparticles, two methanolic precursor solutions of the metal and the ligand are prepared in two different Erlenmeyer flasks: solution A, $Zn(NO_3)_2 \cdot 6\,H_2O$ 1.467 g in 100 mL methanol (0.049 M); solution B, 2-methylimidazole 3.245 g in 100 mL methanol (0.395 M). The two solutions are separately mixed until complete dissolution of the components. Solution A is then rapidly poured into solution B under stirring. The obtained solution is kept under vigorous stirring for 5 minutes, a cloudy product is observed to be formed. The cloudy suspension is quickly poured in four different 50 mL Falcon vials and centrifuged at 150 Hz for 30 min. The supernatant solution is disposed and the product in a pellet form is washed 2 times with fresh methanol (60 mL and 30 mL) and centrifuged each time at 150 Hz for 60 min. After the last centrifugation, the pellet product is left to dry at room temperature and finely crushed with a mortar to get a homogenous white powder.

4.3.2 Methods

4.3.2.1 Equipment for Dynamic PV-Isotherms

The PV-isotherms were measured at a temperature of 295 K using two different experimental setups. For the experiments which were conducted using the pressurization rate, within the range of 0.1-1 MPa min^{-1} a PVT-scanning transitiometer,[131, 132] constructed by BGRTech, was used. The liquid suspension samples were prepared by first weighing the solid into a stainless-steel capsule then submerging it into water. Negative relative pressure was applied to evacuate the gas from the capsule creating the suspension. The steel vessel was then placed into a calorimetric vessel where the sample was subject to a minimum of 3 pressurization cycles to ensure repeatability. For the experiments involving the pressurization rate of up to 1000 MPa min^{-1} PVT-stand developed at the National Technical University of Ukraine "Igor Sikorsky Kyiv Polytechnic Institute" was used.[109, 133] Because of different pressure-transmitting fluids and their different quantity in the hydraulic line for each of the instruments, the PV-isotherms were adjusted with the following the equation, in order to eliminate the effect of pressure-transmitting fluid compressibility:

$$\Delta\nu = \Delta\nu_{\text{recorded}} - (\alpha P + \beta) \tag{4.1}$$

The values of $\Delta\nu_{\text{recorded}}$ ($cm^3\ g^{-1}$) are the original PV-isotherm data, α and β are fitting constants adjusted to reach a similar volume variation upon compression (similar compressibility) below the intrusion pressure. Scaling with this method preserves the apparent pore volume (intrusion/extrusion volume) of each PV-isotherm

and permits the direct comparison of individual PV-isotherms regardless of equipment used.

To avoid any relaxation effects of ZIF-8 framework,[134] sufficient time between cycles was provided. The time required for such relaxation was estimated from our neutrons scattering experiments (see section 4.4.3 below). The PV-isotherms for monolith samples were recorded for multiple grains all of which are demonstrated in Figure 4.2c. The size distribution for these grains is demonstrated in Figure 4.2f.

4.3.2.2 In-situ Small-Angle Neutron Scattering

In-situ Small-Angle Neutron Scattering was carried out at the National Institute of Standards and Technology (NIST) Center for Neutron Research (NCNR, Gaithersburg, USA) using the 45 m vSANS instrument. A complete description of the instrument is located at the NCNR website[1]. The neutron wavelength $\lambda = 4.75$ Å was selected using a double reflection pyrolitic graphite monochromator with a wavelength spread $\Delta\lambda/\lambda$ of 0.95 %. ZIF-8 was first outgassed, ex-situ using a turbomolecular pump at 95 °C down to 1.2×10-6 hPa and transferred into a dry He glovebox. 197.8 mg of the sample was loaded into a SANS block pressure cell equipped with 2 mm x 2.07 mm Ti windows and 2 mm x 3.0 mm SiO_2 spacers to decrease scattering from H_2O. An additional 496.3 mg of ZIF-8 was used to fill a cylindrical steel pressure cell [2]. Before each experiment, the cell was additionally outgassed of He gas at RT using a turbomolecular pump. The D_2O:H_2O 2:1 mixture was prepared from Cambridge Isotope Labs D2O (99.9%, lot M5421) and deionized water (resistivity: 15-20 MΩ, organic content: 20-50 ppm, particulate matter: <0.2 μm). The mixture was then transferred into an evacuated ISCO 100HLX syringe pump which applied and dynamically kept constant pressure (within 0.05 MPa) within each cell. A variable offset between the applied pressure and the sensor was less than 0.2 MPa. The temperature was maintained using a glycol-water bath (NESLAB RTE7) within 0.1 K for ZIF-8.

The collected dataset for each pressure includes one scattering run of 900 s for ZIF-8 with a respective transmission dataset of 100 s. The vSANS data were reduced using NCNR SANS macros,[80] analyzed and visualized using DAVE.[81]

4.3.2.3 Scanning Electron Microscopy (SEM) and Transmission Electron Microscopy (TEM)

Thermo Fisher Quanta 200 FEG high-resolution Scanning Electron Microscope (SEM) was used in high-vacuum mode with electron beam energies of 10 kV, 20 kV and 30 kV with backscattered electron detector (BSED) and Everhart-Thornley Detector (ETD) to image ZIF-8 samples. To avoid drift during image acquisition, sample was gold-coated by means of a Sputter/Carbon Coater from SPI Supplies. The operating plasma current was set at 17.1 mA in Edge Mode for 1 min.

TEM measurements were performed on the Tecnai G2 F20 Super Twin (S-Twin), a high-resolution TEM/STEM from the Thermo Fisher company with a field emission

[1] https://www.nist.gov/ncnr

[2] https://www.nist.gov/ncnr/sample-environment/equipment/high-pressure/hw-03

gun (FEG) and acceleration voltage of 200kV. Samples were dispersed directly on TEM Cu grids with C mesh.

4.3.2.4 X-ray diffraction (XRD)

A Bruker D8 Discover X-ray diffractometer was used with a LYNXEYE-XE detector using CuKα1 radiation (λ = 1.5418 Å) and Bragg-Brentano θ:2θ geometry. The data collection was carried out at room temperature, between 10° and 80° with a step of 0.02° and a dwell time of 1.03 s per step.

4.3.2.5 N_2 Adsorption/Desorption Isotherms

N_2 adsorption isotherms were undertaken at 77 K using a Micromeritics 3Flex and Micromeritics ASAP 2460 instruments. The temperature was controlled by using L-N_2 bath. Brunauer, Emmett and Teller (BET) areas were calculated using the BETSI[135] and the Rouquerol criteria.[135]

4.3.2.6 Molecular dynamic simulations

Simulations of the ZIF-8 grain boundary were performed within the density functional theory (DFT)[136, 137] using the Thonhauser et al. exchange and correlation (xc) functional[138, 139] implementing van der Waals interactions in DFT. Thonhauser et al. xc functional has been validated on metal-organic frameworks,[138] the same class of materials considered in this work. The interaction between valence electrons and nuclei plus core electrons is treated using Rappe-Karin-Rabe-Kaxiras-Joannopoulos soft pseudopotentials,[140] which allowed us to use a relatively small 40 Ry cutoff on the maximum kinetic energy of the plane waves used to expand Kohn-Sham orbitals. Given the large size of the sample, the Brillouin zone has been sampled by the single Γ point (vide infra). For the structure of the grain boundaries (GB), two (110) slab crystallites with armchair termination,[2] containing as many as 1200 atoms each, were faced to each other. At each value of the (nominal) distance, which was controlled by keeping fixed selected atoms in the center of each ZIF-8 slab, the structure is left free to relax to the conditional (fixed nominal distance) equilibrium structure. The intrusion and percolation of a single water molecule was investigated by applying the string method,[141, 40] which allows to identify the most likely path to go from an initial to a final configuration, and the energetics of the process. A detailed description of the string method is provided in the Supplementary Information.

The effect of GB-induced by constraining ZIF-8 expansion upon water intrusion has been investigated resorting to the restrained molecular dynamics (RMD) approach[67, 142], which allowed to compute the free energy of the system as a function of the number of water molecules in the computational MOF sample (see Figure 4.7c). RMD is described in detail in the Supplementary Information. RMD simulations are based on classical force fields, an approach that has already been successfully applied to study intrusion-extrusion in simpler and more complex porous solids.[34, 86] Concerning the force fields, for ZIF-8 we used the force model proposed by Zheng et al.[143], while for water we used the TIP5P model.[144] Following previous works of some of us and other authors, cross interactions between water

and ZIF-8 resulted from electrostatics and Lennard-Jones forces whose parameters were obtained from the standard Lorentz-Berthelot combination rules. In the case of the flexible sample, molecular dynamics is performed at constant pressure, with the simulation box that is allowed to change along all lattice directions. On the contrary, in the case of the rigid framework, the simulation box changes only in the direction orthogonal to the slab ZIF-8 sample, preventing any overall expansion and compression of the computational crystallite in the other two directions. In both the flexible and rigid cases, atoms evolve at constant temperature, i.e., no further constraint is imposed on the atoms apart the fixed simulation box in the slab plane for the rigid case.

4.4 Results and discussion

4.4.1 Materials characterization

Figure 4.1 shows the X-ray diffraction for $_{\text{powder}}$ZIF-8, $_{\text{mono_nano}}$ZIF-8 and the simulated pattern of SOD ZIF-8 (Zn_6(2-methylimidazole)$_{12}$.[145, 146] $_{\text{mono_nano}}$ZIF-8 has broader peaks at the XRD pattern due to the smaller crystal size of the primary particles of the sol-gel process, as reported previously, on the order of ca. 40 nm.[46] While having the same structure, these materials are considerably different in the macroscopic morphology (Figure 4.2a – 4.2c). $_{\text{powder}}$ZIF-8 and $_{\text{powder_nano}}$ZIF-8 have a representative grain size of 300 nm - 500 nm and 15 nm – 60 nm, respectively (Figure 4.2d and 4.2e, Figure SI9). The "Necks" between crystallites in the Figure 4.2b (highlighted by yellow arrows) are grain boundaries (GB), showing that the $_{\text{poweder_nano}}$ZIF-8 is made of aggregates of tightly bound nanocrystallites. Such grain boundaries for ZIF-8 were recently demonstrated by high-resolution TEM.[2] $_{\text{mono_nano}}$ZIF-8 is represented by 1 mm - 3 mm dense and transparent pieces (Figure 4.2c and 4.2f). The transparency of $_{\text{mono_nano}}$ZIF-8 suggests the absence of macroscopic pores and small primary particles.[130] Moreover, N_2 adsorption characterization (Figures SI1 – SI5) reveals improved volumetric characteristics of $_{\text{mono_nano}}$ZIF-8, i.e., higher surface (SBET) and cavity volume per unit volume (V^b_{tot}) of the porous sample (Table 4.1), which is due to its higher density. Its high density, the crystallite size and the transparency of the sample suggest that the monolith consists of a tight aggregate of very small crystallites, probably forming among them tight grain boundaries of the kind observed in the $_{\text{poweder_nano}}$ZIF-8 sample (Figure 4.2b).

Material	S_{BET}	V^b_{tot}	ρ_b	S_{BET}	V^b_{tot}
	m^2/g	cm^3/g	g/cm^3	m^2/cm^3	cm^3/cm^3
$_{\text{mono}}$ZIF-8	1462	0.545	1.05	1535	0.572
$_{\text{powder}}$ZIF-8	1664	0.685	0.35	582	0.240

Table 4.1. N_2 adsorption characterization of $_{\text{powder}}$ZIF-8 and $_{\text{mono_nano}}$ZIF-8 samples.

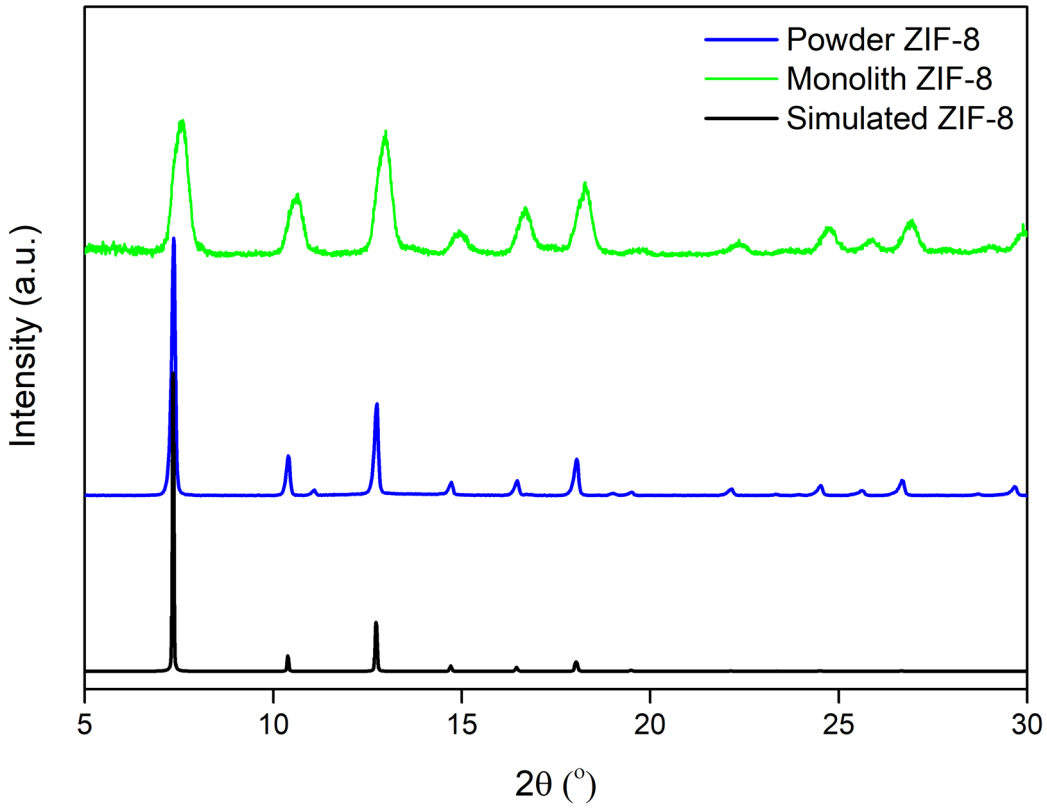

Figure 4.1. N_2 adsorption characterization of $_{powder}$ZIF-8 and $_{mono_nano}$ZIF-8 samples.

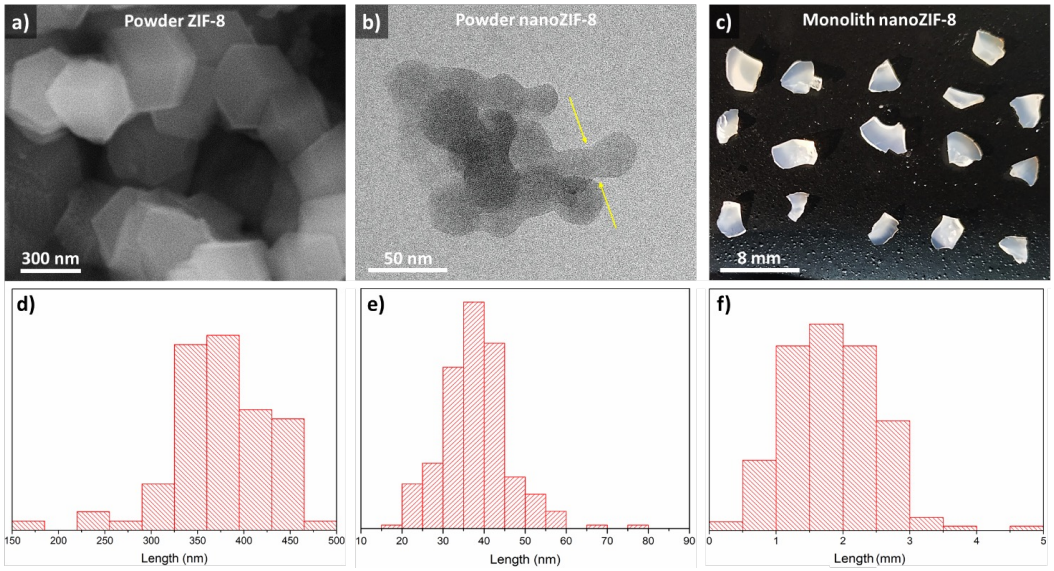

Figure 4.2. Representative images for different ZIF-8 samples: SEM image and crystal size distribution for $_{powder}$ZIF-8 (a and d); TEM image and crystal size distribution for $_{powder_nano}$ZIF-8 (b and e), where yellow arrow indicate grain boundaries between crystals; optical image and monolith size distribution for $_{monolith_nano}$ZIF-8 (c and f).

4.4.2 Intrusion-extrusion study

Figure 4.3 shows the water intrusion-extrusion – PV-isotherm for ZIF-8 samples measured at different rates, from 0.1 MPa/min to 1000 MPa/min. For $_{\text{powder}}$ZIF-8, the shape of the hysteresis loop is of an intermediate type between the one for a molecular spring and a shock-absorber (Figure 4.3a). In other words, the hysteresis is not large enough to make the "$_{\text{powder}}$ZIF-8 + water" system an efficient dissipator, but too large to make it a poorly-performing molecular spring. Moreover, while for some flexible materials the hysteresis loop strongly depends on the compression-decompression (intrusion-extrusion) rate,[16] this is not the case for $_{\text{powder}}$ZIF-8, for which the PV-isotherm remains practically the same in a 5 order of magnitude rate span, even when extreme velocities of 1000 MPa/min are applied (Figure 4.3a). These kinetics of water intrusion-extrusion in seemingly small pores of ZIF-8 (ca. 10.8 Å and 3.4 Å flexible windows) is fascinating. While high-frequency operation has been demonstrated previously for "mesoporous grafted silica + water" systems,[97, 102, 103] a similar feature is surprising for microporous ZIF-8, which under ambient conditions has a pore opening of only 3.4 Å and, perhaps, even more importantly may undergo reversible structural transition upon water intrusion-extrusion, known as a gate-opening effect.[147] Results presented in Figure 4.3a suggest both a rapid intrusion-extrusion of water molecules into-from ZIF-8 as well as its fast framework respond to an external stimulus, such as pressure. To gain a microscopic confirmation of the observed performance, in operando high-pressure neutron diffraction experiments were conducted on the $_{\text{powder}}$ZIF-8 + water system.

4.4.3 In operando neutron scattering study

Figure 4.4a shows the neutron powder diffraction (npd) patterns collected at the BT-1 diffractometer for "$_{\text{powder}}$ZIF-8 + water" system at 20 MPa and 50 MPa. The pattern at 20 MPa corresponds to the empty framework of ZIF-8 below intrusion pressure, while 50 MPa corresponds to water-filled ZIF-8 as this pressure is well-above the intrusion pressure (Figure 4.3a). The obvious difference in two patterns is evident for (110) Bragg peak at 9.85° (Figure 4.4a). The variation in this peak's intensity is due to the contribution of the intruded water to the scattering factor, which periodicity is induced by the crystal lattice. The contribution of water can be quickly extracted from the difference Fourier mapping applied to these patterns at 20 MPa and 50 MPa, which reveals that the main difference is indeed in the occupancy of the pore of ZIF-8 (see yellow iso-surface in Figure 4.4b). Besides, Figure 4.4c shows the dependence of the (110) peak area on pressure, which perfectly mimics the PV-isotherm of the ZIF-8 + water system (Figure 4.3a). This relationship suggests indeed that the (110) peak can be used for in operando tracking of water molecules intrusion-extrusion into-from ZIF-8.

Figure 4.4d demonstrates the dependence of the (110) peak intensity on pressure upon compression-decompression cycles performed with 50 MPa/min ramp. One can clearly see that the variation of intensity closely follows the pressure ramp, confirming that the impressive stability of the PV-isotherm of the "powderZIF-8 + water" system at different compression-decompression ramps (Figure 4.3a) is indeed due to the fast kinetics of water molecules entering-leaving the cages of ZIF-8.

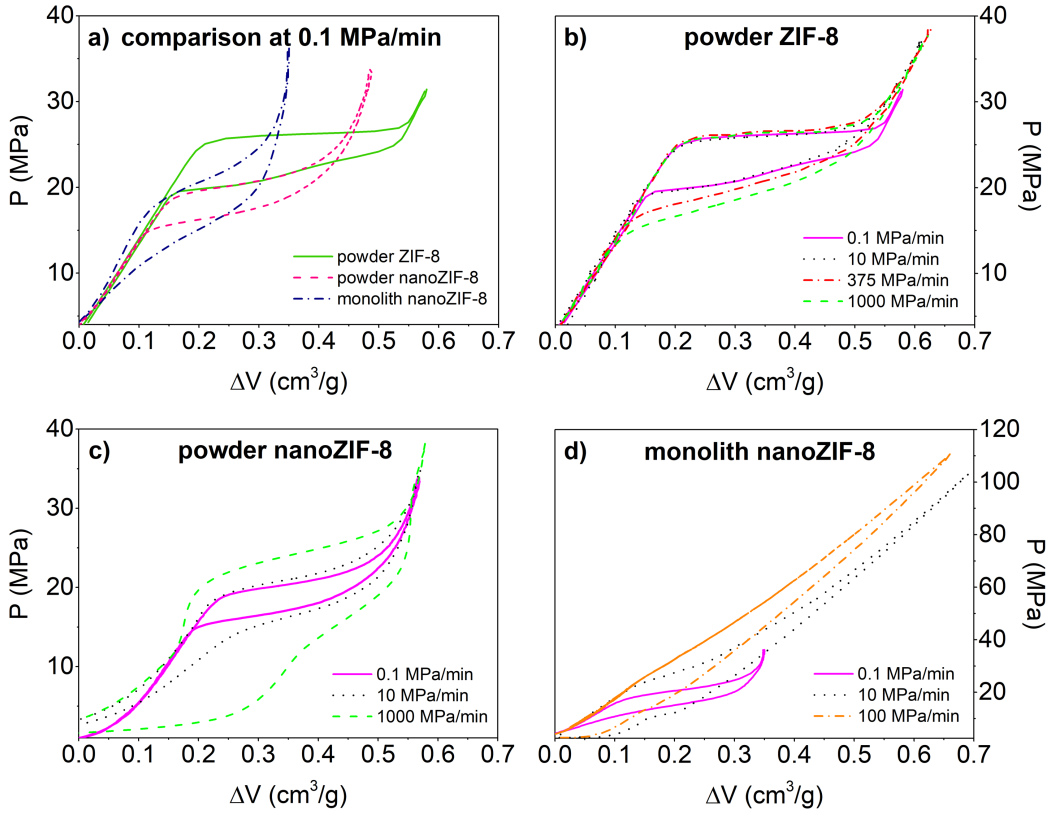

Figure 4.3. Room temperature PV-isotherms for ZIF-8 + water system: a) comparison between $_{powder}$ZIF-8, $_{powder_nano}$ZIF-8 and $_{mono_nano}$ZIF-8 at 0.1 MPa/min compression rate; b) $_{powder}$ZIF-8, c) $_{powder_nano}$ZIF-8 and d) $_{mono_nano}$ZIF-8 at different compression rates.

Another import conclusion from this observation is that a well-known gate-opening effect of ZIF-8,[147] related to the rotation of imidazolate linkers to ease intrusion of guest molecules in the ZIF-8 cavities, does not slow down the intrusion-extrusion process within the timescale of the experiment. While this kinetics is impressive, the practical attractiveness of the "powderZIF-8 + water" system remains questionable due to an intermediate hysteresis loop (neither molecular spring, nor shock-absorber – Scheme 4.1).

4.4.4 Effect of monolith configuration and crystal size

To begin with, we focus on the intrusion/extrusion cycle at quasi-static conditions, i.e., at low pressure scanning rates, 0.1 MPa/min. One notices two main differences between the intrusion/extrusion cycle in the powder_nano and monolith with respect to the powder one: i) lower intrusion pressure and ii) lower intrusion volume (Figure refFig-monolith-figure3a). The former is explained by the already observed relation between crystallite size, which is smaller in both $_{powder_nano}$ZIF-8 and $_{mono_nano}$ZIF-8, and intrusion pressure.[117, 148] The latter, we attribute to the tighter packing of crystallite in both $_{powder_nano}$ZIF-8 and $_{mono_nano}$ZIF-8 samples, which prevents the sizable expansion of ZIF-8 accompanying liquid intrusion, as recently reported.[149]

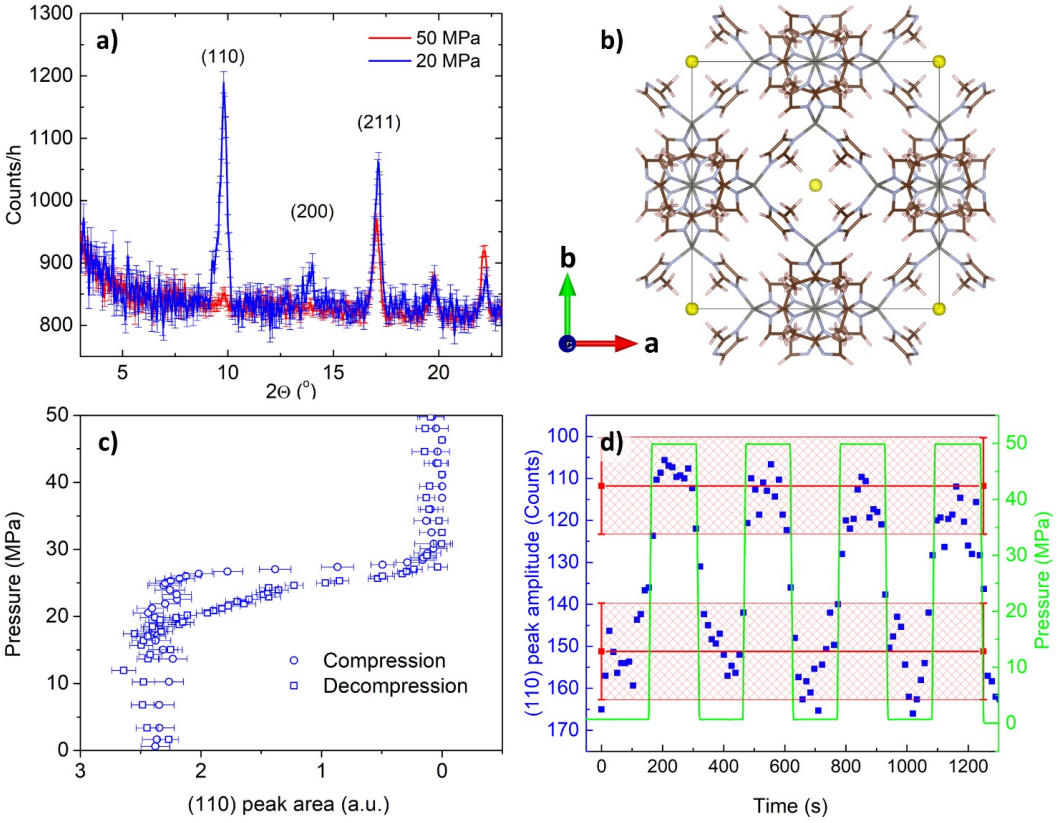

Figure 4.4. Neutron diffraction experiments for the "$_{\text{powder}}$ZIF-8 + water" system: a) diffraction pattern at 20 and 50 MPa (above and below intrusion, respectively); b) Fourier map, showing the yellow isosphere to reflect the occupational difference between 20 and 50 MPa states; c) Pressure dependence of the area of the (110) reflection (note, the similarity with Figure 3a); d) Intensity of the (110) reflection recorded upon dynamic compression-decompression cycling. Error bars indicate 1σ. Red shaded area indicate uncertainty.

This effect is discussed in detail in the theoretical Sec. 4.4.5. Additionally, the tight packing, especially in the monolith sample, might slow down or prevent percolation of water in the core of the sample, thus limiting the amount of ZIF-8 which is actually intruded during a cycle. The atomistic origin of this phenomenon is also discussed in the theoretical section. Finally, one cannot exclude a possible amorphization of the surface layer of crystals, which will result in intrusion volume reduction for $_{\text{powder_nano}}$ZIF-8 and $_{\text{mono_nano}}$ZIF-8 compared to $_{\text{powder}}$ZIF-8.

Another remarkable difference between the three samples is the slope of the intrusion branch of the PV-cycle. One notices that the branch of the PV-cycle corresponding to intrusion is (almost) flat in the case of $_{\text{powder}}$ZIF-8, suggesting that intrusion takes place at a well-defined pressure, while it acquires a slope for the $_{\text{powder_nano}}$ZIF-8 sample, which further increases in the case of $_{\text{mono_nano}}$ZIF-8. The dependence of the slope of the intrusion branch on the arrangement of the ZIF-8 sample is reported here for the first time and suggests that in the $_{\text{powder_nano}}$ZIF-8 and $_{\text{mono_nano}}$ZIF-8 intrusion takes place over a range of pressures. Atomistic simulations helped us to understand and explain the origin of this behaviour, as

discussed in Sec. 4.4.5.

What is very interesting and technologically appealing is the dependence of the dynamic response of the "ZIF-8 + water" system on the compression-decompression rate on the crystal size (powder vs powder_nano – Figure 4.3b vs 4.3c) and compactness of the crystallite aggregate (nano-powder vs nano-monolith configuration Figure 4.3c vs 4.3d). The effect of crystal size of ZIF-8 on the intrusion-extrusion behaviour is somehow expected from previous studies,[117, 148] while the effect of crystallite aggregate compactness – monolith configuration – is unexpected and, to the best of our knowledge, has never been presented previously. More specifically, in the case of monolith configuration, increasing the speed of cycling effectively transforms a poorly-performing molecular spring into a effective shock-absorber (Figure 4.3d). The technological potential of the monolith configuration vs powder cases is illustrated in Figure 4.5, showing the amount of dissipated mechanical energy per intrusion-extrusion cycle (i.e., the area of the hysteresis loop of Figure 4.3). Here, one notices a drastic difference in the dependence of dissipated energy on the compression-decompression rate for the three samples. For the $_{\text{mono_nano}}$ZIF-8, increasing the ramp from 0.1 MPa/min to 10 MPa/min results in a more than threefold increase in dissipated energy, which, despite the reduction of the intruded volume, is more than three times higher compared to $_{\text{powder}}$ZIF-8 under similar conditions (Figure 4.5a). Moreover, considering the higher density of $_{\text{mono_nano}}$ZIF-8, the volumetric dissipated energy density improved more than one order of magnitude compared to $_{\text{powder}}$ZIF-8 (Figure 4.5b). It also interesting to note that at velocities of around 10 MPa/min $_{\text{mono_nano}}$ZIF-8 demonstrated two-step extrusion, which was noted earlier for $_{\text{powder}}$ZIF-8 depending on the compression rate, temperature[150] and perhaps due to the interplay between the extrusion process and opening-the-gate effect or the extrusion of water from the grain boundaries. Such a two-step extrusion is also evident for $_{\text{powder_nano}}$ZIF-8 at high compression-decompression rates (Figure 4.3b). The mechanism behind this behaviour is outside of the scope of this paper and will be explored in the future.

The reported results suggest that both crystal size and monolith configuration have drastic effect on the dynamic intrusion-extrusion performance of water into-from ZIF-8: both smaller crystallites and the monolith configuration help increasing hysteresis with pressure scanning rate. The effect of the monolithic configuration, however, is more pronounced from the energetic point of view. Indeed, it can be seen that with the monolith configuration dissipated energy of 5.3 $J \cdot g^{-1} \cdot cycle^{-1}$ can be reached at compression-decompression rates of 100 MPa/min (Figure 4.5a). $_{\text{powder_nano}}$ZIF-8 requires more than 8 times higher compression-decompression rate to reach similar dissipated energy (Figure 4.5a). Moreover, volumetric energy density of the monolith configuration is more than 5 times higher compared to $_{\text{powder_nano}}$ZIF-8 and $_{\text{powder}}$ZIF-8 at 100 MPa/min compression-decompression rate. Remarkably, powder samples cannot match the high volumetric energy density of the monolith configuration even at the very high-pressure scanning rates. Therefore, while crystal size is indeed important, the monolith configuration clearly introduces additional benefits to the dissipation capabilities of ZIF-8. In other words, present findings suggest a novel tuning strategy that can be exploited to enhance energy dissipation of ZIF-8 samples, which might open novel technological applications of this material and/or other MOFs. To conclude this paragraph, it is worth remarking that even

though the enhancement of dissipated energy due to crystal size is less pronounced as compared to monolith configuration, the benefit of the crystal size-approach in lower intrusion-extrusion pressures (Figure 4.3c), which may be beneficial for certain applications, such as shock-absorbers.

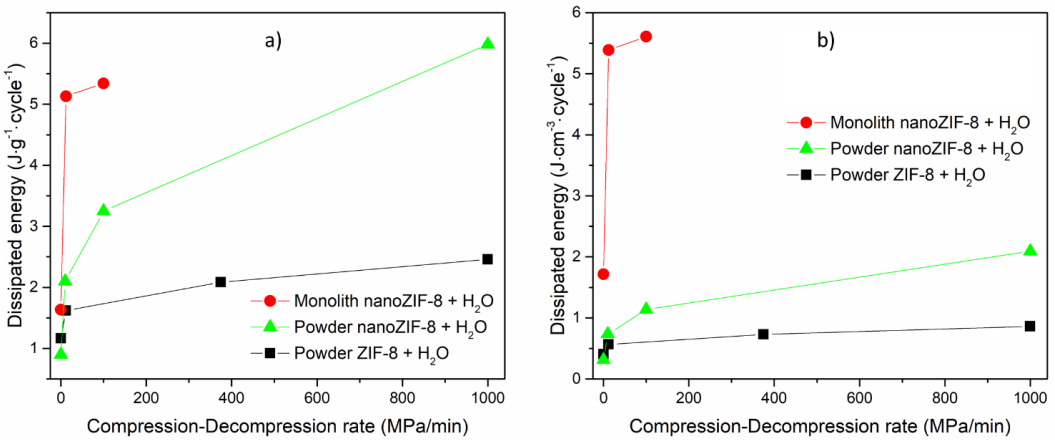

Figure 4.5. Amount of dissipated mechanical energy per intrusion-extrusion cycle for $_{\text{powder}}$ZIF-8 and $_{\text{mono_nano}}$ZIF-8 depending on compression-decompression rate: a) per unit of mass and b) per unit of volume. Note that bulk density of the powder is used to calculate volumetric energy density for the cases of $_{\text{powder}}$ZIF-8 and $_{\text{powder_nano}}$ZIF-8 cases.

In the rest of this section, we propose possible mechanisms underlying the effect of monolith configuration on the intrusion-extrusion dynamics, which are then expounded using atomistic simulations in the next section. Considering that the intrusion-extrusion process in itself is rapid (Figure 4.3b and 4.4d), it is reasonable to assume that the observed differences in the dynamic hysteresis for monolithic and powder ZIF-8 are due to the arrangement of their grains (densely packed monolith vs fine powder). As we mentioned in Sec. 4.4.1, the high density, the crystallite size, and the transparency of the monolith suggest that it is composed of tightly packed crystallites. In this case, it is expected that a longer time is required for water to percolate through, in particular to reach crystallites at the core of the monolith, which causes higher intrusion pressure upon forced compression, as well as lower pressure of spontaneous extrusion upon rapid decompression (Figure 4.3c). This contrasts with $_{\text{powder}}$ZIF-8, with a much higher external surface directly in contact with the bulk liquid, which speeds up the process. Combing this rather straightforward phenomenon with a highly responsive intrusion-extrusion process (Figure 4.3b and 4.4d) allows for the tunability of dynamic hysteresis of heterogeneous lyophobic systems depending on the density of the grains of the porous material (Figure 4.3d and 4.5). This provides an opportunity for the development of energy dissipators with frequency-dependent performance. Moreover, it is useful for the triboelectrification phenomenon, which was previously demonstrated to be linked with mechanical and thermal energy hysteresis in the intrusion-extrusion cycle[1, 16] and will be explored in more detail in upcoming works.

A final remark is in order concerning the potential technological relevance of the monolith or, in general, crystallite packing as a strategy to enhance energy

dissipation: the stability of the sample upon repeated liquid intrusion/extrusion. Stability of porous materials upon intrusion-extrusion cycling is a challenge, and monolith stability is no exception. Nevertheless, after intrusion-extrusion cycling tests (overall 36 cycles), a good repeatability of the results was evident. The samples maintained their size (Figures SI6), even though, some cracks were observed – Figure SI7. Additionally, for the stability verification we compared the intrusion-extrusion cycles at 0.1 MPa/min recorded before and after dynamic cycling. A good reproducibility was evident – Figure SI8.

We believe the obtained effect of monolith configuration may be not just specific to ZIF-8, and other MOFs such as ZIF-67,[150] MAF-7,[151] ZIF-71 and MAF-6[152] can be considered to enhance their energy dissipation capabilities. This will be explored in upcoming works.

4.4.5 MD simulation study

Simulations were performed to validate the hypotheses proposed to explain the differences in the intrusion-extrusion characteristics of powder, powder_nano and monolith samples, i.e., to assess how the structural effects of tight packing of ZIF-8 might alter the intrusion/extrusion dynamics. We focused on grain boundaries: indeed, as mentioned above, $_{\text{powder_nano}}$ZIF-8 and, in particular, $_{\text{mono_nano}}$ZIF-8 are characterized by a high density of grain boundaries, more grain boundaries per crystallite than the standard powder sample. Moreover, smaller crystallites show a rhombic dodecahedral shape (Figure 4.2b) vs the cubic shape typical of larger crystallites (Figure 4.2a). In the literature it is discussed that the (110) surface exposed by the former allows the formation of tightly bound, 'locked', grain boundaries, which are not observed for the (100) surface, exposed by the latter.[2] In the following we show that tight grain boundaries, solely formed for samples containing smaller crystallites - $_{\text{powder_nano}}$ZIF-8 and $_{\text{mono_nano}}$ZIF-8 - may slow down the percolation of water in the interior of the monolith and/or prevent liquid intrusion into ZIF-8.

Grain boundaries are complex structures and some a priori information or assumption is needed for their modelling. In the case of ZIF-8, a previous study[2] has revealed that ZIF-8 nanocrystals of ∼85 nm, a size comparable with those measured in powder_nano and mono_nano samples, have a rhombic dodecahedral shape consistent with images reported in Figure 4.2. These crystals expose (110) surfaces, which can be either 'zigzag' or 'armchair' terminated, the latter being the one experimentally observed. Quoting Ref.[2] "ZIF-8 crystals were 'locked' at (110) interfaces after attachment, [...], indicating that (110) surfaces are particularly important for self-assembly". Given this solid experimental evidence, here we focused on an armchair-terminated (110) grain boundary. Given the complexity of the system, we decided to use an ab initio approach, performing density functional theory calculations as described in detail in Sec. 4.3.2.6.

To start with, we accurately studied the structure of the grain boundary. Here, we refrained from performing a simple structural optimization of the grain boundary as the potential of such a complex system might present roughness, which could trap the structure in local minima, at a distance between the two crystallites different from the equilibrium one. Rather, we searched for the lowest energy structure as

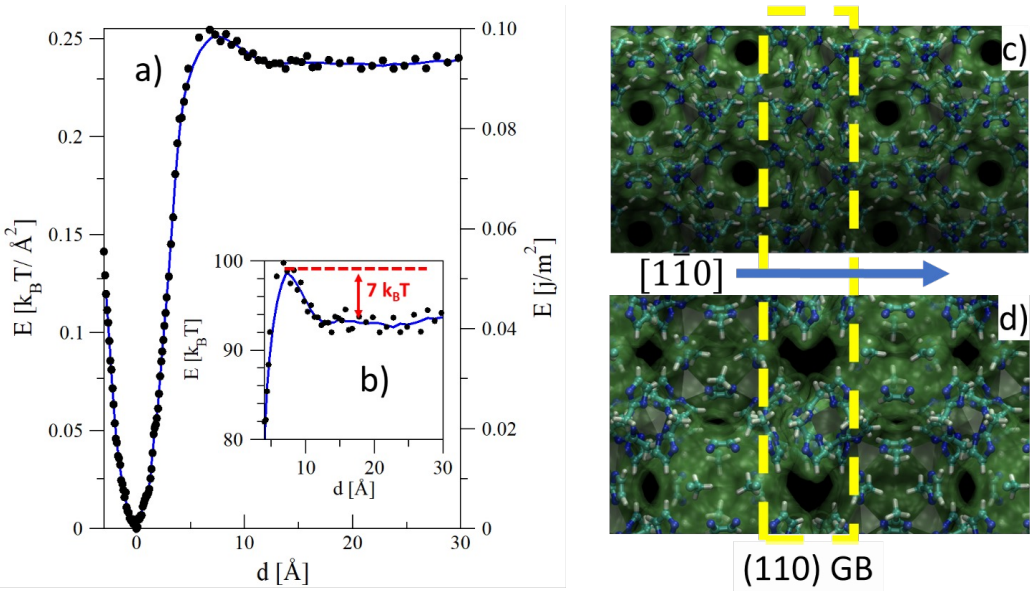

Figure 4.6. a) energy profile of the ZIF-8 (110) GB as a function of the distance between the two crystallites. The profile is characterized by a deep minimum and a barrier at ∼5 Å. b) Zoom on the barrier region. In panel b the energy profile is reported in k_BT for a GB of ∼392 Å^2 of contact area, corresponding to the smallest possible ZIF-8 (110) GB. The height of the barrier with respect to the energy plateau at larger distances 7 k_BT, i.e., 7 times the thermal energy available at room conditions, suggesting, according to the Arrhenius law, that a close approach between two crystallites is energetically non-trivial, especially for large crystallites. c,d) Images illustrating the GB from two different points of view. The crystallites and the GB are shown by both a stick-and-ball representation of the atoms and the surface enveloping the atoms obtained by a probe particle[153] of 3.0 Å of diameter, approximately corresponding to the characteristic size of water in several classical force fields.[144]

a function of the distance d between the two ZIF-8 crystallites forming the grain boundary, exploring a broad ∼35 Å distance range. The profile of the energy per unit area of the grain boundary vs the distance is reported in Figure 4.6a, where distance d = 0 Å has been arbitrarily fixed in correspondence of the minimum of the GB energy. Panels d and e of the same figure show two views of the grain boundary, highlighting how tight the two crystallites are in the stable configuration. Concerning the energy profile, one interesting feature is the energy maximum at ∼5 Å, amounting to a ∼7 k_BT barrier to allow two facing ZIF-8 crystallites to grow along the [110] direction to reach the most stable configuration (Figure 4.6b). Of course, such a barrier increases with the area of the facing crystallites, quickly exceeding the thermal energy or other forces that my push the system beyond the barrier, e.g., the reduction of free energy along the growth of crystallites, which can help to tightly bind crystallites during the self-assembly process. This observation by might explain why this tight binding is observed only for the powder_nano (Figure 4.2b and Figure SI9) and, possibly, the monolith samples and not for the regular powder.

As mentioned above, the tight binding of grains might have two consequences: i) it may prevent expansion of grains during intrusion, the latter being a phenomenon

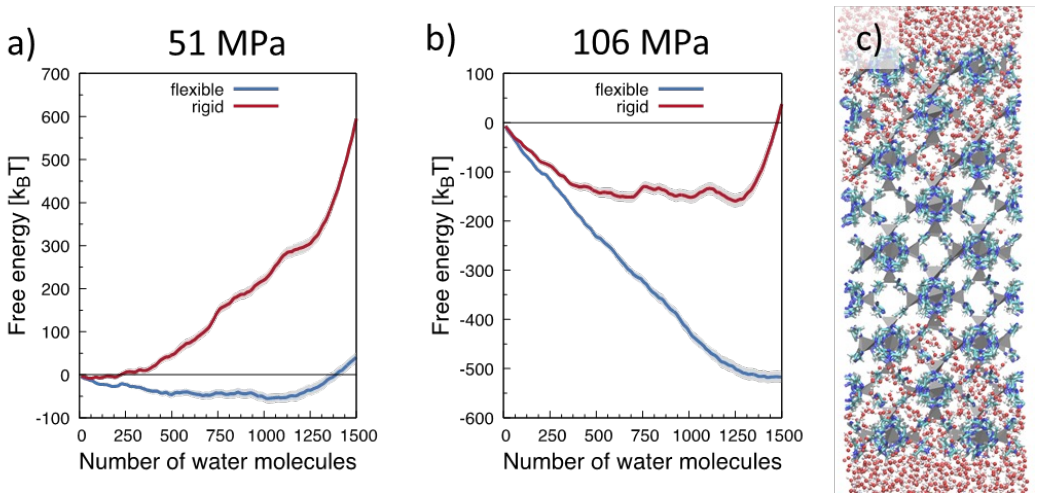

Figure 4.7. a,b) free energy profile of the ZIF-8+water sample as a function of the number of water molecules in the MOF slab, shown in panel c in a partially filled configuration. The grey shadow beneath the solid lines represents the error on the estimation of the free energy (see supporting information). In panel a) we report the free energy profiles at the computational intrusion pressure of the flexible framework, 51 MPa. Indeed, one can notice that in these conditions the free energy of the filled state (1050 water molecules in the framework) is lower than the empty one. At this pressure, on the contrary, for the rigid framework the lowest free energy state corresponds to the empty ZIF-8 framework. At 106 MPa, the lowest free energy state is the filled one also for the rigid framework case, indicating that at this pressure intrusion takes place also in this sample. Due to liquid and lattice compressibility, at 106 MPa the water molecules in the filled ZIF-8 slab are more than at 51 MPa.

recently reported by some of the authors of the present work,[149] and ii) slow down percolation of water, preventing, in practice, the liquid to reach ZIF-8 crystallites in the core of the monolith. Let us analyze in detail how these two mechanisms may affect intrusion, starting with the tight binding among crystallites preventing or limiting their expansion and the consequences on the wetting of the ZIF-8 cavities. Figures 4.7a and 4.7b compare the free energy profiles of liquid intrusion in a flexible and rigid ZIF-8 framework at 51 and 106 MPa, the computational intrusion pressures of the flexible and rigid frameworks (figure 4.7c), respectively. We remark that intrusion free energy profiles have been determined using the restrained molecular dynamics approach, with ZIF-8, water and their interaction modeled by a classical force field, an approach that has been successfully employed in previous works[149, 154] (see Sec. 4.3.2.6 and Supporting Information for further details). In the rigid framework, atoms are still allowed to move; in particular, imidazolate is allowed to rotate to ease liquid intrusion through the 6-member ring windows (see Figure 4.6d), but the crystallite is globally prevented to expand/compress (see Sec. 4.3.2.6). The intrusion pressure can be determined by identifying the value at which the free energy corresponding to full wetting of the ZIF-8 slab, i.e., when all cages of the computational sample (Figure 4.7b) are filled, is lower than that of the empty slab. Due to the liquid compressibility, the actual number of water molecules In the filled slab changes with pressure. It is seen that despite the expansion upon complete intrusion is apparently small, 0.06 Å per unit cell,[149]

rigidity increases the intrusion pressure by $\Delta P_{int} = P_{int}^{rig} - P_{int}^{flex} = 60$ MPa, bringing it from 51 MPa, as predicted for the flexible ZIF-8, to 106 MPa, as determined for the rigid one. Indeed, this effect of flexibility on the intrusion pressure may explain the surprisingly low value of P_{int} of ZIF-8 ($\sim$25 MPa) vs more rigid porous materials of comparable porous size and hydrophobicity, such as MFI ($P_{int} = \sim$90MPa[3]) and TON ($P_{int} = \sim$160MPa[4]), and with respect predictions of the Young-Laplace equation for ZIF-8: $P_{int} = -2\gamma\cos\theta/r$ =130 MPa (γ = 72.8 mN/m is the water surface tension, θ the Young contact angle, here set to the apparent experimental value of 130°, r = 1.7 Å the radius of the 6-member ring apertures allowing intrusion). Our simulations suggests that the apparently small 0.06 Å expansion of the lattice parameter crucially reduces the intrusion pressure of ZIF-8 and that, on the contrary, hindrance of lattice expansion, as the one imposed by tight grain boundaries, may severely limit the number of crystallites that can be intruded in the nano powder and, especially, in the monolith. Of course, we neither expect that tight GBs do completely prevent crystallites expansion, nor that in an experimental sample all crystallites are compressed to a level of tightness corresponding to the GBs equilibrium distance. GB equilibrium distance is the energetically favored configuration of a GB but it is well known that crystallization is controlled by a subtle balance of thermodynamics and kinetics factors[5]. We expect that GBs impose a partial limitation and/or a hindrance on expansion, and that these are more severe in the densely packed monolith than in the powder_nano sample and absent in the standard powder, made by cubic crystallites lacking extended (110) surface allowing the formation of tight grain boundaries. This, possibly, results in intrusion taking place in a pressure range rather than at a well-defined value, depending on the presence of crystallites at various degrees of compression in the powder_nano and mono_nano samples. This will result in the slope of the intrusion branch of the PV cycle of the powder_nano and mono_nano samples shown in Figure 4.3a. The slope of the latter is larger than that of the former, consistently with the higher density of tight grain boundaries one expects in the case of the monolith. The most compressed grains, probably those laying in the core of the monolith or in more tightly bound crystallites of the $_{\text{powder_nano}}$ZIF-8 sample (figure 4.2b), might be completely prevented to be intruded in the relevant pressure range, which explains the sizable reduction of intruded volume of the ZIF-8 configuration .

Let us now focus on the effect of tight GB on water percolation in the monolith sample. Of course, this effect is relevant if the characteristic time of water percolation, τ_{perc}, and water intrusion, τ_{intr}, are comparable. The characteristic time of diffusional processes is associated to the presence of energy barriers molecules must overcome along their path, the energy barrier associated to the crossing of 6-member ring windows, $\Delta E_{intr}^{\dagger}$, and the tangential diffusion along GBs, $\Delta E_{perc}^{\dagger}$, in the case of intrusion and percolation, respectively. Percolation and intrusion times are associated to the corresponding barriers via an Arrhenius-like equation,

[3]https://doi.org/10.1016/S0167-2991(08)80262-5

[4]https://doi.org/10.1016/j.micromeso.2011.03.043

[5]The thermodynamically stable outcome of a crystallization is a single crystal, which presents the lower surface/volume ratio, hence pays the lowest surface energy penalty. Producing a single crystal, however, is notoriously non-trivial, indicating that, in practice, crystallization is determined by both the thermodynamics and kinetics of the process.

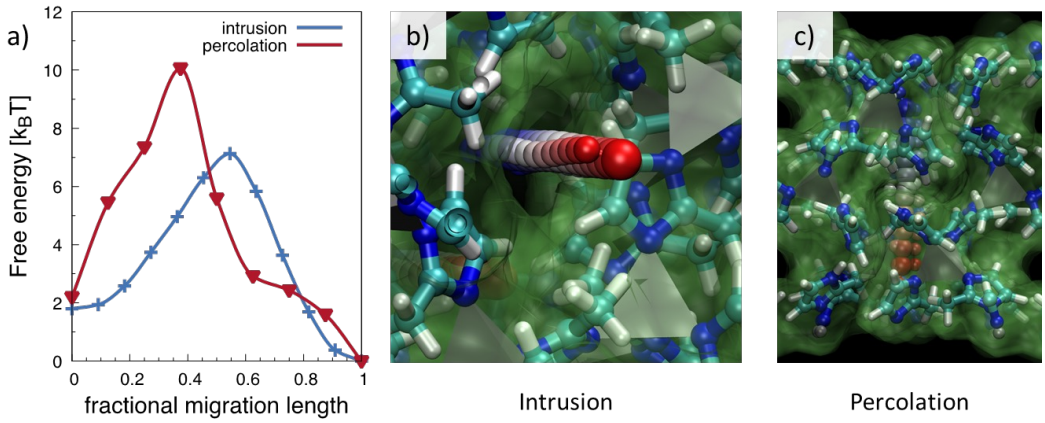

Figure 4.8. a) energy profile of intrusion (blue) and percolation (red) of a water molecule in ZIF-8 and along the (110) GB, respectively. In panel b and c are reported the corresponding paths. Panel a) shows that, on the contrary of the trend with small non-polar molecules,[2] water percolation along a tight GB requires to overcome a higher barrier with respect to intrusion.

$$\tau = \tau_0 \exp\left[-\frac{\Delta E^\dagger}{k_B T}\right] ,$$

where the pre-exponential factor τ_0 is the intrinsic time it takes for the system to complete the process in absence of the barrier.[155] Given the exponential dependence on the barrier, $\Delta E^\dagger$ mainly affects the intrusion or percolation times, and the one that depends the most on the confinement conditions. To evaluate the effect of tight GBs in limiting intrusion because of hindered of percolation, we computed the intrusion and percolation barriers of a single water molecule in the (ab initio) computational sample containing the (110) GB at the equilibrium distance. We recognize that this is a simplistic representation of water intrusion in ZIF-8 and percolation through the monolith, where, for example, there is more than one water molecule per ZIF-8 cavity or in the GB. However, the very high computational cost of the calculations necessary to compute intrusion and percolation barriers forced us to limit the complexity of the computational model. Nevertheless, we believe that these calculations reveal interesting phenomena that help interpreting the experimental results and, possibly, inspire further theoretical and experimental investigations. In Figure 4.8a we report the energy profile of the intrusion and percolation energies, together with the corresponding transition paths (Figure 4.8b and 4.8c). Contrary to previous hypotheses, present results show that the percolation barrier of water in a (110) ZIF-8 GB at the equilibrium distance is slightly higher than the intrusion barrier. We believe that this is due to a combination of two factors: i) at the equilibrium distance, the largest apertures along the GB are not sizably bigger than the 6-member ring windows (see Figure 4.6c); moreover, ii) the interactions between water and imidazolate molecules at GBs is stronger than in the ZIF-8 cavities, namely, water can form hydrogen bonds with nitrogen atoms because at the GB lone pairs of this chemical species are not involved in bonds with Zn. The reduced percolation of water might completely prevent intrusion in the ZIF-8 crystallites laying at the core of the monolith sample. Though this effect is expected to be less

problematic nano_powder because ZIF-8 crystallites are in direct contact with bulk water, figure 4.2b shows that a significant fraction of the surface of crystallites in this sample is engaged in the formation of tight grain boundaries. Thus, also in this sample the direct contact with bulk water is significantly reduced with respect to the standard powder sample. Summarizing, atomistic simulations support the hypotheses proposed on the basis of experimental results to explain the dependence of intrusion/extrusion characteristics at quasi-static and high scanning rates on the type of aggregation of ZIF-8, $_{\text{powder}}$ZIF-8, $_{\text{powder_nano}}$ZIF-8 and $_{\text{mono_nano}}$ZIF-8. Tight grain boundaries present in the powder_nano and mono_nano can be seen as 'extended' surface defects altering the P-V characteristics of these samples with respect the standard powder one alluded in the literature[6].

4.5 Conclusions

Herein, we show that the dynamic hysteresis of a non-wetting liquid intrusion-extrusion process can be drastically affected by a macroscopic grain arrangement of a porous material. The concept is demonstrated by comparing the dynamic hysteresis of water intrusion-extrusion into-from a powder, hydrophobic ZIF-8 MOF, versus its monolithic highly dense analogue. We found that by changing the macroscopic morphology and arrangement of ZIF-8 from a fine powder to compact monolith, it is possible to change the intermediate intrusion-extrusion performance (nor molecular spring, nor shock-absorber) into a desirable shock-absorber type with more than one order of magnitude enhancement of dissipated energy per cycle. The experimental results are supported by atomistic simulations and pave the way for a new strategy for tuning energy performance and applicability of molecular springs and nano-shock absorbers.

[6]DOI: 10.1039/c5ra02636a

Part II

Planar solid-liquid and liquid-liquid interfaces

Preamble

In this part of my research I tried to understand the effect of gas dissolved in a solid-liquid and liquid-liquid interface. Typically, classical continuum theories applied to this kind of systems, e.g. capillarity theory, can possibly take into consideration the presence of gas only as a mean field distribution[156]. Said approach, however, fails to explain some phenomena manifestly demonstrated by experimental evidence. My ambition was to contribute to the extension of these well-known theories for interface systems in the presence of dissolved gas, going beyond the state of the art.

In the solid-liquid interface case, currently available theories fail to predict the nucleation of nanobubbles, and also their extraordinary stability and consequent longevity, even in hostile conditions: in fact, according to these theories, nanobubbles should evaporate quite rapidly, while experiments showed clearly their much longer life-span (orders of magnitude longer than predicted), even in heavily undersaturated liquids. Recently, Tan, An and Ohl proposed a model that, branching from a still classical macroscopic description, tried to represent these unaccounted phenomena by introducing an effective potential, attracting gas molecules dissolved in the liquid to the solid wall. The TAO model lacked an experimental validation, which could even be impossible to achieve, since there is no logical way to measure such effective potential. Besides, through atomistic simulations, I was able to provide support and show how the model can actually fill the gaps of previous theories.

On the other hand, the nucleation of gas (not vapor) bubbles at liquid-liquid interfaces is a completely new, only recently observed phenomenology, for which a possible explanation was still being sought. It is a new phenomenon because cavitation bubbles - that is, bubbles formed under tensile conditions, not heating - were always thought to result from the expansion of pre-existent gas nuclei (gas bubbles), trapped inside the crevices/cavities of solid bodies immersed in the liquids.

Chapter 5

The Interplay Among Gas, Liquid and Solid Interactions Determines the Stability of Surface Nanobubbles

5.1 Abstract

Surface nanobubbles are gaseous domains found at immersed substrates, whose remarkable persistence is still not fully understood. Recently, it has been observed that the formation of nanobubbles is often associated with a local high gas oversaturation at the liquid-solid interface. Tan, An and Ohl have postulated the existence of an effective potential attracting the dissolved gas to the substrate and producing a local oversaturation within 1 nm from it that can stabilize nanobubbles by preventing outgassing in the region where gas flow would be maximum. It is this effective solid-gas potential - which is not the intrinsic, mechanical, interaction between solid and gas atoms - its dependence on chemical and physical characteristics of the substrate, gas and liquid, that controls the stability and the other characteristics of surface nanobubbles. Here, we perform free energy atomistic calculations to determine the effective solid-gas interaction that allows us to identify the molecular origin of the stability and other properties of surface nanobubbles. By combining the Tan-An-Ohl model and the present results we provide a comprehensive theoretical framework allowing, among others, the interpretation of recent unexplained experimental results, such as the stability of surface nanobubbles in degassed liquids, the very high gas concentration in the liquid surrounding nanobubbles, and nanobubbles instability in organic solvents with high gas solubility.

5.2 Introduction

Surface nanobubbles are spherical-cap gas bubbles attached to immersed substrates [157, 158] (Fig. 5.1A). They are noted for their counter-intuitive properties, foremost of all their puzzling longevity. Despite numerous efforts over the years, no

single model for their stability is widely accepted and able to yield a comprehensive explanation of all their properties.

The fundamental challenge in rationalizing the stability of nanobubbles is well illustrated by the early theoretical calculations of Epstein and Plesset [159], which indicate that spherical bubbles can never achieve stationarity — they either grow catastrophically or dissolve into bulk liquid in a subsecond timescale due to their small size and high curvature. Recently this difficulty has been overcome by the insight that the contact line of surface nanobubbles may be pinned at nanoscale surface heterogeneities, thus modifying their diffusive dynamics such that they can attain a stable equilibrium when the bulk liquid is oversaturated with gas. [160, 161] Here, oversaturation is defined as $\zeta = c_\infty/c_{\text{sat}} - 1$, where c_∞ is the dissolved gas concentration in the bulk liquid and c_{sat} is the saturation concentration. Unfortunately, the pinning-oversaturation model cannot be a definitive explanation of the long-term stability of surface nanobubbles. The model requires that $\zeta > 0$, i.e. that gas concentration in the bulk liquid is higher than the saturation value, which is contradicted by the well-established experimental observation of surface nanobubbles in equilibrated open systems ($\zeta = 0$), [162] and even in *undersaturated* conditions ($\zeta < 0$). [163, 164, 165] Indeed, results reported in Ref. [164] led the authors to conclude that "the pinning mechanism alone cannot explain the long-term stability of surface nanobubbles".

In parallel to theoretical progress, numerous simulation studies have been performed to unveil the mechanistic processes governing the stability of surface nanobubbles. [166, 167, 168] While these studies were successful at upholding the importance of contact line pinning to stability, they gave a limited contribution in identifying other key elements to achieve nanobubble stability. Indeed, perhaps influenced by the theoretical hypothesis that nanobubbles are stable only in oversaturated conditions, [160, 161] but in contrast with experimental evidence, [162, 163, 164, 165] these works limited the attention to $\zeta \geq 0$. Moreover, *standard* molecular dynamics techniques adopted in these pioneering studies allow to span a limited timescale, typically few tens of nanoseconds, $11 - 12$ orders of magnitude shorter than the experimentally reported lifetime of nanobubbles, hours to days. This limits the predictability power of these simulations. To cope with these long timescales special simulation techniques are needed, [40, 169] some of which have been adopted in the present study.

To resolve the difficulties of the pinning-oversaturation model, Tan, An and Ohl [170, 3] suggested that an attractive effective potential ϕ of depth $\sim 1\ k_B T$ (k_B is the Boltzmann's constant and T is the temperature) exists between the substrate and gas molecules, which leads to the formation of a *localized* gas-oversaturated layer at the surface. ϕ would rationalize the existence of a permanent *local* oversaturation sustaining surface nanobubbles, while relaxing the unrealistic requirement that the bulk water is indefinitely oversaturated with gas. Combined with pinning, local oversaturation can explain the stability of nanobubbles: i) pinning prevents the shrinking of their footprint and ii) local oversaturation counteracts the loss of gas from nanobubbles driven by their high Laplace pressure associated to small curvatures. In the original article it was shown that a gas-rich water layer of $\sim 1 - 2\ nm$ at the liquid/solid interface would be sufficient to stabilize nanobubbles. This is possible because at the bottom of nanobubbles, where slices of the spherical

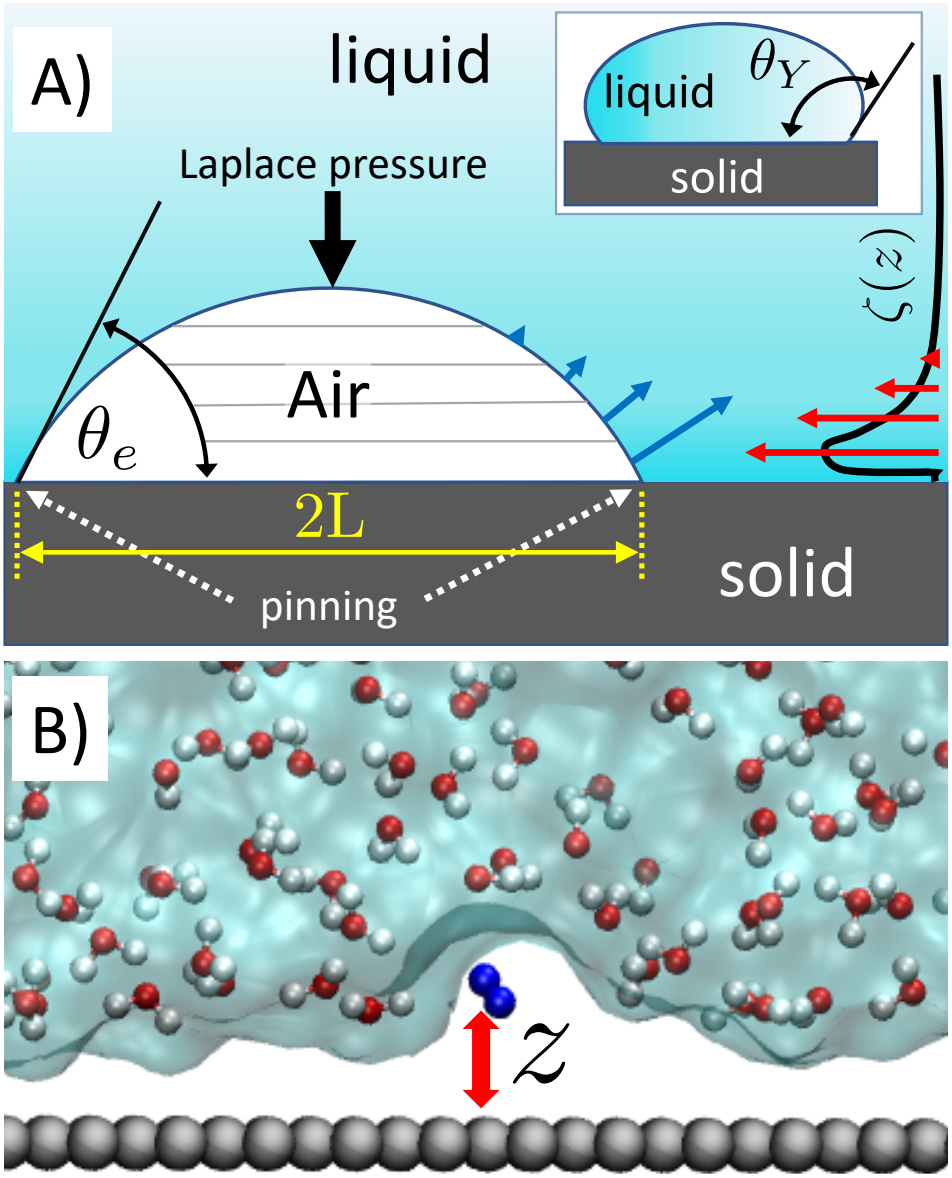

Figure 5.1. A) Sketch of a nanobubble pinned at a solid surface forming a gas side equilibrium contact angle θ_e. Due to the small radius of curvature of the bubble and the corresponding large Laplace pressure, estimated to be several atmospheres, a rapid outgassing and, eventually, dissolution of the bubble is expected. The gas outflow (blue arrows, referring to an entire slice) is maximum at the bottom of the bubble, where the liquid/gas surface per bubble slice (horizontal gray lines) is maximum. This intuitively justifies why a large local gas oversaturation within ∼1-2 nm from the surface is efficient at stabilizing nanobubbles: large local oversaturation near the bottom of the nanobubble (red arrows) can balance the gas outflow in the region where it is maximum. In the inset is shown the Young contact angle, θ_Y, the angle formed by the tangent to a liquid droplet at contact point with the surface B) Snapshot of a portion of the computational sample. Grey spheres represent carbon atoms of the graphite-like slab, the blue dumbbell N_2 and the white and red spheres connected by rods water molecules. The surface enclosing the volume occupied by H_2O is also shown.

cap have the largest area, the gas exchange is more intense (Fig. 5.1A). Thus, a local oversaturation in this region can effectively counteract the nanobubble degassing. A number of recent experiments have shown that, indeed, one can produce a large local gas oversaturation at the solid/water interface [171, 9] and when the oversaturation reaches a critical value, of the order of $\zeta \sim 150 - 250$, nanobubbles are formed. [172, 173, 174] Among the others, Zhou *et al.* have performed near-edge X-ray absorption fine structure experiments showing a large gas oversaturation in the liquid surrounding nanobubbles [9]. Overall, these results calls for a new comprehensive microscopic theory addressing the open questions concerning the stability of nanobubbles in a broader range of experimental conditions and their relation with the possible existence of a permanent local oversaturation.

The stability of surface nanobubbles in water is not their only unique characteristic. While stable in water, surface nanobubbles are unstable in selected protic (e.g. ethanol [175]) and aprotic liquids (organic solvents [176]). Moreover, surface nanobubbles present small contact angles, well below their equilibrium value, that changes significantly, well above the experimental accuracy, among experiments performed in the same nominal conditions (same solid, liquid, gas, degree of oversaturation ζ and temperature). [157] Finally, surface nanobubbles exhibit a remarkable resilience to harsh conditions, such as the near complete degassing of the liquid hosting them. [164]

The TAO model alone does not provide a direct answer to these questions. Indeed, a key conclusion of the TAO model is that the question "what determines the stability of nanobubbles?" must be recast into "what determines the existence of a suitably attracting effective solid-gas potential ϕ?". The form and strength of ϕ, which depends on the nature of the solid, liquid and gas species, determines the properties of nanobubbles summarized above. However, within the TAO model, the effective potential ϕ is an input, i.e., it must be obtained from an independent source. By combining the TAO model and the effective potential ϕ, determined here from atomistic simulations - and its dependence on the chemical and physical characteristics of the solid-liquid-gas three phase system - one obtains i) a comprehensive theory of surface nanobubbles and ii) a multiscale model of surface nanobubble with quantitative predictive capabilities.

Here, the form, strength and range of the effective potential is determined using restrained molecular dynamics (RMD), a simulation technique intruduced in 2006 by Maragliano and Vanden-Eijnden [67, 40] extending and simplifying previous well established approaches, e.g. the Blue-Moon ensemble. [177, 178] This lead us to estimate the local gas oversaturation of the liquid near the substrate and the stability and contact angle of surface nanobubbles hosted in this environment. For solids embedded in water, our results reveal the existence of a potential well of few k_BTs at subnanometric distances from the wall, capable of attracting dissolved gases to the substrate and thus endorsing the viability of local oversaturation as a stabilization mechanism for surface nanobubbles in this liquid. By a systematic variation of the liquid-gas-solid interactions, our simulations provide a mechanistic understanding of a number of counterintuitive, previously unexplained phenomena. For example, we were able to explain, within a unified framework, the large variability of nanobubbles' contact angle at highly ordered pyrolytic graphite immersed in water, [157], why the contact angle of nanobubbles shows a minor dependence on the chemical nature

of the immersed solid (see Ref. [179] and references cited therein), why surface nanobubbles are preferentially formed on hydrophobic substrates [180] but survive also on hydrophilic ones, [181] the tolerance of nanobubbles to gas undersaturation of water [164] as well as their instability in aprotic solvents. [176] Furthermore, we were able to pinpoint how the chemical and physical characteristics of the solid, liquid and gas species contribute to the stability or instability of nanobubbles.

5.3 Computational Methods

5.3.1 Theoretical Background

In this work we use restrained molecular dynamics, RMD, to compute the (Landau) free energy profile as a function of the distance of the center of mass of N_2 or O_2 from a graphite-like surface, z. This free energy is the microscopic analogue of the effective potential ϕ. We remark that the (Landau) free energy is different from the intrinsic interaction potential between N_2 and the solid, i.e. the force field; for example, through the ensemble average the free energy embodies the effect of the liquid intervening between the solid and the gas molecule on the interaction potential, which is a key aspect in determining the stability and instability of nanobubbles in different liquids.

In statistical mechanics, any thermodynamic potential is related to the logarithm of a suitable probability density function in the relevant ensemble. In the present case, the relevant probability density function is $M_z(z^*)$, the probability density that the center of mass of N_2 (or O_2), the function $z(r_{N,s})$ of the atomic positions of nitrogen (or oxygen) and surface atoms $r_{N,s}$, is at a distance z^* from the graphite slab, regardless of the position of all the other atoms in the system. For the sake of simply the notation, in the following we will write the distance between the center of mass of N_2 and the solid surface as a function of the ($3N$ dimensional) atomic positions vector $\mathbf{r}$. In terms of the ensemble distribution $m(\mathbf{r})$, $M_z(z^*)$ reads:

$$M_z(z^*) = \frac{\int d\mathbf{r}\ m(\mathbf{r})\ \delta(z(\mathbf{r}) - z^*)}{\int d\mathbf{r}\ m(\mathbf{r})} \tag{5.1}$$

where $\delta(\cdot)$ is the Dirac delta function, which has the role of selecting only those atomic configurations satisfying the condition $z(\mathbf{r}) = z^*$. In other words, $M_z(z^*)$ is the probability to find the system in any atomic configuration $\mathbf{r}$ satisfying the condition $z(\mathbf{r}) = z^*$.

One can associate a thermodynamic potential to $M_z(z^*)$, here the (Landau) free energy (see, e.g., Refs. [155] and [182]).

$$G(z^*) = -k_B T \log M_z(z^*) \tag{5.2}$$

One notices that this definition has the properties of usual thermodynamics potentials: $G(z^*)$ has a minimum at the stable state, i.e. in correspondence of the maximum of the probability density function, and is expressed in energy units. One may notice that this definition is consistent with the definition of the Boltzmann entropy,

apart the sign, which is opposite, consistently with the property of entropy to be maximum at the stable state, and for the units of measure, which is energy divided by temperature for entropy. Finally, it can be shown that $\Delta G = G(z_2^*) - G(z_1^*)$ between two states can be expressed as the reversible work operated by a generalized force to move the system from z_1^* to z_2^*, [182] which is consistent with the definition of free energies in thermodynamics.

To compute $M_z(z^*)$ - hence $G(z^*)$ - in atomistic simulations one can in principle run a long molecular dynamics trajectory and determine the histogram of z along it; this histogram is a discrete approximation of $M_z(z^*)$ from which one can compute the free energy *via* Eq. (5.2). However, it is well known that this approach is computationally inefficient (see, e.g., Ref. [155] and references cited therein). The key problem is that if the effective interaction is attractive the molecule spends most of the time near the surface, if it is repulsive the molecule is all the simulation far from the substrate; in both cases it is impossible to collect statistics at all relevant z values within the timescale accessible by atomistic simulations (maximum hundreds of ns).

To overcome this problem we use RMD, [67, 40, 142] in which one introduces a controlled bias forcing the system to explore configurations in which the distance $z(\mathbf{r})$ of a gas molecule from the substrate is fixed at the value z^*.[2] In other words, within RMD one forces the system to visit only those configurations consistent with the condition $z(\mathbf{r}) = z^*$. As we will show in the following, this allows us to efficiently estimate the derivative of the free energy $G(z^*)$, i.e. $dG(z^*)/dz^*$, which can then be numerically integrated on z^* to obtain the entire profile of the thermodynamic potential as a function of the distance of N_2 from the graphite slab. Since the estimation of $dG(z^*)/dz^*$ can be expressed as a local average of a suitable observable on the hyperplane $z(\mathbf{r}) = z^*$, one can use restrained MD to compute this average.

In more detail, consider the (Landau) free energy of Eq. (5.2) and for the sake of simplicity assume that the ensemble is canonical, hence

$$m(\mathbf{r}) = \frac{\exp\{[-V(\mathbf{r})/k_BT]\}}{\int d\mathbf{r}\ \exp\{[-V(\mathbf{r})/k_BT]\}}\,, \tag{5.3}$$

where $V(\mathbf{r})$ is the (physical) interacting potential, the so-called *force field*. We remark that the arguments developed below can be straightforwardly extended to other ensembles, e.g. isothermal-isobaric. Within the canonical ensemble the probability density function of Eq. (5.1) reads:

$$M_z(z^*) = \frac{\int d\mathbf{r}\ \exp\{[-V(\mathbf{r})/k_BT]\}\ \delta\left(z(\mathbf{r}) - z^*\right)}{\int d\mathbf{r}\ \exp\{[-V(\mathbf{r})/k_BT]\}} \tag{5.4}$$

[2] Indeed, RMD forces the system to visit atomic configurations *almost* satisfying the condition $z(\mathbf{r}) = z^*$. As explained in the main text, the departure from this condition is determined by the coupling parameter k of the auxiliary potential $k/2\,(z(\mathbf{r}) - z^*)^2$ added to the physical interaction potential. Maragliano and Vanden-Eijnden have proven that the estimate of $dG(z^*)/dz^*$ converges smoothly with k, i.e. one can use a finite value of the coupling parameter to determine the derivative of the mean force within the accuracy of one or few k_BTs. On the other hand, releasing the strict condition of the constraint solves the problem of the implicit - and undesired - additional constraint $\dot{z}(\mathbf{r}) = 0$, which makes more complex the computational determination of $dG(z^*)/dz^*$. [178]

from which one obtains that the derivative of the free energy is

$$\frac{dG(z^*)}{dz^*} = -k_B T \frac{\int d\mathbf{r}\ \exp\{[-V(\mathbf{r})/k_B T]\}\ d\left[\delta\left(z(\mathbf{r}) - z^*\right)\right]/dz^*}{\int d\mathbf{r}\ \exp\{[-V(\mathbf{r})/k_B T]\}\ \delta\left(z(\mathbf{r}) - z^*\right)} \tag{5.5}$$

In Eq. (5.5) one can replace the Dirac delta functions with a smooth Gaussian approximation,

$$\delta(z(\mathbf{r}) - z^*) \approx g_k(z(\vec{r}) - z^*) = \frac{\sqrt{2\pi k_B T}}{k} \exp\left[-\frac{k}{2k_B T}\left(z(\vec{r}) - z^*\right)^2\right]. \tag{5.6}$$

$k_B T/k$ is the variance of the Gaussian function, the parameter determining its width and the accuracy of the approximation to the corresponding Dirac delta function. The reason to express the variance of the gaussian by the apparently more complex form $k_B T/k$ will be clear shortly. Here we just remark that T, the temperature, is determined by the experimental conditions one want to model ($T = 300\ K$, in our case); k is the only parameter of the RMD method, whose suitable value can be determined as explained in the following. By replacing $\delta(z(\mathbf{r}) - z^*)$ with $g_k(z(\mathbf{r}) - z^*)$ in Eq (5.5) one can obtain an explicit, though approximated, formula for the derivative of the free energy

$$\frac{dG(z^*)}{dz^*} \approx \frac{\int d\mathbf{r}\ k\left(z(\mathbf{r}) - z^*\right) \exp\left\{\left\{-\left[V(\mathbf{r}) + k/2\left(z(\mathbf{r}) - z^*\right)^2\right]/k_B T\right\}\right\}}{\int d\mathbf{r}\ \exp\left\{\left\{-\left[V(\mathbf{r}) + k/2\left(z(\mathbf{r}) - z^*\right)^2\right]/k_B T\right\}\right\}} \tag{5.7}$$

Eq. 5.7 shows that, within the Gaussian approximation of the Dirac delta function, the derivative of the free energy can be computed as the expectation value of $k\left(z(\mathbf{r}) - z^*\right)$ over the canonical ensemble of a system driven by the so-called augmented potential $V(\mathbf{r}) + k/2\left(z(\mathbf{r}) - z^*\right)^2$. In practice, one computes $dG(z^*)/dz^*$ at the current value of z^* by averaging the observable $k\left(z(\mathbf{r}) - z^*\right)$ along the trajectory of a constant number of particles/volume/temperature molecular dynamics, restrained by the potential $k/2\left(z(\mathbf{r}) - z^*\right)^2$. The operation is repeated for several values of z^* in the relevant range, here between 0.4 nm and 1.6 nm every 0.02 nm, then the so-obtained $dG(z^*)/dz^*$ is numerically integrated by the trapezoid rule.

The suitable value of k is determined by studying the convergence of the approximate $dG(z^*)/dz^*$, Eq. (5.7), with increasing k at a set of z^* values. In the present case $k = 0.7$ kcal mol^{-1} Å^{-2}.

5.3.2 Simulation Details

The sample we considered in our simulation consists of a 5-layers thick slab of graphite with an ABAB pattern [183] in contact with TIP4P/2005 water [184] containing a single N_2 or O_2 molecule. The molecule interacts with the surface and the liquid through a Lennard-Jones (LJ) potential $v(r_{ij}) = 4\epsilon_{\alpha\beta}((\sigma_{\alpha\beta}/r_{ij})^{12} - (\sigma_{\alpha\beta}/r_{ij})^6)$, where r_{ij} is the distance between an atom of the molecule and one of the surface or water. $\epsilon_{\alpha\beta}$ sets the strength of the interaction between atoms of type α and β and

$\sigma_{\alpha\beta}$ the corresponding range. The values of $\epsilon_{\alpha\beta}$ and $\sigma_{\alpha\beta}$ are determined using the Lorentz-Berthelot combination rules: $\sigma_{\alpha\beta} = 1/2(\sigma_\alpha + \sigma_\beta)$ and $\epsilon_{\alpha\beta} = \sqrt{\epsilon_\alpha \cdot \epsilon_\beta}$, where σ_x and ϵ_x are the parameters characterizing two atoms of the same species. For the purely repulsive gas-solid potential we use the so-called Weeks-Chandler-Andersen potential. This potential is obtained from the N_2-graphite one by cutting off the LJ potential at $r_{ij} = 2^{1/6}\ \sigma_{\alpha\beta}$, i.e. at its minimum, and keeping it constant for $r_{ij} > 2^{1/6}\ \sigma_{\alpha\beta}$. For σ_x and ϵ_x we used the values reported in table 5.1. To model a liquid with a higher air solubility we used a value of ϵ_{NO} three times larger than that used for water. The relation between force field parameters and gas solubility is explained in the *ESI*.

Consistently with the TIP4P/2005 model [184], interaction between graphite and water is modeled by a modified LJ potential, $v(r_{ij}) = 4\epsilon_{CO}((\sigma_{CO}/r_{ij})^{12} - c\,(\sigma_{CO}/r_{ij})^6)$, in which the second term is scaled by a factor c. [82] c can be tuned to control the hydrophobicity of the surface. In practice, we compute the Young contact angle θ_Y formed by a cylindrical droplet deposited on the graphite slab (Fig. ESI1) for 26 values of c in the range $0.5 - 0.75$ with a spacing of 0.01. Over this range we observed a linear relation between θ_Y and c (Fig. ESI2); thus, from the fitting of the θ_Y-c pairs we estimate the values of c corresponding to the Young contact angles of water used in free energy calculations 70°, 80°, 90°, 100° and 110°.

Once again consistently with the TIP4P/2005 model [184], also the gas/water interaction is modeled by a LJ potential in which the parameters are obtained by literature data via the Lorentz-Berthelot combination rules.

In the case of the LJ liquid mimicking aprotic organic solvents, we use the same LJ parameters of oxygen in the TIP4P/2005 water model. Solid-liquid interaction is modeled using the same modified LJ potential used for water, in which the "c" parameter has been optimized to obtain the same Young contact angle values used for H_2O. For the liquid-gas interaction we maintained the values used for water, hence the same affinity between the gas and the liquid.

Species	ϵ [kcal/mol]	σ [nm]
C [185, 186]	0.105067	0.3851
N [187]	0.072332	0.332
O [186]	0.103332	0.299
O_{TIP4P} [184]	0.185200	0.31589

Table 5.1. LJ parameter for the chemical species composing our sample.

The approximation of considering a single gas molecule dissolved in the liquid, which neglects possible interactions among gas molecules, is justified by the low solubility of air in water. In fact, as we will show in Sec. 5.4, even considering the highest computed local oversaturation and the bulk liquid in equilibrium with air (no degassing), the highest value of local molar fraction is ∼0.02, corresponding to one molecule of gas every ∼50 molecules of water. Considering the $N - O$ pair correlation function of N_2 in water (Fig. ESI3), 50 neighbor water molecules per N_2 corresponds to ∼1.4 nm average distance between pairs of gas molecules, twice

the length corresponding to a 50 molecules coordination shell, which is beyond the distance at which $N-N$ interactions are negligible, $\sim$1 nm.

5.4 Results and Discussion

We investigate the attraction of dissolved gas by a solid wall in a simulation sample consisting of a 5-layer-thick slab ($\sim$1.5 nm) of graphite assembled in an ABAB pattern, [183] in contact with liquid (TIP4P/2005 [184]) water. We then introduce either a single N_2 or O_2 molecule (see Fig. 5.1/B) in water; note that these two species alone account for 99% of the composition of air. The choice to simulate a single gas molecule is justified by the fact that, even at the largest local oversaturations, the average distance between pairs of gas molecules is larger than their interaction length (see Sec. 5.3.2). The N and O atoms of the nitrogen and oxygen molecules interact with the carbon atoms of the substrate and the oxygen atoms of the water molecules *via* the Lennard-Jones (LJ) potential, whose parameters have been obtained from literature data (see Sec. *Simulation Details*).We consider several levels of hydrophobicity of the substrate, characterized by the following values of the Young contact angle: $\theta_Y = 70°$, 80°, 90°, 100° and 110°. This is achieved by modifying the graphite/water LJ interaction.This system is designed to model highly ordered pyrolytic graphite (HOPG) immersed in water, typically used in surface nanobubbles experiments. Details of the computational setup and parameters used in the calculations are given in the *Simulation Details* section.

We use the system described above to calculate the effective potential attracting gas molecules to an immersed surface. This, using the TAO model to connect atomistic results with experimental data (see below), allows to develop a microscopic theory of surface nanobubbles' stability. We compute the (Landau) free energy G between a nitrogen/oxygen molecule and the graphite-like slab as a function of z, the separation between the molecule's center of mass and the substrate (Fig. 5.1B). $G(z)$ is the microscopic equivalent of the interaction potential, $\phi(z)$, responsible for the local oversaturation at the core of the TAO model. $G(z)$ is computed using restrained molecular dynamics, RMD, which is described in detail in the *Theoretical Section*.

Our calculations show that between N_2 and graphite immersed in water there is a substantial potential well (Fig. 5.2A) generating a large localized oversaturation within 1 nm of the substrate (see inset). This large localized oversaturation is consistent with recent experimental results. [9] More difficult is the comparison with computational results available in the literature, which also predict a large oversaturation at the solid-liquid interfaces. [171, 189] In fact, in these works the authors use a different computational approach consisting in preparing a sample with a very high gas oversaturation and determining the gas local oversaturation profile as a function of the distance from the surface. In our case, on the contrary, thanks to the use of RMD to compute the free energy, we can consider more realistic bulk oversaturation conditions. In general, the free energy exhibits two properties that are common for all values of the Young contact angle investigated. Firstly, $G(z)$ presents a characteristic minimum at $\sim$0.4 nm from the surface, with a well depth ranging from 4 to 7.5 k_BT; the well depth $G_{\min}$ increases with θ_Y (Fig. 5.2E),

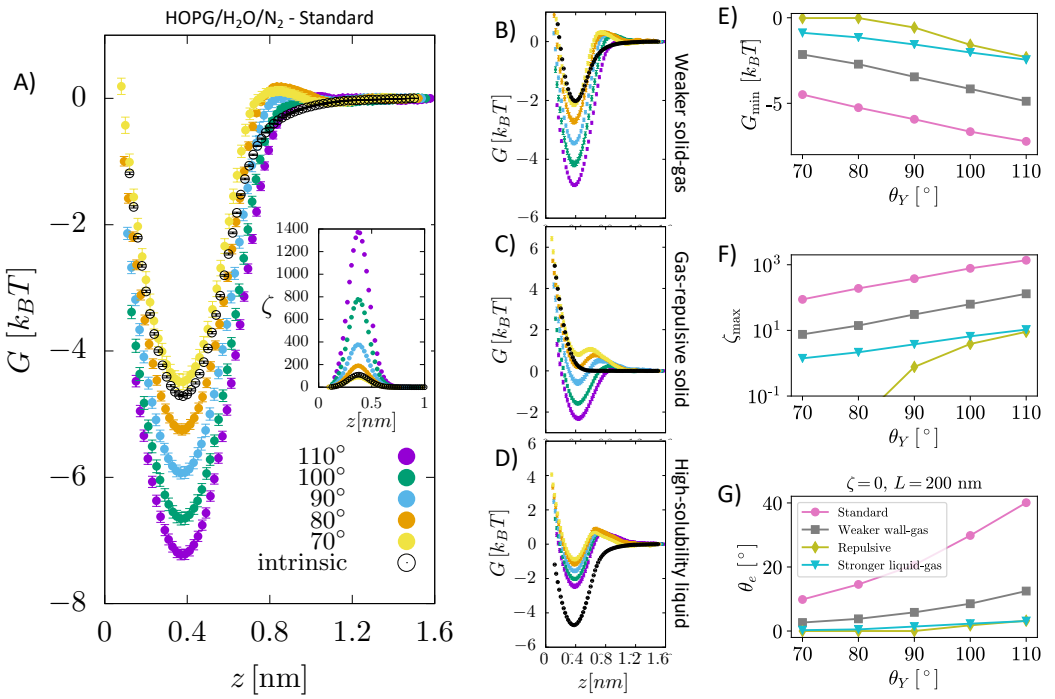

Figure 5.2. A-D) Free energy $G(z)$ of an N_2 molecule in water on a graphite-like slab as a function of the distance from the surface. $G(z)$ is reported for several values of the Young contact angle of the liquid θ_Y, solid-gas intrinsic interaction and liquid-gas interaction strength. As a reference, we report also $G(z)$ in absence of water, i.e. considering only graphite-N_2 interactions (empty circles). Panel A) shows results for the sample modeling $HOPG/H_2O/N_2$, also denoted as standard; B) for a sample with a weaker solid-gas interaction; C) for the case of a purely gas-repulsive surface; [188] D) for a highly soluble gas. The error bars, barely visible in the figure, have size comparable to that of symbols represented in the panels (see *ESI* for a discussion on the method adopted to compute the error in free energy calculations). In the inset the local oversaturation $\zeta(z)$ for the $HOPG/H_2O/N_2$ sample is reported. E-G) Minimum of the free energy $G_{\min}$, maximum of the local oversaturation $\zeta_{\max}$ and equilibrium contact angle of the nanobubbles θ_e as a function of the hydrophobicity of the surface θ_Y for the four systems. θ_e is estimated from Eq. (5.8) considering a nanobubble of $L = 200$ nm radius in a saturated liquid $\zeta_{bulk} = 0$.

i.e., the more hydrophobic the surface, the more it attracts nitrogen dissolved in water (Fig. 5.2F). Secondly, the free energy reaches its bulk value over a distance of ∼1 nm. We remark that the range of this effective interaction is not determined by the cutoff of the solid-gas intrinsic interaction (only), which is 1.6 nm, but by the complex interplay between solid-gas, solid-liquid and liquid-gas interactions. This will be shown more in detail in the following. The free energy profile also presents additional features, such as a tiny maximum at ∼0.7 nm that becomes more pronounced for more hydrophilic surfaces. The origin of the peculiar shape of $G(z)$ and its dependence on the characteristics of the solid, liquid and gas will be discussed in detail in a forthcoming article.

It should be stressed that the general features of $G(z)$ are not specific to nitrogen. In the ESI we present results of analogous calculations for O_2 dissolved in water, illustrating the similarities of the free energy profiles of nitrogen and oxygen (Fig. ESI4).

Next, we connect atomistic results to experimental data, namely nanobubbles' contact angles, using the TAO model, in which the free energy curves of Fig. 5.2 represent the key input (see *ESI* for a brief summary of the TAO model) The model is summarized by Eq. (5.8), which is the condition that must be satisfied for the gas flow at the liquid-gas interface of the bubble to be zero (stationary) in the pinning-local oversaturation theory:

$$\int_0^{h(\theta)} \left(\frac{2\gamma}{LP_0} \sin\theta - \zeta(z) \right) dz = 0, \tag{5.8}$$

Here, the local oversaturation is (inset of Fig. 5.2A)

$$\zeta(z) = \frac{c_\infty}{c_{\text{sat}}} \exp\left(-\frac{\phi(z)}{k_B T} \right) - 1. \tag{5.9}$$

where $\phi(z)$ is replaced by a constrained B-spline of its microscopic counterpart $G(z)$. Note that the height of the nanobubbles $h(\theta)$ is related to the contact angle by the geometric identity $h = L\sqrt{(1-\cos\theta)(1+\cos\theta)}$. The solution of Eq. (5.8) is the nanobubble contact angle θ for which the net gas flux in and out of the bubble is zero, i.e., the equilibrium contact angle θ_e. Fig. 5.2G shows that the effective solid-gas attraction of Fig. 5.2A is sufficient to produce stable nanobubbles with equilibrium contact angles within the typical experimental range. [157] In particular, consistent with recent experimental findings, [176, 181, 175, 190, 191] our results show that nanobubbles can persist on nominally hydrophilic substrates.

The present results allow us to address two puzzling questions about nanobubbles at HOPG in water: i) why is the contact angle much lower than the value one could predict from θ_Y (i.e., $\theta_e \neq 180^\circ - \theta_Y$, considering the opposite convention for the Young and nanobubbles contact angles)? ii) why is the experimental value of contact angle of nanobubbles at HOPG scarcely reproducible? We remark that the TAO model is necessary but not sufficient to address this and the other questions discussed in the following. To answer these questions one needs the calculation from atomistic simulations of the effective solid-gas potential $\phi(z)$. In fact, the TAO model provides a connection between the microscopic properties of the system, namely $G(z)$, and its macroscopic characteristics, the nanobubbles contact angle θ_e, but the TAO

model itself does not provide any estimation of the effective solid-gas interaction. Concerning the first question, our calculations show that given the strength of the solid/gas interaction and the typical Young contact angle of HOPG, which is slightly hydrophilic, one can achieve a local oversaturation that can compensate the outflow gas from the bubble only when θ_e is rather small, 20° or lower (Fig. 5.2G). This is, indeed, a combined effect of the pinning and *local* oversaturation model. Concerning the limited reproducibility of θ_e values, it is known that the variation among data reported by different research groups exceeds the experimental accuracy of contact angle measurements. [157] To answer this question one has to take into account that the preparation history of the HOPG substrate influences the effective affinity between water and graphite. In particular, the Young contact angle θ_Y of water on HOPG depends sensitively on how quickly the liquid is deposited onto the substrate. When deposited on freshly cleaved graphite, a droplet of water has $\theta_Y \approx 70°$, but upon prolonged exposure to ambient air this value substantially increases to $80 - 90°$. [176, 192] Fig. 5.2G (pink dots) shows that if we take this variation in θ_Y into account, the estimated values of θ_e are in the range $5 \leq \theta_e \leq 20°$, spanning an interval matching that reported in the authoritative review by Lohse and Zhang. [157] In summary, for HOPG substrates, the history of the experimental sample affects its hydrophobicity that, in turn, changes the effective HOPG/air attraction and, through it, θ_e.

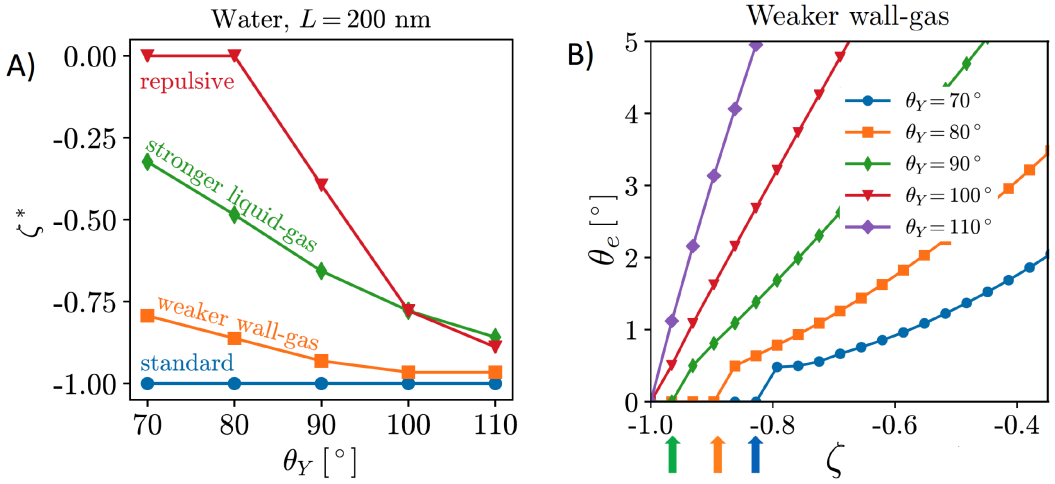

Figure 5.3. A) Tolerance of nanobubbles to degassing measured as critical undersaturation ζ^*. B) The equilibrium contact angle *vs* oversaturation, showing that θ_e decreases monotonically with decreasing air concentration in the bulk liquid [3] until at ζ^* it reaches $\theta_e = 0°$. In particular, in the panel B we report the values of the equilibrium contact angle *vs* ζ for the case of the weaker solid-gas interaction. Each curve corresponds to a different value of the surface hydrophobicity, θ_Y. The colored arrows indicate the ζ^* values.

Can the effective air attraction explain the survival of surface nanobubbles in (bulk) non-oversaturated conditions, i.e., in open ($\zeta = 0$), [162] or degassed systems ($\zeta < 0$)? [163, 164, 165] In Fig. 5.3A we report the degree of undersaturation $\zeta^* = c^*_\infty / c_{sat} - 1$ (< 0) that nanobubbles can withstand before their equilibrium contact angle becomes negligible according to Eq. (5.8). A negative value of ζ^* means

that the gas concentration in the liquid bulk, c^*_∞, is lower than the saturation value, c_{sat}. ζ^* is a convenient measure of the tolerance of nanobubbles to degassing. The equilibrium contact angle decreases monotonically with decreasing air concentration in the bulk liquid [3] until it reaches a critical value ζ^* at which $\theta_e = 0°$ (Fig. 5.3B). One notices that for the HOPG/water/air, nanobubbles can sustain any level of degassing (blue line). Of course, the $\zeta^* = 0$ limit must be understood in the sense that the liquid still contains enough air that can accumulate at surface to counteract nanobubbles degassing. In these conditions the bulk oversaturation ζ is negligible with respect to saturation conditions $\zeta = 1$, virtually corresponding to complete degassing. While the precise value of ζ^* might be critically affected by the limited accuracy of the empirical potentials used in our simulations, our general conclusions are consistent with results reported in a very recent article [164] showing that nanobubbles resisted to the highest level of degassing the authors were able to achieve ($\sim 80\%$ of air dissolved in water was removed). As mentioned in the introduction, their results led Qian *et al.* to conclude that the pinning-supersaturation mechanism is insufficient at explaining the long-term stability of surface nanobubbles. Present work allows to reconcile experiments and theory, adding the missing ingredient – local gas supersaturation at the wall – to the *pinning* model, which can explain the stability of nanobubbles under degassing conditions.

We remark that the TAO model and the present calculations do not allow to completely determine the lifetime of nanobubbles. For example, the TAO model assumes contact line pinning but, indeed, the triple line can depin (see, e.g., Refs. [193]) and, as a consequence, nanobubbles can possibly be destabilized. Indeed, the relation between contact line pinning and nanobubbles lifetime has been experimentally confirmed (see, e.g., Ref. [165]). The characteristic times of contact line depinning and other processes determining the lifetime of nanobubbles are beyond the aim of the TAO model and the present work. Indeed, the theoretical determination of the timescale of these processes requires the use of other advanced simulation techniques. [40, 194, 195]

5.4.1 Effect of solid-liquid-gas interactions on nanobubbles' stability

In the following, through a systematic variation of the solid-liquid-gas interactions, we investigate i) the dependence of the nanobubbles' stability on the characteristics of the three phases and ii) we show that our theory can explain a number of counterintuitive properties observed in experiments.

Interplay between solid-gas and solid-liquid interactions. Nanobubbles have been observed on many substrates including HOPG, glass, mica, talc, molybdenum disulphide, octadecyltrimethylchlorosilane or 1H,1H,2H,2H-perfluorodecyltrichlorosilane coated Si, decanethiol-coated gold and many more. [157] The nature of the solid affects both the value of the Young contact angle and the strength of the intrinsic solid-gas interaction. Certainly, a stronger intrinsic solid-gas interaction increases the local oversaturation and, thus, nanobubbles stability. Here we address the opposite question, whether weaker solid-gas intrinsic interactions still allow to

obtain stable nanobubbles. In other words, we investigate how critical is the intrinsic solid-gas interaction for the stability of nanobubbles.

In addition to the *standard* sample modeling HOPG in water, we considered two alternative cases: in the first the solid-gas interaction strength is half that of HOPG/N_2 (Fig. 5.2B), in the second the solid interacts with the gas *via* a purely repulsive potential, the so-called Weeks-Chandler-Andersen potential [188] (Fig. 5.2C). The standard case shows that – apart for the most hydrophilic case $\theta_Y = 70°$ – the presence of water strengthens the effective solid-gas interaction beyond its intrinsic value, i.e. the well of $G(z)$ in presence of water is deeper than that of a substrate exposed to nitrogen gas only (dashed line in Fig. 5.2A). We stress that this does not mean that the density of gas at the substrate is higher in the liquid than in the nanobubble as $G(z)$ is computed taking as reference the value in the liquid and the pure gas, respectively; our results indicate that there might be a different gas enrichment at the substrate, which for the HOPG/H_2O/N_2 system at $\theta_Y > 70°$ is higher in the liquid than in nanobubbles. Generally speaking, the higher the Young contact angle, the stronger the effective solid-gas attraction, which results in larger nanobubble contact angles (Fig. 5.2G). A similar trend is also observed for the weaker (halved) intrinsic solid-gas interaction (Fig. 5.2B), where the free energy is attractive for all Young contact angles. Comparing results in panels A and B of Fig. 5.2, one notices that the main effect of a weaker solid-gas interaction is a shift of all curves toward less attractive values, with a corresponding reduction of the local oversaturation (Fig. 5.2F) and nanobubbles' contact angles (Fig. 5.2G). The weaker solid-gas attraction reduces the tolerance to undersaturation (Fig. 5.3), which, however, remains high.

It is worth remarking that despite the significant reduction of the solid-gas intrinsic interaction the nanobubble still presents a non-negligible contact angle also at hydrophilic substrates. This is due to the enhancement of the effective gas attraction associated to the presence of water and explains the relative independence of the nanobubbles contact angle on the chemical nature of the substrate (see Ref. [179] and references cited therein). It is worth stressing that the TAO model alone is not sufficient to predict the dependence of nanobubbles' contact angle on the strength of the intrinsic solid-gas interaction, i.e. on the chemical nature of the solid and gas. In fact, the effective potential $G(z)$ determining θ_e critically depends on the presence of the liquid, and this dependence is non-trivial, as we will show in the following. Indeed, in most theoretical models of nanobubbles stability the liquid is considered an inert medium while here we show that the liquid plays a critical and *active* role on the properties of surface nanobubbles.

It is remarkable that also in the case a purely repulsive intrinsic solid-gas interaction the presence of water may bring to an effective attraction, provided that the surface is hydrophobic (Fig. 5.2C). Of course, in this case the effective solid-gas attraction is weaker and the nanobubble contact angle is reduced to a few degrees, see Fig. 5.2G. Nanobubbles with such small contact angles, corresponding to a thickness of $5 - 10$ nm for a nanobubble of 400 nm footprint (radius $L = 200$ nm), are more difficult to detect experimentally. Also in this case the tolerance to degassing is reduced but nanobubbles at purely gas-repulsive surfaces can withstand $\zeta < 0$ provided that the substrate is hydrophobic ($\theta_Y \geq 90°$).

The case of the purely repulsive intrinsic solid-gas interaction illustrates the

relevance of the gas-liquid interaction in determining the effective potential acting on the gas. In fact, one notices that $G(z)$ is non-negligible well beyond the distance of N_2 from the surface where the intrinsic solid-gas interaction is zero. To explain the effect of the liquid and the value of its Young contact angle on the free energy, we propose that the effective solid-gas interaction is due to the balance between its intrinsic strength, i.e. the strength in absence of liquid (dashed line in Figs. 5.2A-C), and the gas solubility. The intuitive argument behind this hypothesis is that if the gas is insoluble, i.e. if hosting it in the liquid is energetically disfavored, it will preferentially accumulate at the solid/water interface, where the hydrogen bond network is already compromised and the energetic cost of insertion is reduced. The more hydrophobic the surface, the less energetically expensive is to replace a molecule of water at the solid/water interface with one of N_2 (or O_2). Moreover, since at the interface with solids liquids are depleted (see, e.g., Ref. [196]), $G(z)$ reaches its plateau value at a z distance where the liquid has fully recovered its bulk density. In fact, for larger distances from the wall, the gas molecule is embedded in a liquid environment that is independent on the position z and the effective interaction potential becomes flat. This explains why the range of $G(z)$ is longer than that of the purely repulsive intrinsic solid-gas interaction, as the range of the effective potential is determined by the width of the depletion zone. The effect of gas solubility in the liquid is discussed in more detail below.

Summarizing, we found that nanobubbles with a contact angle up to $\sim 10^\circ$ can be formed also at surfaces with a weak intrinsic solid-gas attraction; even purely gas-repulsive surfaces can produce stable nanobubbles, although their small contact angle might prevent their experimental identification. For surfaces with low gas attraction, the stabilization of nanobubbles requires a complementary high hydrophobicity, which enhances the strength of the effective solid-gas attraction. On the contrary, relatively strong intrinsic solid-gas interactions (few k_BTs) can lead to stable nanobubbles also at hydrophilic surfaces. By revealing the key and active role of the liquid in determining the strength of the effective solid-gas interaction, our simulations allow to explain the experimental observation that in water surface nanobubbles' contact angle seemingly ceases to be dependent on the substrate chemistry, typically falling in the range $5^\circ \leq \theta_e \leq 20^\circ$. [157]

Effect of the gas solubility. With the insight that stability of nanobubbles depends also on the liquid-gas interaction, we investigate in detail the effect of gas solubility. Starting from the HOPG/N_2/H_2O case (*standard* case), we increase gas solubility by enhancing the strength of the N_2-H_2O interaction by a factor 3, corresponding to a 5-fold increase in solubility [197] (see ESI for additional information) This results in a substantially shallower well (Fig. 5.2D). Correspondingly, both the predicted oversaturation (Fig. 5.2F, cyan triangles) and the equilibrium contact angle (Fig. 5.2G, cyan triangles) are greatly reduced. Also in this case, θ_e might be too low for nanobubbles to be experimentally observed. Tolerance to degassing is reduced as well, though the TAO model predicts that stable nanobubbles are found in liquid with $\zeta < 1$ for all Young contact angles considered (Fig. 5.3).

The effect of gas solubility on the stability of surface nanobubbles has been observed in experiments. Surface nanobubbles are known to be very stable in water

and are insensitive even to the addition of high concentrations of acids, bases or salts. However, a notable exception to their reputed 'superstability' is that when surface nanobubbles in water have their liquid replaced with ethanol they destabilize and dissolve. [175] Systematic experiments have further shown that surface coverage of nanobubbles incubated in water-ethanol mixtures monotonously drops to zero as the mole fraction of ethanol is progressively increased from 0 to 20%. Note that ethanol, which, similar to water, presents strong hydrogen bonding among its molecules as confirmed by a relatively high boiling point ($\sim 79°C$), has *double* the gas solubility of the liquid that we simulate in Fig. 5.2D; thus, consistently with experiments, our theory predicts that surface nanobubbles are unstable in a liquid with a air solubility as high as in ethanol across the entire range of θ_Y, which is again consistent with experiments.

5.4.2 Nanobubbles in aprotic liquids

The fact that experiments are nearly exclusively performed in water has, over time, raised questions about possible specific properties of this liquid in stabilizing surface nanobubbles. Can surface nanobubbles exist in non-aqueous liquids? Is hydrogen bonding responsible for the persistence of surface nanobubbles in water? These questions will be addressed in this section. An influential experimental study by An *et al.* [176] positively answers both questions. The authors used solvent exchange various non-aqueous liquids to nucleate surface nanobubbles on HOPG. They found surface nanobubbles to exist in protic solvents but not in aprotic ones, leading them to propose that a hydrogen bonding network is necessary for the stability of surface nanobubbles.

To isolate the effect of the hydrogen bonding in our simulations we replaced water with a (mono-atomic) Lennard-Jones liquid with the same LJ parameters as in the TIP4P/2005 model. [184] It is worth recalling that the TIP4P/2005 model is characterized by two contributions: i) the electrostatic interactions among point charges centered on H and O atoms, which result in the formation of hydrogen bonding among H_2O molecules reproducing the typical tetrahedral structure of water, and ii) the non-directional interaction among LJ centers positioned slightly off of oxygen atom, determining the "size" of the molecule. Thus, by replacing the TIP4P/2005 water model with the corresponding LJ can effectively investigate the effect of hydrogen bonding. To make the comparison stringent, the solid-liquid interaction is tuned to form the same Young contact angle as for water on HOPG considered above: $70° < \theta_Y < 110°$. Liquid-gas and solid-gas interactions are the same as in the water case (see Sec. *Simulation Details* for additional information). [198] Thus, the only difference with previous simulations is the absence of hydrogen bonding within the liquid. This setup is not meant to model any specific solid/liquid/gas system, here we exploit the flexibility of simulations to model systems with *ad hoc* characteristics to identify the role of hydrogen bonding to stabilize nanobubbles.

Figs. 5.4A, B and C show $G(z)$ for a surface immersed in the aprotic, LJ liquid when the solid-gas intrinsic interaction is *standard*, weakened (halved) and purely repulsive. These panels are equivalent to the corresponding panels of Fig. 5.2 for water. Our results show that strong attractive effective solid-gas interactions may still be present but this is due to the intrinsic characteristics of the solid-gas pair:

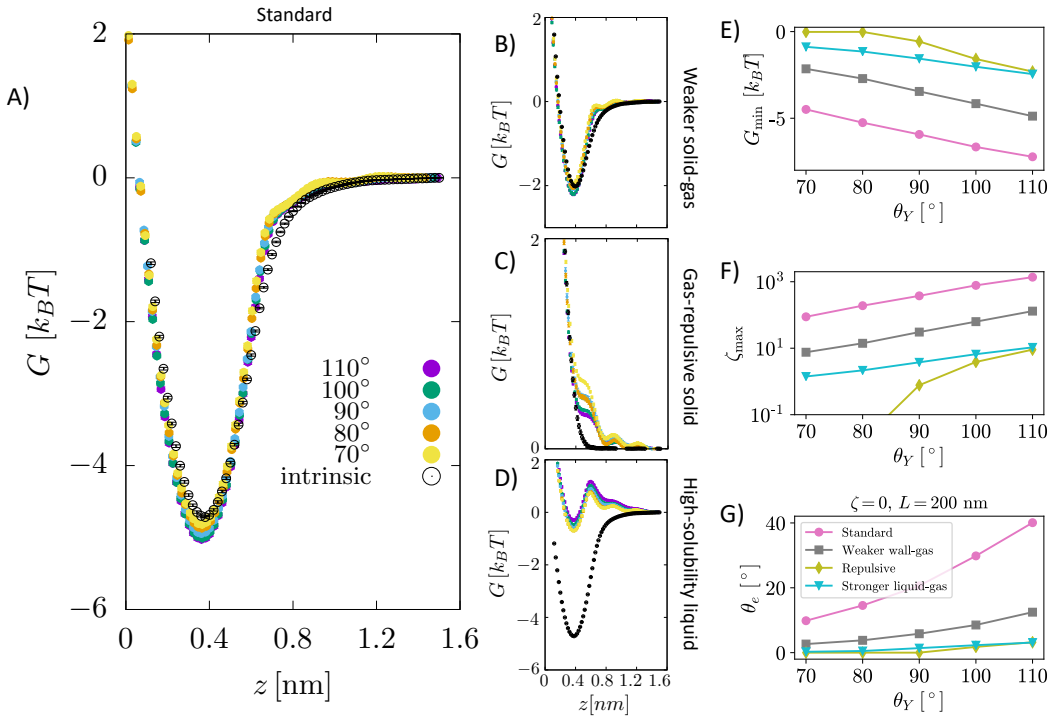

Figure 5.4. Same panels as in Fig. 5.2 for a graphite surface immersed in an aprotic, Lennard-Jones liquid. In particular, in panels A-D we show $G(z)$ for several values θ_Y for HOPG/LJ/N_2, for the halved solid-gas interaction, for the gas-repulsive surface and for a highly gas-soluble liquid, respectively. Apart for the purely repulsive surface, one notices that the effect of an aprotic, *structureless*, liquid on the effective solid/gas interaction is negligible. In other words, the aprotic liquid does not enhance the intrinsic solid-gas attraction. Panels E-G show the values of minimum of the free energy $G_{\min}$, maximum of the oversaturation $\zeta_{\max}$ and equilibrium nanobubbles contact angle θ_e for the cases shown int the A-D panels. θ_e in panel G is computed from Eq. (5.8) considering a nanobubble of $L = 200$ nm radius in a saturated liquid $\zeta_{bulk} = 0$.

aprotic solvents do not enhance this interaction. Thus, in an aprotic liquid one cannot obtain stable nanobubbles at purely gas-repulsive surfaces even if they are highly solvophobic. Present results are consistent with the explicit molecular dynamics simulations by Maheshwari *et al.* [167], which show that a pinned surface nanobubble in a classic LJ liquid could be stable, albeit in the original article these conclusions have been drawn only for a short timescale of 30 ns.

The fact that aprotic solvents do not deepen the solid-gas well seems related to the lack of directional intermolecular interactions, which make the liquid-liquid cohesion stronger in the protic case. Thus, at a variance with water and other protic liquids, there is no or only a minor energetic gain to move the solute gas from the bulk to the solid/liquid interface, and one expects a lower local oversaturation. In the case of purely repulsive surfaces, the presence of an aprotic liquid increases the repulsion because there is an energetic penalty to have an interaction with a gas molecule rather than a (or more) liquid particle, and this is not balanced by the penalty to move the gas molecule in the liquid bulk, like in the case of hydrogen bonded liquids. In short, at a variance with water, an aprotic liquid does not

enhance the intrinsic solid-gas attraction, which must be strong enough to stabilize nanobubbles.

Another effect one has to take into account is that non-polar gases often have a higher solubility in aprotic liquids. In the previous section we have already shown that a higher gas solubility reduces the effective solid-gas attraction, which destabilizes nanobubbles. To prove that the same concept holds also in the case of aprotic liquids, the above calculation were repeated for the case of a stronger liquid-gas interaction. As for the case of water, we increased the liquid-gas interaction strength by a factor 3. Also in this case, a higher solubility weakens the effective solid-gas attraction; moreover, since hydrophobicity plays a minor role in the case of aprotic liquids, here the solid-gas effective interaction is too weak to stabilize nanobubbles over the entire range of θ_Y considered.

The principle we have just identified, that gas solubility is key at determining the stability of nanobubbles, provides a theoretical framework to explain recent experimental results on aprotic liquids. Consider, for example, Dimethyl sulfoxide (DMSO); nitrogen has a solubility in DMSO that is about one order of magnitude higher than in water [199] and An *et al.* [176] have shown that nanobubbles are unstable in the former liquid. Similarly, propylene carbonate (PC), another aprotic liquid that An *et al.* have shown to be unable to form nanobubbles, has a nitrogen solubility which is more than twice that of water. [200, 201] Additionally, both liquids form a lower contact angle at HOPG than water (DMSO $\theta_Y = 45°$, PC $\theta_Y = 31°$, water $\sim 70°$), which further weakens the effective gas-solid interaction.

Summarizing, our results show a more subtle picture of stability of nanobubbles than previously hypothesized: aprotic liquids can still form attractive wells for the dissolved gas and hence form stable nanobubbles of sizable contact angle (Fig. 5.4G) provided that the solid-gas interaction is strong enough. However, another effect competes, and might overcome the strength of solid-gas attraction, i.e. the gas solubility in the liquid, which for air is usually higher in aprotic solvents.

5.5 Conclusions

In this work we have computed the effective interaction potential between a solvated gas molecule and a planar substrate, with a view towards understanding how the effective, liquid-mediated solid-gas interaction affects the stability and other properties of surface nanobubbles. These calculations explain why surface nanobubbles have small contact angles, obtaining theoretical θ_e values in quantitative agreement with experimental results. Moreover, our calculations allow to explain why nanobubbles are stable in water on a surprisingly wide variety of substrates with disparate hydrophobicities and gas affinities, at undersaturated conditions, and yet also catastrophically destabilize in organic solvents. The ability of our calculations, in conjunction with the TAO model, to simultaneously account for the vast majority of experimental observations on surface nanobubbles suggests that it effectively and comprehensively captures the chemsitry and physics of the stability of surface nanobubbles and its dependence on the chemical nature of the solid, liquid and gas species.

5.6 Supplementary Information (extract[1])

θ_Y vs. θ_e (thesis addition[2])

The Young contact angle θ_Y is the equilibrium angle formed by the tangent to the droplet at the triple solid-liquid-gas point *measured on the liquid side* in absence of pinning, and is a property of the three phases through the three surface energy terms $\gamma_{\alpha\beta}$: $\theta_Y = (\gamma_{sg} - \gamma_{sl})/\gamma_{lg}$ We remark that the equilibrium contact angle θ_e is different from θ_Y, as i) it is determined in presence of pinning of the triplie solid-liquid-gas line, and ii) it is conventionally *measured on the gas side.*

The Tan-An-Ohl local oversaturation theory of nanobubbles' stability

The Tan-An-Ohl local oversaturation theory of nanobubbles' stability [170] is an extension of the Lohse and Zhang pinning-oversaturation theory [160]. Eq.[1], the key result of the Tan-An-Ohl theory, is obtained starting from the evolution equation for a dissolving pinned surface nanobubble in a liquid. This problem is analogous to that of an evaporating droplet of liquid, whose exact solution given by Popov [202] has been adapted by Lohse and Zhang [160] to the case of a dissolving spherical cap pinned nanobuble. Lohse and Zhang have obtained the rate of mass change in the hypothesis that the oversaturation ζ is constant through the liquid. By setting the rate of mass change to zero, one obtains the stationarity condition. Tan, An e Ohl. [170] have waived the condition that ζ is constant through the liquid, and Eq. [5.8] represents the stationarity condition for a surface nanobubble if the oversaturation depends on the distance from the solid substrate, $\zeta(z)$.

Relation between force field parameters and gas solubility

Following ref. [197], dissolving a gas in a liquid consisting of two steps: i) creation of a liquid cavity that accommodates a gas molecule and ii) introduction of a gas molecule into the cavity. After its introduction into the cavity, the gas molecule interacts with the surrounding solvent. For very dilute solutions, like air dissolved in water, one can show that: $RT \log K_H = G_c + G_i + RT \log(RT/V_s^0)$; K_H is the Henry's law constant, which relates the amount of gas dissolved in the solvent and its partial pressure: to a higher value of K_H corresponds a higher gas solubility; G_c and G_i are the molar free energies for forming a cavity of prescribed size and inserting a molecule in the cavity, corresponding to steps 'i' and 'ii' of the process outlined above; finally, V_s^0 is the molar volume of the solvent and R is the gas constant. Following Reiss *et al* [203], G_c depends on the characteristic size σ_s of the solvent and solute molecules, which does not change, while G_i depends on the characteristic energy, ϵ, which we increase of a factor 3. Considering that $G_i = -3.555\pi\,\rho\,R\,\sigma^3\,\epsilon\,/k_B$ [197], where ρ is the solvent number density and k_B is the Boltzmann constant, the ratio between the Henry's law constants of two solutions differing in the characteristic interaction energy between the solvent and solute by $\Delta\epsilon = \epsilon' - \epsilon''$ is $K'_H/K''_H = \exp[-3.555\pi\,\rho\,R\,\sigma^3\,\Delta\epsilon\,/k_B]$.

[1] parts already covered in the Methods chapter (Chapter 2) were omitted.

[2] not present in the original article

What about CO_2? (thesis addition[3])

Carbon dioxide (CO_2) is yet another molecule characterized by low water solubility when in its gaseous state, while it can solubilize at higher concentrations as carbonic acid. However, as for nanobubbles formation, only the gaseous component is relevant. As shown by the plots at different values of the solid-gas mechanical interaction, the corresponding nanobubble's contact angle is very weakly dependent on the nature of the gas dissolved in the liquid. A significant difference in the effect of the dissolved gas should not be expected, as long as its properties are sufficiently similar to those of $O_2$and N_2, in particular the gas solubility in the liquid.

[3]not present in the original article

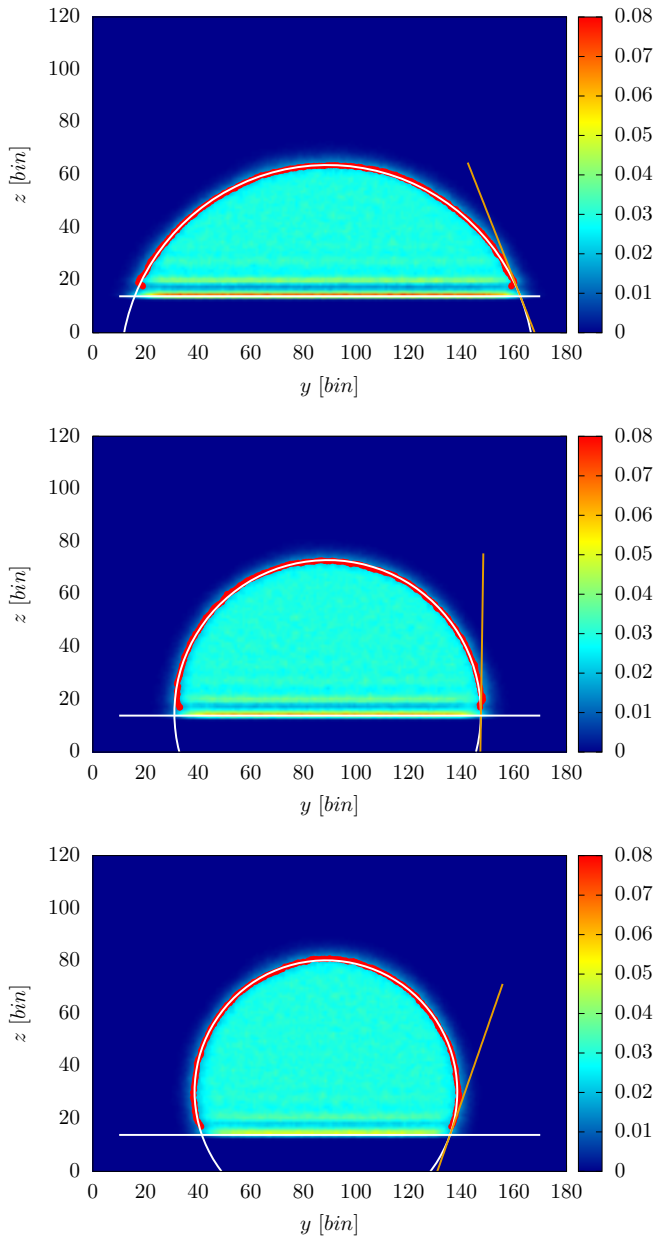

Figure ESI1 - Figure 5.5. To compute the Young contact angle of a surface we deposit a cylindrical water droplet on it, thermalize the system and subsequently compute the average (discretized) density field. From the density field we can identify the Gibbs dividing surface, i.e. the density isosurface with a value halfway between bulk liquid water and vapor. We then fit this surface with a circumference and compute the corresponding tangent formed with the graphite slab. In the panels of this figure we show the density field, Gibbs dividing surface and tangent of three droplets with a Young contact angle of 70° (top), 90° (central) and 110° (bottom).

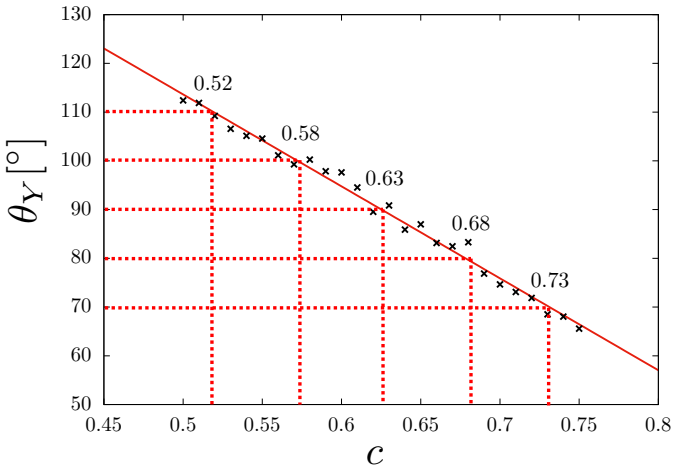

Figure ESI2 - Figure 5.6. Young contact angle θ_Y *vs* the scaling parameter c. The calculations show that there is a linear relation between θ_Y and c over a wide range enclosing the one spanned in our simulations, $[70°, 110°]$. From the linear fitting of simulation data one can determine the value of c necessary to model a solid with a prescribed value of θ_Y.

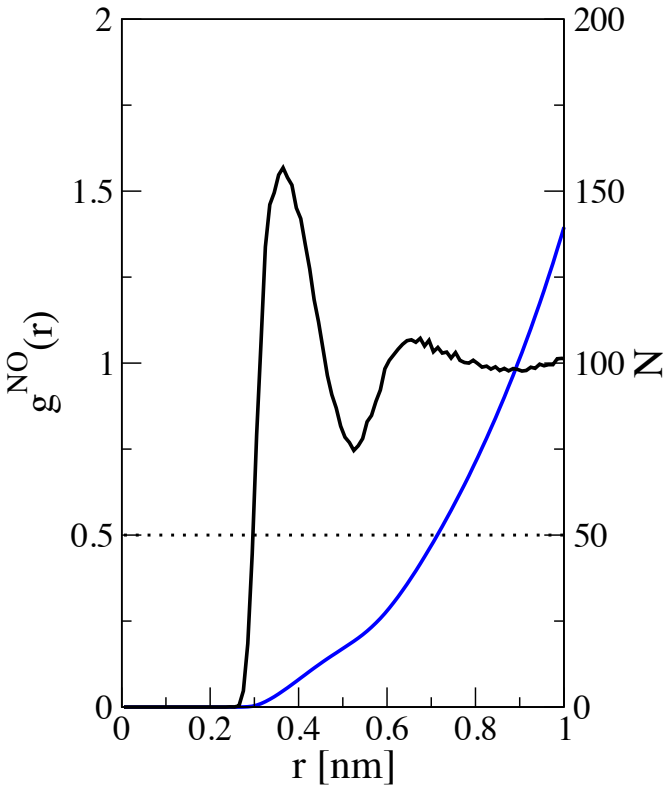

Figure ESI3 - Figure 5.7. Nitrogen-oxygen pair correlation function of an N_2 molecule in bulk water (black) and the corresponding integral, i.e. the number of water molecules within a distance r from N_2 (blue). The dotted line corresponds to 50 nearest neighbor water molecules and is shown to help the reader to appreciate the radius of the shell enclosing the number of water molecules per N_2 at the maximum local oversaturation for a $\zeta = 0$ bulk.

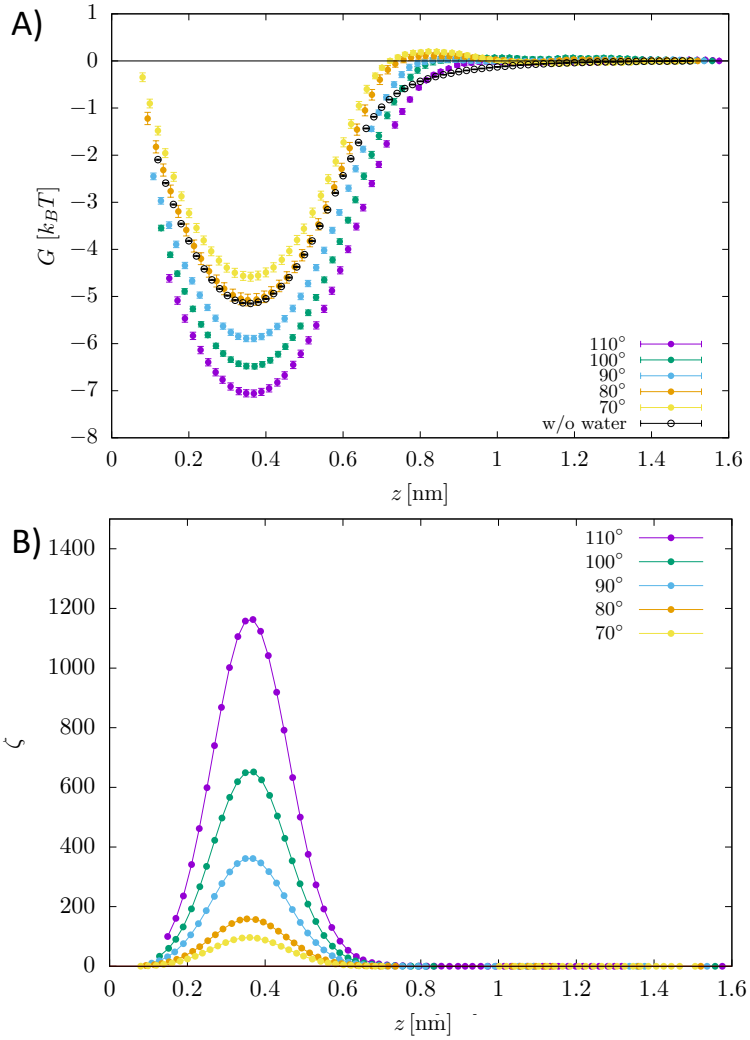

Figure ESI4 - Figure 5.8. A) Free energy $G(z)$ as a function of the distance of the center of mass of the O_2 molecule from the graphite-like surface. In the figure, $G(z)$ is reported for several values of hydrophilicity/hydrophobicity of the surface together with the case without water, i.e. when the sample consists only of the graphite-like slab and O_2. One notices that the profiles are very similar to the N_2 case reported in the main text. B) Supersaturation of O_2 as a function of the distance from the surface.

Chapter 6

Heterogeneous cavitation from atomically smooth liquid-liquid interfaces

6.1 Abstract

Pressure reduction in liquids may result in vaporization and bubble formation, a process known as cavitation. It is commonly observed in hydraulic machinery, ship propellers, and even in the context of medical therapy within the human body. While cavitation may be beneficial for the removal of malign tissue, in many cases it is unwanted due to its ability to erode nearly any material in close contact. The current understanding is that the origin of heterogeneous cavitation are nucleation sites where stable gas cavities reside, for example, on contaminant particles, submerged surfaces, or shell-stabilized microscopic bubbles. Here, we present the discovery of the atomically smooth interface between two immiscible liquids as a nucleation site. The non-polar liquid has a higher gas solubility, and upon pressure reduction it acts as a gas reservoir as gas accumulates at the interface. We describe experiments that reveal the formation of cavitation on non-polar droplets in contact with water, and elucidate the working mechanism that leads to the nucleation of gas pockets through simulations.

6.2 Introduction

Our understanding of the origin of bubble nucleation is still limited. The most accepted model requires pre-existing gas pockets stabilized in a hydrophobic pore [204, 156, 205, 206, 207]. Once a sufficiently strong tension is applied, the gas expands explosively and forms a cavitation bubble. Simulations have been performed to investigate the *ripening* mechanism of pre-existing bubbles [208, 209]. In typical systems these pores are provided by impurities or cracks on a submerged surface [210, 156].

Only very few experiments [211, 212] demonstrated a cavitation threshold in water compatible with the classical nucleation theory [213]. Most experiments however suffer from a considerably lower threshold [214] even when extreme care

is taken in the preparation of the liquid. A possible explanation [215] might be nanoscale solid or gaseous nuclei [216] that reduce the threshold of an otherwise pure liquid.

Here, we report on a potentially novel source for cavitation: droplets of a highly non-polar liquid, which is hydrophobic and lipophobic, namely perfluorocarbons (PFC). The atomically smooth surface does not offer hydrophobic cracks for stabilization of pre-existing gas pockets. Liquid PFCs are very stable, chemically inert, feature high gas solubility, and used for *in vivo* oxygen delivery and further biomedical applications [217, 218, 219]. Its unique properties are an effect of low self cohesion, polarity, and polarizability [219]. The PFC used in the experiments, i. e., 1-Bromoheptadecafluorooctane (PFOB), has a high solubility of gases with low cohesivity, such as O_2, CO_2, N_2, NO, etc. [217]. In fact, pure PFOB theoretically dissolves 360 fold more oxygen than water in terms of molar fraction and 25 times more in terms of volume fraction at ambient conditions [217, 218, 28, 219]. This novel cavitation nucleus might be of interest for some medical applications, such as high intensity focused ultrasound ablation, localized drug delivery, and radiotherapy; or engineering technologies that could reduce cavitation in hydraulic machinery as pumps or injectors. Here, we demonstrate cavitation nucleation from liquid-liquid interfaces. The liquids are constrained by two glass plates to form a few micrometer thick liquid gap. Cavitation inception is induced with strong tensile stresses that are propagated through a Lamb wave travelling within the thin liquid gap. The cavitation nucleating wave is launched by a laser induced plasma; further details are provided in the "Methods" Section and in Ref. [220].

Atomistic simulations are performed on a water/PFC sample containing N_2 to mimic air dissolved in the liquids, to investigate the cavitation origin in this system.

6.3 Results

Figure 6.1 shows experimental snapshots of the cavitation activity in water loaded with (a) microbubbles, (b) particles and (c-d) PFC droplets. The primary cavitation bubble is formed at the very left outside the field of view. Besides the central bubble being the result of the laser plasma, many smaller and seemingly randomly distributed cavitation bubbles become visible. We refer to them as secondary cavitation that are formed once the cavitation threshold is locally met.

In Fig. 6.1(c-d) selected PFC droplets are marked with a cyan circle ($t = 0$). When the Lamb wave passes, on most of these droplets a bubble emerges ($t = 0.2 - 0.4\,\mu s$), which will collapse after a short time and no visible bubbles remain. The PFC droplets are still intact and visible. The expansion of the primary cavitation drives a radial flow that transports the droplets from their original position to a slightly shifted one. During this transport some droplets may deform and eventually split up into several droplets.

Interestingly, a droplet may nucleate multiple times. Initially, some droplets nucleate a bubble upon tension. A later tension wave, which might be a result of reflections of waves within the glass, is able to nucleate bubbles at some of the PFC droplets previously acting as cavitation nuclei (Supplementary Fig. S1). This demonstrates that the droplets are not used up by one cavitation event but can

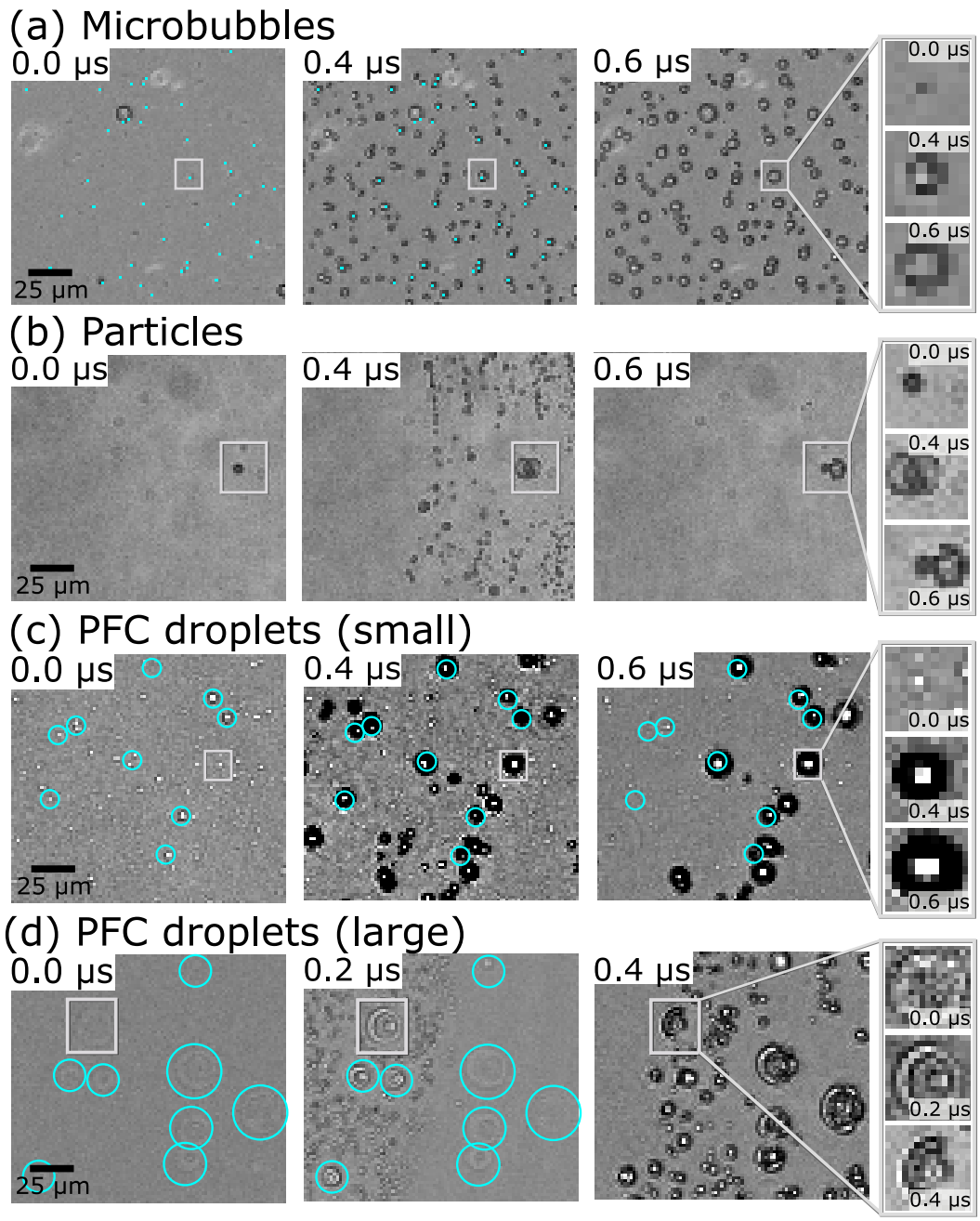

Figure 6.1. Cavitation in a thin liquid gap. Experimental snapshots of secondary cavitation with different cavitation nuclei: (a) microbubbles, (b) magnetic beads, (c) and (d) PFC droplets before ($t = 0$) and after the passage of the Lamb-type wave ($t = 0.2 - 0.6\,\mu s$). The cyan spots in (a) highlight some microbubbles, which expand after the passage of the wave. (b) On a single magnetic bead (dark spot) two bubbles are formed ($t = 0.4\,\mu s$) after the passage of the rarefaction wave. (c) The initial position of some PFOB droplets is marked with a cyan circle. After the wave passage, bubbles are formed on these droplets. (d) On the 4H-PFOB droplets, bubbles are formed mainly at the PFC/water interface.

serve multiple times as a cavitation nucleus (see Suppl. Information). This is called catalyst in chemistry.

The second PFC used here is 1H,1H,2H,2H-Perfluorooctyl bromide (4H-PFOB), which shows larger droplets. Thus, we are able to see exactly where the bubbles are formed (Fig. 6.1(d)). At $t = 0.2\,\mu s$ secondary cavitation bubbles are formed in the left part of the frame. Here, pronounced circles are formed around the droplets. In the right part of the frame no bubbles are visible yet, as the Lamb wave has not entered this region. At $t = 0.4\,\mu s$ the bubbles formed at the interface might break into smaller ones. Overall, we see that bubbles are mostly nucleated along the PFC/water interface.

Atomistic simulations were run to investigate the origin of bubble nucleation. The computational sample, described in detail in the "Methods" Section, consisted of a PFC and a water slab in contact with each other. As nitrogen is the main component of air, we choose this gas for the simulations. N_2 molecules were randomly inserted in the PFC slab to mimic air dissolved in the liquid. Additional nitrogen molecules were randomly inserted in the water slab as well. Given the very low solubility, most of the N_2 inserted in water drifted toward the PFC domain. This simple computational sample contains the key ingredient of the experimental sample, an interface between the two liquids where bubbles nucleate, though admittedly it lacks some more subtle features, such as a curved interface between the two liquids. The sample is thermalized at 0.1 MPa and 300 K for 5 ns and then is aged for 20 ns during which we computed its properties. The Lamb-type wave is mimicked by subjecting the computational sample to a negative pressure of -20 MPa (a maximum tension of -17.6 MPa was obtained in simulations [220]).

At ambient conditions, the sample shows an almost uniform density profile of N_2 in PFC, with a minor increase of concentration of the gas at the interface between the liquids; beyond the interface the N_2 density smoothly drops to a much lower density, as expected due to the much lower gas solubility in H_2O (Fig. 6.3). For the same sample at -20 MPa, one observes a stark change in the N_2 density profile, with a significant reduction of density in the bulk domain of the PFC slab[1], and a significant increase at the liquids' interface. The accumulation of the gas at the interface is accompanied by an increase of separation between the PFC and water slab. The average density of the gas at the interface at -20 MPa is ~ 0.8 g/l, to be compared with the ~ 1.15 g/l N_2 density at ambient conditions, and saturation values of ~ 0.4 g/l and ~ 0.02 g/l, in PFOB and water, respectively. Moreover, the gas density field fluctuates during the simulation, reaching ~ 2.5 g/l local density values at the interface. This, together with the snapshots of the atomistic configurations (Fig. 6.4, Supplementary Fig. S3 and a movie in the Supplementary Material), visually illustrating the pinning of the N_2 density peaks at the depletion region between the two liquids at an atomistic level, suggest that the gas forms a film at the interface. This conclusion, however, must be taken with some caution as, despite the sample is large from the computational point of view, the limited number of

[1] the average values of the normalized N_2 density in the bulk domain of the PFC slab at 1 bar and -20 MPa are reported in Fig. 6.3 as the blue and the red dashed lines, respectively, which show how they are both below 1. These N_2 density averages are evaluated considering only the samples from within the region where the oil recovered its bulk properties, i.e., where its normalized density is back to 1 and does not exhibit significant layering.

nitrogen molecules in the system allow to form only a mono-atomic *layer*, which does not allow identification of three well separated liquid and gas domains.

The positions of water and PFC are considered as Gibbs surfaces, x_{H_2O} and x_{PFC}. The position of these interfaces are taken where their normalized density is equal to 0.5. The distance $|x_{H_2O} - x_{PFC}|$ between the two liquids grows from ~ 0.65 Å to ~ 0.75 Å as the pressure decreases from 0.1 MPa to -20 MPa. We believe that the accumulation of gas at the PFC/water interface follows a *cooperative* mechanism: the decrease of pressure induced by the Lamb-type wave increases the separation between PFC and water, this makes room for air to accumulate in this emptier region and, in turn, the softer gas film forming at the interface helps to further separate the two liquids, making more space for accumulating additional air. On the atomistic space and time scale, we could not identify any ordered sequence between the separation of the PFC and water interfaces and gas accumulation in between them, hence we refrain to state any causality between the two. Here, it is worth remarking that our findings of the separation between two liquid interfaces is consistent with the formation of a gap between a hydrophobized silicon crystal and liquid water previously reported by Mezger et al. [221]. This gap formation is independent on the type of gas dissolved in the liquid.

When does the accumulation of N_2 (or O_2, air, etc.) at the PFC/water interface stop? The local increase of the gas at the interface between the liquids results in a corresponding decrease of dissolved gas in the bulk PFC (and water), which in this process acts as a gas reservoir. This induces a decrease of the chemical potential of the gas in the liquid(s), which arrests the ever growing increase of concentration at the interface, hence the thickness of the film. Given the relatively small size of the computational sample, orders of magnitude smaller than the PFC droplets of the experiments, the transfer of N_2 from the bulk of the PFC slab to the interface is arrested after few molecules moved. For the same reason, the growth of the distance $|x_{H_2O} - x_{PFC}|$ between the water and PFC surface under the action of mimicked Lamb wave (-20 MPa pressure) is limited. We speculate that in the experimental sample, containing micrometer-sized droplets, the cooperative mechanism described above is responsible for the gaseous air film observed around the PFC droplets (Fig. 6.1(d) and Supplementary Fig. S2).

The accumulation of gas at the water/PFC interface can result in the formation of bubbles according several possible mechanisms, or their combination: i) The local gas supersaturation reduces the surface tension γ of the liquids consistent with results on bulk supersaturation of water [222]. The reduction of the surface tension lowers the bubble nucleation barrier, which depends on the cubic power of γ [223, 5], thus diminishing the threshold pressure at which bubble nucleation takes place. An estimation based on literature data [222] shows that 25 fold local supersaturation is sufficient to produce bubble nucleation at a -20 MPa pressure, a level of supersaturation which is within the range observed at the water/PFC interface (see Supplementary Information for a detailed analysis). ii) The gas film acts as a cavitation nucleus, which, perhaps due to inhomogeneities of the two liquids at their interface, can be destabilized, producing cavitation bubbles. Finally, iii) it was recently shown by simulations that a local supersaturation can enhance bubble nucleation, which has been attributed to the weakening of the hydrogen bond network of water [224]. Identifying which mechanism is responsible for the

cavitation at the water/PFC interface is beyond the objective of this work. The important observation, here, is that the enrichment of gas at the water/PFC is the key phenomenon for all the three mechanisms summarized above. This is consistent with a recent publication, where it is shown that cavitation can be induced by local supersaturation obtained by the laser-induced cavitation of a primary vapor bubble [220].

The next question to be addressed is whether enough gas accumulate at the interface for a gas bubble to be formed during the short duration of the rarefaction Lamb-type wave, $\sim 40\,\mathrm{ns}$ [220]. This can be estimated considering the gas volume that can diffuse from the PFC domain to the interface in the prescribed time and comparing it with the critical volume of a gas bubble. This gas volume can be estimated starting from the relation of the diffusion length $L \approx \sqrt{\Delta t \cdot D}$, where $D = 7 \times 10^{-10} \mathrm{m}^2/\mathrm{s}$ is the diffusion coefficient determined in bulk simulations of N_2 in PFOB and Δt is set to 10 ns, 1/4 of the duration of the rarefaction wave. We remark that the diffusion coefficient considered in this work is consistent with experimental and theoretical literature data for the diffusion of O_2 in C_8F_{18} [225, 226]. With these parameters, $L \sim 3\,\mathrm{nm}$ and, considering a 50 vol.% gas solubility in PFOB [217], $\sim 10^7\,\mathrm{nm}^3$ gas accumulate around a PFC droplet of diameter 1 µm, to be compared with the critical size of a gas bubble in water of $\sim 1500\,\mathrm{nm}^3$ at a tension of $-20\,\mathrm{MPa}$ (estimated from the Laplace Law, $r^* = 2\gamma/\Delta P$). Thus, in 10 ns enough gas accumulates around PFC droplet that, driven from fluctuation and the reduction of water/gas interface, can transform into a supercritical bubble.

Our findings have not only a fundamental impact in cavitation, but also implications in medicine, as PFC droplets are used as oxygen carrying blood substitutes, antihypoxants, and radiological contrast agents [219]. Currently, PFC emulsions are tested in preclinical studies for high intensity focused ultrasound tumor ablation [29, 30, 31, 28], as microbubbles have enhanced ablation and reduced treatment times [227]. A potential advantage of droplets is the ability to be sonicated repeatedly without degradation, allowing lower applied powers, reduced prefocal interactions, and reduced treatment times. By understanding and exploiting the cavitation effects, the setup and sonication parameters might be optimized to improve local absorption and treatment efficacy for ablation therapy.

We believe that not only PFC droplets can induce cavitation, but any liquid immiscible with water that has also a high gas solubility. The investigation of the generality of the phenomenon described for the first time in this report is left for a forthcoming work.

6.4 Methods

6.4.1 Experimental

Rapid heating of the liquid through a laser-induced plasma generates a high pressure region that, besides nucleating a central bubble, also launches numerous waves in the solid and the liquid (Fig. 6.2(b)). A particularly interesting wave is the transverse Lamb-type wave that leads to strong tension in the liquid. This Lamb wave is sufficiently strong to nucleate cavitation bubbles within a gap containing water [228, 220].

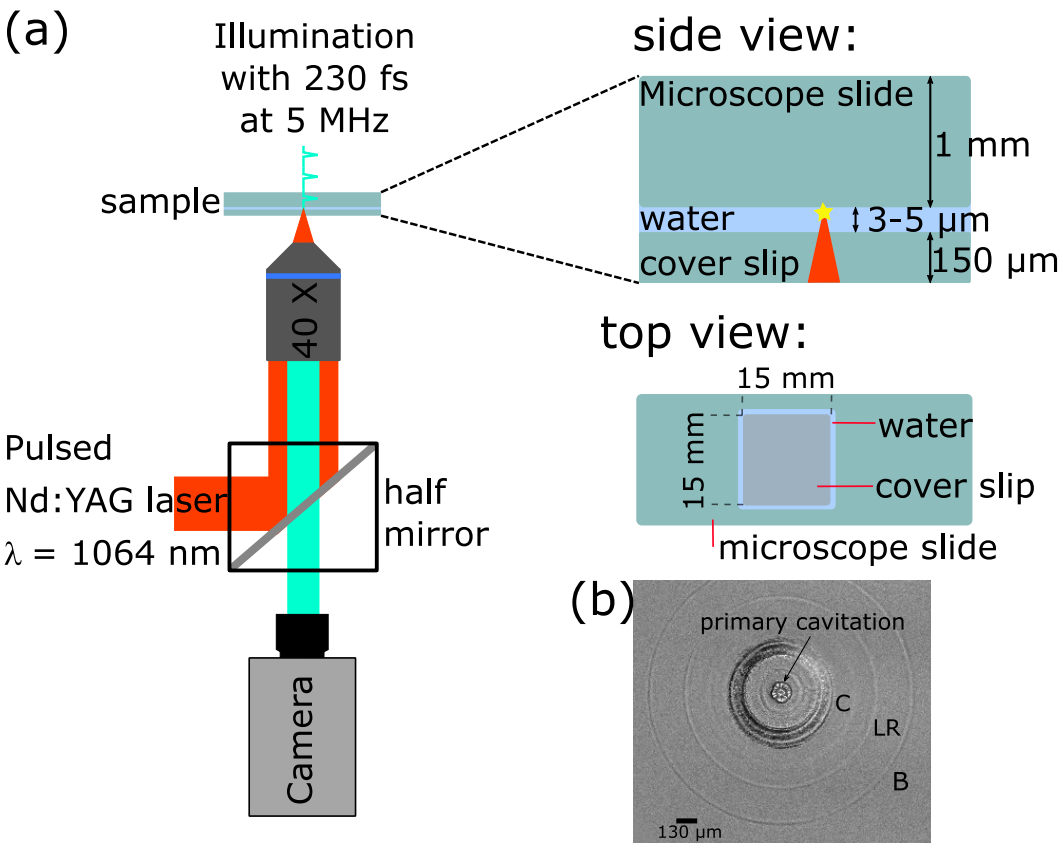

Figure 6.2. Experimental setup for secondary cavitation inception and observation in a thin liquid gap. (a) The gap consists of two glass slides, sandwiching a $3-5\,\mu m$ thick liquid layer. (b) Waves occurring in the thin gap after laser-induced optical breakdown at $t = 0.2\,\mu s$. In the center the main cavitation bubble is formed (primary cavitation). B: longitudinal bulk wave, $v \approx 4000\,m/s$, LR: leaky Rayleigh wave $v \approx 2900\,m/s$, C: Lamb wave $v \approx 1450\,m/s$. The latter induces secondary cavitation (Lamb wave induced cavitation), which consists of many tiny bubbles formed in annular rings behind the wave.

High-speed video recording (HPV-X2, Shimadzu, Kyoto, Japan, 5×10^6 frames/s; spatial resolution 1.3 µm per pixel) is used to observe the fast dynamics of cavitation inception in a thin liquid gap. Stroboscopic illumination is provided by a single light pulse in one frame from a femtosecond laser (FemtoLux 3 SH, EKSPLA, Vilnius, Lithuania, pulse duration 230 fs at a maximum repetition rate of 5 MHz, wavelength 515 nm) (Fig. 6.2(a)). The nanosecond laser pulse inducing the plasma appears 84 ± 5 ns before a femtosecond laser pulse. The short illumination time enables us to visualize the waves traveling in the solid and in the liquid (Fig. 6.2(b)). The primary bubble nucleation (central bubble) is surrounded by annular rings of cavitation bubbles that are created by the Lamb-wave (C). A leaky Rayleigh wave (LR) is considerably faster and travels in the solid along the surface. The longitudinal bulk wave (B) is the fastest wave traveling in the glass.

Loading the gap with a fluorescent dye (Rhodamine 6G), the thickness can be measured with the help of a confocal microscope (SP8 Confocal Laser Scanning microscope, Leica GmbH, Wetzlar, Germany). Using a high magnification lens

(HC PL FLUOTAR L 63x/0.70 DRY), a pixel resolution of 0.019 µm/pixel was achieved. From the gray value profile, the inflection points were determined and from their distance the thickness of the gap was calculated, having a typical value of 3.4 ± 0.1 µm. Here, the error of ± 0.1 µm corresponds to the error of finding the inflection point. In total 10 different samples have been measured with a mean thickness of 3.4 ± 0.9 µm (error corresponds to the standard deviation).

The surface tension of the PFC's have been measured with a force tensiometer (K100, *Krüss GmbH*, Germany) with the Du Noüy ring method. The surface tension at 25 °C of PFOB is 16.3±0.1 mN/m and of 4H-PFOB 18.3±0.1 mN/m (5 different measurements, error corresponds to the standard deviation).

The interfacial tension between water and PFC was measured with the Wilhelmy plate method. The interfacial tension between water and 4H-PFOB is -28.1±0.1 mN/m at 25 °C (10 measurements, error corresponds to the standard deviation). This negative value shows the strong repulsion between both liquids.

Different systems are studied: microbubbles ("Luminity", *CS Diagnostics GmbH*; ultrasonic contrast agent, which is perflutren coated with a lipid layer, diameter 1.1-2.5 µm), particles (magnetic beads, diameter 4.5 µm, tosyl activated in liquid solution; provided by M. Pumera, UCT Prague Nanorobots Research Center), and PFC droplets in DI water with 1-Bromoheptadecafluorooctane (PFOB; 99%; purchased from *Sigma-Aldrich*), and 1H,1H,2H,2H-Perfluorooctyl bromide (4H-PFOB; 97%, purchased from *Fluorochem*, UK). The emulsions are produced mixing 1 % PFC with DI water. The mixture is sonicated for 5 min (0.5 Hz) with a Bandelin Sonopuls Ultrasonics Homogenizer (UW 2200 with the titanium tip MS72) at a power of 36 W. The PFOB droplets have a mean diameter of 2-3 µm, whereas the 4H-PFOB emulsion shows a droplet size between 6-25 µm. Note that due to gap height, the 4H-PFOB droplets are cylindrical.

A droplet (10 µl) of the emulsion is placed on a microscope slide (*Paul Marienfeld GmbH & Co. KG*, Germany) and covered carefully with a cover slip (*Menzel Gläser* #1, Germany), such that no air bubbles remain in the gap. Both glass slides are clamped together. To avoid drying out of the gap which could affect the thickness of the liquid layer an additional droplet of liquid is placed close to the gap.

6.4.2 Simulation Details

The computational sample (Fig. 6.4) consists of a slab of 770 PFC molecules and a slab of $\sim$ 15500 water molecules, for a total of $\sim$ 66500 atoms; 14 nitrogen molecules are introduced randomly inside the PFC slab using Packmol [229] to model the dissolved air. The PFC and water slabs occupy $\sim$ 9 and $\sim$ 11 nm, respectively. At short distance from the nominal, Gibbs interface ($\leq 2 - 3$ nm - see Fig. 6.3 and Supplementary Material) one notices first a depletion region due to the non miscibility of the two liquids. Beyond this distance the liquids recover the bulk behavior, leaving ≥ 3 and ≥ 5 nm of bulk PFC and water, respectively. In a recent article, we have shown that beyond the depletion zone, a gas dissolved in a liquid does not feel the effect of the interface [38] (see also Supplementary Fig. S7), which confirms that the size of our sample is adequate to model the problem at hand.

The N_2 molar fraction in our computational sample is approximately five times higher than the experimental value [199]. This higher N_2 concentration allows

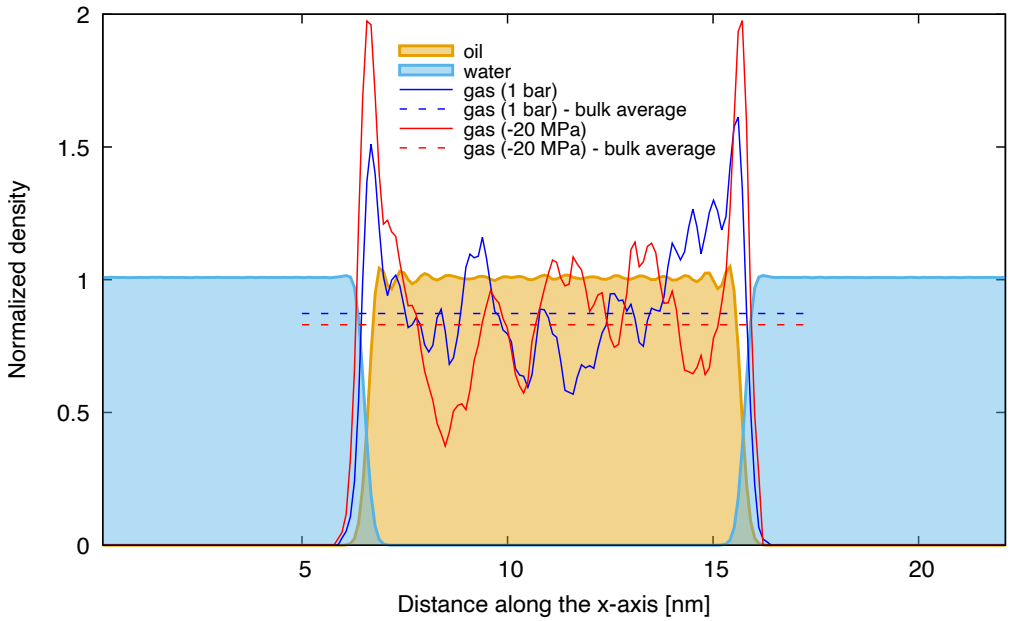

Figure 6.3. Density profiles of the simulation sample. Density profile, normalized with respect to the bulk density value, of water (cyan), PFC (yellow), and N_2 at 0.1 MPa (blue) and -20 MPa (red). See the "Methods" section for a precise definition of the normalized density. The blue and the red dashed lines represent the average values of the normalized N_2 density in the bulk domain of the PFC slab at 1 bar and -20 MPa, respectively. These averages are evaluated considering only the samples from within the region where the oil recovered its bulk properties, i.e., where its normalized density is back to 1 and does not exhibit significant layering. The water and PFC densities drop smoothly at the interface between the two liquids. The PFC density shows the typical ripples observed for liquids at lyophobic interfaces. N_2 tends to accumulate at the interface already at 0.1 MPa, but this behavior is highly enhanced under tensile conditions mimicking the Lamb-type wave.

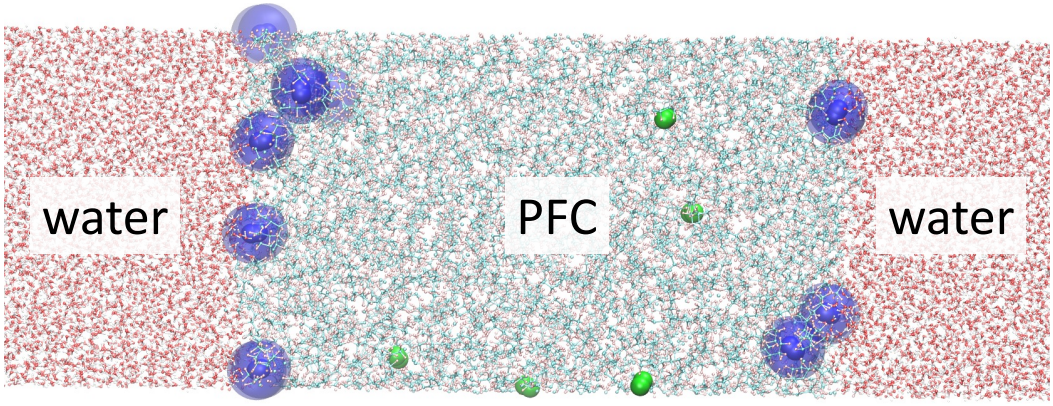

Figure 6.4. Snapshot of the computational sample at -20 MPa. The sample consists of a slab of PFC and a slab of water (the two halves in the pictures are connected through periodic boundary conditions). To highlight N_2, the atoms of these molecules are represented as spheres radius equal to the van der Waals radius of nitrogen, while the liquids are shown in a ball-and-stick representation. Thus, the size of spheres representing nitrogen, water and PFC do not represent the actual size of the various molecules. N_2 molecules at the water/PFC interface, arbitrary identified as those molecules within 2 nm from a molecule of both liquids, are drawn in blue, with a transparent sphere around them. N_2 molecule in the bulk are drawn in green. With the N_2 density of Fig. 6.3, this snapshot shows an accumulation of gas at the two water-PFC interfaces. In the Supplementary Material we present additional selected snapshots of the computational sample (Supplementary Fig. S3) and the Supplementary movie of a 1 ns long branch of the MD trajectory at −20 MPa.

us to determine the properties of the dissolved gas with an adequate statistical accuracy within the timescale accessible by molecular dynamics. In particular, this oversaturation allows one to produce an appreciable accumulation of gas at the interface under the effect of the simulated Lamb-type wave. Costa Gomes *et al.* [230] have already successfully used this approach to investigate the properties of O_2 dissolved in PFC using a gas concentration ~ 12.5 higher than the (computational) solubility of the gas. We validated this approach considering bulk PFC/N_2 samples at growing gas concentration and have verified that the structural characteristics of the mixture, e. g., the partial pair correlation functions of N_2 with PFC and with other gas molecules (see Suppl. Information) do not significantly change among the experimental saturation concentration and the one used in our simulations of the interface system. The suitability of our simulations approach is also confirmed by the uniform distribution of N_2 in the bulk of PFC at 0.1 MPa: despite the higher concentration, no gas bubbles are formed in the PFC bulk along the duration of the simulation (Fig. 6.4).

MD simulations were run at constant temperature (300 K) and pressure (0.1 MPa and -20 MPa) using the Nosé-Hoover chain thermostat [231] and the Martyna-Tobias-Klein barostat [85]. It is sometimes discussed in the literature that the inertia parameter of the barostat (and thermostat), determining the strength of coupling with the particles' degrees of freedom, is a delicate parameter to tune. Indeed, this is mostly connected to the use of Martyna-Tobias-Klein (and analogous) barostat (and thermostats) for computing dynamical properties and/or investigating non-

equilibrium systems. We remark that here we are interested in the stationary properties on the sample, and the difference due to the application of the tensile Lamb-type wave. Thus, here MD is used to sample the ensemble of the system rather than to follow its evolution on time. In this case, the relevant aspect is that the simulation is significantly longer than the characteristic times of the barostat and thermostat. With characteristic times of 10^{-4} and 10^{-3} ns, respectively, the thermostat and barosat *variables* perform 2×10^5 and 2×10^4 cycles per simulation (see below), which is adequate for controlling the temperature and pressure of the system. This, indeed, is reflected on the density profile of the liquids and gas, that satisfies the essential characteristics of symmetry of the system. It is remarkable that our simulations starting from a sample containing just 14 N_2 molecules randomly distributed in the viscous PFOB liquid reproduce a density profile with a good degree of symmetry.

The simulation box is allowed to expand and compress only along the direction orthogonal to the interface, which corresponds to the x-direction in the chosen reference frame. The 1D constant pressure algorithm is applied to prevent the nonphysical shrinking of the simulation box on the PFC/water $y-z$ surface plane resulting from the tendency of the flat interface system to minimize the surface area between the two liquids. Indeed, in a genuine 3D system PFC forms spherical bubbles, as seen in the experiments, and the water/oil interface cannot shrink under the action of the interface energy. It is worth remarking that a genuine 3D computational system containing a spherical droplet of a size treatable by extensive molecular dynamics (one or few nanometers in diameter) will probably introduce several artifacts. For example, in nanometer size PFC droplets the Laplace pressure is much higher than in the micrometer size experimental counterpart. Among the others, the relatively small (and constant) curvature of the PFOB droplets, and the flat water/oil interface computational sample, allowed us to use the Martyna-Tobias-Klein barostat [85], which, on the contrary, might have been unsuitable for a multi-phase systems with domains at (significantly) different pressures [195]. Summarizing, the flat interface system with variable cell along the x direction, the direction orthogonal to the PFC/water interface, is the best compromise between accuracy and feasibility of simulations.

The sample was initially thermalized for 5 ns at 300 K and 0.1 MPa; after thermalization, simulations were run for additional 20 ns, during which we collected data to analyze the gas density distribution. In parallel, the 300 K / 0.1 MPa thermalized sample was brought to -20 MPa, thermalized for additional 5 ns, and then evolved for additional 20 ns for analysis.

Forces acting on atoms are derived from TIP4P/2005 model for water [232] and the GAFF force field for PFC. N_2 is modeled as a rigid molecule. Molecules of the different species interact via electrostatics and van der Waals forces, the latter modeled by the Lennard-Jones potential $\nu(r_{ij}) = 4\varepsilon_{\alpha\beta}\left[(\sigma_{\alpha\beta}/r_{ij})^{12}) - (\sigma_{\alpha\beta}/r_{ij})^6\right]$, where r_{ij} represents the distance between two atoms belonging to different molecules, and $\varepsilon_{\alpha\beta}$ and $\sigma_{\alpha\beta}$ are the characteristic energy and distance, respectively, between atoms of type α and β. As customary, cross-species coefficients, i. e., those between atoms of different types, are obtained from same-species parameters through the Lorentz-Berthelot combination rules, $\varepsilon_{\alpha\beta} = \sqrt{\varepsilon_\alpha \varepsilon_\beta}$ and $\sigma_{\alpha\beta} = (\sigma_\alpha + \sigma_\beta)/2$. N_2

parameters for the cross-species coefficient have been taken from Ref. [187].

The normalized density is defined as the density field divided by the bulk density. The density field is obtained by discretizing the simulation box in slices of $\sim 0.1\,\mathrm{nm}$ in the direction parallel to the interface, and dividing the average number of molecules of a given species in each slice by the volume of the slice. The precise size of the slices is chosen such that they are commensurable with the average size of the simulation box, i. e., so that an integer number of slices fit into it. The bulk density of each liquid phase is computed as the number of molecules within the bulk domain of the corresponding slab, i. e., the region between the virtual borders at 2 nm away from the Gibbs interface, divided by the volume of this region. Similarly, the bulk density of N_2 is defined as the number of nitrogen molecules in the PFOB bulk domain divided by the volume of this region.

6.5 Supplementary Information

Multiple droplet cavitation

A droplet may nucleate multiple times. This is demonstrated in Fig. S1 (6.5). Here, the PFC droplets marked in the upper row with a red circle at $t = 0$ are followed for a longer time until $t = 10.2\,\mu s$. Initially, we see that these two droplets nucleate a bubble at $t = 0.2\,\mu s$ that collapses and is not detected anymore after $t = 1.2\,\mu s$. At $t = 7.6\,\mu s$ the droplets have been displaced slightly to the right and at $t = 8.8\,\mu s$ they again nucleate a bubble. We speculate that reflections of waves within the glass result in this late rarefaction wave. This demonstrates that a droplet is not used up by one cavitation event but can serve multiple times as a cavitation nucleus. A word of caution, some unresolved gas bubbles may remain as a result of the first cavitation event, and this may nucleate the second cavitation event, too.

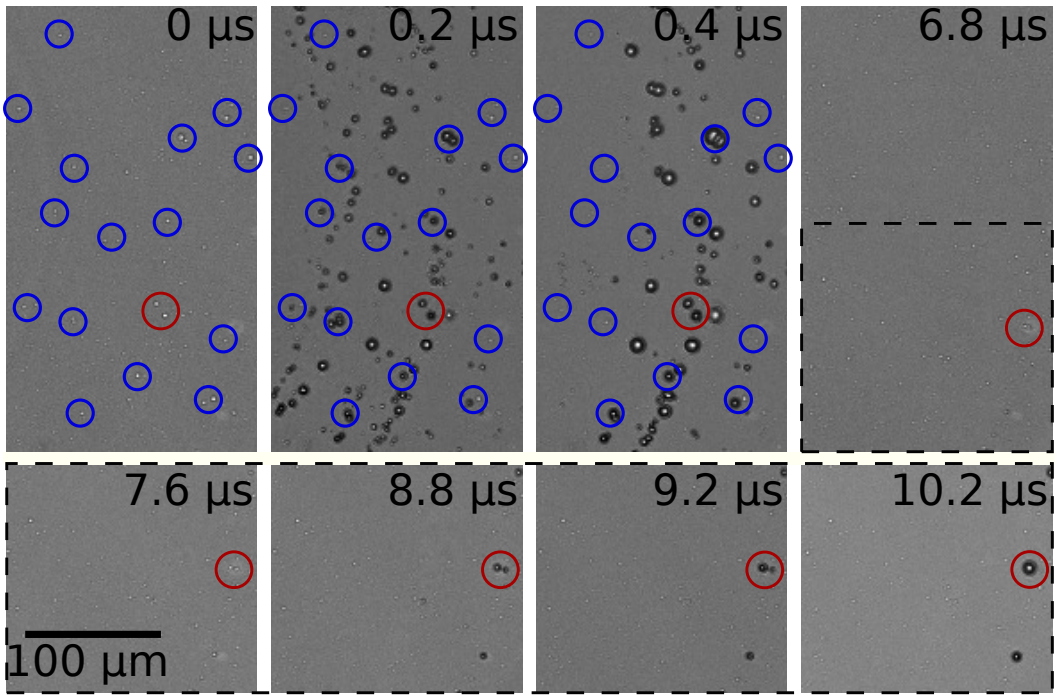

Figure S1 - Figure 6.5. Multiple droplet cavitation. Experimental snapshots of cavitation nucleation in a PFOB emulsion. Some PFOB droplets are marked with a blue circle. At $t = 0.2 - 0.4\,\mu s$, i. e. when the Lamb wave passes, on most of these droplets a bubble is formed. The red circle marks two droplets, which show cavitation at $t = 0.2 - 0.4\,\mu s$. With time they are transported by the flow, created by the main bubble expansion towards the right ($t = 6.8 - 7.6\,\mu s$). At $t = 8.8\,\mu s$, on the very same droplets bubbles are formed again by a tension wave.

Single interface bubble nucleation

During preparation of the droplets through sonication particulate contamination may be generated, e.g. through sub-micrometer sized metal particles eroded from the ultrasonic horn. Those particles may remain in suspension and accumulate at the liquid-liquid interface.

To rule out that the cavitation is due to nanoparticles trapped at the liquid-liquid interface the sonication step was omitted. A clean liquid-liquid interface was created by depositing a macroscopic droplet of water and a droplet of PFOB side-by-side onto a microscope slide and covering them with a cover slip resulting in an interface without the possibility to entrap particles. The Lamb wave was generated then in a rather thick gap where the height was adjusted to 10 µm with suitable spacers. For this thickness the rarefaction wave does *not* nucleate cavitation in either of the two liquids.

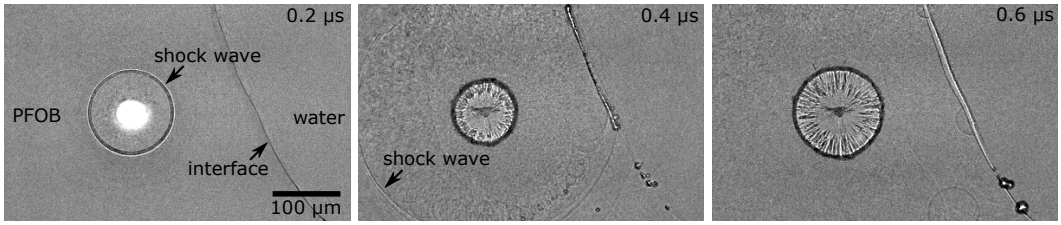

Figure S2 - Figure 6.6. Cavitation activity near a PFOB-water interface in a liquid gap. Secondary cavitation bubbles are mainly formed at the interface.

Figure S2 (6.6) depicts the course of events. At time $t = 0.2\,\mu s$ the plasma from the pulsed laser and the emitted shock wave are visible. Once the shock wave reaches the PFOB-water interface, $t = 0.4\,\mu s$, a line of cavitation bubbles nucleate at this interface and coalesce into a long thin strip of vapor. At $t = 0.6\,\mu s$ most bubbles have collapsed and due to the flow induced by the central bubble the liquid-liquid interface is displaced to the right.

The shape of the cavitation pattern supports the experimental interpretation and molecular dynamics simulation of having as supersaturated region between the liquids.

Gas layer formation at the water/PFC interface

The accumulation of N_2 molecules in the MD simulations are presented in Fig. S3 (6.7). Here, the arrows marks the regions, where cavities in the water phase at the liquid-liquid interface occur due to the accumulation of gas molecules in this area.

Effect of N_2 supersaturation on the properties of the computational sample

In the main text we mentioned that in our simulations we used an N_2 gas concentration ∼5 times higher than the experimental saturation value, which helps obtaining reliable computational results within the timescale accessible to molecular dynamics. Here we support the reliability of this approach showing that on the timescale of simulations this oversaturation produces no artefacts in the computational sample.

Fig. S4 (6.8) shows several partial pair correlation functions, $g(r)$, between N_2 and PFC - including the specific case of N-F and N-Br - and between N_2 molecules for two PFC/N_2 bulk samples at gas molar fraction $\chi = 0.0039$, close to the experimental saturation concentration [199], and $\chi = 0.018$, the concentration used in the water/PFC interface simulations. The pair correlation function represents the

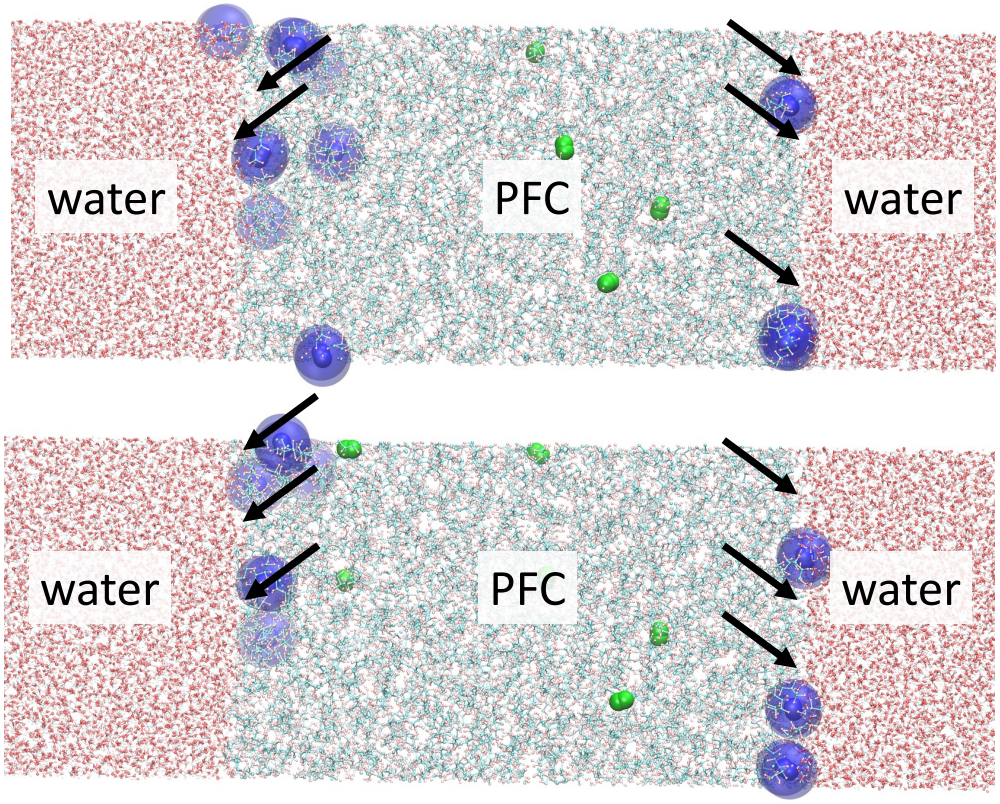

Figure S3 - Figure 6.7. Two more snapshots of the atomistic sample illustrating the formation of a gas layer at the water/PFC interface. Blue spheres highlighted by a spherical shadow of the same color are *interface* nitrogen molecules, arbitrarily defined as those molecules within 2 nm of both water and PFC molecules, i. e., within 2 nm from the interface. The complementary bulk nitrogen molecules are represented as green spheres. The arrows show the opening of cavities in the water domain of the interface due to the presence of gas molecules. This is more visible in some cases as there are several molecules at a short distance from each other. In other cases, this is harder to appreciate as the gas molecules are deeper in the sample. A movie of a 1 ns branch of the MD trajectory at −20 MPa is provided in the Supplementary Materials.

probability (density) to find two atoms at distance r in the system at hand with respect to the case of an uncorrelated system (ideal gas).

Concerning the partial N_2-PFC correlation functions (top row and bottom-left panels of Fig. S4, 6.8), no significant differences between the two samples at different concentrations are observed, apart, as expected, a better statistic in the $\chi = 0.018$ case. Concerning the N-N pair correlation function (bottom-right panel of Fig. S4, 6.8), for the low concentration solution $g(r) = 0$ in the range of intermolecular distances, i. e., beyond twice the N van der Waals radius. This is apparently surprising because even if there were no interaction between N_2 molecules the pair correlation function should be equal to 1 in this region. This, indeed, is an artefact of the insufficient simulation time to reproduce the fundamental structural properties of a highly diluted (gas) solute on the timescale of simulations, here 5 ns. On the contrary, the N-N pair correlation function of the $\chi = 0.018$ sample obtained by a simulation of the same duration shows the expected profile of a (concentrated)

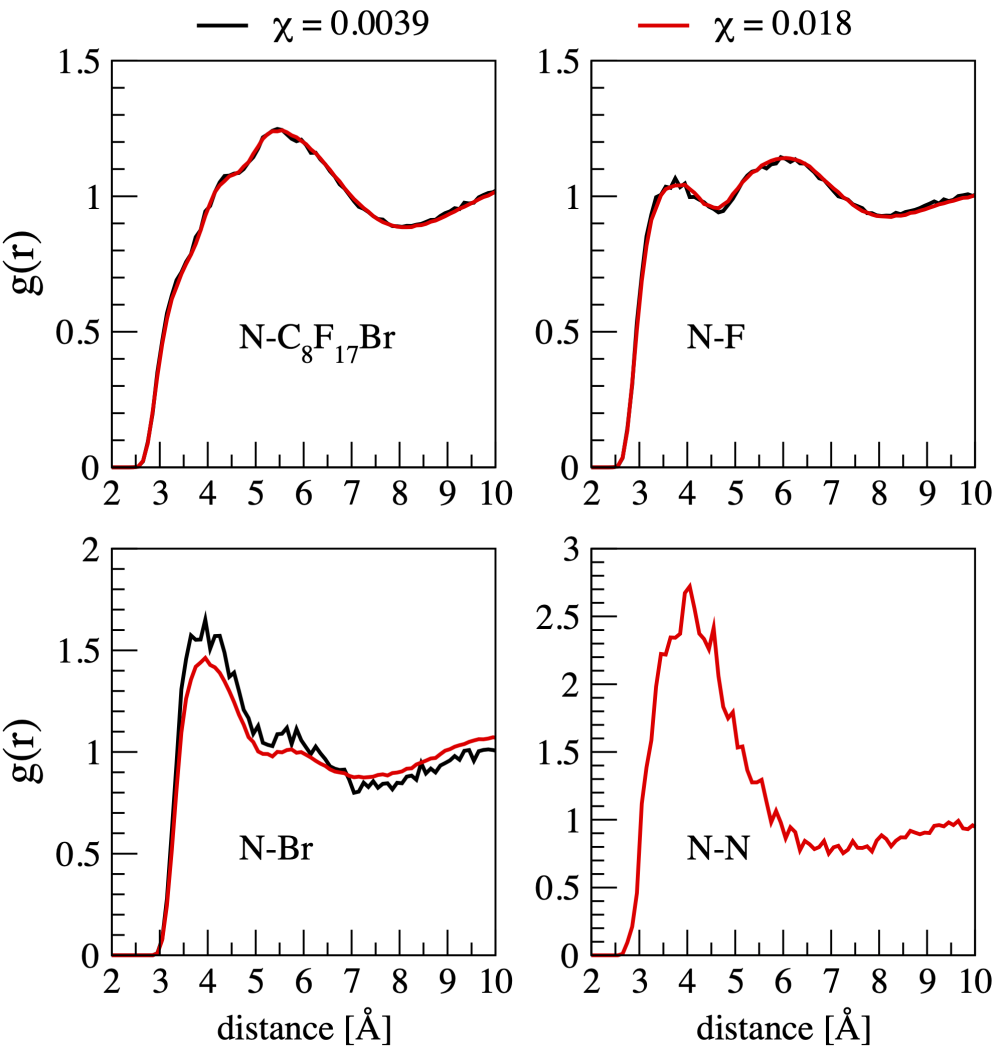

Figure S4 - Figure 6.8. Comparison between (partial) pair correlation functions of two PFC/N_2 bulk samples at molar fraction $\chi = 0.0039$ (black), close to the experimental saturation concentration, and $\chi = 0.018$ (red), the concentration used in the water/PFC interface simulations. Top-left panel shows pair correlation function between atoms of the gas and atoms of PFC; top-right and bottom-left focus on N-F and N-Br pairs. Bottom-right panel shows the pair correlation function between nitrogen atoms belonging to different molecules.

gas, with a peak corresponding to the first coordination shell quickly degrading to 1. Present results confirm the suitability of the "oversaturation" approach: the level of oversaturation considered in this work i) introduces no significant structural changes in the system while ii) allows to achieve well converged properties in short times, compatible with the timescale accessible to molecular dynamics.

Effect of N_2 supersaturation on the bubble nucleation barrier

To estimate the effect of local supersaturation on the bubble nucleation barrier, one can resort to the classical nucleation theory, as adapted by Lubetkin to the case

of a supersaturated liquid [222]. Here, the nucleation rate j depends exponentially on the barrier $\Delta G^{\dagger}$: $j = C \exp\left[-\Delta G^{\dagger}/k_B T\right]$, with k_B the Boltzmann constant and T the temperature of the system. For the pre-exponential factor C several forms have been developed [233, 234, 235], which have been recently tested to be quantitatively accurate when tested against controlled *in silico* experiments [88]. The key conclusion to bear in mind is that with $\Delta G^{\dagger} \sim 5$ k_BT, i. e., 5 times the thermal energy at the operative conditions, nucleation occurs on the nanosecond timescale, which has been also confirmed by direct simulations [86]. Hence, one is interested in identifying the local supersaturation value $\sigma = c/c_{sat} - 1$, with c and c_{sat} the local and saturation gas concentration, respectively, at which the nucleation barrier $\Delta G^{\dagger} \leq 5$, and whether this concentration is achieved at the water/PFC interface.

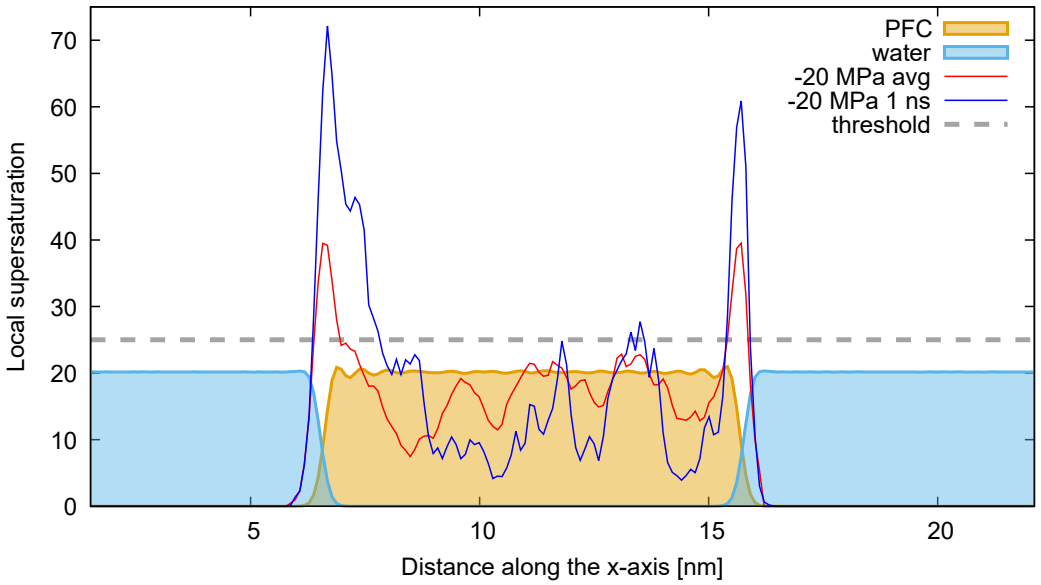

Figure S5 - Figure 6.9. Local supersaturation of N_2 gas at -20 MPa with respect to the saturation value of nitrogen in water at ambient conditions. In the figure are reported both the supersaturation profile averaged over the entire simulation and the one averaged over 1 ns in which the local supersaturation value at the water/PFC interface was specially high. The grey dashed line is the threshold supersaturation value making the nucleation barrier small enough that the process could be experimentally observed.

In the case of **homogeneous** supersaturated systems the barrier for nucleating a (spherical) bubble can be approximated by $\Delta G^{\dagger} = 16/3\pi(\gamma_0 + \sigma b)^3/(\sigma P)^3$, where γ_0 is the surface tension of the pure liquid, $b = -8.5 \times 10^{-5}$ N/(m atm) is the coefficient of reduction of the surface tension as a function of the pressure [236], the pressure being implicitly set to 1 bar and the effect of gas concentration taken into account by σ; finally, $P = 20$ MPa is the driving force for bubble nucleation at the operative conditions of our experiments (-20 MPa of the Lamb-type wave). Usually, nucleation in heterogeneous conditions is taken into account through a reduction of this barrier by a multiplicative parameter that for a solid surface reads $\Phi(\theta) = 1/4(1 + \cos\theta)^2(2 - \cos\theta)$, with θ the contact angle of the liquid: $\Delta G^{\dagger}_{het} = \Delta G^{\dagger}_{homo}\Phi(\theta)$. Here, we develop or argument in the most conservative conditions, i. e., considering the case of homogeneous nucleation. Within this

framework, and data reported in Ref. [236], one obtains the following values of the **homogeneous** nucleation barrier (expressed in k_BT units):

σ	$\Delta G^\dagger/k_BT$
0.1	$\sim 4 \times 10^5$
1	$\sim 4 \times 10^3$
10	~ 40
25	~ 5
50	$\sim 1.$

Table 6.1. Correspondence between the local supersaturation value σ and the corresponding homogeneous nucleation barrier $\Delta G^\dagger$ (in k_BT).

These results show that for $\sigma \gtrsim 25$ nucleation can occur at the operative conditions of our experiments. As mentioned above, the heterogeneity introduced by the hydrophobic PFOB is expected to reduce local supersaturation necessary to produce bubble nucleation.

Generally speaking, obtaining $\sigma \gtrsim 25$ is non-trivial. However, one notices that the gas concentration at the water/PFOB is much larger than this threshold (see Fig. S5, 6.9). In fact, nitrogen reaches a local density up to $\sim 2.5\,\mathrm{g/l}$ concentration in the interface region, against a saturation concentration in water at normal conditions of $\sim 0.02\,\mathrm{g/l}$. Moreover, one must consider that local supersaturation may have fluctuations and for short times can reach much higher values. To illustrate this, in Fig. S5 (6.9) we also report a supersaturation profile averaged over only 1 ns along the MD trajectory when its value at the water/PFC was especially high.

Adequacy of the size of the computational sample

For the computational sample to be suitable for the simulations of a gas at the water/PFOB, both liquid domains must be large enough that the bulk characteristics are recovered. Indeed, the normalized density profiles shown in Fig. 2 of the main text, reproduced in Fig. S6 (6.10) without the gas density profiles, show within $\sim 1 - 2\,\mathrm{nm}$ from the nominal interface, where the normalized densities of the two liquids are the same. There is first a depletion zone, where the density is lower than the bulk value, followed by a region in which gas density increases, and then a *rippling* region, where the densities oscillate around the bulk value. These two phenomena are typical for liquids in contact with lyophobic surfaces, i. e., surfaces repelling the liquid, with a contact angle $\theta \geq 90°$. Indeed, this is consistent with the non miscibility of the two liquids. Beyond $2 - 3\,\mathrm{nm}$ from the interface, however, the density profile of both liquids is essentially flat, with small fluctuation due to the finite duration of MD simulations, which is long on the atomistic timescale but insufficient to sample the configurations space. This is especially visible in the case of PFC, which due to entanglement of longer molecules make the sampling especially difficult.

The above analysis can be made more quantitative resorting to the results

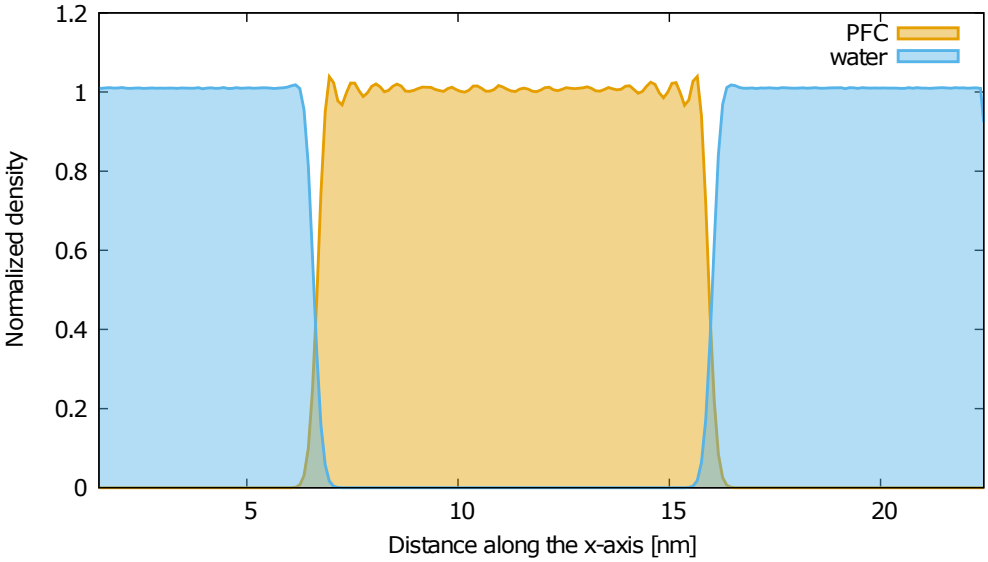

Figure S6 - Figure 6.10. Density profile of the liquids, water (cyan) and PFC (yellow), along the axis transverse to the liquid/liquid interface.

of Ref. [38]. In this former article we computed the effective potential felt by gas molecules, N_2 and O_2, as a function of the distance from a graphene surface immersed in water. It is worth remarking that this effective potential does not only depend on the mechanical (force field - *intrinsic* in Fig. S7, 6.11) solid-gas interaction. Instead in Fig. S7A (6.11A) (reproduced with permission from Ref. [38]), it is seen that for the same graphene/N_2 mechanical interaction, the effective potential depends on the hydrophobicity of the interface. Indeed, the graphene/N_2 effective interaction can be attractive even if the corresponding mechanical interaction is weaker (Fig. S7B, 6.11B) or purely repulsive (Fig. S7C, 6.11C). Finally, the strength of the graphene/N_2 interaction depends on the affinity of the gas for liquid molecules. The reason why the interface is an attractive region for the gas is that there liquid is depleted. As a result this region favors to host the gas. Its attraction increases with the degree of depletion for example by an increase in hydrophobicity. The depletion region may decrease with in increase in gas solubility in the liquid. Overall we want to stress here that: i) The length scale of the attractive interaction is $\sim 1\,\text{nm}$, which is the scale where the liquid density shows depletion and rippling. ii) The non-bulk like density field is found only within $\sim 2\,\text{nm}$ of the water/PFC interface. This supports the choice of the size of our simulation, where each liquid domain is considerably larger.

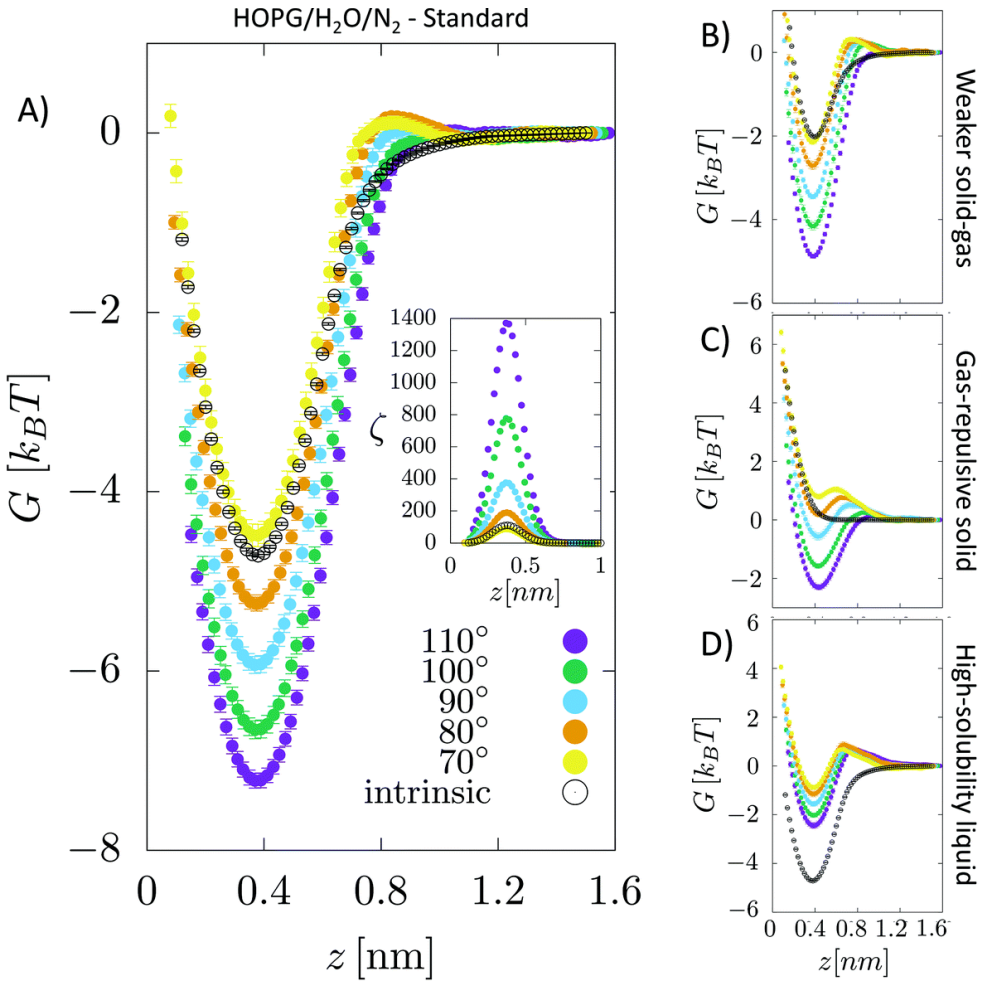

Figure S7 - Figure 6.11. Effective potential between N_2 gas molecules in water as a function of the distance from a graphene sheet. Here, by *effective potential* one means the so-called potential of the mean force, obtained by restrained MD simulations [86, 38]. The effective potential depends on many factors, including the hydrophobicity of the solid, the strength of the gas-solid interaction and the strength of the gas-liquid interaction. Panels A to D show that regardless of these details, the range of the effective potential is on the nanometric scale, with the N_2 molecule subjected to a flat effective potential for distance from the interface ≥ 1 nm. This means that beyond 1 nm from the interface the liquid is bulk-like for what concerns the gas properties. Figure reprinted with permission from Ref. [38].

Chapter 7

Conclusions

7.1 Closing remarks

Despite their similarities, the problems that I tackled during my research are of a different nature from one another, and cannot be always reunited under a single umbrella. This is the reason why I chose to explicitly divide my thesis into two parts, and also to place the conclusions drawn for a specific topic at the end of the chapter (article) where said topic is examined in detail. Here, on the other hand, I will try to offer to the reader more general closing remarks, and future perspectives on how my research could be further advanced.

My analyses showed how classical intrusion and extrusion (wetting and drying) theories need to include a whole class of new phenomena, typically neglected, when the material involved is a MOF or, in general, a nanoporous solid.

Indeed, capillarity theory is not enough to describe the physics of these processes, because is a macroscopic theory which deals with interfaces whose size and geometry count in thousands of water molecules at the same time. Rather, the size of the apertures allowing the progressive wetting of a nanoporous material, belongs to a molecular scale, and only few or even single water molecules can percolate at once. Even the solid at those scales cannot be described with a continuum model, since the pores themselves are constituted by single layers of atoms.

My work also demonstrated heuristically how rigid materials are more resistant to intrusion: more specifically, the simulations illustrated how the free energy intrusion profile changes with respect to the flexibility of the solid. Note how the correlation between flexibility and intrusion feasibility does not imply a causal relation between the two: a solid does not need to be flexible in order to be intruded. Still, it is crucial to understand the origin of such correlation and the related observed phenomenology: indeed, in the future, a deeper understanding of the relation between flexibility and the characteristics of the intrusion process (intrusion pressure, hysteresis cycle, etc.) will guide us in designing advanced metamaterials whose properties are carefully tailored to the specificity of the application at hand. During this phase, I focused on observing and isolating the new phenomenology which forks from the current knowledge of the subject and trying to find an explanation for it. In an forthcoming paper, currently in preparation, the role of flexibility at the atomistic/microscopic level will be examined thoroughly and an explanation of its correlation with intrusion

will be offered.

I would like to remark here that, in this and other similar cases, I treated simulations as experimental phenomenology; to put it in different terms, I employed molecular dynamics to gain insight on how these systems behave, what really happens within them when a liquid is forced inside. MD simulations offer a unique perspective, other than the ability to surgically isolate specific effects, and to control and fine tune a lot of features of the examined setup, in ways that could never be achieved by real-life physical experiments. Such manipulations, despite could appear nonsensical in the beginning, actually constitute a tremendously powerful investigation tool. In this particular case, I was able to obtain the aforementioned result by simulating two versions of ZIF-8, completely identical with respect to one another (interaction, chemistry, topology, atom mobility, etc.), except for one single aspect: one's cell was allowed to expand transversely, while the other's was not.

Similarly to the intrusion theories of solids and their atomistic modeling, the available theories describing the processes happening at the interfaces between a simple solid, such as a plane surface, and a liquid in which a gas is dissolved, are not completely satisfying.

Such phenomena, such as surface nanobubbles, are all but obvious: up until the very recent past, there was no experimental evidence supporting the latest theories conceived to explain their extraordinary stability and longevity; in addition, these theories were still not able to explain the formation of surface nanobubbles in relation to the physico-chemical characteristics of the solid and liquid. To our knowledge, there also had not been a systematic investigation attempt on the cross interactions between all three phases (solid, liquid and gas), saving rare exceptions which focused more on the episodic observation of a phenomenon rather than its analysis.[167, 237] Via free energy atomistic simulations, I was able to meet all the above inquiries and also back up a continuum theory recently developed by prof. Claus-Dieter Ohl, our experimental partner in the research. This theory can also help understand the role played by the gas dissolved within the liquid in the intrusion and extrusion processes in nanoporous solid materials.[92]

The dissolved gas also determines an exotic effect when liquid-liquid interfaces are considered, as surprisingly illustrated by the latest experiments of prof. Ohl involving oil-water interfaces: when the system is subjected to tensile conditions, the gas is released at the interface between the two liquids, where it accumulates up to induce the formation of bubbles. This novel phenomenon, as already identified on an original forthcoming paper (soon to be published on Nature Physics), could pave to way to new application in many different fields, above all the biomedical one, with the cavitation-enhanced ultrasound ablation of cancerous tissues. My simulations explained the origin of this peculiar phenomenon, which is related to the different solubility of the gas between the two liquids.

7.2 Future perspectives

Of course, the work is far from being finished and lots still need to be done. Recently, it has been shown[41] how nanoscopic pores (whose size is comparable to that of the pores of ZIF-8, the material I have focused on) have a non-conventional effect on the wetting of the material. The pore characteristic size suggests (and it has already being confirmed by literature[238]) that quantum nuclear effects may produce a non-negligible contribution to the physics of MOFs. Following this reasoning, the behavior of MOFs may differ significantly using light versus heavy water,[1], which constitutes a strong argument to extend the study of intrusion and extrusion processes and wetting of nanoporous materials to include quantum effects.

There are clear and well-known implementation paths to achieve this task, and indeed I already started working on this topic during the third year of my PhD. I also acquired some preliminary results, but I did not find them mature enough to be properly included and presented within this thesis. Even so, I will still make a hint here about the approach I followed.

Quantum nuclear effects can be taken into account in the class of simulations I have been used throughout my research by using Path Integral Molecular Dynamics (PIMD), a technique which grants the possibility to reproduce the behavior of quantum nuclei within the framework classical MD. The idea behind PIMD is the following: the quantum distribution of a system can be manipulated to resemble the classical partition function of a cyclic polymer chain of P points moving in a classical potential. Such resemblance inspired Chandler and Wolynes[239] to coin the expression *classical isomorphism*. Because a cyclic polymer somehow looks like a necklace, its P points are often referred to as "beads". Each quantum particle in a path integral simulation is represented by a ring-polymer of P quasi-beads, labeled from 1 to P. During the simulation, the quasi-beads interact (1) with the two neighboring quasi-beads, and (2) with beads on the other ring-polymers. The isomorphism - between an approximate (since P is finite) quantum partition function for the original system to a classical partition function for a ring-polymer system - can be exploited to efficiently sample configurations from the quantum ensemble. According to the classical isomorphism, we can treat the cyclic polymer exploiting all the techniques developed for classical systems to obtain an approximation of the quantum properties, and the latter can be systematically improved simply by increasing P. PIMD can be integrated with free energy calculations: Bonella et al.[240] have developed a method to evaluate the free energy of a set of quantum particles using the same techniques I have been employing so far. Their approach offered natural way to extend my research.

[1] light water has the most common hydrogen isotope, called protium, whereas heavy water has deuterium isotope, also known as heavy hydrogen.

Appendix A

Ewald summation for Coulomb interactions in a periodic cell

A.1 Ewald summation for Coulomb interactions in a periodic cell

[DISCLAIMER] I wished to include an in-depth review of Ewald summations in my thesis, to make it as complete as possible with respect to the theory behind the computational tools that I used. While browsing for material, I met with this document [241], which I found so thorough in all the derivations, that basically I could not identify any way to improve it. Despite this, I still decided to include (the most of) it in my thesis, with minimum changes here and there.

A.1.1 Coulomb interactions in a periodic cell

Consider N ions in vacuum, at locations $\mathbf{r}_1$, $\mathbf{r}_2$, $\mathbf{r}_3$, ..., $\mathbf{r}_N$, and possessing point charges q_1, q_2, q_3, ..., q_N, respectively. The total Coulomb interaction energy is

$$E = \frac{1}{4\pi\epsilon_0} \sum_{(i,j)} \frac{q_i q_j}{|\mathbf{r}_i - \mathbf{r}_j|} = \frac{1}{4\pi\epsilon_0} \sum_{i=1}^{N} \sum_{j=i+1}^{N} \frac{q_i q_j}{|\mathbf{r}_i - \mathbf{r}_j|} = \frac{1}{4\pi\epsilon_0} \frac{1}{2} \sum_{i=1}^{N} \sum_{\substack{j=1 \\ j\neq i}}^{N} \frac{q_i q_j}{|\mathbf{r}_i - \mathbf{r}_j|} \quad \text{(A.1)}$$

where $\epsilon_0 = 8.854 \cdot 10^{-12} \mathrm{C}^2\mathrm{N}^{-1}\mathrm{m}^2$ is the vacuum permittivity (or electric constant), and the sum is performed over all distinct ionic pairs (i, j). Notice how the sum can be expressed in three different ways: (1) by specifying implicitly the distinct pairs of ions; (2) by explicitly counting over the distinct pairs; (3) by explicitly counting over all possible pairs, excluding the ones consisting of the same ion and introducing the one-half factor to avoid double counting.

Now let us subject the ions to periodic boundary conditions (PBCs), i.e. we imagine our current system to be nothing more than a single super-cell, described by three vectors $\mathbf{a}_1$, $\mathbf{a}_2$, $\mathbf{a}_3$, in an infinite lattice. This means that for every ion q_i at location $\mathbf{r}_i$, there are also ions with the same charge q_i located at $\mathbf{r}_i + n_1\mathbf{a}_1 + n_2\mathbf{a}_2 + n_3\mathbf{a}_3$, where n_1, n_2, n_3 are arbitrary integers. To simplify the notation, we will define an arbitrary replication vector $\mathbf{r}_C = n_1\mathbf{a}_1 + n_2\mathbf{a}_2 + n_3\mathbf{a}_3$. The total Coulomb

interaction energy for these ions under PBCs (which includes the interactions between periodic images) will thus be:

$$E = \frac{1}{4\pi\epsilon_0} \sum_{\mathbf{r}_C} \sum_{(i,j)} \frac{q_i q_j}{|\mathbf{r}_i - \mathbf{r}_j + \mathbf{r}_C|} \tag{A.2}$$

As pointed out before, the sum over all ion pairs can be rewritten into sums over all ions, multiplied by a factor $1/2$ to cancel the double-counting

$$E = \frac{1}{4\pi\epsilon_0} \frac{1}{2} \sum_{\mathbf{r}_C} \sum_{i=1}^{N} \sum_{\substack{j=1 \\ j\neq i \text{ if } \mathbf{r}_C=0}}^{N} \frac{q_i q_j}{|\mathbf{r}_i - \mathbf{r}_j + \mathbf{r}_C|} = \frac{1}{4\pi\epsilon_0} \frac{1}{2} \sum_{\mathbf{r}_C} \sum_{i=1}^{N} \sum_{j=1}^{N}{}' \frac{q_i q_j}{|\mathbf{r}_i - \mathbf{r}_j + \mathbf{r}_C|} \tag{A.3}$$

where the $'$ symbol is introduced as a lighter notation to exclude the term $j = i$ if $\mathbf{r}_C = 0$. The infinite sum in eq. A.3 not only converges very slowly but also is conditionally convergent, meaning that the result depends on the order of the summation. The Ewald method evaluates E by transforming it into summations that converge not only rapidly but also absolutely. The final expression of energy in the Ewald method is given by eq. A.66. In the following we describe how and why we arrive at such an expression.

To gain more physical insight, we consider the electrical potential field generated by the ions. The potential field generated by a single ion with charge q_i at location $\mathbf{r}_i$ is given by

$$\phi_i(\mathbf{r}) = \frac{1}{4\pi\epsilon_0} \frac{q_i}{|\mathbf{r} - \mathbf{r}_i|} \tag{A.4}$$

The potential field generated by N ions, together with their periodic images under PBCs, is then

$$\phi(\mathbf{r}) = \sum_{\mathbf{r}_C} \sum_{j=1}^{N} \phi_j(\mathbf{r} + \mathbf{r}_C) = \frac{1}{4\pi\epsilon_0} \sum_{\mathbf{r}_C} \sum_{j=1}^{N} \frac{q_j}{|\mathbf{r} - \mathbf{r}_j + \mathbf{r}_C|} \tag{A.5}$$

We can then define $\phi_{[i]}(\mathbf{r})$ as the potential field generated by all the N ions plus their periodic images, but excluding the i-th ion

$$\phi_{[i]}(\mathbf{r}) = \phi(\mathbf{r}) - \phi_i(\mathbf{r}) = \frac{1}{4\pi\epsilon_0} \sum_{\mathbf{r}_C} \sum_{j=1}^{N}{}' \frac{q_j}{|\mathbf{r} - \mathbf{r}_j + \mathbf{r}_C|} \tag{A.6}$$

Again, the $'$ symbol, introduced in eq. A.3, means that the term $j = i$ is excluded, if $\mathbf{r}_C = 0$. Comparing Eqs. A.3 and A.6, we see that

$$E = \frac{1}{2} \sum_{i=1}^{N} q_i \phi_{[i]}(\mathbf{r}_i) \tag{A.7}$$

A.1.2 Charge distribution function

The charge density distribution for the system of point charges considered above is described by a collection of Dirac delta functions. In particular, the charge density for point charge q_i is

$$\rho_i(\mathbf{r}) = q_i \delta(\mathbf{r} - \mathbf{r}_i) \tag{A.8}$$

However, we can consider a more general problem, in which the charge distribution for each ion is not necessarily a delta function, but could spread out in space. The potential field generated by this charge distribution is the solution of the Poisson's equation

$$\nabla^2 \phi_i(\mathbf{r}) = -\frac{\rho_i(\mathbf{r})}{\varepsilon_0} \tag{A.9}$$

and can be written as

$$\phi_i(\mathbf{r}) = \frac{1}{4\pi\epsilon_0} \int \frac{\rho_i(\mathbf{r}')}{|\mathbf{r} - \mathbf{r}'|} \, \mathrm{d}^3\mathbf{r}' \tag{A.10}$$

The total Coulomb interaction energy can then be written as

$$E = \frac{1}{2} \frac{1}{4\pi\epsilon_0} \sum_{\mathbf{r}_C} \sum_{i=1}^{N} {\sum_{j=1}^{N}}' \int \frac{\rho_i(\mathbf{r}) \, \rho_j(\mathbf{r}')}{|\mathbf{r} - \mathbf{r}' + \mathbf{r}_C|} \, \mathrm{d}^3\mathbf{r} \, \mathrm{d}^3\mathbf{r}' \tag{A.11}$$

The potential field generated by all ions excluding ion i becomes

$$\phi_{[i]}(\mathbf{r}) = \frac{1}{4\pi\epsilon_0} \sum_{\mathbf{r}_C} {\sum_{j=1}^{N}}' \int \frac{\rho_j(\mathbf{r}')}{|\mathbf{r} - \mathbf{r}' + \mathbf{r}_C|} \, \mathrm{d}^3\mathbf{r}' \tag{A.12}$$

When the charge densities are described by eq. A.8, Eqs. A.11 and A.12 reduce to Eqs. A.3 and A.6 respectively.

A.1.3 Splitting (cleverly) the charge distribution

We now return to our original problem, in which the charge distributions are described by Dirac delta functions. Such distributions can be split in two terms, by adding and subtracting a Gaussian distribution as follows

$$\rho_i(\mathbf{r}) = \rho_i^S(\mathbf{r}) + \rho_i^L(\mathbf{r}) \tag{A.13}$$

$$\rho_i^S(\mathbf{r}) = q_i \delta(\mathbf{r} - \mathbf{r}_i) - q_i g_{\sigma^2 \boldsymbol{I}_3}(\mathbf{r} - \mathbf{r}_i) \tag{A.14}$$

$$\rho_i^L(\mathbf{r}) = q_i g_{\sigma^2 \boldsymbol{I}_3}(\mathbf{r} - \mathbf{r}_i) \tag{A.15}$$

where we followed the notation introduced in B.7

$$g_{\sigma^2 \boldsymbol{I}_3}(\mathbf{r}) = \frac{1}{\sqrt{(2\pi)^3 \det(\sigma^2 \boldsymbol{I}_3)}} \exp\left[-\frac{1}{2} \mathbf{r}^T \left(\sigma^2 \boldsymbol{I}_3 \right)^{-1} \mathbf{r} \right] = \tag{A.16}$$

$$= \frac{1}{\sqrt{(2\pi)^3 \, \sigma^6}} \exp\left[-\frac{|\mathbf{r}|^2}{2\sigma^2} \right] = \frac{1}{\sqrt{(2\pi\sigma^2)^3}} \exp\left[-\frac{|\mathbf{r}|^2}{2\sigma^2} \right] \ . \tag{A.17}$$

It is important to note that the Dirac delta function can be considered as a limit of the Gaussian distribution when $\sigma \longrightarrow 0$ (as proven in B.9). Also notice how, according the the adopted notation, $g_\sigma(r)$ and $g_{\sigma^2 \boldsymbol{I}_3}(\mathbf{r})$ represent the same function but with different normalization factors

$$g_\sigma(r) = \frac{1}{\sqrt{2\pi\sigma^2}} \exp\left[-\frac{r^2}{2\sigma^2}\right] \tag{A.18}$$

$$g_{\sigma^2 \boldsymbol{I}_3}(\mathbf{r}) = \frac{1}{\sqrt{(2\pi\sigma^2)^3}} \exp\left[-\frac{|\mathbf{r}|^2}{2\sigma^2}\right] = \frac{1}{\sqrt{(2\pi\sigma^2)^3}} \exp\left[-\frac{r^2}{2\sigma^2}\right] = g_{\sigma^2 \boldsymbol{I}_3}(r) \ . \tag{A.19}$$

As of the splitting of charge, the potential field $\phi_i(\mathbf{r})$ can also also be split into two terms

$$\phi_i(\mathbf{r}) = \phi_i^S(\mathbf{r}) + \phi_i^L(\mathbf{r}) \tag{A.20}$$

$$\phi_i^S(\mathbf{r}) = \frac{q_i}{4\pi\epsilon_0} \int \frac{\delta(\mathbf{r}' - \mathbf{r}_i) - g_{\sigma^2 \boldsymbol{I}_3}(\mathbf{r}' - \mathbf{r}_i)}{|\mathbf{r} - \mathbf{r}'|} \, \mathrm{d}^3\mathbf{r}' \tag{A.21}$$

$$\phi_i^L(\mathbf{r}) = \frac{q_i}{4\pi\epsilon_0} \int \frac{g_{\sigma^2 \boldsymbol{I}_3}(\mathbf{r}' - \mathbf{r}_i)}{|\mathbf{r} - \mathbf{r}'|} \, \mathrm{d}^3\mathbf{r}' \tag{A.22}$$

The potential field generated by all ions excluding the i-th ion can be split in a similar way

$$\phi_{[i]}(\mathbf{r}) = \phi_{[i]}^S(\mathbf{r}) + \phi_{[i]}^L(\mathbf{r}) \tag{A.23}$$

$$\phi_{[i]}^S(\mathbf{r}) = \frac{1}{4\pi\epsilon_0} \sum_{\mathbf{r}_C} {\sum_{j=1}^{N}}' \int \frac{q_j \left[\delta(\mathbf{r}' - \mathbf{r}_j) - g_{\sigma^2 \boldsymbol{I}_3}(\mathbf{r}' - \mathbf{r}_j)\right]}{|\mathbf{r} - \mathbf{r}' + \mathbf{r}_C|} \, \mathrm{d}^3\mathbf{r}' \tag{A.24}$$

$$\phi_{[i]}^L(\mathbf{r}) = \frac{1}{4\pi\epsilon_0} \sum_{\mathbf{r}_C} {\sum_{j=1}^{N}}' \int \frac{q_j g_{\sigma^2 \boldsymbol{I}_3}(\mathbf{r}' - \mathbf{r}_j)}{|\mathbf{r} - \mathbf{r}' + \mathbf{r}_C|} \, \mathrm{d}^3\mathbf{r}' \tag{A.25}$$

This leads to the splitting of the Coulomb interaction energy

$$E = \frac{1}{2} \sum_{i=1}^{N} q_i \phi_{[i]}^S(\mathbf{r}_i) + \frac{1}{2} \sum_{i=1}^{N} q_i \phi_{[i]}^L(\mathbf{r}_i) \tag{A.26}$$

For reasons that will become clear later, we further split the energy E by adding and subtracting a self-interaction term

$$E = \frac{1}{2} \sum_{i=1}^{N} q_i \phi_{[i]}^S(\mathbf{r}_i) + \frac{1}{2} \sum_{i=1}^{N} q_i \phi^L(\mathbf{r}_i) - \frac{1}{2} \sum_{i=1}^{N} q_i \phi_i^L(\mathbf{r}_i) = E^S + E^L - E^{self} \tag{A.27}$$

where

$$E^S = \frac{1}{2} \sum_{i=1}^{N} q_i \phi_{[i]}^S(\mathbf{r}_i) \tag{A.28}$$

$$E^L = \frac{1}{2} \sum_{i=1}^{N} q_i \phi^L(\mathbf{r}_i) \tag{A.29}$$

$$E^{self} = \frac{1}{2} \sum_{i=1}^{N} q_i \phi_i^L(\mathbf{r}_i) \tag{A.30}$$

A.1.4 Potential field of a Gaussian charge distribution

The potential field generated by a Gaussian charge distribution can be obtained by solving the Poisson's equation

$$\nabla^2 \phi_g(\mathbf{r}) = -\frac{g_{\sigma^2 \boldsymbol{I}_3}(\mathbf{r})}{\varepsilon_0} \tag{A.31}$$

By symmetry, we know that $\phi_g(\mathbf{r})$ only depends on the magnitude $r = |\mathbf{r}|$. In spherical coordinates, remembering eq. A.19, the Poisson's equation becomes

$$\frac{1}{r}\frac{\partial^2}{\partial r^2}\left[r\phi_g(r)\right] = -\frac{g_{\sigma^2 \boldsymbol{I}_3}(r)}{\varepsilon_0} \tag{A.32}$$

$$\frac{\partial^2}{\partial r^2}\left[r\phi_g(r)\right] = -\frac{r g_{\sigma^2 \boldsymbol{I}_3}(r)}{\varepsilon_0} \tag{A.33}$$

$$\frac{\partial}{\partial r}\left[r\phi_g(r)\right] = -\int_r^{+\infty} \frac{r' g_{\sigma^2 \boldsymbol{I}_3}(r')}{\varepsilon_0}\,\mathrm{d}r' = \frac{\sigma^2}{\varepsilon_0} g_{\sigma^2 \boldsymbol{I}_3}(r) \tag{A.34}$$

$$r\phi_g(r) = \frac{\sigma^2}{\varepsilon_0}\int_0^r g_{\sigma^2 \boldsymbol{I}_3}(r')\;\mathrm{d}r' = \frac{\sigma^2}{\varepsilon_0}\frac{1}{\sqrt{(2\pi\sigma^2)^3}}\sqrt{\frac{\pi}{2}}\sigma\,\mathrm{erf}\left(\frac{r}{\sigma\sqrt{2}}\right) \tag{A.35}$$

$$\phi_g(r) = \frac{1}{4\pi\varepsilon_0 r}\,\mathrm{erf}\left(\frac{r}{\sigma\sqrt{2}}\right) \tag{A.36}$$

where

$$\mathrm{erf}(x) \coloneqq \frac{2}{\sqrt{\pi}}\int_0^x e^{-t^2}\,\mathrm{d}t \tag{A.37}$$

Therefore

$$\phi_i^S(\mathbf{r}) = \frac{1}{4\pi\epsilon_0}\frac{q_i}{|\mathbf{r}-\mathbf{r}_i|}\,\mathrm{erfc}\left(\frac{|\mathbf{r}-\mathbf{r}_i|}{\sigma\sqrt{2}}\right) \tag{A.38}$$

$$\phi_i^L(\mathbf{r}) = \frac{1}{4\pi\epsilon_0}\frac{q_i}{|\mathbf{r}-\mathbf{r}_i|}\,\mathrm{erf}\left(\frac{|\mathbf{r}-\mathbf{r}_i|}{\sigma\sqrt{2}}\right) \tag{A.39}$$

where $\mathrm{erfc}(x) \coloneqq 1 - \mathrm{erf}(x)$. Since

$$\lim_{x\to+\infty}\mathrm{erf}(x) = 1 \tag{A.40}$$

we deduce that $\phi_i^L(\mathbf{r})$ is a long-range potential, while $\phi_i^S(\mathbf{r})$ is a short-range singular potential. The Coulomb potential of a point charge is both long-ranged and singular. Given this result, we also have

$$\phi_{[i]}^S(\mathbf{r}) = \frac{1}{4\pi\epsilon_0}\sum_{\mathbf{r}_C}\sum_{j=1}^{N}{}' \frac{q_j}{|\mathbf{r}-\mathbf{r}_j+\mathbf{r}_C|}\,\mathrm{erfc}\left(\frac{|\mathbf{r}-\mathbf{r}_j+\mathbf{r}_C|}{\sigma\sqrt{2}}\right) \tag{A.41}$$

as well as the short-range part of the total Coulomb interaction energy (eq. A.28)

$$E^S = \frac{1}{2}\sum_{i=1}^{N} q_i \phi_{[i]}^S(\mathbf{r}_i) = \frac{1}{2}\frac{1}{4\pi\epsilon_0}\sum_{\mathbf{r}_C}\sum_{i=1}^{N}\sum_{j=1}^{N}{}' \frac{q_i q_j}{|\mathbf{r}_i-\mathbf{r}_j+\mathbf{r}_C|}\,\mathrm{erfc}\left(\frac{|\mathbf{r}_i-\mathbf{r}_j+\mathbf{r}_C|}{\sigma\sqrt{2}}\right) \tag{A.42}$$

This is similar to the total Coulomb interaction energy E, except for the erfc term that truncates the potential function at large distances. Due to the erfc truncation, $E^S_{[i]}$ can be directly computed from a sum in real space.

Now that we have the analytic expression for the long-range potential, we can easily obtain the self energy term

$$\text{for } x \ll 1 \longrightarrow \operatorname{erf}(x) \approx \frac{2}{\sqrt{\pi}} \frac{x}{\sigma\sqrt{2}} = \frac{1}{\sigma}\sqrt{\frac{2}{\pi}}x \tag{A.43}$$

$$\phi^L_i(\mathbf{r}_i) = \lim_{\mathbf{r}\to\mathbf{r}_i} \phi^L_i(\mathbf{r}) = \frac{q_i}{4\pi\varepsilon_0}\frac{1}{\sigma}\sqrt{\frac{2}{\pi}} \tag{A.44}$$

$$E^{self} = \frac{1}{4\pi\varepsilon_0}\frac{1}{\sqrt{2\pi\sigma^2}}\sum_{i=1}^{N} q_i^2 \tag{A.45}$$

A.1.5 Long-range potential in the reciprocal space

Because $\phi^L_i(\mathbf{r})$ is long-ranged, the long-range interaction E^L defined in eq. A.29 cannot be directly computed by a sum in real space. The basic idea of the Ewald sum is to transform it into a sum in the reciprocal space, given that this potential is no longer singular [242]. By not excluding the contribution from any ion, $\phi^L_i(\mathbf{r})$ is the potential field generated by a periodic array of ions. Because the total charge density field

$$\rho^L(\mathbf{r}) = \sum_{\mathbf{r}_C}\sum_{i=1}^{N} \rho^L_i(\mathbf{r}+\mathbf{r}_C) \tag{A.46}$$

is a periodic function, so is $\phi^L(\mathbf{r})$. Hence it makes sense to Fourier transform $\phi^L(\mathbf{r})$ to the reciprocal space. Let $\hat{\rho}^L(\mathbf{k})$ and $\hat{\phi}^L(\mathbf{k})$ be the Fourier transform of $\rho^L(\mathbf{r})$ and $\phi^L(\mathbf{r})$ respectively, i.e.,

$$\hat{\rho}^L(\mathbf{k}) = \int_V \rho^L(\mathbf{r})\, e^{-i\mathbf{k}\cdot\mathbf{r}} \mathrm{d}^3\mathbf{r} \tag{A.47}$$

$$\hat{\phi}^L(\mathbf{k}) = \int_V \phi^L(\mathbf{r})\, e^{-i\mathbf{k}\cdot\mathbf{r}} \mathrm{d}^3\mathbf{r} \tag{A.48}$$

where the integral is over the volume V of the supercell. The inverse Fourier transform is

$$\rho^L(\mathbf{r}) = \frac{1}{V}\sum_{\mathbf{k}} \hat{\rho}^L(\mathbf{k})\, e^{i\mathbf{k}\cdot\mathbf{r}} \tag{A.49}$$

$$\phi^L(\mathbf{r}) = \frac{1}{V}\sum_{\mathbf{k}} \hat{\phi}^L(\mathbf{k})\, e^{i\mathbf{k}\cdot\mathbf{r}} \tag{A.50}$$

The summation is over the reciprocal lattice of the real lattice defied by the base vectors $\mathbf{a}_1$, $\mathbf{a}_2$, $\mathbf{a}_3$. The potential field and the charge distribution are related to each other by the Poisson's equation

$$\nabla^2\phi^L(\mathbf{r}) = -\frac{\rho^L(\mathbf{r})}{\varepsilon_0} \tag{A.51}$$

which can be transformed into reciprocal space to give

$$k^2 \hat{\phi}^L(\mathbf{k}) = \frac{\hat{\rho}^L(\mathbf{k})}{\varepsilon_0} \tag{A.52}$$

where $k^2 = \mathbf{k} \cdot \mathbf{k}$. Hence our strategy of computing E^L is the following:

(1) first, we obtain $\hat{\phi}^L(\mathbf{k})$, as the Fourier transform of the charge density $\rho^L(\mathbf{r})$;

(2) dividing the result by $k^2\varepsilon_0$, we obtain $\hat{\phi}^L(\mathbf{k})$, the Fourier transform of the long range potential $\phi^L(\mathbf{r})$;

(3) the long-range potential in real space $\phi^L(\mathbf{r})$ is then obtained by inverse Fourier transform;

(4) $\phi^L(\mathbf{r})$ finally gives rise to E_L.

This passages are embodied by the following expressions

$$\rho^L(\mathbf{r}) = \sum_{\mathbf{r}_C} \sum_{j=1}^{N} q_j g_{\sigma^2 \boldsymbol{I}_3}(\mathbf{r} - \mathbf{r}_j + \mathbf{r}_C) \tag{A.53}$$

$$\hat{\rho}^L(\mathbf{k}) = \int_V \sum_{j=1}^{N} q_j g_{\sigma^2 \boldsymbol{I}_3}(\mathbf{r} - \mathbf{r}_j + \mathbf{r}_C)\, e^{-i\mathbf{k}\cdot\mathbf{r}}\, \mathrm{d}^3\mathbf{r} = \tag{A.54}$$

$$= \sum_{j=1}^{N} q_j \int_{\mathbb{R}^3} g_{\sigma^2 \boldsymbol{I}_3}(\mathbf{r} - \mathbf{r}_j)\, e^{-i\mathbf{k}\cdot\mathbf{r}}\, \mathrm{d}^3\mathbf{r} = \tag{A.55}$$

$$= \sum_{j=1}^{N} q_j e^{-i\mathbf{k}\cdot\mathbf{r}_j} e^{-\sigma^2 k^2/2} \tag{A.56}$$

In the above derivation, we have used the fact that $\mathbf{k}$ is a reciprocal vector and $\exp(-i\mathbf{k} \cdot \mathbf{r}_C) = 1$. Notice that

$$\hat{\rho}_j^L(\mathbf{k}) = q_j e^{-i\mathbf{k}\cdot\mathbf{r}_j} e^{-\sigma^2 k^2/2} \tag{A.57}$$

is the Fourier transform of $\rho_i^L(\mathbf{r})$ and

$$\hat{\rho}^L(\mathbf{k}) = \sum_{i=1}^{N} \hat{\rho}_i^L(\mathbf{k}) \tag{A.58}$$

The potential field in reciprocal space is

$$\hat{\phi}^L(\mathbf{k}) = \frac{1}{\varepsilon_0} \sum_{j=1}^{N} q_j e^{-i\mathbf{k}\cdot\mathbf{r}_j} \frac{e^{-\sigma^2 k^2/2}}{k^2} \tag{A.59}$$

Now applying inverse Fourier transform, we get

$$\phi_L(\mathbf{r}) = \frac{1}{V}\sum_{\mathbf{k}\neq\mathbf{0}} \hat{\phi}^L(\mathbf{k})\, e^{i\mathbf{k}\cdot\mathbf{r}} = \tag{A.60}$$

$$= \frac{1}{\varepsilon_0 V}\sum_{\mathbf{k}\neq\mathbf{0}}\sum_{j=1}^{N} q_j e^{i\mathbf{k}\cdot(\mathbf{r}-\mathbf{r}_j)}\frac{e^{-\sigma^2k^2/2}}{k^2} \tag{A.61}$$

The contribution to the $\mathbf{k}=\mathbf{0}$ term is zero if the super-cell is charge neutral, i.e. $\sum_i^N q_i = 0$. The long-range interaction energy is

$$E^L = \frac{1}{2}\sum_{i}^{N} q_i \phi_L(\mathbf{r}_i) = \tag{A.62}$$

$$= \frac{1}{2\varepsilon_0 V}\sum_{\mathbf{k}\neq\mathbf{0}}\sum_{i=1}^{N}\sum_{j=1}^{N} q_i q_j e^{i\mathbf{k}\cdot(\mathbf{r}_i-\mathbf{r}_j)}\frac{e^{-\sigma^2k^2/2}}{k^2} \tag{A.63}$$

For convenience, let us define the structure factor $S(\mathbf{k})$ of the charge distribution

$$S(\mathbf{k}) \coloneqq \sum_{i}^{N} q_i e^{i\mathbf{k}\cdot\mathbf{r}_i} \tag{A.64}$$

Then the long-range interaction energy can be simply expressed as

$$E^L = \frac{1}{2\varepsilon_0 V}\sum_{\mathbf{k}\neq\mathbf{0}} \frac{e^{-\sigma^2k^2/2}}{k^2}\,|S(\mathbf{k})|^2 \tag{A.65}$$

A.1.6 The final result

Combining Eqs. A.42, A.45, A.65, the total Coulomb interaction energy can be finally written as

$$\begin{aligned} E &= E^S + E^L - E^{self} = \\ &= \frac{1}{2}\frac{1}{4\pi\epsilon_0}\sum_{\mathbf{r}_C}\sum_{i=1}^{N}\sum_{j=1}^{N}{}' \frac{q_i q_j}{|\mathbf{r}_i-\mathbf{r}_j+\mathbf{r}_C|}\operatorname{erfc}\left(\frac{|\mathbf{r}_i-\mathbf{r}_j+\mathbf{r}_C|}{\sigma\sqrt{2}}\right) + \\ &\quad + \frac{1}{2\varepsilon_0 V}\sum_{\mathbf{k}\neq\mathbf{0}}\frac{e^{-\sigma^2k^2/2}}{k^2}\,|S(\mathbf{k})|^2 + \\ &\quad - \frac{1}{4\pi\varepsilon_0}\frac{1}{\sqrt{2\pi\sigma^2}}\sum_{i=1}^{N} q_i^2 \end{aligned} \tag{A.66}$$

The summation for $E^S_{[i]}$ is short-ranged in the real space (it is truncated by the erfc function) and the summation for E^L is short-ranged in the reciprocal space (it is truncated by the exponential term $e^{-\sigma^2k^2/2}$).

A.1.7 Implementation issues

In MD simulations, we need to compute not only the interaction energy E, but also the forces on the ions due to this interaction. The force on ion j is

$$\mathbf{f}_j = -\frac{\partial E}{\partial \mathbf{r}_j} = -\frac{\partial E^S}{\partial \mathbf{r}_j} - \frac{\partial E^L}{\partial \mathbf{r}_j} = \mathbf{f}_j^S + \mathbf{f}_j^L \tag{A.67}$$

The short-range force $\mathbf{f}_j^S$ is essentially the force due to the pair potential $\phi(r) \propto \operatorname{erf}\left(\frac{r}{\sigma\sqrt{2}}\right)$ and can be computed directly from a sum in real space. The long-range force $\mathbf{f}_j^L$ can be computed by evaluating the derivative of the structural factor

$$\frac{\partial S(\mathbf{k})}{\partial \mathbf{r}_j} = i\mathbf{k} q_j e^{i\mathbf{k}\cdot\mathbf{r}_j} \tag{A.68}$$

and then applying the chain rule

$$\mathbf{f}_j^L = \frac{1}{2\varepsilon_0 V} \sum_{\mathbf{k}\neq\mathbf{0}} \frac{e^{-\sigma^2 k^2/2}}{k^2} \left[S^*(\mathbf{k}) \frac{\partial S(\mathbf{k})}{\partial \mathbf{r}_j} + S(\mathbf{k}) \frac{\partial S^*(\mathbf{k})}{\partial \mathbf{r}_j} \right] \tag{A.69}$$

The method described above is called the Classical Ewald (CE) method [242, 243, 244], whose computational cost scales as $\mathcal{O}\left(N^{3/2}\right)$ (with optimal choice of σ for each N). The Particle Mesh Ewald (PME) method [245] is a more advanced method which scales as $\mathcal{O}(N \log(N))$. Hence PME is more efficient than CE in the limit of large N.

A.2 Alternative derivation of Ewald summation

Suppose we would like to compute the potential field generated by point charge q_i at $\mathbf{r}_i$ and its periodic images. The result is

$$\varphi_i(\mathbf{r}) = \frac{1}{4\pi\varepsilon_0} \sum_{\mathbf{r}_C} \frac{q_i}{|\mathbf{r} - \mathbf{r}_i + \mathbf{r}_C|} \tag{A.70}$$

This summation is actually divergent. But the divergent component is due to a constant term which keeps building up along the sum and this constant will disappear if we sum up the potential field of a collection of point charges whose total charge is zero, which we will assume will always be the case. Its Fourier transform is

$$\hat{\varphi}_i(\mathbf{k}) = \frac{q_i}{\varepsilon_0 k^2} e^{-i\mathbf{k}\cdot\mathbf{r}_i} \tag{A.71}$$

Notice that the $\mathbf{k} = \mathbf{0}$ term is ill-defined, which corresponds to the constant term in real-space potential $\varphi(\mathbf{r})$. If we want to obtain the total energy, we may sum over the $\mathbf{k}$ vector over the reciprocal space, but the summation over the reciprocal space is also conditionally convergent. To construct an absolutely convergent summation, we use the mathematical identity

$$\int_0^{+\infty} e^{-k^2 t}\, \mathrm{d}t = \frac{1}{k^2} \tag{A.72}$$

Hence

$$\hat{\varphi}_i(\mathbf{k}) = \frac{q_i}{\varepsilon_0} e^{-i\mathbf{k}\cdot\mathbf{r}_i} \int_0^{+\infty} e^{-k^2 t}\, \mathrm{d}t \tag{A.73}$$

Next we break the integral into two parts and assign them to the short- and long-range part of the potential field, as follows

$$\hat{\varphi}_i(\mathbf{k}) = \hat{\varphi}^S(\mathbf{k}) + \hat{\varphi}^L(\mathbf{k}) = \frac{q_i}{\varepsilon_0} e^{-i\mathbf{k}\cdot\mathbf{r}_i} \left[\int_0^{+\eta} e^{-k^2 t}\,\mathrm{d}t + \int_\eta^{+\infty} e^{-k^2 t}\,\mathrm{d}t \right] \tag{A.74}$$

$$\hat{\varphi}_i^S(\mathbf{k}) = \frac{q_i}{\varepsilon_0} e^{-i\mathbf{k}\cdot\mathbf{r}_i} \int_0^{+\eta} e^{-k^2 t}\,\mathrm{d}t \tag{A.75}$$

$$\hat{\varphi}_i^L(\mathbf{k}) = \frac{q_i}{\varepsilon_0} e^{-i\mathbf{k}\cdot\mathbf{r}_i} \int_\eta^{+\infty} e^{-k^2 t}\,\mathrm{d}t \tag{A.76}$$

The long-range potential can be integrated analytically to give

$$\hat{\varphi}_i^L(\mathbf{k}) = \frac{q_i}{\varepsilon_0 k^2} e^{-i\mathbf{k}\cdot\mathbf{r}_i} e^{-\eta k^2} \tag{A.77}$$

With $\eta = \sigma^2/2$, this expression is connected to the expression of E^L discussed in Section A.1.5 (eq. A.63). The next step is to convert $\hat{\varphi}^S(\mathbf{k})$ to the real space. We do so by inverse Fourier transform.

$$\varphi_i^S(\mathbf{r}) = \frac{1}{V} \sum_{\mathbf{k}} \hat{\phi}^S(\mathbf{k})\, e^{i\mathbf{k}\cdot\mathbf{r}} = \tag{A.78}$$

$$= \frac{1}{V\varepsilon_0} \sum_{\mathbf{k}} \int_0^{\eta} e^{i\mathbf{k}\cdot(\mathbf{r}-\mathbf{r}_i)} e^{-k^2 t}\,\mathrm{d}t = \tag{A.79}$$

$$= \frac{1}{V\varepsilon_0} \int_0^{\eta} \sum_{\mathbf{k}} e^{i\mathbf{k}\cdot(\mathbf{r}-\mathbf{r}_i)} e^{-k^2 t}\,\mathrm{d}t \tag{A.80}$$

Notice that, in the last step, the summation is simply the inverse Fourier transform of a Gaussian distribution, identifying t with $\sigma^2/2$. Hence

$$\varphi_i^S(\mathbf{r}) = \frac{1}{\varepsilon_0} \sum_{\mathbf{r}_C} \int_0^{\eta} \frac{e^{-|\mathbf{r}-\mathbf{r}_i+\mathbf{r}_C|^2/4t}}{\sqrt{(4\pi t)^3}}\,\mathrm{d}t = \tag{A.81}$$

$$= \frac{1}{4\pi\epsilon_0} \sum_{\mathbf{r}_C} \frac{q_i}{|\mathbf{r}-\mathbf{r}_i+\mathbf{r}_C|} \operatorname{erfc}\left(\frac{|\mathbf{r}-\mathbf{r}_i+\mathbf{r}_C|}{2\sqrt{\eta}} \right) = \tag{A.82}$$

$$= \frac{1}{4\pi\epsilon_0} \sum_{\mathbf{r}_C} \frac{q_i}{|\mathbf{r}-\mathbf{r}_i+\mathbf{r}_C|} \operatorname{erfc}\left(\frac{|\mathbf{r}-\mathbf{r}_i+\mathbf{r}_C|}{\sigma\sqrt{2}} \right) \tag{A.83}$$

This expression is connected to the expression of E^S discussed in Section A.1.4 (eq. A.42). The one developed in this section is a "standard" derivation of Ewald summation in many papers and books. It makes use of the "magical" split of $1/k^2$ into two integrals, given in eq. A.76. This approach may be mathematically appealing to some readers but may look like "black-magic" to others who are looking for more physical intuition.

Appendix B

Mathematical tools

B.1 Taylor series (single-variable scalar function)

Using the following notation for higher-order derivatives

$$\overbrace{f''\cdots'}^{n \text{ times}}(a) = f^{(n)}(a) = \left.\frac{\mathrm{d}^n f(x)}{\mathrm{d}x^n}\right|_{x=a} \quad \text{with } f^{(0)}(a) = f(a) \tag{B.1}$$

the Taylor series[1] of a function $f(x)$ at the point $x = a$ is the infinite sum defined as

$$f(x) = \sum_{n=0}^{+\infty} \frac{1}{n!} f^{(n)}(a)\,(x-a)^n = \tag{B.2}$$

$$= f(a) + f'(a)\,(x-a) + \frac{1}{2} f''(a)\,(x-a)^2 + \ldots \tag{B.3}$$

Notice how the Taylor series itself is a function of x. For most common functions, the Taylor series converges and its sum is equal to the original function.

The partial sum obtained by keeping the first n terms of a Taylor series is a polynomial of degree n, called the n-th Taylor polynomial of the function. Taylor polynomials are approximations of the starting function, which become increasingly more accurate with n: truncating the series at n, introduces an error of order $\mathcal{O}\Big((x-a)^{n+1}\Big)$. Therefore, the approximation is valid only near the expansion point.

Renaming the variables in the following way, $a \longrightarrow x$ and $x \longrightarrow a$, one gets:

$$f(a) = \sum_{n=0}^{+\infty} \frac{1}{n!} f^{(n)}(x)\,(a-x)^n \tag{B.4}$$

Then, noting that a can be always expressed with respect of x as $a = x + \delta x$ (δx can be positive or negative), the previous equation becomes:

$$f(x+\delta x) = \sum_{n=0}^{+\infty} \frac{1}{n!} f^{(n)}(x)\,\delta x^n = \tag{B.5}$$

$$= f(x) + f'(x)\,\delta x + \frac{1}{2} f''(x)\,\delta x^2 + \ldots \tag{B.6}$$

[1] if $x = 0$, the Taylor series is also called Maclaurin series.

The one above is the so-called incremental form of the Taylor series expansion. It is fully equivalent to eq. B.2, yet it gives it a different twist which proves to be more effective, putting greater emphasis on the distance δx between the evaluation and the expansion point.

B.2 Taylor series (multivariable scalar function)

The Taylor series can also be defined for a scalar function of n variables $f(\boldsymbol{x})$, where $\boldsymbol{x} = (x_1, x_2, \ldots, x_n)$ is a n-tuple representing a point in $\mathbb{R}^n$. It is worth recalling that a point in $\mathbb{R}^n$ can be equivalently identified with the bound vector whose terminal point is the given one and initial point is the origin: the latter point x can be legitimately confused with the column vector $\boldsymbol{x} = [x_1, x_2, \ldots, x_n]^T$. Using the above notation for the gradient and its higher-order analogues

$$\nabla f(\boldsymbol{x}) = \frac{\partial}{\partial \boldsymbol{x}} f(\boldsymbol{x}) = \left[\frac{\partial f(\boldsymbol{x})}{\partial x_1}, \frac{\partial f(\boldsymbol{x})}{\partial x_2}, \ldots, \frac{\partial f(\boldsymbol{x})}{\partial x_N} \right]^T \tag{B.7}$$

$$\nabla^{(n)} = \underbrace{\nabla \otimes \nabla \otimes \ldots \otimes \nabla}_{n \text{ times}} = \underbrace{\frac{\partial}{\partial \boldsymbol{x}} \otimes \frac{\partial}{\partial \boldsymbol{x}} \otimes \ldots \otimes \frac{\partial}{\partial \boldsymbol{x}}}_{n \text{ times}} \tag{B.8}$$

and defyining a vector of increments as

$$\delta \boldsymbol{x} = [\delta x_1, \delta x_2, \ldots, \delta x_N]^T \tag{B.9}$$

the incremental form of the Taylor series of $f(\boldsymbol{x})$ is

$$f(\boldsymbol{x} + \delta \boldsymbol{x}) = \sum_{n=0}^{+\infty} \frac{1}{n!} \nabla^{(n)} f(\boldsymbol{x}) : \left(\underbrace{\delta \boldsymbol{x} \otimes \delta \boldsymbol{x} \otimes \ldots \otimes \delta \boldsymbol{x}}_{n \text{ times}} \right) = \tag{B.10}$$

$$= f(\boldsymbol{x}) + f'(\boldsymbol{x}) \cdot \delta \boldsymbol{x} + \frac{1}{2} f''(\boldsymbol{x}) : (\delta \boldsymbol{x} \otimes \delta \boldsymbol{x}) + \ldots = \tag{B.11}$$

$$= f(\boldsymbol{x}) + \sum_{i=1}^{n} \frac{\partial f(\boldsymbol{x})}{\partial x_i} \delta x_i + \sum_{i=1}^{n} \sum_{j=1}^{n} \frac{\partial f(\boldsymbol{x})}{\partial x_i \partial x_j} \delta x_i \delta x_j + \ldots \tag{B.12}$$

where "$\cdot$" is the scalar product between two vectors of $\mathbb{R}^n$, while ":" represents the complete contraction between two equal-rank tensors. Also, the components of the displacement tensor $\delta \boldsymbol{x} \otimes \delta \boldsymbol{x} \otimes \ldots \otimes \delta \boldsymbol{x}$ are simply

$$\left[\underbrace{\delta \boldsymbol{x} \otimes \delta \boldsymbol{x} \otimes \ldots \otimes \delta \boldsymbol{x}}_{i \text{ times}} \right]_{\alpha_1 \alpha_2 \ldots \alpha_i} = \delta x_{\alpha_1} \delta x_{\alpha_2} \ldots \delta x_{\alpha_i} \qquad \text{with} \quad 1 \leq \alpha_1, \alpha_2, \ldots, \alpha_i \leq n \tag{B.13}$$

Renaming the gradient as follows

$$\boldsymbol{g} = \boldsymbol{g}_f(\boldsymbol{x}) = \nabla f(\boldsymbol{x}) = \frac{\partial}{\partial \boldsymbol{x}} f(\boldsymbol{x}) \tag{B.14}$$

and introducing the Hessian matrix[2]

$$\boldsymbol{H} = \boldsymbol{H}_f(\boldsymbol{x}) = \nabla \boldsymbol{g}(\boldsymbol{x}) = \frac{\partial}{\partial \boldsymbol{x}} \boldsymbol{g}(\boldsymbol{x}) = \nabla \otimes \nabla f(\boldsymbol{x}) = \frac{\partial}{\partial \boldsymbol{x}} \otimes \frac{\partial}{\partial \boldsymbol{x}} f(\boldsymbol{x}) = \tag{B.15}$$

$$= \begin{bmatrix} \dfrac{\partial^2 f(\boldsymbol{x})}{\partial x_1^2} & \dfrac{\partial^2 f(\boldsymbol{x})}{\partial x_1 \partial x_2} & \cdots & \dfrac{\partial^2 f(\boldsymbol{x})}{\partial x_1 \partial x_N} \\ \dfrac{\partial^2 f(\boldsymbol{x})}{\partial x_2 \partial x_1} & \dfrac{\partial^2 f(\boldsymbol{x})}{\partial x_2^2} & \cdots & \dfrac{\partial^2 f(\boldsymbol{x})}{\partial x_2 \partial x_N} \\ \vdots & \vdots & \ddots & \vdots \\ \dfrac{\partial^2 f(\boldsymbol{x})}{\partial x_N \partial x_1} & \dfrac{\partial^2 f(\boldsymbol{x})}{\partial x_N \partial x_2} & \cdots & \dfrac{\partial^2 f(\boldsymbol{x})}{\partial x_N^2} \end{bmatrix} \tag{B.16}$$

the Taylor series can also be expressed as

$$f(\boldsymbol{x} + \delta \boldsymbol{x}) = f(\boldsymbol{x}) + \boldsymbol{g}^T \cdot \delta \boldsymbol{x} + \frac{1}{2} \delta \boldsymbol{x}^T \cdot \boldsymbol{H} \cdot \delta \boldsymbol{x} + \ldots \tag{B.17}$$

B.3 The Gaussian integral

The Gaussian integral, named after the German mathematician Carl Friedrich Gauss, is

$$\int_{-\infty}^{+\infty} e^{-x^2}\, dx = \sqrt{\pi} \tag{B.18}$$

The most widely known proof of this, due to Simeon Denis Poisson and popularized by Jacob Karl Franz Sturm, consists in expressing the square of the Gaussian integral as a double integral and then using polar coordinates, as follows:

$$\left(\int_{-\infty}^{+\infty} e^{-x^2}\, dx \right)^2 = \left(\int_{-\infty}^{+\infty} e^{-x^2}\, dx \right) \left(\int_{-\infty}^{+\infty} e^{-y^2}\, dy \right) = \tag{B.19}$$

$$= \int_{-\infty}^{+\infty} dx \int_{-\infty}^{+\infty} dy\, e^{-\left(x^2+y^2\right)} \tag{B.20}$$

Here we apply the transformation to polar coordinates

$$x = x(r, \theta) = r \cos \theta \tag{B.21}$$

$$y = y(r, \theta) = r \sin \theta \tag{B.22}$$

The Jacobian associated to the above coordinate transformation is

$$\boldsymbol{J}(r, \theta) = \frac{\partial (x, y)}{\partial (r, \theta)} = \begin{bmatrix} \dfrac{\partial x}{\partial r} & \dfrac{\partial x}{\partial \theta} \\ \dfrac{\partial y}{\partial r} & \dfrac{\partial y}{\partial \theta} \end{bmatrix} = \begin{bmatrix} \cos \theta & -r \sin \theta \\ \sin \theta & r \cos \theta \end{bmatrix} \tag{B.23}$$

[2] here the denominator-layout notation is used (cfr. "Matrix calculus" on Wikipedia)

and its determinant is simply equal to

$$\det \boldsymbol{J}(r,\theta) = r\cos^2\theta + r\sin^2\theta = r \tag{B.24}$$

Going back to eq. B.20, we are now able to find

$$\left(\int_{-\infty}^{+\infty} e^{-x^2}\,dx\right)^2 = \int_{-\infty}^{+\infty} dx \int_{-\infty}^{+\infty} dy\; e^{-\left(x^2+y^2\right)} = \tag{B.25}$$

$$= \int_0^{+\infty} dr \int_0^{2\pi} d\theta\;\; |\det \boldsymbol{J}(r,\theta)|\, e^{-r^2} = \tag{B.26}$$

$$= \int_0^{+\infty} dr \int_0^{2\pi} d\theta\; re^{-r^2} = \tag{B.27}$$

$$= 2\pi \int_0^{+\infty} re^{-r^2}\,dr = \tag{B.28}$$

$$= \pi \int_0^{+\infty} e^{-r^2}\,d\Big(r^2\Big) = \pi \tag{B.29}$$

Equating the first and last terms in the previous chain of derivations and extracting the square root on both sides, gives exactly eq. B.18. Just a quick note: the improper integrals were just assumed to be well-behaved, as they actually are, and so no comment was made about their convergence. It is a thorny topic, which would require too much sidetracking to be properly treated here and also that is best to leave to a mathematician to handle.[3]
Two immediate extensions of the Gaussian integral are:

$$\int_{-\infty}^{+\infty} e^{-a(x+b)^2}\,dx = \frac{1}{\sqrt{a}} \int_{-\infty}^{+\infty} e^{-a(x+b)^2}\,d\big(\sqrt{a}\,(x+b)\big) = \sqrt{\frac{\pi}{a}} \tag{B.30}$$

$$\int_{-\infty}^{+\infty} e^{-ax^2+bx+c}\,dx = \int_{-\infty}^{+\infty} \exp\left\{\left[-a\left(x-\frac{b}{2a}\right)^2 + \frac{b^2}{4a} + c\right]\right\} dx = \sqrt{\frac{\pi}{a}} \exp\left\{\left(\frac{b^2}{4a}+c\right)\right\} \tag{B.31}$$

B.4 The n-dimensional Gaussian integral

The Gaussian integral can be generalized even further, extending it to higher dimensions. Using the following notation for the volume element of $\mathbb{R}^n$ in Cartesian coordinates

$$d\boldsymbol{x} = d^n x = dx_1 dx_2 \ldots dx_n \tag{B.32}$$

the n-dimensional Gaussian integral (with a linear term[4]) is defined as

[3] just as a reference, the essential tools one wants to refer to when dealing with the convergence of improper integrals are: Cauchy's principal value, Lebesgue's dominated convergence theorem and the squeeze theorem.

[4] we prove directly the harder case in order to spare space and time, since the simpler one (and its proof as well) can be immediately deducted from it.

$$\int_{\mathbb{R}^n} \exp\left\{\left(-\frac{1}{2}\boldsymbol{x}^T\boldsymbol{A}\boldsymbol{x}+\boldsymbol{b}^T\boldsymbol{x}\right)\right\} d\boldsymbol{x} = \int_{\mathbb{R}^n} \exp\left\{\left(-\frac{1}{2}\sum_{i,j=1}^{n} A_{ij}x_ix_j+\sum_{k=1}^{n} b_kx_k\right)\right\} d^nx \tag{B.33}$$

where $\boldsymbol{A}$ is a $n \times n$ positive-definite (hence invertible) real symmetric matrix, while $\boldsymbol{x}$ and $\boldsymbol{b}$ are n-dimensional vectors.[5] A real symmetric square matrix has all real entries and is equal to its transpose; that is, $\boldsymbol{A}$ satisfies

$$\boldsymbol{A} = \boldsymbol{A}^T \tag{B.34}$$

Notice how, with these definitions, the exponent in eq. B.33 is a scalar, except it now contains n independent variables x_i for $i = 1, \ldots, n$ rather than just one that has been considered so far. Before proceeding forward, I recall here the formulas for the transpose and the inverse of the product of two generic $n \times n$ matrices $\boldsymbol{A}$ and $\boldsymbol{B}$:

$$(\boldsymbol{AB})^T = \boldsymbol{B}^T\boldsymbol{A}^T \tag{B.35}$$

$$(\boldsymbol{AB})^{-1} = \boldsymbol{B}^{-1}\boldsymbol{A}^{-1} \tag{B.36}$$

In order to solve B.33, we have to appeal to the spectral theorem for real self-adjoint (i.e. real symmetric) matrices, such is $\boldsymbol{A}$. The theorem states that any real symmetric matrix always possess a full set of real eigenvalues and so can be decomposed in the following form

$$\boldsymbol{A} = \boldsymbol{O}^{-1}\boldsymbol{D}\boldsymbol{O} = \boldsymbol{O}^T\boldsymbol{D}\boldsymbol{O} \tag{B.37}$$

where D is a diagonal matrix whose diagonal elements are the eigenvalues of A, and O is an orthogonal matrix, that is a matrix such that

$$\boldsymbol{O}^{-1} = \boldsymbol{O}^T\,. \tag{B.38}$$

The linear transformation associated to an orthogonal matrix preserves the inner product between vectors, i.e. lengths. In fact, since the squared length of a n-dimensional vector $\boldsymbol{v}$, written with respect to an orthonormal basis, is $\boldsymbol{v}^T\boldsymbol{v}$, the following holds

$$\boldsymbol{v}^T\boldsymbol{v} = (\boldsymbol{O}\boldsymbol{v})^T(\boldsymbol{O}\boldsymbol{v}) = \boldsymbol{v}^T\boldsymbol{Q}^T\boldsymbol{Q}\boldsymbol{v} \tag{B.39}$$

Therefore, an orthogonal matrix acts as an isometry, and more specifically a (pure or) proper rotation, a pure reflection or a combination of the two, called an improper rotation. As futher confirmation of this, the determinant of any orthogonal matrix is either $+1$ or -1 (the reverse is not true)

$$1 = \det\{\boldsymbol{I}\} = \det\left\{\left(\boldsymbol{O}^T\boldsymbol{O}\right)\right\} = \left(\det\left\{\boldsymbol{O}^T\right\}\right)(\det\{\boldsymbol{O}\}) = (\det\{\boldsymbol{O}\})^2\,, \tag{B.40}$$

with $\boldsymbol{I}$ being the identity matrix. The $+1$ corresponds to proper rotations, while -1 to pure reflections or, in general, improper rotations. The minus sign comes from the fact that improper rotations reverse (flip) the orientation.

[5] unless otherwise stated, bold upper-case letters indicate matrices, whilst bold lower-case letters indicate vectors.

Having laid the necessary groundwork, we are now equipped accordingly to tackle the n-dimensional Gaussian integral. First, we will simplify it through the following change of variables

$$\boldsymbol{y} = \boldsymbol{O}\boldsymbol{x}\,, \tag{B.41}$$

(so $\boldsymbol{y}^T = \boldsymbol{x}^T\boldsymbol{O}^T$), with the inverse transformation given by

$$\boldsymbol{x} = \boldsymbol{O}^{-1}\boldsymbol{y} = \boldsymbol{O}^T\boldsymbol{y}\,. \tag{B.42}$$

The associated Jacobian is just

$$\boldsymbol{J}(y_1, y_2, \dots y_n) = \frac{\partial(x_1, x_2, \dots x_n)}{\partial(y_1, y_2, \dots y_n)} = \boldsymbol{O}^T\,, \tag{B.43}$$

hence we already now its determinant

$$\det \boldsymbol{J}(y_1, y_2, \dots y_n) = \det \boldsymbol{O}^T = \pm 1\,. \tag{B.44}$$

The ambiguity of the sign is linked to the fact that the orientation of the integration domain gets inverted for improper rotations. However, apart from the sign, the value of the integral remains the same. Except for specific and more abstract contexts, one usually does not care about orientation, and that is precisely the reason why only the absolute value of the Jacobian is taken into consideration when changing variables. Having clarified that, we evidently have

$$d\boldsymbol{x} = |\det \boldsymbol{J}(y_1, y_2, \dots y_n)|\, d\boldsymbol{y} = d\boldsymbol{y}\,. \tag{B.45}$$

The above substitution, along with eq. B.37, will reshape the exponent of B.33 into

$$-\frac{1}{2}\boldsymbol{x}^T\boldsymbol{A}\boldsymbol{x} + \boldsymbol{b}^T\boldsymbol{x} = -\frac{1}{2}\boldsymbol{x}^T\left(\boldsymbol{O}^T\boldsymbol{D}\boldsymbol{O}\right)\boldsymbol{x} + \boldsymbol{b}^T\boldsymbol{x} = \tag{B.46}$$

$$= -\frac{1}{2}\left(\boldsymbol{x}^T\boldsymbol{O}^T\right)\boldsymbol{D}(\boldsymbol{O}\boldsymbol{x}) + \boldsymbol{b}^T\boldsymbol{x} = \tag{B.47}$$

$$= -\frac{1}{2}\boldsymbol{y}^T\boldsymbol{D}\boldsymbol{y} + \boldsymbol{b}^T\boldsymbol{O}^T\boldsymbol{y} = \tag{B.48}$$

$$= -\frac{1}{2}\boldsymbol{y}^T\boldsymbol{D}\boldsymbol{y} + (\boldsymbol{O}\boldsymbol{b})^T\,\boldsymbol{y} \tag{B.49}$$

Plugging this back into eq. B.33, one gets

$$\int_{\mathbb{R}^n} \exp\left\{\left(-\frac{1}{2}\boldsymbol{x}^T\boldsymbol{A}\boldsymbol{x} + \boldsymbol{b}^T\boldsymbol{x}\right)\right\} d\boldsymbol{x} = \int_{\mathbb{R}^n} \exp\left\{\left(-\frac{1}{2}\boldsymbol{y}^T\boldsymbol{D}\boldsymbol{y} + (\boldsymbol{O}\boldsymbol{b})^T\,\boldsymbol{y}\right)\right\} d\boldsymbol{y} = \tag{B.50}$$

$$= \int_{\mathbb{R}^n} \exp\left\{\left(-\frac{1}{2}\sum_{i=1}^{n} D_{ii}y_i^2 + \sum_{k=1}^{n}(Ob)_k\, y_k\right)\right\} d^n y = \tag{B.51}$$

$$= \int_{\mathbb{R}^n} \exp\left\{\left(\sum_{i=1}^{n}\left[-\frac{1}{2}D_{ii}y_i^2 + (Ob)_i\, y_i\right]\right)\right\} d^n y = \tag{B.52}$$

$$= \prod_{i=1}^{n}\left[\int_{-\infty}^{+\infty} \exp\left\{\left(-\frac{1}{2}D_{ii}y_i^2 + (Ob)_i\, y_i\right)\right\} dy_i\right] = \tag{B.53}$$

$$= \left(\prod_{i=1}^{n}\sqrt{\frac{2\pi}{D_{ii}}}\right)\exp\left\{\left(\sum_{i=1}^{n}\frac{(Ob)_i^2}{2D_{ii}}\right)\right\} \tag{B.54}$$

That is, the n-dimensional Gaussian integral has decoupled into a product of n independent one-dimensional ones, each of the form B.31. The last term cab be further massaged into a more appealing form. First, taking the determinant of eq. B.37, one (re)discovers that

$$\det \boldsymbol{A} = \det \boldsymbol{D} = \prod_{i=1}^{n} D_{ii} \,. \tag{B.55}$$

Then, from eq. B.36 and B.37, one can write

$$\boldsymbol{A}^{-1} = \boldsymbol{O}^{-1}\boldsymbol{D}^{-1}\boldsymbol{O} = \boldsymbol{O}^{T}\boldsymbol{D}^{-1}\boldsymbol{O} \,, \tag{B.56}$$

and since the inverse of a diagonal matrix is another diagonal matrix whose diagonal elements are the reciprocacals of the original ones

$$\left(\boldsymbol{D}^{-1}\right)_{ii} = \frac{1}{D_{ii}} \,, \tag{B.57}$$

one can do the following manipulation

$$\sum_{i=1}^{n} \frac{(Ob)_i^2}{2D_{ii}} = \frac{1}{2}\left(\boldsymbol{O}\boldsymbol{b}\right)^{T} \boldsymbol{D}^{-1} \left(\boldsymbol{O}\boldsymbol{b}\right) = \tag{B.58}$$

$$= \frac{1}{2}\boldsymbol{b}^{T}\boldsymbol{O}^{T}\boldsymbol{D}^{-1}\boldsymbol{O}\boldsymbol{b} = \tag{B.59}$$

$$= \frac{1}{2}\boldsymbol{b}^{T}\left(\boldsymbol{O}^{T}\boldsymbol{D}^{-1}\boldsymbol{O}\right)\boldsymbol{b} = \tag{B.60}$$

$$= \frac{1}{2}\boldsymbol{b}^{T}\boldsymbol{A}^{-1}\boldsymbol{b} \tag{B.61}$$

Finally, the n-dimensional Gaussian integral with a linear term is equal to

$$\int_{\mathbb{R}^n} \exp\left\{\left(-\frac{1}{2}\boldsymbol{x}^{T}\boldsymbol{A}\boldsymbol{x} + \boldsymbol{b}^{T}\boldsymbol{x}\right)\right\} d\boldsymbol{x} = \sqrt{\frac{(2\pi)^n}{\det \boldsymbol{A}}} \exp\left\{\left(\frac{1}{2}\boldsymbol{b}^{T}\boldsymbol{A}^{-1}\boldsymbol{b}\right)\right\} \tag{B.62}$$

The plain n-dimensional Gaussian integral is readily recovered by setting $\boldsymbol{b} = 0$

$$\int_{\mathbb{R}^n} \exp\left\{\left(-\frac{1}{2}\boldsymbol{x}^{T}\boldsymbol{A}\boldsymbol{x}\right)\right\} d\boldsymbol{x} = \sqrt{\frac{(2\pi)^n}{\det \boldsymbol{A}}} \,. \tag{B.63}$$

B.5 The Gaussian function

The Gaussian function, or simply gaussian, also named after Carl Friedrich Gauss, will be defined in the context of this thesis as follows

$$g_\sigma(x) = g(x;\sigma) \coloneqq \frac{1}{\sqrt{2\pi\sigma^2}} \exp\left(-\frac{x^2}{2\sigma^2}\right) \tag{B.64}$$

Different definitions, involving alternative choices of parameters and/or numerical coefficients, are utterly equivalent; they generally arise depending on the convention used, the scientific area or even, as in this case, local convenience.

The above definition corresponds, according to probability theory, to a gaussian distribution[6] with zero mean ($\mu = 0$) and variance σ^2 (or, equivalently, standard deviation σ). In order to change the mean μ, one just has to translate the function

$$g_\sigma(x-\mu) = g(x-\mu;\sigma)\,\frac{1}{\sqrt{2\pi\sigma^2}}\exp\left[-\frac{(x-\mu)^2}{2\sigma^2}\right] \tag{B.65}$$

Note how the mean μ is *not* a parameter of the gaussian, only the variance is. The reason behind this choice will be clear in the section about the Dirac delta function.

For later convenience, I will evaluate here the following integral involving the gaussian

$$\int_{-\infty}^{+\infty}(x-y)^k\,g_\sigma(x-y)\,dx, \tag{B.66}$$

where k is a positive integer. Such integrals correspond to the (plain) moments of integer order k of a normally distributed (mean y and variance σ^2) random variable.

If k is odd, i.e. $k = 2n+1$ with $n = 1, 2, 3, \ldots$, by the symmetry around the vertical axis, eq. B.66 identically vanish

$$\int_{-\infty}^{+\infty}(x-y)^{2n+1}\,g_\sigma(x-y)\,dx = 0, \quad n = 1, 2, \ldots\,. \tag{B.67}$$

If k is even, things get a little bit trickier. Let us consider the special case $k = 2$ first: using integration by parts, one gets

$$\int_{-\infty}^{+\infty}(x-y)^2\,g_\sigma(x-y)\,dx = \tag{B.68}$$

$$= \int_{-\infty}^{+\infty} -\sigma^2\,(x-y)\,\frac{d}{dx}\big[g_\sigma(x-y)\big]dx = \tag{B.69}$$

$$= \sigma^2\int_{-\infty}^{+\infty}\left\{\frac{d}{dx}\big[-(x-y)\,g_\sigma(x-y)\big] + g_\sigma(x-y)\right\}dx = \tag{B.70}$$

$$= \sigma^2\int_{-\infty}^{+\infty} g_\sigma(x-y)\,dx = \sigma^2. \tag{B.71}$$

Such approach can be extended, with a little care, to the general case, i.e. $k = 2n$ with $n = 1, 2, 3, \ldots$, as follows

$$\int_{-\infty}^{+\infty}(x-y)^{2n}\,g_\sigma(x-y)\,dx = \tag{B.72}$$

$$= \sigma^2\int_{-\infty}^{+\infty}\left\{\frac{d}{dx}\Big[-(x-y)^{2n-1}\,g_\sigma(x-y)\Big] + (2n-1)\,(x-y)^{2n-2}\,g_\sigma(x-y)\right\}dx = \tag{B.73}$$

$$= \sigma^2\,(2n-1)\int_{-\infty}^{+\infty}(x-y)^{2n-2}\,g_\sigma(x-y)\,dx\,. \tag{B.74}$$

[6] normalization follows easily from eq. B.30

At this point, the strategy should be clear: one just has to integrate by parts for n times consecutively, in order to annihilate the $(x-y)^{2n}$ factor multiplying the gaussian

$$\int_{-\infty}^{+\infty} (x-y)^{2n}\, g_\sigma(x-y)\, dx = \tag{B.75}$$

$$= \sigma^2 (2n-1) \int_{-\infty}^{+\infty} (x-y)^{2n-2}\, g_\sigma(x-y)\, dx = \tag{B.76}$$

$$= \sigma^4 (2n-1)(2n-3) \int_{-\infty}^{+\infty} (x-y)^{2n-4}\, g_\sigma(x-y)\, dx = \tag{B.77}$$

$$= \sigma^6 (2n-1)(2n-3)(2n-5) \int_{-\infty}^{+\infty} (x-y)^{2n-6}\, g_\sigma(x-y)\, dx = \tag{B.78}$$

$$\vdots$$

$$= \sigma^{2n} (2n-1)!! \; . \tag{B.79}$$

So, to summarize

$$\int_{-\infty}^{+\infty} (x-y)^k\, g_\sigma(x-y)\, dx = \begin{cases} 0 & \text{if } k \text{ is odd,} \\ \sigma^k (k-1)!! & \text{if } k \text{ is even.} \end{cases} \tag{B.80}$$

B.6 The Fourier transform of a Gaussian function

Eq. B.31 allows to easily evaluate the Fourier transform of a Gaussian function, as follows

$$\int_{-\infty}^{+\infty} g_\sigma(x)\, e^{-ikx}\, dx = \frac{1}{\sqrt{2\pi\sigma^2}} \int_{-\infty}^{+\infty} \exp\left[-\frac{x^2}{2\sigma^2}\right] e^{-ikx}\, dx = \tag{B.81}$$

$$= \frac{1}{\sqrt{2\pi\sigma^2}} \int_{-\infty}^{+\infty} \exp\left[-\frac{x^2}{2\sigma^2} - ikx\right] dx = \tag{B.82}$$

$$= \frac{1}{\sqrt{2\pi\sigma^2}} \sqrt{2\pi\sigma^2} e^{-\sigma^2 k^2/2} = e^{-\sigma^2 k^2/2} \tag{B.83}$$

The general case ($\mu \neq 0$) can be recovered from this result using the translation property of the Fourier transform.

B.7 The n-dimensional Gaussian function

Just for the sake of completeness, I will define here the n-dimensional Gaussian function using the same conventions employed in Sec. B.5. The generalization to n dimensions of B.64 is

$$g_{\boldsymbol{\Sigma}}(\boldsymbol{x}) = g(\boldsymbol{x}; \boldsymbol{\Sigma}) = \frac{1}{\sqrt{(2\pi)^n \det \boldsymbol{\Sigma}}} \exp\left(-\frac{1}{2} \boldsymbol{x}^T \boldsymbol{\Sigma}^{-1} \boldsymbol{x}\right) , \tag{B.84}$$

where now $\boldsymbol{x}$ is a n-dimensional vector and $\boldsymbol{\Sigma}$ is a $n \times n$ positive-definite (hence invertible) real symmetric matrix, called the covariance matrix. The equation above reduces to the one-dimensional one if $\boldsymbol{\Sigma}$ is a 1×1 matrix, i.e. a single real number.

Again, this definition corresponds, according to probability theory, to a multivariate gaussian distribution[7] with zero mean ($\boldsymbol{\mu} = \mathbf{0}$) and covariance matrix $\boldsymbol{\Sigma}$. Analogously to eq. B.65, the mean can be changed through a translation

$$g_{\boldsymbol{\Sigma}}(\boldsymbol{x} - \boldsymbol{y}) = \frac{1}{\sqrt{(2\pi)^n \det \boldsymbol{\Sigma}}} \exp\left[-\frac{1}{2} (\boldsymbol{x} - \boldsymbol{y})^T \boldsymbol{\Sigma}^{-1} (\boldsymbol{x} - \boldsymbol{y})\right] . \tag{B.85}$$

B.8 The Fourier transform of a n-dimensional Gaussian function

Analogously to what was done in Sec. B.6, using eq. B.62 one can easily evaluate the Fourier transform of a n-dimensional Gaussian function, as follows

$$\int_{\mathbb{R}^n} \exp\left\{\left(-\frac{1}{2}\boldsymbol{x}^T \boldsymbol{A} \boldsymbol{x}\right)\right\} e^{-i\boldsymbol{k}\cdot\boldsymbol{x}}\, d\boldsymbol{x} = \int_{\mathbb{R}^n} \exp\left\{\left(-\frac{1}{2}\boldsymbol{x}^T \boldsymbol{A} \boldsymbol{x} - i\boldsymbol{k}^T \boldsymbol{x}\right)\right\} d\boldsymbol{x} = \tag{B.86}$$

$$= \sqrt{\frac{(2\pi)^n}{\det \boldsymbol{A}}} \exp\left\{\left(-\frac{1}{2}\boldsymbol{k}^T \boldsymbol{A}^{-1} \boldsymbol{k}\right)\right\} \tag{B.87}$$

Again, the general case ($\boldsymbol{b} \neq \mathbf{0}$) can be recovered from this result using the translation property of the Fourier transform.

B.9 The Dirac delta function

The Dirac delta function $\delta(x)$ is a generalized function (or distribution) conceived by the physicist Paul Audrien Maurice Dirac in order to model ideal finite distributions of mass or charge, for example, concentrated in a single point in space. A regular function able to describe such hypothetical system does not exist. So, despite the name, the Dirac delta function is not a function. However, mathematically is still possible to formalize and validate the concept Dirac bore in mind. I will try to sketch the idea behind the Dirac delta, starting with considering the following integral

$$\lim_{\sigma \to 0} \int_{-\infty}^{+\infty} g_\sigma(x - y)\, f(x)\, dx \tag{B.88}$$

Using the (original) Taylor series (eq. B.2), $f(x)$ can expressed as

$$f(x) = \sum_{k=0}^{+\infty} \frac{1}{k!} f^{(k)}(y)\, (x - y)^k = \tag{B.89}$$

$$= f(y) + f'(y)\, (x - y) + \frac{1}{2} f''(y)\, (x - y)^2 + \dots . \tag{B.90}$$

Then, noting that eq. B.80 implies

[7] normalization follows from eq. B.63

$$\int_{-\infty}^{+\infty} (x-y)^k \, g_\sigma(x-y)\, dx = \begin{cases} 0 & \text{if } k \text{ is odd,} \\ \mathcal{O}\left(\sigma^k\right) & \text{if } k \text{ is even.} \end{cases} \tag{B.91}$$

the integral B.88 can be solved as follows

$$\lim_{\sigma\to 0} \int_{-\infty}^{+\infty} g_\sigma(x-y)\, f(x)\, dx = \lim_{\sigma\to 0} \int_{-\infty}^{+\infty} g_\sigma(x-y) \left[\sum_{k=0}^{+\infty} \frac{1}{k!}\, f^{(k)}(y)\, (x-y)^k\right] = \tag{B.92}$$

$$= \sum_{k=0}^{+\infty} \left[\frac{1}{k!}\, f^{(k)}(y) \left(\lim_{\sigma\to 0} \int_{-\infty}^{+\infty} (x-y)^k \, g_\sigma(x-y)\, dx\right)\right] = \tag{B.93}$$

$$= f(y) + \lim_{\sigma\to 0} \mathcal{O}\left(\sigma^2\right) = f(y) \tag{B.94}$$

The point was not solving the integral, but rather, taking the fist and last terms of the previous derivation, to show that

$$\lim_{\sigma\to 0} \int_{-\infty}^{+\infty} g_\sigma(x-y)\, f(x)\, dx = f(y)\ , \tag{B.95}$$

because, by analogy, the Dirac delta function is often defined as the function satisfying

$$\int_{-\infty}^{+\infty} \delta(x-y)\, f(x)\, dx = f(y)\ . \tag{B.96}$$

But the thing is: there is no true function for which the above property holds. Actually, it is even worse: no mathematical object can be rigorously defined to match the role of $\delta(x-y)$ in eq. B.96. As a result, eq. B.96 is not a standard (Riemann or Lebesgue) integral, but rather just a (very) convenient, and consequently ubiquitous, *abuse of notation*. The right way to consistently capture the notion of the Dirac delta function is through more sophisticated mathematical theories, such as measure theory or the theory of distributions, but at the price of more abstraction and less practicality.

The message I would like to pass here is that eq. B.96 seizes the spirit of the Dirac delta, but it should not be taken as a literal definition because is not mathematically true. On the other hand, eq. B.95 is. So, basically, we have proven that the weak limit of a linear functional based on a Gaussian, as its σ approaches to zero, behaves exactly as we would like the Dirac delta to. Weak limit means that the limit has to be taken after performing the integration, i.e. that the limit and integral operations can not be inverted; hence the convergence is on the functional, not on the function. Sure, it is not great, we wish we had a stronger condition, but it is still better than nothing. Essentially, what all this tells us is that we can use and write eq. B.96 for convenience, yet when we do, we must always keep in mind that what we actually mean is eq. B.95, i.e. that there is always an hidden limit lurking around outside the integral. Eq. B.95 actually holds for other functions too; a few notable examples are the Lorentzian function

$$l_\gamma(x) = \frac{1}{\pi} \frac{\gamma}{x^2 + \gamma^2}\ , \tag{B.97}$$

the sinc function

$$\mathrm{sinc}_n(x) = \frac{n}{\pi}\,\mathrm{sinc}(nx)\ , \tag{B.98}$$

the rectangular function

$$\mathrm{rect}_\Delta(x) = \begin{cases} 0 & \text{for } x < -\dfrac{1}{2\Delta}, \\ \Delta & \text{for } -\dfrac{1}{2\Delta} \le x \le \dfrac{1}{2\Delta}, \\ 0 & \text{for } x > \dfrac{1}{2\Delta}. \end{cases} \tag{B.99}$$

B.10 The Fourier transform of the Dirac delta function

For the sake of completeness, it is reported here the (trivial) Fourier transform of the Dirac delta function:

$$\int_{-\infty}^{+\infty} \delta(x)\, e^{-ikx} dx = 1\,. \tag{B.100}$$

B.11 The n-dimensional Dirac delta function

The concept of Dirac delta can be extended to n dimensions quite straightforwardly; in fact, following the same steps of the previous section, one can prove

$$\lim_{\sigma\to 0} \int_{\mathbb{R}^n} g_\sigma(\boldsymbol{x}-\boldsymbol{y})\, f(\boldsymbol{x})\, d\boldsymbol{x} = f(\boldsymbol{y}) \tag{B.101}$$

where $g_\sigma(\boldsymbol{x}-\boldsymbol{y})$ is defined as follows

$$g_\sigma(\boldsymbol{x}-\boldsymbol{y}) = \frac{1}{(2\pi\sigma^2)^{n/2}} \exp\left(-\frac{|\boldsymbol{x}-\boldsymbol{y}|^2}{2\sigma^2}\right) = \tag{B.102}$$

$$= \frac{1}{(2\pi\sigma^2)^{n/2}} \exp\left(-\frac{(x_1-y_1)^2 + (x_2-y_2)^2 + \ldots + (x_n-y_n)^2}{2\sigma^2}\right) = \tag{B.103}$$

$$= \prod_{i=1}^{n} \frac{1}{\sqrt{2\pi\sigma^2}} \exp\left(-\frac{(x_i-y_i)^2}{2\sigma^2}\right) = \tag{B.104}$$

$$= \prod_{i=1}^{n} g_\sigma(x_i-y_i)\ . \tag{B.105}$$

Basically $g_\sigma(\boldsymbol{x}-\boldsymbol{y})$ is the product of n independent Gaussians with different mean but the same variance σ^2. This allows to expand the multiple integral on the left-hand side of eq. B.101 into

$$\int_{\mathbb{R}^n} g_\sigma(\boldsymbol{x}-\boldsymbol{y})\, f(\boldsymbol{x})\, d\boldsymbol{x} = \tag{B.106}$$

$$= \int_{-\infty}^{+\infty} dx_1\, g_\sigma(x_1-y_1)\cdot \tag{B.107}$$

$$\int_{-\infty}^{+\infty} dx_2\, g_\sigma(x_2-y_2)\cdot \tag{B.108}$$

$$\dots \tag{B.109}$$

$$\int_{-\infty}^{+\infty} dx_n\, g_\sigma(x_n-y_n)\, f(x_1,x_2,\dots,x_n) \tag{B.110}$$

which suggests, sticking to the (abusive) notation of eq. B.96, to write

$$\delta(\boldsymbol{x}-\boldsymbol{y}) = \delta(x_1-y_1)\,\delta(x_2-y_2)\dots\delta(x_n-y_n)\ . \tag{B.111}$$

B.12 The Fourier transform of the n-dimensional Dirac delta function

Finally, just as already done for the one-dimensional case (and the single- and multi-dimensional Gaussian functions), we show here the Fourier transform of the n-dimensional Dirac delta function:

$$\int_{\mathbb{R}^n} \delta(\boldsymbol{x})\, e^{-i\boldsymbol{k}\cdot\boldsymbol{x}} d\boldsymbol{x} = 1 \tag{B.112}$$

Bibliography

[1] Y. Grosu, M. Mierzwa, V. A. Eroshenko, S. Pawlus, M. Chorażewski, J.-M. Nedelec, and J.-P. E. Grolier, "Mechanical, Thermal, and Electrical Energy Storage in a Single Working Body: Electrification and Thermal Effects upon Pressure-Induced Water Intrusion–Extrusion in Nanoporous Solids," *ACS Applied Materials & Interfaces*, vol. 9, pp. 7044 – 7049, Feb. 2017.

[2] Y. Zhu, J. Ciston, B. Zheng, X. Miao, C. Czarnik, Y. Pan, R. Sougrat, Z. Lai, C.-E. Hsiung, K. Yao, I. Pinnau, M. Pan, and Y. Han, "Unravelling surface and interfacial structures of a metal–organic framework by transmission electron microscopy," *Nature Materials*, vol. 16, no. 5, pp. 532–536, 2017.

[3] B. H. Tan, H. An, and C.-D. Ohl, "Stability, dynamics, and tolerance to undersaturation of surface nanobubbles," *Physical Review Letters*, vol. 122, no. 13, p. 134502, 2019.

[4] B. S. Clausen, J. Schiøtz, L. Gråbæk, C. V. Ovesen, K. W. Jacobsen, J. K. Nørskov, and H. Topsøe, "Wetting/ non-wetting phenomena during catalysis: Evidence from in situ on-line exafs studies of cu-based catalysts," *Topics in Catalysis*, vol. 1, no. 3, pp. 367–376, 1994.

[5] A. Giacomello, M. Chinappi, S. Meloni, and C. M. Casciola, "Geometry as a catalyst: how vapor cavities nucleate from defects," *Langmuir*, vol. 29, no. 48, pp. 14873–14884, 2013.

[6] J. Zhang, J. Chen, S. Peng, S. Peng, Z. Zhang, Y. Tong, P. W. Miller, and X.-P. Yan, "Emerging porous materials in confined spaces: from chromatographic applications to flow chemistry," *Chem. Soc. Rev.*, vol. 48, pp. 2566–2595, 2019.

[7] M. Amabili, A. Giacomello, S. Meloni, and C. M. Casciola, "Intrusion and extrusion of a liquid on nanostructured surfaces," *Journal of Physics: Condensed Matter*, vol. 29, p. 014003, nov 2016.

[8] Y. Grosu, A. Giacomello, S. Meloni, L. González-Fernández, M. Chorazewski, M. Geppert-Rybczynska, A. Faik, J.-M. Nedelec, and J.-P. Grolier, "Viscosity at the nanoscale: Confined liquid dynamics and thermal effects in self-recovering nanobumpers," *The Journal of Physical Chemistry C*, vol. 122, pp. 14248–14256, 07 2018.

[9] L. Zhou, X. Wang, H.-J. Shin, J. Wang, R. Tai, X. Zhang, H. Fang, W. Xiao, L. Wang, C. Wang, X. Gao, J. Hu, and L. Zhang, "Ultrahigh density of gas

molecules confined in surface nanobubbles in ambient water," *Journal of the American Chemical Society*, vol. 142, no. 12, pp. 5583–5593, 2020.

[10] C. C. Coussios and R. A. Roy, "Applications of acoustics and cavitation to noninvasive therapy and drug delivery," *Annu. Rev. Fluid Mech.*, vol. 40, pp. 395–420, 2008.

[11] K. Kooiman, S. Roovers, S. A. Langeveld, R. T. Kleven, H. Dewitte, M. A. O'Reilly, J.-M. Escoffre, A. Bouakaz, M. D. Verweij, K. Hynynen, I. Lentacker, E. Stride, and C. K. Holland, "Ultrasound-responsive cavitation nuclei for therapy and drug delivery," *Ultrasound in Medicine and Biology*, vol. 46, no. 6, pp. 1296–1325, 2020.

[12] J. Wischhusen and F. Padilla, "Ultrasound-targeted microbubble destruction (utmd) for localized drug delivery into tumor tissue," *IRBM*, vol. 40, no. 1, pp. 10–15, 2019.

[13] O. M. Yaghi, M. O'Keeffe, N. W. Ockwig, H. K. Chae, M. Eddaoudi, and J. Kim, "Reticular synthesis and the design of new materials," *Nature*, vol. 423, no. 6941, pp. 705–714, 2003.

[14] H. Wang, X. Dong, J. Lin, S. J. Teat, S. Jensen, J. Cure, E. V. Alexandrov, Q. Xia, K. Tan, Q. Wang, D. H. Olson, D. M. Proserpio, Y. J. Chabal, T. Thonhauser, J. Sun, Y. Han, and J. Li, "Topologically guided tuning of zr-mof pore structures for highly selective separation of c6 alkane isomers.," *Nat Commun*, vol. 9, p. 1745, May 2018.

[15] A. E. Baumann, D. A. Burns, B. Liu, and V. S. Thoi, "Metal-organic framework functionalization and design strategies for advanced electrochemical energy storage devices," *Communications Chemistry*, vol. 2, no. 1, p. 86, 2019.

[16] A. Lowe, N. Tsyrin, M. Chorążewski, P. Zajdel, M. Mierzwa, J. B. Leão, M. Bleuel, T. Feng, D. Luo, M. Li, D. Li, V. Stoudenets, S. Pawlus, A. Faik, and Y. Grosu, "Effect of flexibility and nanotriboelectrification on the dynamic reversibility of water intrusion into nanopores: Pressure-transmitting fluid with frequency-dependent dissipation capability," *ACS Applied Materials & Interfaces*, vol. 11, pp. 40842–40849, 10 2019.

[17] M. A. Abdelkareem, L. Xu, M. K. A. Ali, A. Elagouz, J. Mi, S. Guo, Y. Liu, and L. Zuo, "Vibration energy harvesting in automotive suspension system: A detailed review," *Applied Energy*, vol. 229, pp. 672–699, 2018.

[18] DRiV Inc. © 2022 | All Rights Reserved, "Shock absorbers explained."

[19] L. Guillemot, T. Biben, A. Galarneau, G. Vigier, and É. Charlaix, "Activated drying in hydrophobic nanopores and the line tension of water," *Proceedings of the National Academy of Sciences*, vol. 109, no. 48, pp. 19557–19562, 2012.

[20] M. Amabili, A. Giacomello, S. Meloni, and C. M. Casciola, "Unraveling the salvinia paradox: Design principles for submerged superhydrophobicity," *Advanced Materials Interfaces*, vol. 2, no. 14, p. 1500248, 2015.

[21] N. Lior, "Energy resources and use: The present situation and possible paths to the future," *Energy*, vol. 33, pp. 842–857, 06 2008.

[22] S. Smirnov, I. Vlassiouk, P. Takmakov, and F. Rios, "Water confinement in hydrophobic nanopores. pressure-induced wetting and drying," *ACS nano*, vol. 4, pp. 5069–75, 09 2010.

[23] F. Rouquerol, J. Rouquerol, K. Sing, P. Llewellyn, and G. Maurin, *Adsorption by Powders and Porous Solids (Second Edition)*. Oxford: Academic Press, second edition ed., 2014.

[24] J. H. Irving and J. G. Kirkwood, "The statistical mechanical theory of transport processes. iv. the equations of hydrodynamics," *The Journal of Chemical Physics*, vol. 18, no. 6, pp. 817–829, 1950.

[25] M. E. Tuckerman, *Statistical Mechanics: Theory and Molecular Simulations*. Oxford University Press, 2010.

[26] K. Huang, *Statistical Mechanics*. Wiley, 1987.

[27] M. P. Allen and D. J. Tildesley, *Computer Simulation of Liquids*. Clarendon Press New York, NY, USA, 1988.

[28] S. Desgranges, O. Lorton, L. Gui-Levy, P. Guillemin, Z. Celicanin, J.-N. Hyacinthe, R. Breguet, L. A. Crowe, C. D. Becker, M. Soulié, N. Taulier, C. Contino-Pépin, and R. Salomir, "Micron-sized pfob liquid core droplets stabilized with tailored-made perfluorinated surfactants as a new class of endovascular sono-sensitizers for focused ultrasound thermotherapy," *J. Mater. Chem. B*, vol. 7, pp. 927–939, 2019.

[29] J. A. Kopechek, E. Park, C.-S. Mei, N. J. McDannold, and T. M. Porter, "Accumulation of phase-shift nanoemulsions to enhance mr-guided ultrasound-mediated tumor ablation in vivo.," *J Healthc Eng*, vol. 4, no. 1, pp. 109–126, 2013.

[30] L. C. Moyer, K. F. Timbie, P. S. Sheeran, R. J. Price, G. W. Miller, and P. A. Dayton, "High-intensity focused ultrasound ablation enhancement in vivo via phase-shift nanodroplets compared to microbubbles.," *J Ther Ultrasound*, vol. 3, p. 7, 2015.

[31] O. Lorton, P. Guillemin, R. Holman, S. Desgranges, L. Gui, L. A. Crowe, S. Terraz, A. Nastasi, F. Lazeyras, C. Contino-Pépin, and R. Salomir, "Enhancement of hifu thermal therapy in perfused tissue models using micron-sized ftac-stabilized pfob-core endovascular sonosensitizers.," *Int J Hyperthermia*, vol. 37, no. 1, pp. 1116–1130, 2020.

[32] F. Payri, V. Bermúdez, R. Payri, and F. Salvador, "The influence of cavitation on the internal flow and the spray characteristics in diesel injection nozzles," *Fuel*, vol. 83, no. 4, pp. 419–431, 2004.

[33] J. Manin, K. Yasutomi, and L. M. Pickett, "Transient cavitation in transparent diesel injectors," 4 2018.

[34] A. Giacomello, S. Meloni, M. Chinappi, and C. M. Casciola, "Cassie–baxter and wenzel states on a nanostructured surface: Phase diagram, metastabilities, and transition mechanism by atomistic free energy calculations," *Langmuir*, vol. 28, pp. 10764–10772, 07 2012.

[35] M. Amabili, S. Meloni, A. Giacomello, and C. M. Casciola, "Activated wetting of nanostructured surfaces: Reaction coordinates, finite size effects, and simulation pitfalls," *The Journal of Physical Chemistry B*, vol. 122, pp. 200–212, 01 2018.

[36] M. Amabili, A. Giacomello, S. Meloni, and C. M. Casciola, "Collapse of superhydrophobicity on nanopillared surfaces," *Phys. Rev. Fluids*, vol. 2, p. 034202, Mar 2017.

[37] W. Janke, "Statistical analysis of simulations: Data correlations and error estimation," *Quantum Simulations of Complex Many-Body Systems: From Theory to Algorithms*, vol. 10, pp. 423–445, 2002.

[38] M. Tortora, S. Meloni, B. H. Tan, A. Giacomello, C.-D. Ohl, and C. M. Casciola, "The interplay among gas, liquid and solid interactions determines the stability of surface nanobubbles," *Nanoscale*, vol. 12, pp. 22698–22709, 2020.

[39] S. Grimme, "Accurate description of van der waals complexes by density functional theory including empirical corrections.," *J Comput Chem*, vol. 25, pp. 1463–1473, Sep 2004.

[40] S. Bonella, S. Meloni, and G. Ciccotti, "Theory and methods for rare events," *The European Physical Journal B*, vol. 85, no. 3, p. 97, 2012.

[41] Y. G. Bushuev, Y. Grosu, M. A. Chora Żewski, and S. Meloni, "Subnanometer topological tuning of the liquid intrusion/extrusion characteristics of hydrophobic micropores.," *Nano Lett*, vol. 22, pp. 2164–2169, Mar 2022.

[42] A. B. Cairns and A. L. Goodwin, "Negative linear compressibility," *Phys. Chem. Chem. Phys.*, vol. 17, pp. 20449–20465, 2015.

[43] R. Lakes and K. Wojciechowski, "Negative compressibility, negative poisson's ratio, and stability," *physica status solidi (b)*, vol. 245, pp. 545 – 551, 03 2008.

[44] R. Baughman, S. Stafstrom, C. Cui, and S. Dantas, "Materials with negative compressibilities in one or more dimensions.," *Science*, vol. 279, pp. 1522–1524, Mar 1998.

[45] R. Baughman, "Auxetic materials: Avoiding the shrink," *Nature*, vol. 425, p. 667, 11 2003.

[46] N. Fang, D. Xi, J. Xu, M. Ambati, W. Srituravanich, C. Sun, and X. Zhang, "Ultrasonic metamaterials with negative modulus.," *Nat Mater*, vol. 5, pp. 452–456, Jun 2006.

[47] J. Grima, R. Caruana-Gauci, K. Wojciechowski, and K. Evans, "Smart hexagonal truss systems exhibiting negative compressibility through constrained angle stretching," *Smart Materials and Structures*, vol. 22, p. 084015, 08 2013.

[48] R. Lakes, "Foam structures with a negative poisson's ratio," *Science*, vol. 235, no. 4792, pp. 1038–1040, 1987.

[49] A. Yeganeh-Haeri, D. J. Weidner, and J. B. Parise, "Elasticity of agr-cristobalite: A silicon dioxide with a negative poisson's ratio.," *Science*, vol. 257, pp. 650–652, Jul 1992.

[50] J. Dagdelen, J. Montoya, M. de Jong, and K. Persson, "Computational prediction of new auxetic materials," *Nature Communications*, vol. 8, no. 1, p. 323, 2017.

[51] N. Almora-Barrios, A. Gómez, A. R. Ruiz-Salvador, M. Mistry, and D. W. Lewis, "Understanding si/al distributions in al-rich zeolites: the role of water in determining the structure of goosecreekite," *Chem. Commun.*, pp. 531–532, 2001.

[52] E. F. Skelton, J. L. Feldman, C. Y. Liu, and I. L. Spain, "Study of the pressure-induced phase transition in paratellurite (teo_2)," *Phys. Rev. B*, vol. 13, pp. 2605–2613, Mar 1976.

[53] Y. Lee, T. Vogt, J. A. Hriljac, J. B. Parise, and G. Artioli, "Pressure-induced volume expansion of zeolites in the natrolite family," *Journal of the American Chemical Society*, vol. 124, pp. 5466–5475, 05 2002.

[54] K. J. Griffith, K. M. Wiaderek, G. Cibin, L. E. Marbella, and C. P. Grey, "Niobium tungsten oxides for high-rate lithium-ion energy storage," *Nature*, vol. 559, no. 7715, pp. 556–563, 2018.

[55] A. Mirgorodsky and M. Smirnov, "Mechanical modelling of structural phase transitions," *Ferroelectrics*, vol. 159, pp. 345–355, 1994.

[56] C. F.-X. and J. D. Evans, "Nanoscale metamaterials: Meta-mofs and framework materials with anomalous behaviour," *Coord. Chem. Rev.*, vol. 388, pp. 48–62, 2019.

[57] S. Moggach, T. Bennett, and A. Cheetham, "The effect of pressure on zif-8: Increasing pore size with pressure and the formation of a high-pressure phase," *Angewandte Chemie International Edition*, vol. 48, no. 38, pp. 7087–7089, 2009.

[58] P. Serra-Crespo, A. Dikhtiarenko, E. Stavitski, J. Juan-Alcañiz, F. Kapteijn, F.-X. Coudert, and J. Gascon, "Experimental evidence of negative linear compressibility in the mil-53 metal–organic framework family," *CrystEngComm*, vol. 17, pp. 276–280, 2015.

[59] Z. Chen, B. Xu, Q. Li, Y. Meng, Z. Quan, and B. Zou, "Selected negative linear compressibilities in the metal-organic framework of [cu(4,4'-bpy)2(h2o)2] · sif6," *Inorganic Chemistry*, vol. 59, pp. 1715–1722, 02 2020.

[60] Q. Zeng, K. Wang, and B. Zou, "Negative linear compressibility response to pressure in multitype wine-rack metal–organic frameworks," *ACS Materials Letters*, vol. 2, pp. 291–295, 04 2020.

[61] W. Cai, A. Gładysiak, M. Anioła, V. J. Smith, L. J. Barbour, and A. Katrusiak, "Giant negative area compressibility tunable in a soft porous framework material," *Journal of the American Chemical Society*, vol. 137, pp. 9296–9301, 07 2015.

[62] Y. Yan, A. E. O'Connor, G. Kanthasamy, G. Atkinson, D. R. Allan, A. J. Blake, and M. Schröder, "Unusual and tunable negative linear compressibility in the metal-organic framework mfm-133(m) (m = zr, hf).," *J Am Chem Soc*, vol. 140, pp. 3952–3958, Mar 2018.

[63] W. Cai and A. Katrusiak, "Giant negative linear compression positively coupled to massive thermal expansion in a metal–organic framework," *Nature Communications*, vol. 5, no. 1, p. 4337, 2014.

[64] A. B. Cairns, J. Catafesta, C. Levelut, J. Rouquette, A. van Der Lee, L. Peters, A. L. Thompson, V. Dmitriev, J. Haines, and A. L. Goodwin, "Giant negative linear compressibility in zinc dicyanoaurate," *Nature Materials*, vol. 12, pp. 212–216, Jan. 2013.

[65] Q. Zeng, K. Wang, and B. Zou, "Large negative linear compressibility in inh(bdc)2 from framework hinging," *Journal of the American Chemical Society*, vol. 139, pp. 15648–15651, 11 2017.

[66] A. L. Goodwin, D. A. Keen, and M. G. Tucker, "Large negative linear compressibility of ag₃[co(cn)₆]," *Proceedings of the National Academy of Sciences*, vol. 105, no. 48, pp. 18708–18713, 2008.

[67] L. Maragliano and E. Vanden-Eijnden, "A temperature accelerated method for sampling free energy and determining reaction pathways in rare events simulations," *Chemical Physics Letters*, vol. 426, no. 1, pp. 168–175, 2006.

[68] J. B. Abrams and M. E. Tuckerman, "Efficient and direct generation of multidimensional free energy surfaces via adiabatic dynamics without coordinate transformations.," *J Phys Chem B*, vol. 112, pp. 15742–15757, Dec 2008.

[69] B. Zheng, M. Sant, P. Demontis, and G. B. Suffritti, "Force field for molecular dynamics computations in flexible zif-8 framework," *The Journal of Physical Chemistry C*, vol. 116, pp. 933–938, 01 2012.

[70] G. Fraux, A. Boutin, A. H. Fuchs, and F.-X. Coudert, "Structure, dynamics, and thermodynamics of intruded electrolytes in zif-8," *The Journal of Physical Chemistry C*, vol. 123, pp. 15589–15598, 06 2019.

[71] J. Qu, A. Gerber, F. Mayer, M. Kadic, and M. Wegener, "Experiments on metamaterials with negative effective static compressibility," *Phys. Rev. X*, vol. 7, p. 041060, Dec 2017.

[72] C.-W. Tsai and E. H. Langner, "The effect of synthesis temperature on the particle size of nano-zif-8," *Microporous and Mesoporous Materials*, vol. 221, pp. 8–13, 2016.

[73] V. F. Rozsa and T. A. Strobel, "Triple guest occupancy and negative compressibility in hydrogen-loaded β-hydroquinone clathrate," *The Journal of Physical Chemistry Letters*, vol. 5, pp. 1880–1884, 06 2014.

[74] S. Krause, V. Bon, I. Senkovska, U. Stoeck, D. Wallacher, D. M. Többens, S. Zander, R. S. Pillai, G. Maurin, F.-X. Coudert, and S. Kaskel, "A pressure-amplifying framework material with negative gas adsorption transitions," *Nature*, vol. 532, no. 7599, pp. 348–352, 2016.

[75] R. Gatt and J. Grima, "Negative compressibility," *physica status solidi (RRL) - Rapid Research Letters*, vol. 2, pp. 236 – 238, 10 2008.

[76] J. Qu, M. Kadic, and M. Wegener, "Poroelastic metamaterials with negative effective static compressibility," *Applied Physics Letters*, vol. 110, no. 17, p. 171901, 2017.

[77] H. B. Callen, *Thermodynamics and an Introduction to physical theories of thermostatistics and irreversible thermodynamics*. John Wiley & Sons, 1960 (page 135).

[78] K. W. Wojciechowski, P. Pieranski, and J. MałeckiJerzy, "An instability in a hard disk system in a narrow box," *J. Phys. A*, vol. 16, pp. 2197–2203, 1983.

[79] N. Y. V. Y. Antonchenko, V. V. Ilyn, N. N. Makivsky, A. N. Pavlov, and V. P. Sokhan, "On the nature of disjoining pressure oscillations in fluid films," *Mol. Phys.*, vol. 52, pp. 345–355, 1984.

[80] S. R. Kline, "Reduction and analysis of SANS and USANS data using IGOR Pro," *Journal of Applied Crystallography*, vol. 39, pp. 895–900, Dec 2006.

[81] R. T. Azuah, L. R. Kneller, Y. Qiu, P. L. W. Tregenna-Piggott, C. M. Brown, J. R. D. Copley, and R. M. Dimeo, "Dave: A comprehensive software suite for the reduction, visualization, and analysis of low energy neutron spectroscopic data," *J. Res. Natl. Inst. Stand. Technol.*, vol. 114 (6), pp. 341–358, 2009.

[82] L. Joly, C. Ybert, E. Trizac, and L. Bocquet, "Hydrodynamics within the electric double layer on slipping surfaces," *Physical review letters*, vol. 93, no. 25, p. 257805, 2004.

[83] J. P. Perdew, K. Burke, and M. Ernzerhof, "Generalized gradient approximation made simple," *Phys. Rev. Lett.*, vol. 77, pp. 3865–3868, Oct 1996.

[84] S. Marchio, S. Meloni, A. Giacomello, C. Valeriani, and C. M. Casciola, "Pressure control in interfacial systems: Atomistic simulations of vapor nucleation," *The Journal of Chemical Physics*, vol. 148, no. 6, p. 064706, 2018.

[85] G. J. Martyna, D. J. Tobias, and M. L. Klein, "Constant pressure molecular dynamics algorithms," *The Journal of Chemical Physics*, vol. 101, no. 5, pp. 4177–4189, 1994.

[86] E. Lisi, M. Amabili, S. Meloni, A. Giacomello, and C. M. Casciola, "Self-recovery superhydrophobic surfaces: Modular design," *ACS Nano*, vol. 12, pp. 359–367, 01 2018.

[87] A. Giacomello, S. Meloni, M. Müller, and C. Casciola, "Mechanism of the Cassie-Wenzel transition via the atomistic and continuum string methods," *The Journal of Chemical Physics*, vol. 142, no. 10, p. 104701, 2015.

[88] G. Menzl, M. A. Gonzalez, P. Geiger, F. Caupin, J. L. F. Abascal, C. Valeriani, and C. Dellago, "Molecular mechanism for cavitation in water under tension," *Proceedings of the National Academy of Sciences*, vol. 113, no. 48, pp. 13582–13587, 2016.

[89] K. Kelton and A. L. Greer, *Nucleation in condensed matter: applications in materials and biology*, vol. 15. Elsevier, 2010.

[90] R. Zwanzig, *Nonequilibrium Statistical Mechanics*. Oxford University Press, 2001.

[91] D. Hlushkou and U. Tallarek, "Faster dewetting of water from c8- than from c18-bonded silica particles used in reversed-phase liquid chromatography solving the paradox," *Journal of Chromatography A*, vol. 1602, 05 2019.

[92] G. Camisasca, A. Tinti, and A. Giacomello, "Gas-induced drying of nanopores," *The Journal of Physical Chemistry Letters*, vol. 11, pp. 9171–9177, 11 2020.

[93] S. L. Meadley and F. A. Escobedo, "Thermodynamics and kinetics of bubble nucleation: Simulation methodology," *The Journal of Chemical Physics*, vol. 137, no. 7, p. 074109, 2012.

[94] V. Eroshenko, "Hydrocapillary battery," *943444*, 1980.

[95] V. Eroshenko, R.-C. Regis, M. Soulard, and J. Patarin, "Energetics: A new field of applications for hydrophobic zeolites," *Journal of the American Chemical Society*, vol. 123, pp. 8129–8130, 08 2001.

[96] Y. Qiao, V. K. Punyamurtula, A. Han, X. Kong, and F. B. Surani, "Temperature dependence of working pressure of a nanoporous liquid spring," *Applied Physics Letters*, vol. 89, no. 25, p. 251905, 2006.

[97] C. V. Suciu and K. Yaguchi, "Endurance tests on a colloidal damper destined to vehicle suspension," *Experimental Mechanics*, vol. 49, no. 3, p. 383, 2008.

[98] Y. Grosu, G. Renaudin, V. Eroshenko, J.-M. Nedelec, and J.-P. E. Grolier, "Synergetic effect of temperature and pressure on energetic and structural characteristics of ZIF-8 + water molecular spring," *Nanoscale*, vol. 7, pp. 8803–8810, 2015.

[99] E. V.A., "The unexpected properties of a complex thermodynamical system," *R. Acad. Sci. Ukr. SSR, Ser. A*, vol. 10, pp. 79–82, 1990.

[100] F. B. Surani, X. Kong, D. B. Panchal, and Y. Qiao, "Energy absorption of a nanoporous system subjected to dynamic loadings," *Applied Physics Letters*, vol. 87, no. 16, p. 163111, 2005.

[101] L. Tzanis, M. Trzpit, M. Soulard, and J. Patarin, "Energetic performances of channel and cage-type zeosils," *The Journal of Physical Chemistry C*, vol. 116, pp. 20389–20395, 09 2012.

[102] V. A. Eroshenko, I. Piatiletov, L. Coiffard, and V. Stoudenets, "A new paradigm of mechanical energy dissipation. part 2: Experimental investigation and effectiveness of a novel car damper," *Proceedings of the Institution of Mechanical Engineers, Part D: Journal of Automobile Engineering*, vol. 221, no. 3, pp. 301–312, 2007.

[103] L. Guillemot, *Systèmes Hétérogènes Lyophobes: Influence de la température et de la vitesse sur les cycles d'intrusion/extrusion forcées de liquides non mouillants dans des matériaux mésoporeux.* Theses, INSA de Lyon, Dec. 2010.

[104] L. Coiffard, V. A. Eroshenko, and J.-P. E. Grolier, "Thermomechanics of the variation of interfaces in heterogeneous lyophobic systems," *AIChE Journal*, vol. 51, no. 4, pp. 1246–1257, 2005.

[105] T. Karbowiak, M.-A. Saada, S. Rigolet, A. Ballandras, G. Weber, I. Bezverkhyy, M. Soulard, J. Patarin, and J.-P. Bellat, "New insights in the formation of silanol defects in silicalite-1 by water intrusion under high pressure," *Phys. Chem. Chem. Phys.*, vol. 12, pp. 11454–11466, 2010.

[106] M. Trzpit, S. Rigolet, J.-L. Paillaud, C. Marichal, M. Soulard, and J. Patarin, "Pure silica chabazite molecular spring: A structural study on water intrusion-extrusion processesextrusion processes," *The Journal of Physical Chemistry B*, vol. 112, pp. 7257–7266, 06 2008.

[107] Y. Grosu, V. Eroshenko, J. M. Nedelec, and J. P. E. Grolier, "A new working mode for molecular springs: water intrusion induced by cooling and associated isobaric heat capacity change of a ZIF-8 + water system," *Phys. Chem. Chem. Phys.*, vol. 17, pp. 1572–1574, 2015.

[108] Y. Grosu, M. Li, Y.-L. Peng, D. Luo, D. Li, A. Faik, J.-M. Nedelec, and J.-P. Grolier, "A highly stable nonhysteretic Cu2(tebpz) MOF+water molecular spring," *ChemPhysChem*, vol. 17, no. 21, pp. 3359–3364, 2016.

[109] A. Y. Fadeev and V. A. Eroshenko, "Study of penetration of water into hydrophobized porous silicas," *Journal of Colloid and Interface Science*, vol. 187, no. 2, pp. 275–282, 1997.

[110] B. Lefevre, A. Saugey, J. L. Barrat, L. Bocquet, E. Charlaix, P. F. Gobin, and G. Vigier, "Intrusion and extrusion of water in hydrophobic mesopores," *The Journal of Chemical Physics*, vol. 120, no. 10, pp. 4927–4938, 2004.

[111] L. Guillemot, A. Galarneau, G. Vigier, T. Abensur, and É. Charlaix, "New device to measure dynamic intrusion/extrusion cycles of lyophobic heterogeneous systems," *Review of Scientific Instruments*, vol. 83, no. 10, p. 105105, 2012.

[112] N. Gokulakrishnan, T. Karbowiak, J. P. Bellat, L. Vonna, M.-A. Saada, J. L. Paillaud, M. Soulard, J. Patarin, and J. Parmentier, "Improved hydrophobicity of inorganic–organic hybrid mesoporous silica with cage-like pores," *Colloids and Surfaces A: Physicochemical and Engineering Aspects*, vol. 421, pp. 34–43, 2013.

[113] N. Gokulakrishnan, J. Parmentier, M. Trzpit, L. Vonna, J. L. Paillaud, and M. Soulard, "Intrusion/extrusion of water into organic grafted sba-15 silica materials for energy storage.," *J Nanosci Nanotechnol*, vol. 13, pp. 2847–2852, Apr 2013.

[114] G. Ortiz, H. Nouali, C. Marichal, G. Chaplais, and J. Patarin, "Energetic performances of "zif-71–aqueous solution"systems: A perfect shock-absorber with water," *The Journal of Physical Chemistry C*, vol. 118, pp. 21316–21322, 09 2014.

[115] W. Li, S. Henke, and A. K. Cheetham, "Research update: Mechanical properties of metal-organic frameworks – influence of structure and chemical bonding," *APL Materials*, vol. 2, no. 12, p. 123902, 2014.

[116] N. C. Burtch, J. Heinen, T. D. Bennett, D. Dubbeldam, and M. D. Allendorf, "Mechanical properties in metal–organic frameworks: Emerging opportunities and challenges for device functionality and technological applications," *Advanced Materials*, vol. 30, no. 37, p. 1704124, 2018.

[117] Y. Sun, S. Rogge, A. Lamaire, S. Vandenbrande, J. Wieme, C. Siviour, V. Van Speybroeck, and J. C. Tan, "High-rate nanofluidic energy absorption in porous zeolitic frameworks," *Nat. Mater.*, pp. 1–9, 2021.

[118] G. Y. Zhou and L. Z. Sun, "Smart colloidal dampers with on-demand controllable damping capability," *Smart Materials and Structures*, vol. 17, p. 055023, sep 2008.

[119] A. Han, W. Lu, V. K. Punyamurtula, X. Chen, F. B. Surani, T. Kim, and Y. Qiao, "Effective viscosity of glycerin in a nanoporous silica gel," *Journal of Applied Physics*, vol. 104, no. 12, p. 124908, 2008.

[120] C. V. Suciu, "Ride-comfort of an automobile equipped with colloidal dampers at its frontal suspensions," in *Proceedings of ISMA 2010 - International Conference on Noise and Vibration Engineering, including USD 2010*, p. 4233, 2010.

[121] C. Suciu and S. Buma, *On the Structural Simplification, Compact and Light Design of a Vehicle Suspension, Achieved by Using a Colloidal Cylinder with a Dual Function of Absorber and Compression-Spring*, vol. 198, pp. 21–32. 01 2013.

[122] I. Khay, L. Tzanis, T. J. Daou, H. Nouali, A. Ryzhikov, and J. Patarin, "Energetic behavior of the pure silica itq-12 (itw) zeolite under high pressure water intrusion," *Phys. Chem. Chem. Phys.*, vol. 15, pp. 20320–20325, 2013.

[123] A. Han and Y. Qiao, "Infiltration pressure of a nanoporous liquid spring modified by an electrolyte," *Journal of Materials Research*, vol. 22, no. 3, pp. 644–648, 2007.

[124] A. Ryzhikov, I. Khay, H. Nouali, T. J. Daou, and J. Patarin, "Energetic performances of pure silica stf and mtt-type zeolites under high pressure water intrusion," *RSC Adv.*, vol. 4, pp. 37655–37661, 2014.

[125] I. Khay, T. J. Daou, H. Nouali, A. Ryzhikov, S. Rigolet, and J. Patarin, "High pressure intrusion–extrusion of licl aqueous solutions in silicalite-1 zeolite: Influence on energetic performances," *The Journal of Physical Chemistry C*, vol. 118, pp. 3935–3941, 02 2014.

[126] L. Tzanis, H. Nouali, T. J. Daou, M. Soulard, and J. Patarin, "Influence of the aqueous medium on the energetic performances of silicalite-1," *Materials Letters*, vol. 115, pp. 229–232, 2014.

[127] A. Ryzhikov, I. Khay, H. Nouali, T. Daou, and J. Patarin, "High pressure intrusion–extrusion of electrolyte solutions in aluminosilicate fau and *bea-type zeolites," *Microporous and Mesoporous Materials*, vol. 221, pp. 1–7, 2016.

[128] M. Amabili, Y. Grosu, A. Giacomello, S. Meloni, A. Zaki, F. Bonilla, A. Faik, and C. M. Casciola, "Pore morphology determines spontaneous liquid extrusion from nanopores," *ACS Nano*, vol. 13, pp. 1728–1738, 02 2019.

[129] B. M. Connolly, D. G. Madden, A. E. H. Wheatley, and D. Fairen-Jimenez, "Shaping the future of fuel: Monolithic metal–organic frameworks for high-density gas storage," *Journal of the American Chemical Society*, vol. 142, pp. 8541–8549, 05 2020.

[130] T. Tian, J. Velazquez-Garcia, T. D. Bennett, and D. Fairen-Jimenez, "Mechanically and chemically robust zif-8 monoliths with high volumetric adsorption capacity," *J. Mater. Chem. A*, vol. 3, pp. 2999–3005, 2015.

[131] M. Chorążewski, A. Grzybowski, and M. Paluch, "The complex, non-monotonic thermal response of the volumetric space of simple liquids," *Phys. Chem. Chem. Phys.*, vol. 16, pp. 19900–19908, 2014.

[132] M. Chorążewski, A. Grzybowski, and M. Paluch, "Isobaric thermal expansion of compressed 1,4-dichlorobutane and 1-bromo-4-chlorobutane: Transitiometric results and a novel application of the general density scaling-based equation of state," *Industrial & Engineering Chemistry Research*, vol. 54, pp. 6400–6407, 06 2015.

[133] V. A. Eroshenko and A. Y. Fadeev, "Intrusion and extrusion of water in hydrophobized porous silica," *Colloid journal of the Russian Academy of Sciences*, vol. 57, pp. 446–449, 1995.

[134] Y. Sun, Y. Li, and J.-C. Tan, "Framework flexibility of zif-8 under liquid intrusion: discovering time-dependent mechanical response and structural relaxation," *Phys. Chem. Chem. Phys.*, vol. 20, pp. 10108–10113, 2018.

[135] J. W. M. e. a. Osterrieth, "How reproducible are surface areas calculated from the bet equation?," 2021.

[136] A. K. Rajagopal and J. Callaway, "Inhomogeneous electron gas," *Phys. Rev. B*, vol. 7, pp. 1912–1919, Mar 1973.

[137] W. Kohn and L. J. Sham, "Self-consistent equations including exchange and correlation effects," *Phys. Rev.*, vol. 140, pp. A1133–A1138, Nov 1965.

[138] T. Thonhauser, S. Zuluaga, C. A. Arter, K. Berland, E. Schröder, and P. Hyldgaard, "Spin signature of nonlocal correlation binding in metal-organic frameworks," *Phys. Rev. Lett.*, vol. 115, p. 136402, Sep 2015.

[139] D. C. Langreth, B. I. Lundqvist, S. D. Chakarova-Käck, V. R. Cooper, M. Dion, P. Hyldgaard, A. Kelkkanen, J. Kleis, L. Kong, S. Li, P. G. Moses, E. Murray, A. Puzder, H. Rydberg, E. Schröder, and T. Thonhauser, "A density functional for sparse matter," *Journal of Physics: Condensed Matter*, vol. 21, p. 084203, jan 2009.

[140] A. M. Rappe, K. M. Rabe, E. Kaxiras, and J. D. Joannopoulos, "Optimized pseudopotentials," *Phys. Rev. B*, vol. 41, pp. 1227–1230, Jan 1990.

[141] W. E, W. Ren, and E. Vanden-Eijnden, "Simplified and improved string method for computing the minimum energy paths in barrier-crossing events," *The Journal of Chemical Physics*, vol. 126, no. 16, p. 164103, 2007.

[142] S. Meloni and G. Ciccotti, "Free energies for rare events: Temperature accelerated md and mc," *The European Physical Journal Special Topics*, vol. 224, no. 12, pp. 2389–2407, 2015.

[143] B. Zheng, M. Sant, P. Demontis, and G. B. Suffritti, "Correction to "force field for molecular dynamics computations in flexible zif-8 framework"," *The Journal of Physical Chemistry C*, vol. 117, pp. 24662–24662, 11 2013.

[144] M. W. Mahoney and W. L. Jorgensen, "A five-site model for liquid water and the reproduction of the density anomaly by rigid, nonpolarizable potential functions," *The Journal of Chemical Physics*, vol. 112, no. 20, pp. 8910–8922, 2000.

[145] K. S. Park, Z. Ni, A. P. Côté, J. Y. Choi, R. Huang, F. J. Uribe-Romo, H. K. Chae, M. O'Keeffe, and O. M. Yaghi, "Exceptional chemical and thermal stability of zeolitic imidazolate frameworks," *Proceedings of the National Academy of Sciences*, vol. 103, no. 27, pp. 10186–10191, 2006.

[146] X.-C. Huang, Y.-Y. Lin, J.-P. Zhang, and X.-M. Chen, "Ligand-directed strategy for zeolite-type metal–organic frameworks: Zinc(ii) imidazolates with unusual zeolitic topologies," *Angewandte Chemie International Edition*, vol. 45, no. 10, pp. 1557–1559, 2006.

[147] D. Fairen-Jimenez, S. A. Moggach, M. T. Wharmby, P. A. Wright, S. Parsons, and T. Düren, "Opening the gate: Framework flexibility in zif-8 explored by experiments and simulations," *Journal of the American Chemical Society*, vol. 133, pp. 8900–8902, 06 2011.

[148] I. Khay, G. Chaplais, H. Nouali, C. Marichal, and J. Patarin, "Water intrusion–extrusion experiments in zif-8: impacts of the shape and particle size on the energetic performances," *RSC Adv.*, vol. 5, pp. 31514–31518, 2015.

[149] M. Tortora, P. Zajdel, A. R. Lowe, M. Chorążewski, J. B. Leão, G. V. Jensen, M. Bleuel, A. Giacomello, C. M. Casciola, S. Meloni, and Y. Grosu, "Giant negative compressibility by liquid intrusion into superhydrophobic flexible nanoporous frameworks," *Nano Letters*, vol. 21, pp. 2848–2853, 04 2021.

[150] Y. Grosu, S. Gomes, G. Renaudin, J.-P. E. Grolier, V. Eroshenko, and J.-M. Nedelec, "Stability of zeolitic imidazolate frameworks: effect of forced water intrusion and framework flexibility dynamics," *RSC Adv.*, vol. 5, pp. 89498–89502, 2015.

[151] H. Gao, W. Wei, L. Dong, G. Feng, X. Jiang, R. Wu, Z. Lin, and W. Li, "Enhanced framework rigidity of a zeolitic metal-azolate via ligand substitution," *Crystals*, vol. 7, no. 4, 2017.

[152] B. Mortada, G. Chaplais, H. Nouali, C. Marichal, and J. Patarin, "Phase transformations of metal–organic frameworks maf-6 and zif-71 during intrusion–extrusion experiments," *The Journal of Physical Chemistry C*, vol. 123, pp. 4319–4328, 02 2019.

[153] A. Varshney, F. Brooks, and W. Wright, "Computing smooth molecular surfaces," *IEEE Computer Graphics and Applications*, vol. 14, no. 5, pp. 19–25, 1994.

[154] A. Giacomello, C. M. Casciola, Y. Grosu, and S. Meloni, "Liquid intrusion in and extrusion from non-wettable nanopores for technological applications," *The European Physical Journal B*, vol. 94, no. 8, p. 163, 2021.

[155] B. Peters, *Reaction rate theory and rare events*. Elsevier, 2017.

[156] L. A. CRUM, "Tensile strength of water," *Nature*, vol. 278, no. 5700, pp. 148–149, 1979.

[157] D. Lohse and X. Zhang, "Surface nanobubbles and nanodroplets," *Reviews of modern physics*, vol. 87, no. 3, p. 981, 2015.

[158] M. Alheshibri, J. Qian, M. Jehannin, and V. S. Craig, "A history of nanobubbles," *Langmuir*, vol. 32, no. 43, pp. 11086–11100, 2016.

[159] P. S. Epstein and M. S. Plesset, "On the stability of gas bubbles in liquid-gas solutions," *The Journal of Chemical Physics*, vol. 18, no. 11, pp. 1505–1509, 1950.

[160] D. Lohse and X. Zhang, "Pinning and gas oversaturation imply stable single surface nanobubbles," *Physical Review E*, vol. 91, no. 3, p. 031003, 2015.

[161] C. U. Chan, M. Arora, and C.-D. Ohl, "Coalescence, growth, and stability of surface-attached nanobubbles," *Langmuir*, vol. 31, no. 25, pp. 7041–7046, 2015.

[162] H. An, B. H. Tan, Q. Zeng, and C.-D. Ohl, "Stability of nanobubbles formed at the interface between cold water and hot highly oriented pyrolytic graphite," *Langmuir*, vol. 32, no. 43, pp. 11212–11220, 2016.

[163] X. H. Zhang, G. Li, N. Maeda, and J. Hu, "Removal of induced nanobubbles from water/graphite interfaces by partial degassing," *Langmuir*, vol. 22, no. 22, pp. 9238–9243, 2006.

[164] J. Qian, V. S. Craig, and M. Jehannin, "Long-term stability of surface nanobubbles in undersaturated aqueous solution," *Langmuir*, vol. 35, no. 3, pp. 718–728, 2018.

[165] X. Zhang, D. Y. Chan, D. Wang, and N. Maeda, "Stability of interfacial nanobubbles," *Langmuir*, vol. 29, no. 4, pp. 1017–1023, 2013.

[166] Y. Liu and X. Zhang, "A unified mechanism for the stability of surface nanobubbles: Contact line pinning and supersaturation," *The Journal of chemical physics*, vol. 141, no. 13, p. 134702, 2014.

[167] S. Maheshwari, M. van der Hoef, X. Zhang, and D. Lohse, "Stability of surface nanobubbles: A molecular dynamics study," *Langmuir*, vol. 32, pp. 11116–11122, 11 2016.

[168] J. H. Weijs, J. H. Snoeijer, and D. Lohse, "Formation of surface nanobubbles and the universality of their contact angles: a molecular dynamics approach," *Physical review letters*, vol. 108, no. 10, p. 104501, 2012.

[169] S. Meloni, A. Giacomello, and C. M. Casciola, "Focus article: Theoretical aspects of vapor/gas nucleation at structured surfaces," *The Journal of Chemical Physics*, vol. 145, no. 21, p. 211802, 2016.

[170] B. H. Tan, H. An, and C.-D. Ohl, "Surface nanobubbles are stabilized by hydrophobic attraction," *Physical review letters*, vol. 120, no. 16, p. 164502, 2018.

[171] W. Chun-Lei, L. Zhao-Xia, L. Jing-Yuan, X. Peng, H. Jun, and F. Hai-Ping, "High density gas state at water/graphite interface studied by molecular dynamics simulation," *Chinese Physics B*, vol. 17, no. 7, p. 2646, 2008.

[172] Q. Chen, H. S. Wiedenroth, S. R. German, and H. S. White, "Electrochemical nucleation of stable n2 nanobubbles at pt nanoelectrodes," *Journal of the American Chemical Society*, vol. 137, no. 37, pp. 12064–12069, 2015.

[173] S. R. German, M. A. Edwards, H. Ren, and H. S. White, "Critical nuclei size, rate, and activation energy of h2 gas nucleation," *Journal of the American Chemical Society*, vol. 140, no. 11, pp. 4047–4053, 2018.

[174] H. Ren, S. R. German, M. A. Edwards, Q. Chen, and H. S. White, "Electrochemical generation of individual o2 nanobubbles via h2o2 oxidation," *The journal of physical chemistry letters*, vol. 8, no. 11, pp. 2450–2454, 2017.

[175] C. U. Chan and C.-D. Ohl, "Total-internal-reflection-fluorescence microscopy for the study of nanobubble dynamics," *Physical review letters*, vol. 109, no. 17, p. 174501, 2012.

[176] H. An, G. Liu, R. Atkin, and V. S. J. Craig, "Surface nanobubbles in nonaqueous media: looking for nanobubbles in dmso, formamide, propylene carbonate, ethylammonium nitrate, and propylammonium nitrate," *ACS Nano*, vol. 9, no. 7, pp. 7596–7607, 2015.

[177] M. Sprik and G. Ciccotti, "Free energy from constrained molecular dynamics," *The Journal of chemical physics*, vol. 109, no. 18, pp. 7737–7744, 1998.

[178] E. Carter, G. Ciccotti, J. T. Hynes, and R. Kapral, "Constrained reaction coordinate dynamics for the simulation of rare events," *Chemical Physics Letters*, vol. 156, no. 5, pp. 472–477, 1989.

[179] J. R. Seddon and D. Lohse, "Nanobubbles and micropancakes: gaseous domains on immersed substrates," *Journal of physics: Condensed matter*, vol. 23, no. 13, p. 133001, 2011.

[180] L. Wang, X. Wang, L. Wang, J. Hu, C. L. Wang, B. Zhao, X. Zhang, R. Tai, M. He, L. Chen, *et al.*, "Formation of surface nanobubbles on nanostructured substrates," *Nanoscale*, vol. 9, no. 3, pp. 1078–1086, 2017.

[181] C. U. Chan, L. Chen, M. Arora, and C.-D. Ohl, "Collapse of surface nanobubbles," *Physical review letters*, vol. 114, no. 11, p. 114505, 2015.

[182] G. Stoltz, M. Rousset, *et al.*, *Free energy computations: A mathematical perspective*. World Scientific, 2010.

[183] D. D. L. Chung, "Review graphite," *Journal of Materials Science*, vol. 37, no. 8, pp. 1475–1489, 2002.

[184] J. L. Abascal and C. Vega, "A general purpose model for the condensed phases of water: Tip4p/2005," *The Journal of chemical physics*, vol. 123, no. 23, p. 234505, 2005.

[185] J. Walther, R. Jaffe, T. Halicioglu, and P. Koumoutsakos, "Molecular dynamics simulations of carbon nanotubes in water," in *Center for turbulence research: proceedings of the summer program*, no. 1987, pp. 5–20, 2000.

[186] T. Werder, J. H. Walther, R. Jaffe, T. Halicioglu, and P. Koumoutsakos, "On the water- carbon interaction for use in molecular dynamics simulations

of graphite and carbon nanotubes," *The Journal of Physical Chemistry B*, vol. 107, no. 6, pp. 1345–1352, 2003.

[187] J. Jiang and S. I. Sandler, "Separation of co2 and n2 by adsorption in c168 schwarzite: A combination of quantum mechanics and molecular simulation study," *Journal of the American Chemical Society*, vol. 127, pp. 11989–11997, 08 2005.

[188] J. D. Weeks, D. Chandler, and H. C. Andersen, "Role of repulsive forces in determining the equilibrium structure of simple liquids," *The Journal of chemical physics*, vol. 54, no. 12, pp. 5237–5247, 1971.

[189] S. Wang, L. Zhou, X. Wang, C. Wang, Y. Dong, Y. Zhang, Y. Gao, L. Zhang, and J. Hu, "Force spectroscopy revealed a high-gas-density state near the graphite substrate inside surface nanobubbles," *Langmuir*, vol. 35, no. 7, pp. 2498–2505, 2019.

[190] N. Hain, D. Wesner, S. I. Druzhinin, and H. Schönherr, "Surface nanobubbles studied by time-resolved fluorescence microscopy methods combined with afm: The impact of surface treatment on nanobubble nucleation," *Langmuir*, vol. 32, no. 43, pp. 11155–11163, 2016.

[191] D. Seo, S. R. German, T. L. Mega, and W. A. Ducker, "Phase state of interfacial nanobubbles," *The Journal of Physical Chemistry C*, vol. 119, no. 25, pp. 14262–14266, 2015.

[192] A. I. Aria, P. R. Kidambi, R. S. Weatherup, L. Xiao, J. A. Williams, and S. Hofmann, "Time evolution of the wettability of supported graphene under ambient air exposure," *The Journal of Physical Chemistry C*, vol. 120, no. 4, pp. 2215–2224, 2016.

[193] A. Murmur, "Thermodynamics aspects of contact angle hysteresis," *Advances in Colloid and Interface Science*, vol. 50, pp. 121–141, 1994.

[194] A. Giacomello, L. Schimmele, and S. Dietrich, "Wetting hysteresis induced by nanodefects," *Proceedings of the National Academy of Sciences*, vol. 113, no. 3, pp. E262–E271, 2016.

[195] S. Marchio, S. Meloni, A. Giacomello, and C. M. Casciola, "Wetting and recovery of nano-patterned surfaces beyond the classical picture," *Nanoscale*, vol. 11, no. 44, pp. 21458–21470, 2019.

[196] M. Maccarini, R. Steitz, M. Himmelhaus, J. Fick, S. Tatur, M. Wolff, M. Grunze, J. Janecek, and R. Netz, "Density depletion at solid- liquid interfaces: a neutron reflectivity study," *Langmuir*, vol. 23, no. 2, pp. 598–608, 2007.

[197] E. Wilhelm and R. Battino, "Estimation of lennard-jones (6, 12) pair potential parameters from gas solubility data," *The Journal of Chemical Physics*, vol. 55, no. 8, pp. 4012–4017, 1971.

[198] "N_2 interaction with water." We remark that in the water case nitrogen (and oxygen) atoms interacted only with the oxygen atom of water *via* a LJ interaction. Here, we maintain the same interaction, hence the same affinity between the gas and the liquid.

[199] R. Battino, T. R. Rettich, and T. Tominaga, "The solubility of nitrogen and air in liquids," *Journal of Physical and Chemical Reference Data*, vol. 13, no. 2, pp. 563–600, 1984.

[200] A. Kohl and R. Nielsen, "Physical solvents for acid gas removal," *Gas purification. Houston: Gulf Professional Publishing*, pp. 1188–1234, 1997.

[201] V. Baranenko, V. Sysoev, L. Fal'kovskii, V. Kirov, A. Piontkovskii, and A. Musienko, "The solubility of nitrogen in water," *Soviet Atomic Energy*, vol. 68, no. 2, pp. 162–165, 1990.

[202] Y. O. . Popov, "Evaporative deposition patterns: Spatial dimensions of the deposit," *Phys. Rev. E*, vol. 71, p. 036313, 2005.

[203] H. Reiss, "Scaled particle methods in the statistical thermodynamics of fluids," *Advances in Chemical Physics*, pp. 1–84, 1965.

[204] E. N. Harvey, W. D. McElroy, and A. H. Whiteley, "On cavity formation in water," *Journal of Applied Physics*, vol. 18, no. 2, pp. 162–172, 1947.

[205] A. A. Atchley and A. Prosperetti, "The crevice model of bubble nucleation," *The Journal of the Acoustical Society of America*, vol. 86, no. 3, pp. 1065–1084, 1989.

[206] H. B. Marschall, K. A. Mørch, A. P. Keller, and M. Kjeldsen, "Cavitation inception by almost spherical solid particles in water," *Physics of Fluids*, vol. 15, no. 2, pp. 545–553, 2003.

[207] B. M. Borkent, S. Gekle, A. Prosperetti, and D. Lohse, "Nucleation threshold and deactivation mechanisms of nanoscopic cavitation nuclei," *Physics of Fluids*, vol. 21, no. 10, p. 102003, 2009.

[208] S. ichi Tsuda, S. Takagi, and Y. Matsumoto, "A study on the growth of cavitation bubble nuclei using large-scale molecular dynamics simulations," *Fluid Dynamics Research*, vol. 40, no. 7, pp. 606–615, 2008. Selected articles from the 1st International Colloquium on Dynamics, Physics and Chemistry of Bubbles and Gas-Liquid Boundaries.

[209] H. Watanabe, H. Inaoka, and N. Ito, "Ripening kinetics of bubbles: A molecular dynamics study," *The Journal of Chemical Physics*, vol. 145, no. 12, p. 124707, 2016.

[210] J. W. Holl, "Nuclei and Cavitation," *Journal of Basic Engineering*, vol. 92, pp. 681–688, 12 1970.

[211] Q. Zheng, D. J. Durben, G. H. Wolf, and C. A. Angell, "Liquids at large negative pressures: Water at the homogeneous nucleation limit," *Science*, vol. 254, no. 5033, pp. 829–832, 1991.

[212] M. E. M. Azouzi, C. Ramboz, J.-F. Lenain, and F. Caupin, "A coherent picture of water at extreme negative pressure," *Nature Physics*, vol. 9, no. 1, pp. 38–41, 2013.

[213] P. G. DEBENEDETTI, *Metastable Liquids: Concepts and Principles*, vol. 1. Princeton University Press, 1996.

[214] F. Caupin and E. Herbert, "Cavitation in water: a review," *Comptes Rendus Physique*, vol. 7, no. 9, pp. 1000–1017, 2006. Nucleation.

[215] Z. Gao, W. Wu, and B. Wang, "The effects of nanoscale nuclei on cavitation," *Journal of Fluid Mechanics*, vol. 911, p. A20, 2021.

[216] J. M. Rosselló and C.-D. Ohl, "On-demand bulk nanobubble generation through pulsed laser illumination," *Phys. Rev. Lett.*, vol. 127, p. 044502, Jul 2021.

[217] J. G. Riess, "Understanding the fundamentals of perfluorocarbons and perfluorocarbon emulsions relevant to in vivo oxygen delivery.," *Artif Cells Blood Substit Immobil Biotechnol*, vol. 33, no. 1, pp. 47–63, 2005.

[218] O. Lorton, J.-N. Hyacinthe, S. Desgranges, L. Gui, A. Klauser, Z. Celicanin, L. A. Crowe, F. Lazeyras, E. Allémann, N. Taulier, C. Contino-Pépin, and R. Salomir, "Molecular oxygen loading in candidate theranostic droplets stabilized with biocompatible fluorinated surfactants: Particle size effect and application to in situ(19)f mri mapping of oxygen partial pressure.," *J Magn Reson*, vol. 295, pp. 27–37, Oct 2018.

[219] R. Holman, O. Lorton, P. C. Guillemin, S. Desgranges, C. Contino-Pépin, and R. Salomir, "Perfluorocarbon emulsion contrast agents: A mini review," *Frontiers in Chemistry*, vol. 9, 2022.

[220] P. Pfeiffer, J. Eisener, H. Reese, M. Li, X. Ma, C. Sun, and C.-D. Ohl, "Thermally assisted heterogeneous cavitation through gas supersaturation," *Phys. Rev. Lett.*, vol. 128, p. 194501, May 2022.

[221] M. Mezger, H. Reichert, S. Schöder, J. Okasinski, H. Schröder, H. Dosch, D. Palms, J. Ralston, and V. Honkimäki, "High-resolution in situ x-ray study of the hydrophobic gap at the water–octadecyltrichlorosilane interface," *Proceedings of the National Academy of Sciences*, vol. 103, no. 49, pp. 18401–18404, 2006.

[222] S. D. Lubetkin, "Why is it much easier to nucleate gas bubbles than theory predicts?," *Langmuir*, vol. 19, pp. 2575–2587, 04 2003.

[223] J. W. Cahn and J. E. Hilliard, "Free energy of a nonuniform system. iii. nucleation in a two-component incompressible fluid," *The Journal of Chemical Physics*, vol. 31, no. 3, pp. 688–699, 1959.

[224] Y. Zhou, B. Li, Y. Gu, and M. Chen, "A molecular dynamics simulation study on the cavitation inception of water with dissolved gases," *Molecular Physics*, vol. 117, no. 14, pp. 1894–1902, 2019.

[225] N. Kuritz, M. Murat, M. Balaish, Y. Ein-Eli, and A. Natan, "Pfc and triglyme for li–air batteries: A molecular dynamics study," *The Journal of Physical Chemistry B*, vol. 120, pp. 3370–3377, 04 2016.

[226] A. Schürmann, R. Haas, M. Murat, N. Kuritz, M. Balaish, Y. Ein-Eli, J. Janek, A. Natan, and D. Schröder, "Diffusivity and solubility of oxygen in solvents for metal/oxygen batteries: A combined theoretical and experimental study," *Journal of The Electrochemical Society*, vol. 165, no. 13, pp. A3095–A3099, 2018.

[227] L. Huang, K. Zhou, J. Zhang, Y. Ma, W. Yang, L. Ran, C. Jin, D. D. Dimitrov, and H. Zhu, "Efficacy and safety of high-intensity focused ultrasound ablation for hepatocellular carcinoma by changing the acoustic environment: microbubble contrast agent (sonovue) and transcatheter arterial chemoembolization.," *Int J Hyperthermia*, vol. 36, no. 1, pp. 244–252, 2019.

[228] J. Rapet, P. A. Quinto-Su, and C.-D. Ohl, "Cavitation inception from transverse waves in a thin liquid gap," *Phys. Rev. Applied*, vol. 14, p. 024041, Aug 2020.

[229] L. Martínez, R. Andrade, E. G. Birgin, and J. M. Martínez, "Packmol: A package for building initial configurations for molecular dynamics simulations," *Journal of Computational Chemistry*, vol. 30, no. 13, pp. 2157–2164, 2009.

[230] M. F. Costa Gomes, J. Deschamps, and A. A. Pádua, "Effect of bromine substitution on the solubility of gases in hydrocarbons and fluorocarbons," *Fluid Phase Equilibria*, vol. 251, no. 2, pp. 128–136, 2007.

[231] G. J. Martyna, M. L. Klein, and M. Tuckerman, "Nosé–hoover chains: The canonical ensemble via continuous dynamics," *The Journal of Chemical Physics*, vol. 97, no. 4, pp. 2635–2643, 1992.

[232] J. L. F. Abascal and C. Vega, "A general purpose model for the condensed phases of water: Tip4p/2005," *The Journal of Chemical Physics*, vol. 123, no. 23, p. 234505, 2005.

[233] H. A. Kramers, "Brownian motion in a field of force and the diffusion model of chemical reactions," *Physica*, vol. 7, no. 4, pp. 284–304, 1940.

[234] K. Schulten, Z. Schulten, and A. Szabo, "Dynamics of reactions involving diffusive barrier crossing," *The Journal of Chemical Physics*, vol. 74, no. 8, pp. 4426–4432, 1981.

[235] M. Blander and J. L. Katz, "Bubble nucleation in liquids," *AIChE Journal*, vol. 21, no. 5, pp. 833–848, 1975.

[236] R. Massoudi and A. D. King, "Effect of pressure on the surface tension of water. adsorption of low molecular weight gases on water at 25.deg.," *The Journal of Physical Chemistry*, vol. 78, pp. 2262–2266, 10 1974.

[237] S. Maheshwari, M. van der Hoef, A. Prosperetti, and D. Lohse, "Dynamics of formation of a vapor nanobubble around a heated nanoparticle," *The Journal of Physical Chemistry C*, vol. 122, pp. 20571–20580, 09 2018.

[238] I. Weinrauch, I. Savchenko, D. Denysenko, S. M. Souliou, H.-H. Kim, M. Le Tacon, L. L. Daemen, Y. Cheng, A. Mavrandonakis, A. J. Ramirez-Cuesta, D. Volkmer, G. Schütz, M. Hirscher, and T. Heine, "Capture of heavy hydrogen isotopes in a metal-organic framework with active cu(i) sites," *Nature Communications*, vol. 8, no. 1, p. 14496, 2017.

[239] D. Chandler and P. G. Wolynes, "Exploiting the isomorphism between quantum theory and classical statistical mechanics of polyatomic fluids," *The Journal of Chemical Physics*, vol. 74, no. 7, pp. 4078–4095, 1981.

[240] A. Poma, M. Monteferrante, S. Bonella, and G. Ciccotti, "The quantum free energy barrier for hydrogen vacancy diffusion in na3alh6.," *Phys Chem Chem Phys*, vol. 14, pp. 15458–15463, Nov 2012.

[241] H. Lee and W. Cai, "Ewald summation for coulomb interactions in a periodic supercell," January 2009.

[242] P. P. Ewald, "The calculation of optical and electrostatic grid potential," *Ann. Phys. (Leipzig)*, no. 64, p. 253, 1921.

[243] J. W. P. S. W. de Leeuw and E. R. Smith, "Simulation of electrostatic systems in periodic boundary conditions. i. lattice sums and dielectric constants," *Proc. Roy. Soc. Lond. A*, vol. 373, pp. 27–56, 1980.

[244] J. W. P. S. W. de Leeuw and E. R. Smith, "Simulations of electrostatic systems in periodic boundary conditions. ii. equivalence of boundary conditions," *Proc. Roy. Soc. Lond. A*, vol. 373, pp. 57–66, 1980.

[245] D. Y. T. Darden and L. Pedersen, "Particle mesh ewald: An n log(n) method for ewald sums in large systems," *J. Chem. Phys*, vol. 98, p. 10089, 1993.